

EVOLUTION OF THE SIZE DISTRIBUTION OF
DROPS SETTLING IN A NON-CONTINUUM,
TURBULENT GAS

A Dissertation

Presented to the Faculty of the Graduate School

of Cornell University

in Partial Fulfillment of the Requirements for the Degree of

Doctor of Philosophy

by

Johnson Dhanasekaran

December 2019

© 2019 Johnson Dhanasekaran
ALL RIGHTS RESERVED

EVOLUTION OF THE SIZE DISTRIBUTION OF DROPS SETTLING IN A
NON-CONTINUUM, TURBULENT GAS

Johnson Dhanasekaran, Ph.D.

Cornell University 2019

The evolution of droplets in clouds is studied with focus on the 'size-gap' regime of 15-40 μm radius, where condensation and differential sedimentation are least effective in promoting growth. This bottleneck leads to inaccurate growth models and turbulence can potentially rectify disagreement with in-situ cloud measurements. Turbulent shear and differential sedimentation will both drive collisional growth in the 'size-gap' and the resulting coupled configurational dynamics is rigorously studied.

Droplet inertia will not significantly alter the local collision dynamics as it is weak in typical cloud conditions. However, weak inertia acting over a range of separation scales enhances the concentration of neighbouring drops available for collision. An inertial clustering model is developed which incorporates an inertia-induced drift velocity, relative diffusion due to turbulent shear and acceleration and differential sedimentation. This model is built upon available direct-numerical simulations and theoretical predictions in limiting conditions. It allows predictions over a broad range of particle separations, Stokes numbers, settling velocities and Taylor scale Reynolds numbers Re_λ .

The inertia-less local collision dynamics of sub-Kolmogorov droplets due to turbulence and gravity is studied for both a frozen linear flow approximation, in line with the classical work by Saffman & Turner, and for a stochastically fluctuating linear flow based on a Lagrangian velocity gradient model. It is found that the ideal collision rate has a significant dependence on Re_λ that has not been recognized in previous work. Inclusion of interparticle interactions strongly retards the collision rate. Non-continuum

hydrodynamic interactions of droplets in clouds dominates over colloidal forces, deformation, interface mobility, and medium compressibility but has not found extensive treatment in the previous literature. Hence, the collision efficiency, capturing retardation, is calculated over a large parameter space including Knudsen number (Kn), the ratio of mean free path to mean sphere radius, relative size of the interacting spheres, Re_λ , and strength of differential sedimentation relative to turbulence. Analytical fits of the collision rate results facilitate their use in drop population models. The steady linear flow approximation facilitated a detailed examination of the complex trajectory evolution that results from the competition of gravity and shear in the presence of non-continuum hydrodynamic interactions.

Utilising the collision rate results an evolution study is carried for cloud droplets from condensation controlled sizes of a few micron to differential sedimentation dominated sizes through the ‘size-gap’. For a complete description of cloud droplet dynamics non-collisional components of turbulence, mixing of droplets and water vapour fluctuations, are included. To resolve turbulent intermittency and retain a discrete drop distribution with manageable computational load a Monte Carlo scheme is used. Cloud packets are used to capture multiple realisations of the stochastic turbulent processes. The collection of droplets within each packet represents a unique history of turbulent intensity and water vapour concentration and so different packets represent different regions of the cloud. Turbulent mixing is modelled by moving droplets between different packets. The simulations reveal the strong effect of hydrodynamic interactions and the mean-free path on drop size evolution. Condensation in a uniform environment tends to create a nearly monodisperse drop size distribution making differential sedimentation weak. It is shown that turbulent shear and clustering as well as water vapour fluctuations play important roles in producing polydispersity and allowing droplet growth through the size gap.

BIOGRAPHICAL SKETCH

Johnson Dhanasekaran was born on 14th September, 1991 in a village near the city of Madurai in the state of Tamil Nadu in India. His nascent interest in science and math was encouraged by his mother and developed through the conducive environment at TVS matriculation higher secondary school in Madurai. He graduated in 2009 and moved to the Indian Institute of Technology, Madras for undergraduate studies and majored in Mechanical Engineering. His interactions with professors and fellow students led to an interest in academic research. His decision to pursue higher studies in fluid dynamics was made while working on his undergraduate project with Professor Sarit Das. Through advice of professors and peers he applied for and joined the Cornell mechanical engineering PhD program. There he immediately resonated with the research work carried out by Professor Donald Koch and joined his lab. He has spent the last six years working on various transport problems in fluid mechanics, ranging from fibres in near-creeping flow to droplets in turbulent clouds.

ACKNOWLEDGEMENTS

The last many years have been a journey that I could not have planned in my wildest dream in the summer of 2013. I am grateful to all who have shaped it and me.

I am thankful to my mum, dad, and sister for all the incalculable ways in which you have shaped, sacrificed for, and impacted my life. You have taught and shown me the true love. From this solid base I can trace all the significant achievements in my life.

I would like give my heartfelt gratitude to my PhD advisor Professor Donald Koch. Thank you for putting in the hours and effort towards my professional development. I have learnt a lot on how to frame and tackle research problems. I have a much broader and deeper problem solving skill-set. On the writing and presentation side your honest criticism and positive feedback have immensely helped.

I cannot fully express the many ways my friends have had an influence. I am ever in debt to my aunt Nirmala and her family for all the love and care I got when I first came to the US in 2013. Thank you Deb and Jay for opening up your house to my family and being such good friends to them. I am grateful for the patient piano lessons, the many awesome meals, and the care you have for people. My deep gratitude to Dee Dee for the hospitality towards my family. I appreciate your friendship Edith and the uncountable ways you have helped me and others. Thank you Ko-Ying for patiently teaching me driving and being a good friend. Thank you Esther for the many ways you have shared your time and resources to make a positive impact on many lives, including mine. Thank you Zhen Wah for driving me around in the bitter Ithaca winter. Mark and Jan your food, garden, and heart are beautiful. It made my time in Ithaca that much more beautiful. I would be remiss not to mention Ashok, Keerthi, Angel, Venus, Kaz, Sam, Dhyan, Shaun, Teddy, Hanna, Joanna, Kristy, David, Beth, and Daniel. You have individually and collectively impacted my life for which I am eternally grateful.

I am thankful to the many people who helped me navigate through graduate school. I

know I can count on Preetish after having gone through the pressure cooker of undergrad and challenges of living in a foreign country together. I am thankful to Mukul for helping me prepare for my A-exam and all the small helps that add up over time. I am happy to have collaborated with Anubhab for a significant portion of my PhD. I have learnt invaluable technical and interpersonal skills which, I am confident, will make me a better researcher and person. Thank you Neeraj for all the hours of talking through problems, academic or otherwise. I am grateful to Uday for sharing his code to implement the turbulent velocity field and saving me a lot of time. No less important are the many intellectually stimulating conversations we have had ranging from ramified particles in turbulence to the more abstract aspects of life. I am honoured to call you all friends.

I thank professors Lance Collins and Gregory Bewley for being on my committee. I would also like to recognise professor Roseanna Zia who previously was on my committee and provided very useful input during my A-exam preparation.

I thank U.S. National Science Foundation (NSF) grants 1435953, 1505795, 1803156, and Cornell Graduate fellowship for supporting me during my graduate studies. I am also thankful to professors Wolfgang Sachse and Michel Louge for the teaching assistant opportunities.

TABLE OF CONTENTS

Biographical Sketch	iii
Acknowledgements	iv
Table of Contents	vi
List of Tables	viii
List of Figures	ix
1 Introduction	1
1.1 Collision of bidisperse spheres settling in a non-continuum gas flow . .	2
1.2 Radial distribution function of polydisperse inertial spheres settling in homogeneous, isotropic turbulence	6
1.3 The effect of turbulence, gravity and microphysics on drop size distri- bution in clouds	8
1.4 The hydrodynamic lift of a slender, neutrally buoyant fibre in a wall bounded shear flow at small Reynolds number	10
1.5 Organization of the dissertation	13
2 Collision rate of bidisperse spheres settling in a non-continuum compres- sional gas flow	14
2.1 Abstract	14
2.2 Introduction	15
2.3 Formulation	21
2.4 Ideal collision rate	28
2.5 Mobility	30
2.5.1 Radial mobility	32
2.5.2 Tangential mobility	36
2.6 Collision rate with hydrodynamic interactions	38
2.7 Collision efficiency	50
2.8 Discussion	54
3 Collision rate of bidisperse spheres settling in a non-continuum turbulent gas flow	58
3.1 Abstract	58
3.2 Introduction	59
3.3 Formulation	65
3.4 Ideal collision rate	69
3.5 Collision rate with hydrodynamic interactions	73
3.6 Analytical approximation for the collision efficiency	79
3.7 Discussion	87
4 A model for the radial distribution function of polydisperse inertial spheres settling in homogeneous, isotropic turbulence	93
4.1 Abstract	93

4.2	Introduction	94
4.3	Inertial clustering model	98
4.4	Comparison against experiments	107
4.5	Application in cloud system	112
4.6	Summary	115
5	The effect of turbulence, gravity and microphysics on drop size distribution in clouds	119
5.1	Abstract	119
5.2	Introduction	120
5.3	Formulation	123
5.4	Results and discussion	128
5.5	Conclusion	140
6	The hydrodynamic lift of a slender, neutrally buoyant fibre in a wall bounded shear flow at small Reynolds number	142
6.1	Abstract	142
6.2	Introduction	143
6.3	Lift velocity of a fibre in the absence of wall contact	148
6.4	Lift velocity of a fibre experiencing wall contacts	161
6.5	Discussion	172
6.6	Conclusions	176
A	Inertial clustering model	180
A.1	Inertial clustering of monodisperse spheres with gravity	180
A.2	Algebraic model for inertial clustering	180
	Bibliography	184

LIST OF TABLES

- 3.1 Values of the coefficients of asymptotic forms of the continuum mobilities: $B_0, B_1, M_0, M_1, A, L_1$ at various values of κ . These have been obtained from the work by Jeffrey & Onishi[59] and Jeffrey[58] 83
- 3.2 Values of the fit parameters $p_{1,\epsilon}, p_{2,\epsilon}, p_{1g}$ and $p_{2,g}$ at various values of κ 84

LIST OF FIGURES

2.1	Sketch of the two spheres separated by \mathbf{r} and acted on by gravity and uniaxial compressional. 'I' is the test sphere of radius a_1 placed at the origin. It is approached by satellite sphere 'II' of radius a_2 . 'III', referred to as the collision sphere, is the locus of the centre of sphere 'II' when it is geometrically closest with sphere 'I'. The axis of compression indicated by the dash-dot line is inclined at an angle of α relative to gravity.	23
2.2	The surface-to-surface separation (h^*) at which various physical mechanisms become significant for drops is plotted as a function of the mean radius (a^*). The breakdown of continuum occurs at a separation that is independent of the droplet radius. Van der Waals forces become more important with decreasing a^* , eventually overtaking the breakdown of continuum at very small sizes. Deformability is the first mechanism to overtake non-continuum effects at large a^* . Compressibility and interface mobility never overtake non-continuum effects in the size range under consideration.	27
2.3	The collision rate for $\alpha = 0$ and the rate averaged over α are given as functions of Q , the relative strength of gravity to uniaxial compressional flow. The pure uniaxial compressional flow ($4\pi/(3\sqrt{3})$) and pure differential sedimentation results ($(\pi/2)Q$) are included for reference.	29
2.4	The percentage deviation of the $\alpha = 0$ ideal collision rate ($K_{ij}^0(\alpha = 0)$) from the angle averaged ideal rate (K_{ij}^0) as a function of Q , the relative strength of gravity to uniaxial compressional flow.	30
2.5	Λ_{11} is plotted as a function of ξ at $\text{Kn} = 10^{-2}$ and $\kappa = 0.9$ and compared with Λ_{11}^{bi} , Λ_{11}^c and Λ_{11}^{nc} . A small discontinuity at $\delta_0 = 0.26$ in the fit presented by Sundararajakumar & Koch[113] and given in equation (2.16) leads to the discontinuity seen at $\xi = 2.6 \times 10^{-3}$	35
2.6	A and L as a function of ξ for $\text{Kn} = 10^{-2}$ and $\kappa = 0.9$	35
2.7	Tangential mobility for sedimentation from twin multipole (M_f), lubrication (M_n) and the uniformly valid expressions (M) at $\kappa = 0.9$. Here $e_1 = 2 \times 10^{-2}$ is used in equation (2.19) to obtain the uniformly valid M	37
2.8	B and M as functions of ξ for $\kappa = 0.9$	38
2.9	The influx-efflux boundary on the collision sphere is shown for various configurations. In (a) $Q = 10$ and $\alpha = 30^\circ$ and two distinct influx regions exist on the collision sphere. In (b), with $Q = 20$ and $\alpha = 60^\circ$, the two influx regions are close to each other. In (c), with $Q = 40$ and $\alpha = 45^\circ$, there is only one influx region, but the influx-efflux boundary is has two lobes reflecting the lingering effects of the uniaxial compressional flow. In (d), with $Q = 60$ and $\alpha = 89^\circ$, there is a single influx region and the two lobes are less prominent.	41

2.10	The boundaries of the collection of trajectories constituting \mathbb{S} (at r_∞) is shown for $\text{Kn} = 10^{-3}$. The angles are in degrees. In (a) $Q = 10$ and $\alpha = 30^\circ$. This configuration has two nearly identical patches at r_∞ and only one of them has been shown here. For $Q = 20$ and $\alpha = 60^\circ$ (b) and (c) shows two distinct envelopes of colliding trajectories at r_∞ . In (b) the trajectories through the traversal mechanism close to the collision sphere form the bump on the left end. For $Q = 40$ and $\alpha = 45^\circ$ there is only one envelope of colliding trajectories at r_∞ which is shown in (d). Only one envelope of colliding trajectories is expected at higher Q , except for $\alpha \approx \pi/2$. Two envelopes exist for $Q = 60$ and $\alpha = 89^\circ$, which are shown in (e) and (f) respectively.	43
2.11	The collision rate is plotted as a function of Q , the relative strength of gravity to uniaxial compressional flow, for $\kappa = 0.9$, $\alpha = 0$, and $\text{Kn} = 10^{-1}$, 10^{-2} , and 10^{-3} . The collision rate is higher for larger values of Kn	46
2.12	The time-reversed trajectories in the X-Z plane are shown for $\kappa = 0.9$, $\alpha = 0$ and $\text{Kn} = 10^{-3}$. Symmetry is exploited to analyse only half of the collision sphere. In (a) $Q = 10$ and both the northern and southern trajectories are plotted. The subsequent plots only show trajectories which are in the southern hemisphere for $\xi \ll 1$. In (b) for $Q = 26$ closed trajectories start to appear. In (c) $Q = 30$ and a few southern hemisphere trajectories traverse over the efflux region of the collision sphere and pass around the northern hemisphere with increasing ξ . In (d) $Q = 32$ and it is only by passing around the northern hemisphere that southern hemisphere trajectories can contribute towards collision rate. In (e) $Q = 34$ and there is no route remaining for southern hemisphere trajectories to contribute towards collision. At $Q = 50$, as seen in (f) there are no trajectories arising in the southern hemisphere of the collision sphere.	47
2.13	The collision rate is plotted for Q , the relative strength of gravity to uniaxial compressional flow, spanning 26 to 33 for $\kappa = 0.9$, $\alpha = 0$ and $\text{Kn} = 10^{-3}$. The monotonically decreasing curve corresponds to the collision rate due to trajectories that stay in the negative Z half space at all separations. The curve with a maximum corresponds to the collision rate of traversal particles that collide in the southern hemisphere but have positive Z coordinates at large separations.	48
2.14	The collision rate is plotted as a function of Q , the relative strength of gravity to uniaxial compressional flow, for $\kappa = 0.5$, $\alpha = 0$, and $\text{Kn} = 10^{-1}$, 10^{-2} , and 10^{-3} . The collision rate is higher for larger values of Kn	48

2.15	The collision rate is plotted as a function of Q , the relative strength of gravity to uniaxial compressional flow, for $\kappa = 0.9$, $\text{Kn}=10^{-3}$ and $\alpha = 30^\circ, 45^\circ, 60^\circ$ and 89° along with $\alpha = 0$ for comparison. They start off together at $Q = 0$ and converge in the $Q \rightarrow \infty$ limit. At intermediate Q the spread across α is large.	49
2.16	The collision efficiency is plotted as a function of Q , the relative strength of gravity and uniaxial compressional flow at $\alpha = 0$ for $\kappa = 0.9$ and $\text{Kn}=10^{-1}, 10^{-2}$, and 10^{-3} . The collision efficiency decreases with decreasing Kn	50
2.17	The collision rate is plotted as a function of Q , the relative strength of gravity and uniaxial compressional flow at $\alpha = 0$ for $\kappa = 0.5$ and $\text{Kn}=10^{-1}, 10^{-2}$, and 10^{-3} . For all Q and Kn the collision efficiency is lower than that for $\kappa = 0.9$	51
2.18	The collision efficiency is plotted as a function of Kn for the pure differential sedimentation and pure uniaxial compressional flow cases at $\kappa = 0.9$ and $\kappa = 0.5$. The two curves with the highest collision efficiency correspond to the pure uniaxial compressional flow while the two lowest are for pure differential sedimentation. In each case $\kappa = 0.9$ is more efficient than $\kappa = 0.5$ at all values of Kn	53
3.1	'I' is ideal collision rate K_{ij}^0 given as a function of the Re_λ for $Q = 0$, i.e. no gravitational effects. Variation of the inward flux with Taylor's Reynolds number is given by 'II'. Calculations performed with frozen velocity gradient during any given satellite sphere evolution is denoted by 'III'. All the error bars shown correspond to one standard error. 'IV' is the reference calculation of Saffman & Turner[97] and is insensitive to Re_λ . $\int P_\Phi \Phi^{1/2} d\Phi$ decreases with increasing Taylor's Reynolds number and has been multiplied by $\int_{(r=2)\&(n_i \Gamma_{ij} n_j < 0)} dAn_i \Gamma_{ij} n_j / \Phi^{1/2} \approx 1.7$ and given in 'V'. The predictions of the ideal collision rate fit, given in equation (3.7), has been shown with 'VI'.	70
3.2	The ideal collision rate K_{ij}^0 is given as a function of Q at only $\text{Re}_\lambda = 90$ and 2500 for sake of conciseness. The symbols correspond to the numerically calculated collision rate and the solid lines to the fit. The higher Re_λ corresponds to lower collision rate. The error bars correspond to one standard error. For reference the ideal collision rate predicted by Smoluchowski[106] for spheres settling in quiescent flow is given by the dashed line.	72
3.3	β decreasing with Kn is shown for $\kappa = 0.7$ and $\text{Re}_\lambda = 2500$. Figure (a) is in the pure turbulence limit ($Q = 0$) and figure (b) is for differential sedimentation limit ($Q \rightarrow \infty$).	76
3.4	The collision efficiency is shown as a decreasing function of κ for $\text{Kn}=10^{-3}$ and $\text{Re}_\lambda = 2500$. Figure (a) is in the absence of gravitational effects ($Q = 0$) and figure (b) is in a purely gravity driven flow ($Q \rightarrow \infty$). The error bars correspond to one standard error.	77

3.5	The dependence on Re_λ of the collision efficiency is shown here for $Kn= 10^{-2}$, $\kappa = 0.9$ at (a) $Q = 0$, (b) $Q \approx 1$ and (c) $Q \approx 10$. The error bars correspond to one standard error. β varies with Re_λ for moderate Q	77
3.6	The variation of collision efficiency with Q is shown for $Kn= 10^{-3}$ and $\kappa = 0.5$. The curve with symbols corresponds to the stochastic linear flow field with $Re_\lambda = 2500$. The error bars show one standard error. The solid line is the for frozen uni-axial compressional flow calculation, with compression axis aligned with gravity.	79
3.7	The collision efficiency is plotted as a function of Kn for $\kappa = 0.4$. Figure (a) is in the pure turbulence limit ($Q = 0$) and figure (b) is for pure-differential sedimentation ($Q \rightarrow \infty$). The symbols represent the results of the numerical calculation. The error bars correspond to one standard error. The solid lines are the analytical approximation, given in equation (3.14). The errors, when compared against the results of the numerical calculation, is minimal.	84
3.8	β is shown as function of κ at $Kn= 10^{-2}$. Figure (a) is in the absence of gravitational effects ($Q = 0$) and figure (b) is in a purely gravity driven flow ($Q \rightarrow \infty$). The symbols represent the results of the numerical calculation with errors bars of one standard error. The solid line is from equation (3.14) and agrees well with the data.	85
3.9	β versus Q is plotted for $Kn= 10^{-3}$ for $\kappa = 0.6$. The symbols represent the results of the numerical calculation and the error bars are at one standard error. The solid line is from the modified version of equation (3.14), with fitting parameters given in (3.16). The agreement is good across the parameter space.	86
4.1	$g(r)$ is shown as a function of r/η for $Re_\lambda = 597$ at $St = 0.1, 2, 20$ with symbols denoting DNS data from Ireland et al [53] and solid lines our model shown in equation (4.3). There is good agreement between the model and DNS results across the parameter space. As $r \rightarrow 0$ the highest value of $g(r)$ is at the intermediate value of St , which is in line with expected behaviour.	101
4.2	$g(r)$ is shown as a function of r for $St = 0.5$ and $Re_\lambda = 88, 224, 597$ with symbols denoting DNS data from Ireland et al[53] and solid lines are the radial distribution function obtained from equation (4.5). There is good agreement between the model and DNS results across the parameter space.	102
4.3	$g_{ij}(r)$ is shown as a function of r/η for three bidisperse calculations performed at $Re_\lambda = 90$ and $Fr = 0.3$. The symbols denote DNS data from Dhariwal & Bragg[34] and solid lines, representing our inertial clustering model, agree well with it.	104

4.4	$g_{ij}(a_i + a_j)$ is plotted as a function of a_j , with $a_i = 40\mu m$. This corresponds to a variation of St from 0.06 to 2.23. The DNS data from Ayala et al[4], calculated at $\epsilon = 0.04m^2/s^3$ and $Re_\lambda = 72.41$, is shown with symbols, while the solid lines show the results of our model. The errors are minimal at all points of comparison.	107
4.5	$g(r)$ is plotted as a function of r/η , with symbols corresponding to the experimental data from Salazar et al[99] and solid lines the predictions by our model. Here $\epsilon = 1.33, 4.9, 11 m^2/s^3$ corresponds to Re_λ of 108, 134, 147 and a mean $St = 0.08, 0.13, 0.2$	108
4.6	$g_{ij}(r)$ is shown as a function of r/η , with symbols denoting the experiment by Saw et al[100] performed at $\epsilon = 0.6m^2/s^3$ and $Re_\lambda = 440$ while the solid lines show the results of our model under these conditions. The binning of the reported size distribution is done with $St_i = 0.2-0.3$ and three different St_j , thus capturing both an effective monodispersity as well as bidispersity of droplets.	110
4.7	$g(r)$ is shown as a function of r/η for $Re_\lambda = 300, Fr = 1.2$, mean $St = 0.63$, and $\eta = 0.27mm$. The symbols and dashed line are the DNS data from the experiments and predictions of the fit by Petersen et al [90] respectively. The solid line shows our model which agrees with available experimental data and demonstrates the weakness of the reported experimental data based fit.	111
4.8	$g(r)$ is shown as a function of r/η . The symbols are the experimental data from Yavuz et al[124] while the solid lines are the predictions of our inertial clustering model. We compare against three experimental configurations corresponding to a mean $St = 0.22, 0.46, 0.84$, a mean radius of $7.1, 10, 20.7\mu m$ and standard deviation of $0.3, 0.6, 0.7\mu m$ respectively. The flow condition for the first two correspond to $\epsilon = 2.1m^2/s^3, Re_\lambda = 229$ while the last one is at $\epsilon = 0.3m^2/s^3$ and $Re_\lambda = 155$. Poor agreement is seen across the parameter space and is attributed to experimental errors.	112
4.9	$\log_{10}(K/K^0)$ is shown using a contour plot spanning a_m and σ_a . Significant enhancement is observed across the parameter space. $g(r)$ plays the strongest role close to monodispersity and in size range of about 40 to $70\mu m$	115
4.10	K/K^0 is shown as a function of σ_a at $a_m = 20, 30, 40, 50\mu m$, representing typical sizes in and around the 'size-gap'. For the sizes shown here larger sizes leads to more enhancement. Rapid decay is observed with σ_a at all values of a_m	116
5.1	The number density of droplets per given radius n_a is plotted against radius at early (600 seconds), intermediate (4800 seconds) and long (7200 seconds) time evolution of our model. The drop size distribution does not conform to any specific form at all times. Starting off Gaussian it transitions to a skewed distribution as the system evolve.	129

5.2	Shown is the evolution under the influence of condensation and water vapour fluctuations and it leads to a nearly monodisperse drop size distribution insensitive to initial conditions. Figure (a) shows evolution of a_v while figure (b) shows \mathcal{D} . In the Legend 'I', 'II', 'III', 'IV', and 'V' correspond initial Gaussian drop size distributions with means of 0.25, 0.5, 1, 1, 2 μm and standard deviations of 0.25, 0.1, 0.1, 0.5, 2 μm , respectively.	131
5.3	a_v (a) and \mathcal{D} (b) are shown as a function of time for droplets evolving by condensation, gravitational collisions, turbulent mixing of droplets, and water vapour fluctuations. Increasing f from %0.1 to %1 enhances the growth rate.	132
5.4	The growth across the 'size-gap' due to turbulent collisions is shown by varying ϵ from 0.001 to $0.1\text{m}^2/\text{s}^3$. The collision rate used couples turbulence with differential sedimentation and the evolution dynamics include condensation but exclude turbulent mixing of droplets and water vapour fluctuations. Figure (a) shows evolution of a_v while figure (b) shows \mathcal{D}	133
5.5	The complex role turbulence plays in crossing the 'size-gap' is shown by plotting a_v against time for the full calculation (solid lines) and the the result from figure 5.4 with only condensation, and coupled turbulent-gravitational collisions (dashed lines). The dashed curve with larger radius growth corresponds to $\epsilon = 0.1\text{m}^2/\text{s}^3$ while the other is for $\epsilon = 0.001\text{m}^2/\text{s}^3$	134
5.6	a_v evolution for $\beta = 1$, $g(r) = 1$, and $\Gamma_0 = \frac{1}{\tau_\eta}$ along with the full calculation for reference is shown.	135
5.7	Cumulative average of $g(a_1+a_2)$ for the full calculation is shown for $\epsilon = 0.001, 0.003, 0.01, 0.03, 0.1 \text{ m}^2/\text{s}^3$. A non-monotonic behaviour with time is observed for the enhancement of collision rate due to inertial clustering.	136
5.8	Evolution of the two important parameters of inertial clustering as a function of time shown for $\epsilon = 0.001, 0.003, 0.01, 0.03, 0.1 \text{ m}^2/\text{s}^3$. Figure (a) shows the mean Stokes number and figure (b) the magnitude of the difference in non-dimensional settling velocity.	137
5.9	Evolution of the drop size distribution is shown the full calculation performed at fixed mean free path. Figure (a) shows evolution of a_v while figure (b) shows \mathcal{D} . $\lambda_g = 50, 70, 100, 200, 500 \text{ nm}$ are chosen along with $\beta = 1$ calculation for reference.	138
5.10	Impact of varying initial ground conditions is shown by tracking a_v . Figure (a) considers different initial pressures, from $P_0 = 1$ to 0.85 atmospheres. In figure (b) we vary the initial temperature from $T_0 = 283$ to 313 K . The dashed line corresponds to evolution with $T_0 = 313K$ but λ_g given a history of evolution corresponding to $T_0 = 293K$	139

6.1	Sketch of fibre motion in the flow gradient plane of the imposed shear flow inner region close to a wall. '1' is along the direction of the flow, '2' is the velocity gradient direction which is normal to the wall and '3' is along the vorticity of the imposed flow. The fibre is oriented along the unit vector \mathbf{p} , with s being the coordinate along the fibre.	149
6.2	Lift velocity for a sphere as a function of distance from the wall in the inner region. h^* represents the dimensional distance of the sphere of radius a from the wall. The lift velocity is obtained using the lift force calculation of Cherukat & McLaughlin[25] in conjunction with Stokes resistance functions [18, 29]	159
6.3	Variation of the $O(\epsilon\text{Re})$ fibre lift velocity as a function of distance from the wall. Circles show the evaluated data and the line shows the fit given by $v_{l1} = -0.0057/h^2 - 0.0044/h + 0.0303$	160
6.4	Variation of the $O(\text{Re})$ lift velocity calculated based on the first two terms of the slender body theory expansion for a fibre and expressed as a function of distance from the wall at various aspect ratios. The aspect ratio of the curves going from highest to lowest asymptote values are 25, 100, 700, and 10^4 . Circles represent the lift velocity at $O(\epsilon)$	161
6.5	Trajectory of the fibre centre-of-mass for $\kappa = 100$ in a flow with $\text{Re}=10^{-3}$	167
6.6	Trajectory of the fibre centre-of-mass for $\kappa = 100$ in a flow with $\text{Re}=10^{-3}$ shown over a long period of time. The rate at which the fibre moves away from the wall is faster for a sticking contact. The model evolution from equations (6.48) and (6.49) agrees well with the full simulation.	167
6.7	Lift velocity experienced by the fibre for $h < 1$	170
6.8	Variation of lift velocity v_l over the inner region, at aspect ratios of 25 and 100. For $h > 1$ the curves are in ascending order of aspect ratio going from top to bottom. For $h < 1$ the scaled velocity is independent of aspect ratio and both the sticking and frictionless contact cases are shown.	173
A.1	$g(r)$ is shown as a function of r/η for $\text{Re}_\lambda = 398$ at $Fr = 0.052$ and $St = 0.2, 1$ with symbols denoting DNS data from Ireland et al[54] and solid lines our model shown in equation (4.3). There is good agreement between the model and DNS results across the parameter space.	181
A.2	$g_{ij}(r)$ is shown as a function of r/η for three bidisperse calculations performed at $\text{Re}_\lambda = 90$ and $Fr = 0.3$. The symbols denote DNS data from Dhariwal & Bragg[34] and the solid lines are the predictions of the algebraic model of inertial clustering shown in equation (A.2). Good agreement is observed across the parameter space.	181

CHAPTER 1

INTRODUCTION

The evolution of the size distribution of droplets, especially in the 'size-gap' regime, of 15 to 40 μm radius is not well understood and will be the focus of this dissertation. For drops smaller than the 'size-gap' condensation controls growth while larger droplets collide through through differential sedimentation to form even bigger droplets. The bottleneck at the 'size-gap' can potentially be resolved through turbulence[48]. Hence a significant portion of the dissertation is dedicated towards accurately calculating the collision rate due to the coupled effects of turbulent shear and differential sedimentation.

Droplet inertia is weak in typical conditions in clouds[4] and, hence, not expected to impact the collision dynamics. In the absence of inertia, the collision rate is calculated for the coupled configuration. A frozen background flow analysis, in line with the approximation used in the classical study by Saffman & Turner[97] for the sub-Kolmogorov $O(10\mu\text{m})$ droplets present in a clouds with typical Kolmogorov length scale of 1 mm[48], is carried out to understand the qualitative behaviour of the collision dynamics. To capture stochasticity arising from the highly non-Gaussian turbulent velocity fields a Lagrangian velocity gradient model developed by Girimaji & Pope[44] is used. In both of these calculations uniformly valid hydrodynamic interactions that include non-continuum lubrication smoothly transitioning to continuum results at large separation are used. It will be shown that this is the dominant interparticle interaction for $O(10\mu\text{m})$ droplets in clouds. While droplet inertia might not affect collision dynamics of droplets in clouds it will increase local concentration and thus boost the collision rate. A model will be developed evaluates this, including the attenuation of clustering induced by differential sedimentation for disparate particle sizes. Resolving this will be crucial to studying growth in the 'size-gap' as condensation drives the drops to a nearly

monodisperse distribution while differential sedimentation requires a difference in the size of interacting droplets. Incorporating all these results on the collision dynamics an evolution study is performed. It will be used to show the role of various mechanisms in the drop size evolution and inform physics relevant to the droplets of interest.

While the major thrust is on spherical entities colliding and growing the transport of non-spherical shapes is also studied. The drift of a fibre away from the wall at near Stokes flow conditions is calculated. The lift velocity is evaluated for two cases: of not touching and solid-body contact with the wall. These results will inform design of filtration devices that can exploit the hydrodynamic transport based on size as well as shape to retain particles.

1.1 Collision of bidisperse spheres settling in a non-continuum gas flow

In clouds the droplets are much smaller than the typical Kolmogorov length scale of about 1 mm. On such small scales the turbulence is experienced as a local instantaneous linear flow. If only the straining component is considered, that can drive collisions, there is only about 20% difference in ideal collision rate between the cases of infinite and correct correlation time[20]. Hence two separate calculations are performed. With a frozen linear flow important features of collision process are analysed. Using a stochastic linear flow the role of turbulent intermittency in the collision dynamics is captured. Next collision rate is calculated over a large parameter space pertinent to droplets in turbulent clouds and other such systems.

The first analytical result on collision rate was by Smoluchowski[106] for differential sedimentation without any interparticle interactions. In turbulent flow Saffman

& Turner[97] assumed a frozen uniaxial compressional flow with Gaussian statistics for the compression rate to determine the collision rate. An equivalent calculation in a frozen uniaxial compressional flow was carried out by Zeichner & Schowlater[130]. There is no result which spans between the gravity dominated and either linear flow limits. This is integral to evolution in the 'size-gap', where both gravity and turbulence are expected to be important, and the collision rate is evaluated over this parameter space.

Non-continuum hydrodynamics predominates for conditions typical of $O(10\mu m)$ water droplets in clouds over Van Der Waals forces, surface deformation, interface mobility, and compressibility of the gaseous media in facilitating drop-drop contact[113, 5]. However, collision studies, such as those by Wang et al[117], typically focus on Van Der Waals due to its dominance in liquid media. Davis[32] does consider breakdown of continuum in the differential sedimentation collision rate calculation but the hydrodynamics is not valid at surface to surface separations comparable to and smaller than the mean free path of the media. Chun & Koch[27] use the result for breakdown of continuum valid at all separations calculated by Sundararajakum & Koch[113] for turbulent collisions. However, they only consider a monodisperse suspension. In this study, in addition to bidispersity and accurate non-continuum hydrodynamics, the coupling of gravity with linear flow is included.

To capture size difference of interacting droplets a bidisperse analysis is performed. Three or higher droplet interactions are very rare in clouds due to very low volume fraction, of $O(10^{-6})$ [48]. Similar dilute conditions exist in aerosol reactors[7] and other systems of interest.

Particle inertia can shape the dynamics close to contact and increase the local concentration to impact the collision rate. We show that the former is very weak for conditions typical in clouds. The latter does not alter the collision dynamics and is treated

separately. Combining the collision rate result at zero inertia with the enhancement due to local inertial clustering is expected to generate accurate results for a droplet evolution study.

The results of this study while focusing on drop size evolution in clouds can be extended to other applications. In addition to industrial reactors this study will inform pollutant aggregation, secondary collisions in aerosol impactors, and collisions of droplets in sprays to name a few. The background flow in all of these cases can be approximated by one of the two forms of linear flow considered in this study. Acceleration can be visualised as an effective body force in application such as sprays. The role of inertia on collision dynamics and clustering is not expected to be significantly altered as the faster particle response is compensated by shorter characteristic times for the turbulent velocity field in the higher dissipation rate industrial flows. The media of interaction is air in all of these cases and so non-continuum hydrodynamics is expected to play a significant role. Thus this study performed with hard sphere collisions, due to ineffectiveness of surface deformation, will be relevant in capturing the evolution dynamics of the above mentioned suspensions.

For the frozen linear flow case, a uniaxial compressional flow is chosen, the most likely realisation in a turbulent flow[2]. In the ideal case an expression is obtained for the collision based on the inward radial velocity at contact and valid at all strengths of differential sedimentation to uniaxial compressional flow. With hydrodynamic interactions we derive an expression for the retardation in collision rate for the uncoupled problem using the evolution of the pair-probability, as estimate of the local particle concentration, first derived by [10] for particles in linear flow and extended to settling particles by [9]. For the coupled problem with hydrodynamics such an approach is not possible and trajectory analysis is used. One sphere is placed at the origin and the inward ve-

locity at contact of satellite spheres approaching from infinitely large separations sets the collision rate. The relative velocity is determined by uniaxial compressional flow, differential sedimentation, and uniformly valid hydrodynamic interactions, that include breakdown of continuum in lubrication and transitions to the continuum result at large separations.

Due to the complex coupling of uniaxial compressional flow, differential sedimentation, and uniformly valid hydrodynamic interactions highly convoluted trajectories arise. To properly resolve all of them trajectory analysis is used and the parameter space, including the relative strength and orientation of gravity to linear flow as well as the Knudsen number setting the relative size of breakdown of continuum and so the strength of hydrodynamic forces, is extensively spanned. Due to computational limitations the relative size of the interacting spheres is not spanned, but the results at the two different size ratios indicate this parameter is not important in generating qualitatively new trajectory evolution.

To obtain the collision rate for the stochastic linear flow case trajectory analysis and Monte Carlo integration are used. The linear flow itself is obtained from a model for the turbulent velocity field developed by Girimaji & Pope[44], which accurately captures the tails of the velocity gradient statistics. Variation of the ideal collision rate with the Reynolds number based on the Taylor microscale (Re_λ) is observed and has not been reported in previous studies such as those by Saffman & Turner[97]. This Re_λ dependence persists with the inclusion of differential sedimentation. Only in the gravity dominated extreme is there a convergence of collision rates at different Re_λ , to the result of differential sedimentation result of Smoluchowski[106].

Non-continuum hydrodynamics retards the collision rate. The collision efficiency is used to quantify this retardation over a large parameter space in Knudsen number

(Kn) capturing mean free path to characteristic size of interacting spheres, relative size of the interacting spheres, relative strength of differential sedimentation to turbulent characteristic velocities, and Re_λ . To concisely capture all of this a fit is developed based on a power law in Kn. This power law arises from an analytical solution for the asymptotic cases, of pure differential sedimentation and pure turbulence, and has been adapted to a fitting function. It is used to capture variation over Kn, relative size of the interacting spheres, and relative strength of differential sedimentation to turbulent characteristic velocities with high fidelity. There is no theory available to incorporate the dependence on Re_λ into the fit. The dependence of collision efficiency on Re_λ is weak and appears only in certain regions of the parameter space. Hence Re_λ dependence on the collision dynamics is captured through the ideal rate.

1.2 Radial distribution function of polydisperse inertial spheres settling in homogeneous, isotropic turbulence

Particle inertia delays particle response to the background flow leading to clustering in certain regions. Thus particles are more likely to encounter each other and so increase the probability of collision. In clouds, inertial clustering can potentially make a significant impact on the collision rate[91]. However, maximum enhancement is seen for perfect monodispersity. Rapid decorrelation in polydisperse cases is brought on by turbulent and gravitational accelerations[3]. Direct numerical simulation (DNS) studies such as those by Ayala et al[4] and Dhariwal & Bragg[34] only look at a very limited parameter space. Available analytical results, such as those by Ayala et al[3] and Lu et al[76] do not capture DNS results. Hence in this study a model for inertial clustering is developed that accounts for difference in size and differential sedimentation. The results

of this study will find application in $O(10\mu m)$ droplets evolving through collisions in clouds[91, 48] and planetesimal formation in proto-planetary disks[85] to name a few.

To capture the difference in size in a dilute suspension, as is typical in clouds[48], bidispersity of pairwise interactions is used. The relative acceleration induced, both by turbulence and gravity, decorrelates the turbulent shear induced motions that drive clustering below a certain separation of particle pairs[26, 76]. This crossover length can occur at any separation due to large variations possible in the parameter space. Hence, the radial distribution function, a measure of concentration enhancement at a given separation from a test particle, needs to be resolved at all length scales of turbulence. This result is not available in literature even for the monodisperse case.

First the radial distribution function is calculated for the monodisperse case at all length scales of turbulence using theoretical insights available at different regimes of turbulence[26, 17] and direct numerical simulation data[53, 54]. This result is valid at all possible strengths of particle response time to fluid response time.

An analytical expression for the radial distribution function of unequal particles in a turbulent flow, without any effects of gravity, has been derived by Chun et al[26] by solving the drift-diffusion equation for clustering. The balance leads to a result containing the crossover length from the effectively monodisperse large separation to the plateauing when particles are close. Lu et al[76] include gravitational effects by estimating the crossover length at which the differential sedimentation and turbulent velocities become equal. In this study decorrelation due to differential sedimentation is accurately resolved through estimating a diffusion it induces in the particle clusters. This, in turn, is used to solve the drift-diffusion equation, with inputs from literature on diffusion due to turbulent shear and acceleration. The drift component is not expected to be sensitive to size difference and is determined from an equivalent monodisperse result. The order one fit-

ting parameters are determined by comparing the model against DNS data for bidisperse inertial clustering in the presence of gravity performed by Dhariwal & Bragg[34].

The inertial clustering model is used to predict radial distribution functions reported by experimental studies. To account for the polydispersity inherent in experiments the bidisperse radial distribution function is averaged over the reported particle size distribution. The model is surprisingly robust as the errors, when compared with experiments, are minimal despite not having determined the order one corrections for conditions typical in experiments. It also provides a reliable means of determining the radial distribution function to small particle separations, in the dissipative range. In contrast fits of the radial distribution function using experimental, such as those by Peteresen et al[90], show significant errors when extrapolated to the dissipative range.

The clustering model is used to predict the enhancement of collision rate for conditions typical in clouds. The effect of the mean radius and the spread in the distribution are measured. Maximum enhancement is found to occur at sizes just beyond the 'size-gap', the regime of interest in cloud modelling. Significant enhancement within the 'size-gap' is found but it rapidly decays as the size distribution becomes broad. This indicates that inertial clustering can play a significant role in drop size evolution especially condensation leads to a nearly monodisperse distribution.

1.3 The effect of turbulence, gravity and microphysics on drop size distribution in clouds

Differential sedimentation drives collisional growth to drizzle sized drops in clouds. For this mechanism the necessary relative velocity is achieved through significant difference

in settling velocities of the interacting droplets. The settling velocity is significant only for droplets of radii greater than $40 \mu\text{m}$. On the other end of the spectrum condensation controls the growth of droplets less than $15 \mu\text{m}$ radius and creates a nearly monodisperse distribution. This leaves the 15 to $40 \mu\text{m}$ size range, referred to as the 'size-gap', unaccounted for, with current models underpredicting the polydispersity and overpredicting the time to rain formation[48]. Many mechanisms have been proposed to resolve this, such as ultra-giant cloud condensation nuclei[69]. In this study the focus is on the role of turbulence, including its effect on collisional growth.

Turbulence can drive collisions, mix droplets, and induce fluctuations in the local water vapour content. All of these mechanisms of turbulence are explored along with condensation and differential sedimentation driven growth. Turbulent intermittent events can form a few large droplets that can aid in crossing the 'size-gap'[65]. To resolve this properly the discrete nature of the distribution is retained. However, for a computationally manageable simulation a Monte Carlo scheme is used with one Monte Carlo droplet representing many real droplets.

The probability of collision in the Monte Carlo scheme is set by the collision rate that couples differential sedimentation with turbulence and incorporates the effects of non-continuum hydrodynamics. The inertial clustering developed in this study captures droplet inertia effects on the collision rate.

Packets are used to capture different regions and histories of evolution in the cloud. Each packet represents a collection of droplets with one realisation of the turbulent processes. Moving droplets across packets allows getting an estimate of mixing of droplets due to large scale turbulent motion.

There are multiple parameters and various mechanisms under consideration in the

simulation of clouds. To concisely capture their impact on the evolution, metrics of the drop size distribution are reported, namely the volume averaged mean radius and dispersion. The full size distribution is shown only for a few sample cases.

The importance of the various mechanisms of turbulence is tested by selectively turning them off and performing the evolution. A similar test for the components of the collision dynamics, namely non-continuum hydrodynamics and inertial clustering, will be carried out. This will inform the physics important to evolution dynamics of the droplets in clouds.

Finally simulations representative of altitude, latitude, and seasonal variations are performed, by changing ground pressure and temperature. Trends in the observed droplet growth are explained through the insight obtained into the physics important for their evolution.

1.4 The hydrodynamic lift of a slender, neutrally buoyant fibre in a wall bounded shear flow at small Reynolds number

The hydrodynamic transport of particles can play a crucial role in filtration[38]. Filtration studies that focus on this mechanism typically consider spheres but shape can also play a role[79]. To understand the role of shape a high aspect ratio fibre is considered. To quantify the impact on filtration the drift velocity near a wall in simple shear flow is calculated.

Stokes flow reversibility implies that a fibre at zero Reynolds number will undergo periodic motion but have no net drift away from the wall[123]. Thus, small but finite, inertia is needed to break the stress symmetry and move the fibre perpendicular to the

wall. The lift velocity is evaluated with a regular perturbation analysis in inertia in the viscous dominated 'inner' region, corresponding to separation from the wall being much smaller than the Oseen length. There are two scenarios possible close to the wall: no wall contact and solid-body contact driven evolution. Detailed calculations are performed for both these cases. In the 'outer' region, with separations from the wall being comparable to or greater than the Oseen length, requires singular perturbation analysis in inertia. Hence only a qualitative description of the inertial lift in this large separation regime is given.

For a fibre close to but not touching the wall the finite inertia disturbance velocity drives the motion away from the wall. However this velocity field is very hard to compute. Instead the generalised reciprocal theorem, that only requires knowledge of the Stokes disturbance velocity, to compute the net drift away from the wall at finite inertia is used.

To obtain the disturbance velocity the fibre is represented with a collection of point force singularities and an associated force distribution. The force distribution is obtained from slender-body theory solved for high aspect ratio[8] and the first two terms of the expansion are retained. The no-slip wall is captured by an appropriate collection of image point forces, force dipoles and potential dipoles[14].

The configuration of the fibre plays a very important role in the drift away from the wall. To obtain a net lift velocity the instantaneous drift is averaged over the periodic motion executed by the fibre[123]. This periodic motion is accurately described by Jeffery orbits[57, 108, 82]. Only the Jeffery orbit in the flow-gradient plane is considered as finite inertia causes high aspect ratio particles to spiral towards this configuration[110, 96, 39, 40, 31]. In this Jeffery orbit the fibre spends most of the time aligned in the flow direction and produces weak disturbance velocity. Significant contribution to lift

velocity happens only during the short-lived flipping. This effect is incorporated into the scaling of the lift velocity, along with finite inertia and thinness of the fibre. The time averaged lift velocity is reported that accounts for all of these effects at leading order in inertia and the first two terms in the expansion are obtained from slender-body theory.

Solid-body contact with the wall is possible when the fibre centre lies closer to the wall than the fibre half-length. In this configuration the preferred motion in the flow-gradient plane is not accessible. The resulting rotational torque coupled with contact force drives drift of the fibre away from the wall. It will be shown that the direct influence of the disturbance velocity on drift is not significant in this case. The nature of the wall contact, though, will be important. Hence the two extreme cases are considered. They are no-slip and frictionless contact.

To evaluate the lift velocity, analysis is performed on a quasi-steady Jeffery orbit, where the fibre just grazes the wall during flipping. The orientation perturbation induced by inertial rotation and wall contact is calculated over half of the Jeffery orbit. While the orientation change does not shift the centre of the fibre it does displace its ends. Enforcing a no penetration constraint at the wall results in the displacement of the whole fibre. This displacement of the centre of the fibre away from the wall averaged over the half Jeffery orbit period gives the lift velocity. The lift velocity obtained for both types of wall contact is verified by tracking the trajectory of the fibre. Excellent agreement is found for both no-slip and frictionless contact.

Finally the results are collated and lift velocity will be presented at all distances from the wall. It will be used to highlight important features of the hydrodynamic transport. It will also be used to give insight into designing a cross-flow filtration system.

1.5 Organization of the dissertation

The collision dynamics of a bidisperse suspension of spheres settling in non-continuum compressional gas flow is presented in §2. In §3 collision rate is calculated for a stochastic model, of spheres settling in a non-continuum turbulent gas flow. The radial distribution function is evaluated for polydisperse inertial spheres settling in homogeneous, isotropic turbulence in §4. In §5 the results obtained on the collision dynamics are used, along with pertinent microphysics as well as important mechanisms of turbulence, to study the evolution of the drop size distribution in clouds. In §6 a different type of transport problem is considered. The inertial drift of a high aspect ratio fibre is calculated near a wall at small but finite inertia.

CHAPTER 2
COLLISION RATE OF BIDISPERSE SPHERES SETTLING IN A
NON-CONTINUUM COMPRESSIONAL GAS FLOW

2.1 Abstract

Collisions in a dilute polydisperse suspension of spheres of negligible inertia interacting through non-continuum hydrodynamics and settling in a slow uniaxial compressional flow are studied. The ideal collision rate is evaluated as a function of the relative strength of gravity to uniaxial compressional flow and it deviates significantly from a linear superposition. This non-trivial behaviour is exacerbated by interparticle interactions based on uniformly valid non-continuum hydrodynamics, that captures non-continuum lubrication at small separations and full continuum hydrodynamic interactions at larger separations, retarding collisions driven purely by sedimentation significantly more than those driven purely by the linear flow. While the ideal collision rate is weakly dependent on the orientation of gravity with the axis of compression, with hydrodynamic interactions a change of more than 100% can be observed in some cases. This dramatic shift can be attributed to complex trajectories driven by interparticle interaction that prevents particle pairs from colliding or enable a circuitous path to collision. These and other important features of the collision process are studied in detail using trajectory analysis at near unity and significantly smaller than unity size ratios of the interacting spheres. For each case analysis is carried for a large range of relative strengths and orientations of gravity to the uniaxial compressional flow, and Knudsen number (ratio of mean free path of the media to mean radius).

2.2 Introduction

Collision and subsequent coalescence of drops or aggregation of particles influence the evolution of many commonly encountered systems. The evolution of cloud droplets experiences a bottleneck in the size-gap of 15 to 40 μm radius where condensation and coalescence driven by differential sedimentation are both slow processes[48]. For drops in this size range, turbulence driven motion is expected to augment differential sedimentation to enhance the coalescence rate. Theoretical studies on turbulence typically rely on direct numerical simulation. However, for Taylor's Reynolds number, of $O(10^4)$ typical in clouds, computational power is still insufficient to obtain results in a reasonable amount of time. Here, we will adopt a simple model of the turbulent flow experienced by colliding drops as a persistent uniaxial compressional flow. This model was first proposed by Saffman & Turner[97] and forms the basis of their well known prediction for the ideal collision rate of non-sedimenting drops in isotropic turbulence. Drops smaller than the Kolmogorov scale $O(1 \text{ mm in a cloud})$ experience turbulence as a local linear flow consisting of superimposed straining and rotational motions with the former being most effective in driving collisions. The distribution of straining flows in turbulence is skewed toward motions resembling uniaxial compressional motion [2]. While the strain rate in turbulence only persists for a strain of about $2.3(\epsilon/\nu)^{-1/2}$ [125] Brunk et al[20] found only about a 20% change of the ideal collision rate when accounting for the finite correlation time of the strain rate. Here ϵ is the dissipation rate of the turbulent process and ν the kinematic viscosity

Hydrodynamic interactions play an important role in interparticle collisions in a gas or liquid. Continuum hydrodynamic lubrication forces do not allow collisions to occur in finite time. Thus, other interparticle interactions become crucial to obtain a non-zero collision rate. In a gas, collision can occur due to the breakdown of the

continuum[113, 27]. We will see that for drop sizes where straining flow and sedimentation typically compete, non-continuum lubrication gas flow is more important than other considerations that may lead to collision including van der Waals attractions, mobility of the interface of the water droplets with air, and compressibility of the gas. Thus, we will evaluate the collision rate of particles driven by the coupled action of gravity and uniaxial compressional flow in the presence of a non-continuum gas. Additionally, since deformation of the droplets is not expected to be important we will treat them as hard spheres.

Our model will find application beyond cloud physics. One good example is industrial reactors producing carbon black, pigments and other commercially valuable materials [21]. These materials typically consist of aggregated particle clusters that develop in the turbulent gas flow of the aerosol reactor. The results of this study could provide a better understanding of the design of flow conditions to produce a desired degree of aggregation.

Collision of spheres settling in a local linear flow may arise in many non-turbulent systems. In systems designed to remove particles such as porous aerosol filters [55] and impactors [77] interparticle collisions driven by gravity and the local linear flow may affect the particle size distribution in non-dilute aerosols. The efficiency of atomization of drops in applications such as engines can be impeded by coalescence [70] driven by deceleration of the spray, experienced by droplets of different size as a differential body force, and a local uniaxial compressional flow in the jet.

One of the earliest studies on coalescence was carried out by Smoluchowski[106] who found the ideal collision rate for two non-interacting spheres, with species i of radius a_i and number density n_i , settling in quiescent flow with a relative velocity of V_{rel} to be $n_1 n_2 [a_1 + a_2]^2 V_{rel}$. Zeichner & Schowalter[130] determined the col-

lision rate of non-interacting spheres in a frozen uniaxial compressional flow to be $[4\pi/(3\sqrt{3})]n_1n_2\dot{\gamma}[a_1 + a_2]^3$, where $\dot{\gamma}$ is the compression rate. The coupled system, of spheres settling in linear flow, has not been analysed and will be the focus of this study. Literature exists that studies the uncoupled problems of particle motion due the linear flow [30, 117] or sedimentation [32] and includes continuum hydrodynamic interactions and colloidal forces with focus typically on van der Waals attractions. These collision studies are pertinent to particle motion in liquids where the van der Waals force is the predominant mechanism to overcome lubrication forces and enable surface-to-surface contact. In contrast, particle collision in a gas usually results from the non-continuum behaviour of the medium [113, 27]. But this case has not been extensively studied. For sedimenting spheres Davis[32] used a Maxwell slip approximation. This is only an accurate description of non-continuum behaviour at separations much larger than the mean free path of the gas. However, during a collision, particle pairs will pass through all possible separation gaps including those comparable to and smaller than the mean free path. The non-continuum behaviour valid at all separations was calculated by Sundararajakumar & Koch[113] and used by Chun & Koch[27] for a monodisperse suspension coagulating due to isotropic turbulence. There is no comparable study for a polydisperse system, frozen linear flow or differential sedimentation. In our study, we will analyse the collision rate for polydisperse spheres settling in a linear flow while interacting through non-continuum hydrodynamic interactions.

The collision dynamics and rate can be influenced by inertia. Gas inertia is weak relative to particle inertia and so only the latter is expected to exert any significant influence. An estimate of the particle inertia is Stokes number $St = \tau_p/\tau_f$, where the particle response time of species i is $\tau_{p,i} = 2\rho(a_i)^2/(9\rho_f\nu)$, ν is the kinematic viscosity, ρ is the particle density, ρ_f is the fluid density, g acceleration due to gravity, and the fluid response time is τ_f . If we consider $V_{rel} = 2((a_2)^2 - (a_1)^2)g/9\nu$ setting τ_f we get it to be

$(a_1 + a_2)/2V_{rel}$. We choose some typical values for water droplets in clouds: $\rho/\rho_f \approx 10^3$, $a_1 = 40\mu m$, $a_2/a_1 = 0.9$, and $\nu = 1.5 \times 10^{-5} m^2/s$ in air. This gives an estimate of St as 0.028 and establishes a very weak effect of particle inertia on the collision dynamics. If, instead, we consider τ_f set correlation of the local turbulent fluid flow it will be $(\nu/\epsilon)^{1/2}$. This St will not be so small, about 0.6 for $\epsilon = 0.01 m^2/s^3$. This is in line with the small to at most $O(1)$ estimates of St at typical conditions in clouds by Ayala et al [4]. Under such conditions the primary action of particle inertia is to enhance local concentration without altering the collision dynamics [112]. This enhancement has been extensively studied [53, 54, 34] and will not be considered here. Hence our study will be restricted to the case of $St = 0$, which will also reduce the parameter space to be explored. It should be noted that for smaller particles inertia leads to a body force which acts as a substitute for gravity, for example in industrial aggregators with particles typically smaller than $10\mu m$. However, the particles also experience significantly higher strain rates which is expected to lead to similar estimates of St .

We consider a dilute system since particle volume fractions are typically small $O(10^{-6})$ in clouds [48] and aerosol reactors, [7] and separators. Thus, we consider pairwise interactions. The flux of two spheres coming into contact with each other sets the collision rate. This flux, in turn, is related to the number density of spheres, the relative velocity of the spheres, and the particle pair trajectories resulting from this relative velocity. The relative velocity is given as the vector sum of contributions driven by uniaxial compression and differential sedimentation. These themselves, due to the inertia-less nature of the system, are expressed through a mobility formulation. These mobilities will capture the hydrodynamic, interparticle interactions.

For an ideal collision with no interparticle interactions, the relative velocity is solenoidal everywhere and the pair distribution function at contact equals the square

of the number density in the bulk suspension. Thus, it is possible to evaluate, for a pure uniaxial compressional flow or pure sedimentation (uncoupled) problem, the collision rate in terms of an explicit analytical expression [106, 130]. When coupled we obtain a closed form analytical result as a function of the relative strength of gravity to the linear flow for the special case in which the compressional axis is aligned with gravity. For the case of a distribution of compressional flows whose axes are isotropically distributed, we obtain a numerical result. These results capture collision dynamics pertinent to vertically aligned compressional flows and persistent isotropic turbulent flows, respectively.

Including hydrodynamic interactions changes the pair distribution function and retards the relative velocity when the spheres approach each other causing the collision rate to diminish relative to the ideal case. The collision efficiency, defined as the collision rate with interparticle interactions divided by the ideal collision rate, is used to quantify this effect. The collision efficiency cannot be expressed in a closed analytical form even for uncoupled driving forces. However it is possible to express it in terms of an integral over radial positions of an integrand involving the mobilities, which capture interparticle interactions [10, 9, 32, 117]. For coupled driving forces, even this is not possible and so trajectory analysis is used in our study. In this method a test sphere is fixed at the origin and its collision rate with a set of satellite spheres is used evaluated. Satellite spheres leading to collision, i.e, possessing inward radial velocity during contact, are integrated backward in time until they reach large separations. At large separations the flux is easier to evaluate since the pair probability reverts to its bulk value and the relative velocity can be computed without interparticle interactions. As a result, the collision rate can be evaluated in terms of the collisional area through which particles destined for collision pass.

The mobility matrix for a pair of particles can be expressed in terms of a set of coefficients that depend only on the radial separation and capture the hydrodynamic interactions between the particles. Comprehensive results are available for the mobilities of unequal sized spheres with continuum Stokes flow interactions[59, 58, 62]. However, continuum lubrication does not allow contact to occur in finite time and leads to a collision rate of zero. Sundararajakumar & Koch[113] showed that non-continuum hydrodynamic interactions allow collisions to occur in finite time. The importance of non-continuum interactions is quantified by the Knudsen number, Kn , defined as $\text{Kn}=\lambda_0/a^*$, where λ_0 is the mean free path and $a^* = (a_1 + a_2)/2$ is mean of the sphere radii a_1 and a_2 . We will use an expression for the non-continuum mobility that is valid when $\text{Kn} \ll 1$ for all interparticle separations h^* including separations $h^*/a^* = O(\text{Kn})$ that are comparable to the mean free path of the gas. Tangential mobilities are not expected to be strongly influenced by the breakdown of continuum, because the continuum flow tangential mobility remains finite at contact. Thus, continuum hydrodynamics will be used for the tangential motion at all separations.

The collision rate with non-continuum hydrodynamic interactions depends on the Knudsen number, representing the strength of non-continuum effects, the orientation of the compressional axis relative to gravity, and the relative strength of gravity and compressional flow as well as the particle size ratio $\kappa = a_2/a_1$. We will consider $\kappa = 0.9$ and 0.5 to sample cases with nearly equal and widely separated radii. We will more thoroughly span the other parameters to capture important features of the collision dynamics. We will particularly focus on the manner in which complex particle pair trajectories lead to non-trivial behaviour of the observed collision rate. A majority of the non-trivial behaviour is seen when the satellite and test sphere are close to each other. The hydrodynamic interactions cause the satellite sphere to be excluded from certain regions or open up new regions for the collision to occur. In a time reversed motion,

these complex trajectories include the satellite sphere either starting and ending on the test sphere or taking a circuitous path around the test sphere. Even at large separations from the test sphere the satellite sphere trajectories can change direction sharply due to the coupling of gravity with the uniaxial compressional flow. However, this class of complex trajectories does not directly affect the collision rate.

In the following sections, we will derive the collision rate for an inertia-less dilute system of spheres settling in uniaxial compressional flow. In §2.3 we will set up the governing equations and present the relevant scales in the system. Then we will evaluate the ideal collision rate for coupled gravitational and straining driven motion in §2.4. In §2.5 we will obtain the uniformly valid radial mobility, that has non-continuum lubrication as well as the continuum far field hydrodynamic effects included and the uniformly valid continuum tangential mobility. This will be used in §2.6 to evaluate the collision rate for a wide range of Kn, strength and orientation of the linear uniaxial compressional flow with respect to gravity. These calculations will be carried out for nearly similar as well as vastly different spheres. In §2.7 we will present results for the collision efficiency to describe the impact hydrodynamics has on the collision rate. We will also derive an expression for the collision efficiency in the pure linear flow as well as the purely gravity dominated case and present these results. Finally in §2.8 we will summarize the results of our study and discuss their implications.

2.3 Formulation

The collision rate K_{12} specifies the number of collisions per unit volume per time between spheres with radii a_1 and a_2 and number densities n_1 and n_2 . For drops that coalesce on collision, K_{12} can be used to determine the rate of change of the drop num-

ber density. For the simple case in which only two species are present gives the number of co is given as,

$$\frac{dn_1}{dt} = -K_{12} \quad (2.1)$$

In more general circumstances, the rate constant $C_{12} = K_{12}/(n_1n_2)$ can be used in an integral equation for the drop size distribution. Due to the dilute nature of the suspension three or higher body interactions are highly unlikely and only the interaction and collision of two species is considered. The two-species rate K_{ij} can be expressed as an integral of the flux of particle pairs over the collision area,

$$K_{12} = -n_1n_2 \int_{(r'=a_1+a_2)\&(\mathbf{v}' \cdot \mathbf{n}' < 0)} (\mathbf{v}' \cdot \mathbf{n}')P dA' \quad (2.2)$$

where \mathbf{v}' is the relative velocity, r' is the radial separation between the centre of the two spheres, P is the pair probability and captures the local species concentration relative to the bulk, \mathbf{n}' represents the outward normal at the contact surface. The inward radial velocity is $\mathbf{v}' \cdot \mathbf{n}' < 0$.

To simplify the analysis, we scale the problem. The characteristic length is chosen to be $a^* = (a_1 + a_2)/2$. This sets the range of non-dimensional radial separation between the centres of the two spheres to be $r = 2$ (referred to as the collision sphere) to ∞ (where one sphere does not influence the other). The geometry of the two-species system is captured through $\kappa = a_2/a_1$ the relative size of the spheres, with $\kappa \in (0, 1]$. Assuming negligible inertia, of both fluid and particle, allows scaling of the relative velocity with $\dot{\gamma}a^*$, the characteristic velocity in the frozen uniaxial compressional flow (the imposed linear flow), with $\dot{\gamma}$ being the strain rate along the axis of compression. The relative velocity due to gravity is captured through $Q = (2\rho g(a_2^2 - a_1^2)/[9\mu])/(\dot{\gamma}(a_1 + a_2)/2)$, where g is the acceleration due to gravity, and μ is the gas viscosity. A sketch of the two sphere system is shown in figure 2.1. The collision rate over the collision sphere, which

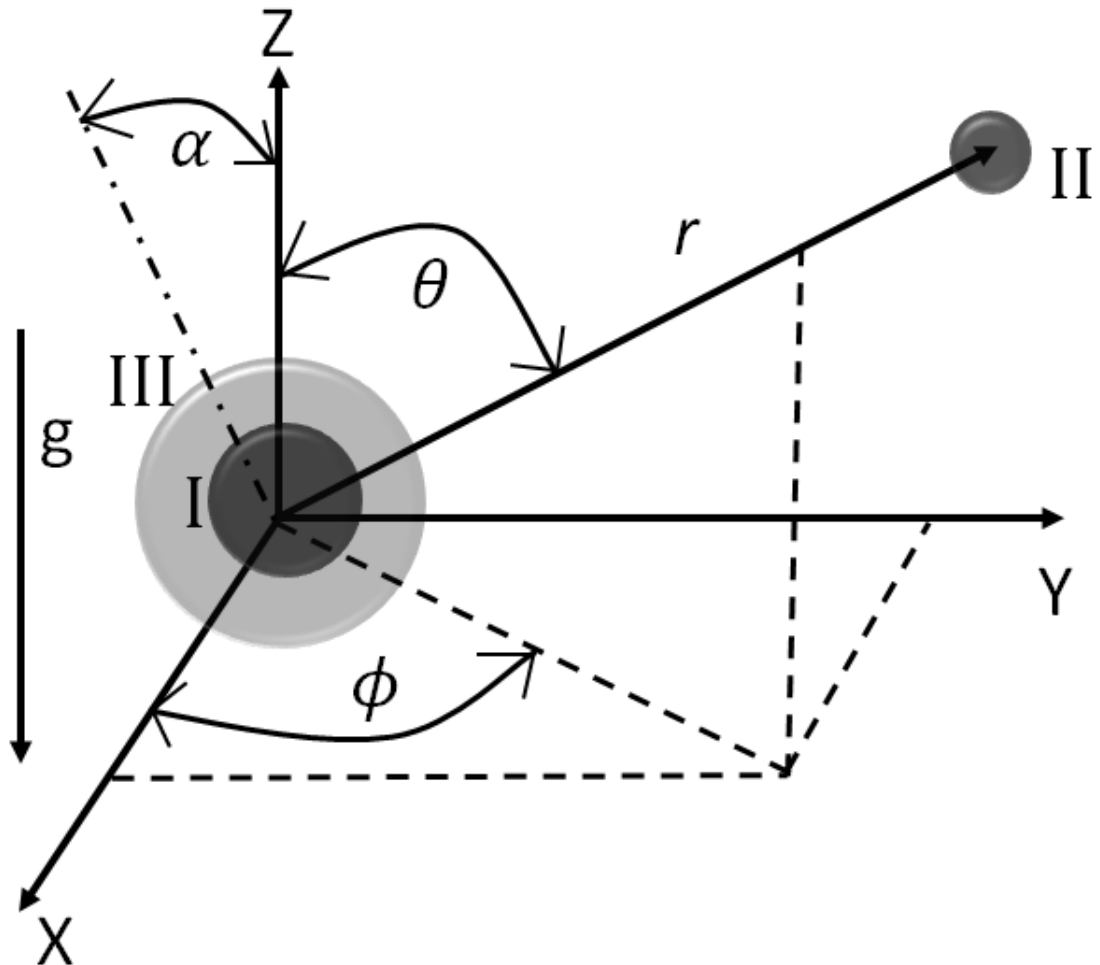


Figure 2.1: Sketch of the two spheres separated by r and acted on by gravity and uniaxial compressional. 'I' is the test sphere of radius a_1 placed at the origin. It is approached by satellite sphere 'II' of radius a_2 . 'III', referred to as the collision sphere, is the locus of the centre of sphere 'II' when it is geometrically closest with sphere 'I'. The axis of compression indicated by the dash-dot line is inclined at an angle of α relative to gravity.

scales as $n_1 n_2 \dot{\gamma} (a_1 + a_2)^3$, can be expressed as,

$$\frac{K_{12}}{n_1 n_2 \dot{\gamma} (a_1 + a_2)^3} = - \int_{(r=2) \& (\mathbf{v} \cdot \mathbf{n}' < 0)} (\mathbf{v} \cdot \mathbf{n}') P dA \quad (2.3)$$

The non-dimensional relative velocity \mathbf{v} in an extensional flow with rate of strain rate tensor \mathbf{E} and gravity directed along the negative Z-axis is given as,

$$\begin{aligned} v_i = & E_{ij} r_j - \left[A \frac{r_i r_k}{r^2} + B \left(\delta_{ik} - \frac{r_i r_k}{r^2} \right) \right] E_{kl} r_l \\ & - \left[L \frac{r_i r_k}{r^2} + M \left(\delta_{ik} - \frac{r_i r_k}{r^2} \right) \right] Q \delta_{k3} \end{aligned} \quad (2.4)$$

The mobility formulation is used because of the inertia-less nature of the system. A and B correspond to the radial and tangential mobility in linear flow while L and M correspond to the radial and tangential mobility due to sedimentation. The uniaxial compressional flow has one of its extensional axes parallel to the Y axis. The other extensional axis and the compressional axis lie in the X-Z plane. The angle between the compressional axis and gravity, is α . The rate of strain tensor is given as,

$$\mathbf{E} = \frac{1}{4} \begin{bmatrix} 3 \cos 2\alpha - 1 & 0 & -3 \sin 2\alpha \\ 0 & 2 & 0 \\ -3 \sin 2\alpha & 0 & -3 \cos 2\alpha - 1 \end{bmatrix} \quad (2.5)$$

In spherical coordinates (r, θ, ϕ) with the polar angle θ measured from the positive Z axis and the azimuthal angle ϕ measured from the X axis, the relative velocity is given as,

$$\begin{aligned} v_r = & -LQ \cos \theta + \frac{(A-1)r}{8} \{8 + 3[\cos 2\theta + \cos 2\alpha(1 + 3 \cos 2\theta) \\ & + 4 \cos 2\phi \sin^2 \alpha \sin^2 \theta + 4 \cos \phi \sin 2\alpha \sin 2\theta]\} \end{aligned} \quad (2.6)$$

$$\begin{aligned} v_\theta = & \frac{(B-1)r}{8} (4 \cos 2\theta \cos \phi \sin 2\alpha + \sin 2\theta [2 \cos 2\phi \sin^2 \alpha - 1 - 3 \cos \alpha]) \\ & + MQ \sin \theta \end{aligned} \quad (2.7)$$

$$v_\phi = -3(B-1)r \sin \alpha \sin \phi (\cos \alpha \cos \theta + \cos \phi \sin \alpha \sin \theta) \quad (2.8)$$

When calculating the ideal collision rate, there is no interparticle interaction of any kind and so the mobilities will take the trivial values, of $A = 0$, $B = 0$, $L = 1$, $M = 1$. For the full collision calculation the mobilities will capture the hydrodynamic interaction. The uniformly valid mobilities will capture non-continuum lubrication and long range continuum hydrodynamics.

The continuum hydrodynamic interactions between rigid spheres, while relevant at large separations, do not fully account for particle dynamics upon close approach. They would predict an infinite time for collision and so other mechanisms must become important to describe the relative velocity at small separations between colliding drops. For drops colliding in air due to the coupled effects of gravity and shearing flows, we expect the breakdown of the continuum to be the predominant mechanism facilitating collision. To test this hypothesis, we compare the surface to surface separation at which non-continuum gas flow modifies the velocity substantially to the separation where other mechanisms such as van der Waals forces, interface mobility, gas compressibility and drop deformability become important. We will use h^* to denote the dimensional surface-to-surface separation. We will consider water droplets in air, thus assuming the drop-to-medium viscosity to be ratio to be about $\hat{\mu} \approx 10^2$ and the density difference to be $\Delta\rho \approx 10^3 \text{ kg/m}^3$. We will consider nearly equal sized droplets $\kappa = 0.9$.

The mean free path of air at an altitude of a few kilometres, the height of typical atmospheric clouds, is about $0.1\mu\text{m}$. At $h_{\text{nc}}^* \approx 0.24\mu\text{m}$ the non-continuum lubrication force is half of its continuum counterpart (see Sundararajakumar & Koch[113] for details) and we define this as the critical gap for the onset of non-continuum effects. The finite viscosity ratio of drop and air allows the drop surfaces to move tangentially at sufficiently small h^* . The lubrication resistance between two drops transitions from an $O(\mu V_{\text{rel}} a^{*2}/h^*)$ scaling for nearly rigid drops to an $O(\hat{\mu}\mu V_{\text{rel}} a^* \sqrt{a^*/h^*})$ scaling for a

highly mobile interface [33], where the relative velocity of two droplets, V_{rel} , is given as,

$$V_{rel} = \frac{2(1 - \kappa^2)(\hat{\mu} + 1)\Delta\rho(a^*)^2g}{3(3\hat{\mu} + 2)\mu} \quad (2.9)$$

The gap at which the lubrication force between drops with mobile interfaces becomes half that for rigid particles is $h_{mob}^* \sim 1.61 \times 10^{-6}a^*$. The attractive van der Waals force acts against the resistive lubrication force to bring two spheres close together. The van der Waals radial mobility for this small separation limit is $(1 + \kappa)^2h^*/(2\kappa a^*)$ and competes with continuum lubrication at $h^* \sim [(1 + \kappa)/(2a^*)] \sqrt{\hat{A}/(4\pi L_1 \Delta\rho \kappa (1 - \kappa^2)g)}$. \hat{A} is the Hamaker constant and $L_1 = \lim_{r \rightarrow 2}(L/(r - 2))$ [32]. For $\kappa = 0.9$ we have $h_{vdW}^* \sim 1.43 \times 10^{-12}/a^* \mu m$. Lubrication flows can lead to a large increase in pressure. When the separation between two colliding particles reaches $h_c \equiv (3\mu V_{rel} a^*/2p_0)^{1/2}$, the change in pressure across the lubrication gap becomes comparable with the atmospheric pressure the p_o . Thereafter, the gas compresses more easily than it flows out of the gap. Gopinath & Koch[45] showed that this leads to a reduction of the lubrication force by a factor of two at a separation $h_{com}^* \approx 0.35h_c \approx 0.028a^{*3/2} \mu m$. Experiments on axisymmetric and non-axisymmetric aerosol droplet collisions have shown that different sets of collision outcomes are possible after the droplets start to deform - ranging from bouncing to coalescence [93, 6]. These outcomes would usually be associated with significantly large deformation of the droplet. Deformability becomes significant when the lubrication pressure becomes comparable to the Laplace pressure, corresponding to $2\sigma/a^* \sim 3\mu V_{rel} a^*/2h^{*2}$. The gap at which deformation becomes important is then $h_{def}^* \approx 67.37a^{*2} \mu m$ assuming the surface tension is $\sigma = 70$ mN/m [46].

The gap thicknesses at which the physical processes described above become important are shown as a function of drop radius in figure 2.2. The drop size range $a^* = 1 - 100 \mu m$ is chosen to correspond to cloud droplets. It is also the range of length scales at which particles or drops are likely to experience the combined effects

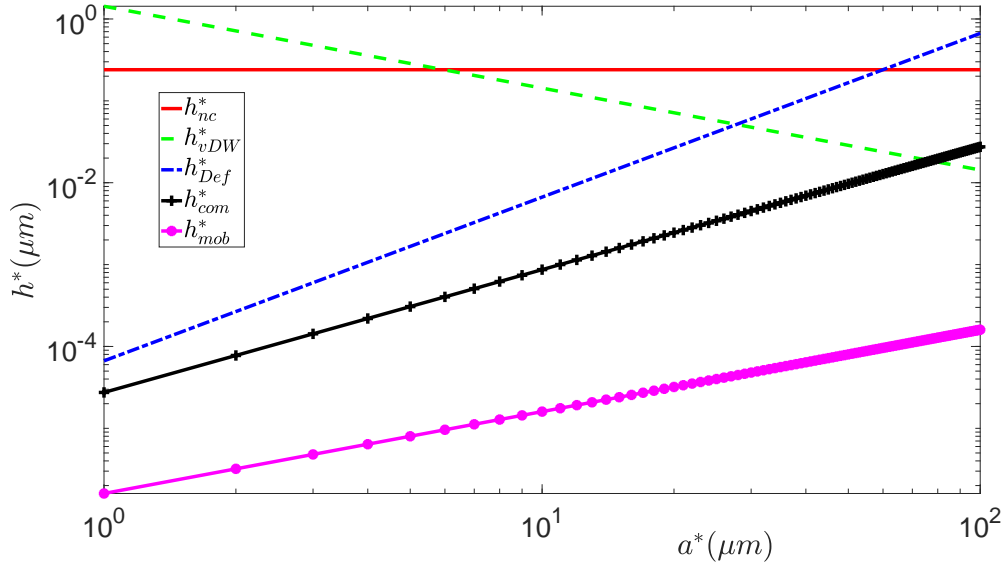


Figure 2.2: The surface-to-surface separation (h^*) at which various physical mechanisms become significant for drops is plotted as a function of the mean radius (a^*). The breakdown of continuum occurs at a separation that is independent of the droplet radius. Van der Waals forces become more important with decreasing a^* , eventually overtaking the breakdown of continuum at very small sizes. Deformability is the first mechanism to overtake non-continuum effects at large a^* . Compressibility and interface mobility never overtake non-continuum effects in the size range under consideration.

of gravitational settling and shearing motions with low to moderate inertia and little to no Brownian motion. While there is some influence of van der Waals forces at small particle size and drop deformation begins to play a role at the largest drop sizes non-continuum gas flow plays a predominant role in modifying the particle relative velocity at small separations in this size range. We will incorporate non-continuum hydrodynamics into the mobilities in §2.5 and present the resulting collision rate in §2.6. To better understand the underlying dynamics, however, we will first calculate the ideal collision rate, without any interparticle interactions, in the following section.

2.4 Ideal collision rate

In the ideal rate calculation, $P = 1$ everywhere due to the absence of interparticle interactions and the ideal collision rate K_{ij}^0 is,

$$\frac{K_{ij}^0}{n_1 n_2 \dot{\gamma} (a_1 + a_2)^3} = - \int_{(r=2) \& (\mathbf{v} \cdot \mathbf{n}' < 0)} (\mathbf{v} \cdot \mathbf{n}') dA \quad (2.10)$$

with \mathbf{v} determined using equation (2.6), (2.7) and (2.8) with $A = 0, B = 0, L = 1, M = 1$ everywhere due to the absence of hydrodynamic interactions.

For the special case, $\alpha = 0$, it is possible to obtain a closed form expression for equation (2.10). When the flow is purely uniaxial compressional flow ($Q = 0$ limit) there are two regions where collisions occur. One is in the northern hemisphere over the north pole with a boundary at the $\theta = \theta_1$ circle and the other is over the south pole with boundary at $\theta_2 = \pi - \theta_1$. Here $\theta_1 = \cos^{-1}(1/\sqrt{3})$. When the flow is purely due to differential sedimentation ($Q \rightarrow \infty$ limit) only the southern hemisphere contributes to the collision rate. Effectively $\theta_1 = 0$ and $\theta_2 = \pi/2$. For intermediate values of Q , θ_1 and θ_2 are given by,

$$\theta_{1,2} = \cos^{-1}\left(\pm \frac{\sqrt{Q^2 + 192} - Q}{24}\right) \quad (2.11)$$

Here, the positive sign is for θ_1 and the negative for θ_2 . Using this equation (2.10) is evaluated and the $\alpha = 0$ result is given as,

$$\begin{aligned} \frac{K_{12}^0(\alpha = 0)}{n_1 n_2 \dot{\gamma} (a_1 + a_2)^3} &= \frac{2\pi}{3\sqrt{3}} \left[c_+ + \mathcal{H}\left(4 - \frac{Q}{2}\right) c_- \right] \\ \text{where } c_{\pm} &= \left(1 + \frac{Q^2}{192}\right)^{\frac{3}{2}} \pm Q \frac{\sqrt{3}}{8} \left(1 - \frac{Q^2}{576}\right) \end{aligned} \quad (2.12)$$

where \mathcal{H} is the heaviside function. Insight into the collision rate at a fixed inclination of gravity to the uniaxial compressional flow will be important to the dynamics of particles in fibrous aerosol filters, impactors, and laminar jets since the flow experienced

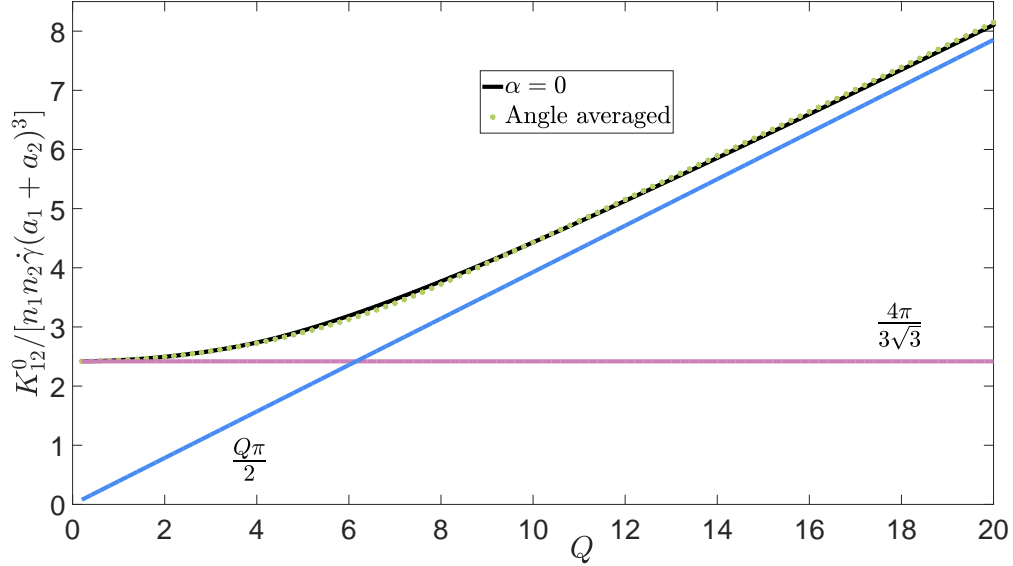


Figure 2.3: The collision rate for $\alpha = 0$ and the rate averaged over α are given as functions of Q , the relative strength of gravity to uniaxial compressional flow. The pure uniaxial compressional flow ($4\pi/(3\sqrt{3})$) and pure differential sedimentation results ($(\pi/2)Q$) are included for reference.

is expected to be steady and often gravity is aligned with the compressional axis. This result is shown in figure 2.3 as a function of relative strength of gravity to the linear flow. Plotted along with it is the collision rate averaged over all possible orientation of the compressional axis with gravity. This angle averaged result will inform the collision rate experienced by particles in isotropic turbulence, as is the case for droplets in size-gap regime of clouds and particles in industrial aggregators.

From figure 2.3 it is evident that the $\alpha = 0$ and the angle averaged result nearly overlap each other and have the same asymptotic behaviours. As $Q \rightarrow 0$ they correspond to pure uniaxial compressional flow and as $Q \rightarrow \infty$ to pure differential sedimentation. The collision rate for pure uniaxial compressional flow was found by Zeichner & Schowalter[130] to be $n_1 n_2 4\pi/(3\sqrt{3})\dot{\gamma}(a_1 + a_2)^3$. Smoluchowski[106] found the collision rate for pure differential sedimentation to be $n_1 n_2 2\rho g(a_2^2 - a_1^2)(a_1 + a_2)^2/(9\mu)$. For intermediate Q values, the ideal collision rate result is not a linear combination of

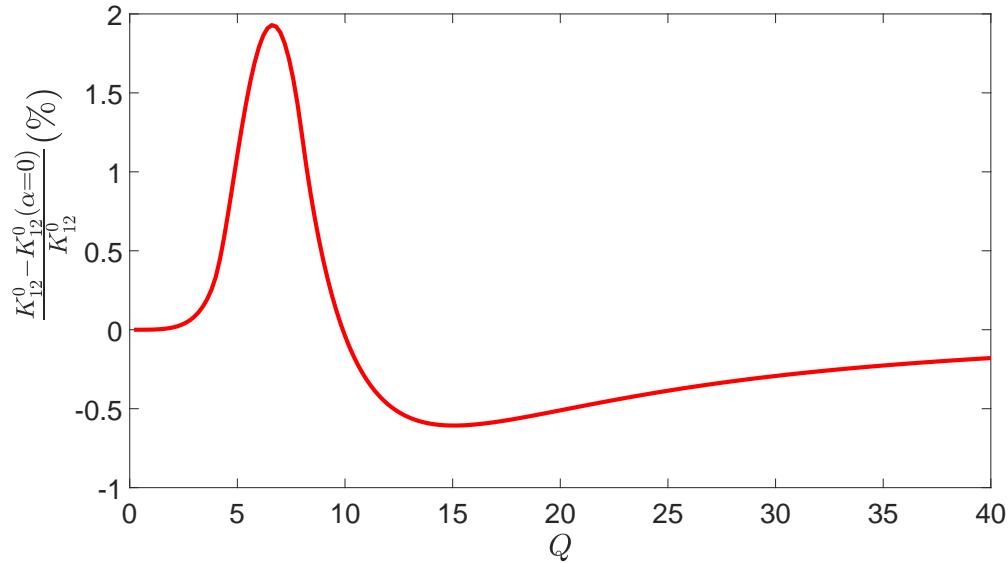


Figure 2.4: The percentage deviation of the $\alpha = 0$ ideal collision rate ($K_{ij}^0(\alpha = 0)$) from the angle averaged ideal rate (K_{ij}^0) as a function of Q , the relative strength of gravity to uniaxial compressional flow.

the rates resulting from the two driving forces acting independently. To highlight the slight dependence of the ideal rate on α , figure 2.4 gives the percentage deviation of the $\alpha = 0$ rate from the angle averaged rate. At moderate Q the deviation shows a highly non-trivial behaviour. The largest deviation occurs at around $Q \approx 6$ with another local extreme at $Q \approx 14$ and a change of sign at $Q \approx 10$. Thus, it is abundantly clear that the ideal collision rate cannot be expressed through any simple combination of the pure gravity or pure uniaxial compressional flow calculation.

2.5 Mobility

The mobility formulation for Stokesian suspensions is used when the forces acting on the particles are known and their motion needs to be determined. Thus, it is applicable to our collision rate calculation in an inertia-less system of spheres driven by a uniax-

ial compressional flow as well as an imposed gravitational force. The relative velocity due to these coupled effects is shown in equations (2.6), (2.7) and (2.8). We identified $A(r)$ and $B(r)$ as the radial and tangential mobility in linear flow while $L(r)$ and $M(r)$ correspond to the radial and tangential mobility due to sedimentation. These mobility components depend on r and are independent of θ or ϕ . Hydrodynamic interactions decay as $r \rightarrow \infty$ and so $A \rightarrow 1, B \rightarrow 1$ and $L \rightarrow 0, M \rightarrow 0$. Separate calculations for the mobilities can be performed at moderately large separations $\xi = r - 2 = O(1)$ and in the lubrication regime $\xi \ll 1$. Continuum lubrication will become important for $\xi < 10^{-1}$ leading to a radial mobility that decreases in proportion to ξ that would not allow for contact in finite time. Sundararajakumar & Koch[113] showed that non-continuum hydrodynamic interaction offers a weaker resistance to the radial motion of the two spheres approaching each other and allows contact in finite time. This, weaker, interparticle force will arise at $\xi = O(\text{Kn})$, where the Knudsen number is defined as $\text{Kn} = \lambda_0/a^*$, with λ_0 being the mean free path and $a^* = (a_1 + a_2)/2$. Thus, radial motion is set by non-continuum hydrodynamics for $\xi \leq O(\text{Kn})$ and full continuum hydrodynamics for $\xi \gg 1$ with a matching region corresponding to continuum lubrication valid for $\text{Kn} \ll \xi \ll 1$. This will be captured in the uniformly valid radial mobility derived below.

An important aspect of the tangential motion is the spheres rolling at the point of contact. It is possible due to the finite values tangential lubrication mobilities take at contact even with continuum hydrodynamics. In contrast to finite velocities induced by continuum-flow tangential mobilities, even at contact, non-continuum hydrodynamics is needed in the radial motion to decrease the rate of decay of normal velocities and allow for collision in finite time. This non-continuum hydrodynamics, though, is not expected to be important for the tangential motion of inertia-less spheres, with the $O(\text{Kn})$ correction to tangential lubrication mobilities likely to be small. Hence, we will calcu-

late the uniformly valid tangential mobility over all values of ξ using only continuum hydrodynamics.

2.5.1 Radial mobility

To evaluate the radial mobility we will use solutions of the Stokes equations in bispherical coordinates derived by Wang et al[117]. They give the force acting along the line of centres of spheres 1 and 2 as,

$$\begin{aligned} F_1 &= -6\pi\mu a_1[\Lambda_{11}(V_1 - V_2) + \Lambda_{12}V_2] - 6\pi\mu a_1 r\dot{\gamma}D_1 \\ F_2 &= -6\pi\mu a_2[\Lambda_{21}(V_2 - V_1) + \Lambda_{22}V_2] - 6\pi\mu a_2 r\dot{\gamma}D_2 \end{aligned} \quad (2.13)$$

where Λ_{ij} is the non-dimensional resistance giving the force on particle i due to the velocity of particle j . The resistance experienced by particle i due to the straining motion along the axis of compression is D_i . The authors used V_i and F_i to denote the velocities and forces on each of the spheres i . From this the radial mobility in straining flow is determined to be,

$$A = 1 - \frac{1}{2} \frac{D_1\Lambda_{22} + D_2\Lambda_{12}}{\Lambda_{11}\Lambda_{22} + \Lambda_{21}\Lambda_{12}} \quad (2.14)$$

To obtain the radial mobility for sedimentation from individual resistance functions, results from Batchelor[9] are used in combination with equation (2.13) to obtain,

$$L = \frac{1}{1 - \kappa^2} \frac{\Lambda_{22} - \kappa^2 \Lambda_{12}}{\Lambda_{11}\Lambda_{22} + \Lambda_{21}\Lambda_{12}} \quad (2.15)$$

The functions $\Lambda_{ij}(r)$ and $D_i(r)$ are given in the appendix of Wang et al[117]. The results pertinent to our study can be obtained by considering the case of infinite viscosity ratio of drop to medium to obtain the behaviour of hard spheres.

The leading terms in the solution obtained from the bispherical coordinates method accurately capture far-field continuum hydrodynamics. Using more terms in the series

solution improves accuracy at smaller separation. With enough terms the series solutions will reproduce the continuum lubrication behaviour of $1 - A$ and L . This near-field behaviour corresponds to the mobilities decaying as ξ , which can be related to the two individual resistance components Λ_{11} and Λ_{21} diverging as $1/\xi$. This continuum lubrication behaviour was studied by Batchelor & Green[10] in linear flow and Batchelor [9] for settling particles. They found it would take infinite time for two spheres experiencing continuum lubrication to make contact with each other. Finite time to contact is possible through non-continuum hydrodynamics. Sundararajakumar & Koch[113] carried out this analysis and found the non-continuum resistance shows a weaker divergence of $O(\ln[\ln(\text{Kn}/\xi)])$. This is evident in their evaluated lubrication force for the non-continuum case, f^{nc} , given in terms of the rescaled radial separation, $\delta_0 = \xi/\text{Kn}$ and $t_0 = \ln(1/\delta_0) + 0.4513$, as

$$\begin{aligned}
f^{nc} &= \frac{\pi}{6} \left(\ln t_0 - \frac{1}{t_0} - \frac{1}{t_0^2} - \frac{2}{t_0^3} \right) + 2.587 \delta_0^2 + 1.419 \delta_0 + 0.3847 & (\delta_0 < 0.26) \\
&5.607 \times 10^{-4} \delta_0^4 - 9.275 \times 10^{-3} \delta_0^3 + 6.067 \times 10^{-2} \delta_0^2 \\
&\quad - 0.2082 \delta_0 + 0.4654 + \frac{0.05488}{\delta_0} & (0.26 < \delta_0 < 5.08) \\
&- 1.182 \times 10^{-4} \delta_0^3 + 3.929 \times 10^{-3} \delta_0^2 \\
&\quad - 5.017 \times 10^{-2} \delta_0 + 0.3102 & (5.08 < \delta_0 < 10.55) \\
&0.0452 \left[(6.649 + \delta_0) \ln \left(1 + \frac{6.649}{\delta_0} \right) - 6.649 \right] & (10.55 < \delta_0) \quad (2.16)
\end{aligned}$$

Here the resistivity f^{nc} has been scaled with $3\pi\mu V_{rel} a_0^2/\lambda_0$, with the characteristic length given as $a_0 = 2a_1 a_2/(a_1 + a_2)$, the harmonic mean of the two interacting spheres. This has been rescaled to be consistent with the description given in §2.3. Please note that the difference between equation (2.16) and the equivalent expression presented in Sundararajakumar & Koch[113] is due to a typographical error in the previous paper.

In equation (2.16) it can be seen that for $\delta_0 \gg 1$, f^{nc} approaches the continuum lubrication result $1/\xi$. This continuum lubrication resistance is approached by the series

solution for $\xi \ll 1$. Thus it is possible to obtain the matched resistance, Λ_{11} and Λ_{21} , that is valid at all separations. This is given as,

$$\begin{aligned}\Lambda_{11} &= \Lambda_{11}^{bi} - \Lambda_{11}^c + \Lambda_{11}^{nc} \\ \Lambda_{21} &= \Lambda_{21}^{bi} - \Lambda_{21}^c + \Lambda_{21}^{nc}\end{aligned}\tag{2.17}$$

Here, Λ_{11}^{bi} and Λ_{21}^{bi} are from the series solution in bispherical coordinates performed by Wang et al[117], Λ_{11}^c and Λ_{21}^c correspond to the continuum lubrication result, while Λ_{11}^{nc} and Λ_{21}^{nc} is for the non-continuum resistance. The lubrication results are given as,

$$\begin{aligned}\Lambda_{11}^c &= \frac{2\kappa^2}{1 + \kappa^3} \frac{1}{\xi} + c_0 \\ \Lambda_{21}^c &= \frac{\Lambda_{11}^c - \Lambda_{12}}{\kappa} \\ \Lambda_{11}^{nc} &= \frac{2\kappa^2}{1 + \kappa^3} \frac{f^{nc}}{\text{Kn}} + c_0 \\ \Lambda_{21}^{nc} &= \frac{\Lambda_{11}^{nc} - \Lambda_{12}}{\kappa}\end{aligned}\tag{2.18}$$

where c_0 is a numeric constants used to match the various regimes and so obtain a smooth and uniformly valid resistance. For the smooth behaviour we choose a transition between far-field and continuum lubrication at $\xi = 10^{-3}$ and c_0 is evaluated such that $\Lambda_{11} = \Lambda_{11}^c$ at this point. The uniformly valid resistance Λ_{11} is shown in figure 2.5 as a function of ξ at $\text{Kn} = 10^{-2}$, $\kappa = 0.9$ along with Λ_{11}^{bi} , Λ_{11}^c and Λ_{11}^{nc} .

The uniformly valid Λ_{11} and Λ_{21} resistances are used in equations (2.14) and (2.15) to calculate the uniformly valid radial mobilities A and L . These will capture non-continuum lubrication at small separations and full continuum hydrodynamic interactions at larger separations. These results for A and L are presented in figure 2.6 as a function of ξ for $\text{Kn} = 10^{-2}$ and $\kappa = 0.9$.

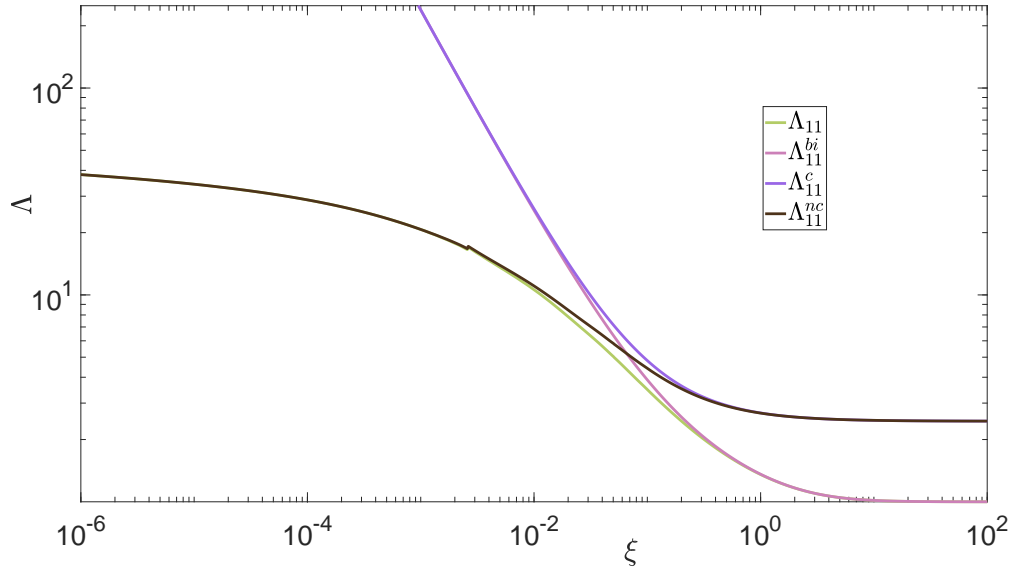


Figure 2.5: Λ_{11} is plotted as a function of ξ at $\text{Kn} = 10^{-2}$ and $\kappa = 0.9$ and compared with Λ_{11}^{bi} , Λ_{11}^c and Λ_{11}^{nc} . A small discontinuity at $\delta_0 = 0.26$ in the fit presented by Sundararajakumar & Koch[113] and given in equation (2.16) leads to the discontinuity seen at $\xi = 2.6 \times 10^{-3}$.

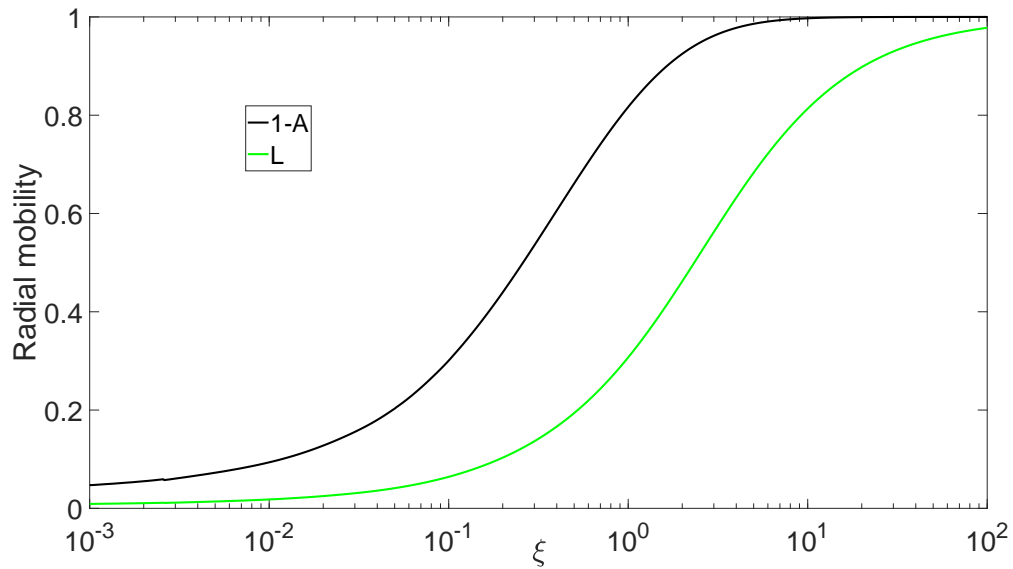


Figure 2.6: A and L as a function of ξ for $\text{Kn} = 10^{-2}$ and $\kappa = 0.9$.

2.5.2 Tangential mobility

To evaluate the tangential mobilities we will use twin multipole solutions. For this purpose we use the analysis carried out by Jeffrey & Onishi[59] on mobility under the action of a body force and Jeffrey[58] on motion in a straining flow. Just like the normal motion, we will use the radial coordinate $\xi = r - 2$ for ease of analysis. Unlike the radial motion we will not consider non-continuum hydrodynamics in the tangential mobility calculation.

Jeffrey & Onishi[59] evaluated components of the tangential mobility when a body force acts on the spheres. They calculate the mobilities using the twin-multipole method. The leading order terms, expressed in terms of a power series in $1/r$, captures the far field behaviour $\xi \gg 1$. With more terms included in the power series the results can capture behaviour at smaller values of ξ . Spanning all of ξ would necessitate including all the infinite terms in the power series. Thus, a separate analysis is carried out for the lubrication behaviour. The lubrication behaviour been analysed for the resistance problem [59]. Using these lubrication resistivities a matrix inversion is performed to obtain the lubrication mobilities. These take the form $(d_0 \ln(\xi^{-1})^2 + d_1 \ln(\xi^{-1}) + d_2)/(\ln(\xi^{-1})^2 + d_3 \ln(\xi^{-1}) + d_4)$, where d_0, d_1, d_2, d_3, d_4 are constants that depend only on κ . The lubrication mobility components can be combined to obtain the compound near-field tangential mobility for sedimentation M_n [9]. Similarly the far-field compound tangential mobility for sedimentation M_f can be obtained. We combine M_f and M_n to obtain M , the uniformly valid compound tangential mobility due to sedimentation, using exponential smoothing. This is given as,

$$M = M_n \exp\left(\frac{-\xi}{e_1}\right) + M_f \left[1 - \exp\left(-\frac{\xi}{e_1}\right)\right] \quad (2.19)$$

Here e_1 is set by the value of ξ at which M_f and M_n have the closest value. Figure 2.7 shows M for all ξ at $\kappa = 0.9$. This result is compared with M_f and M_n .

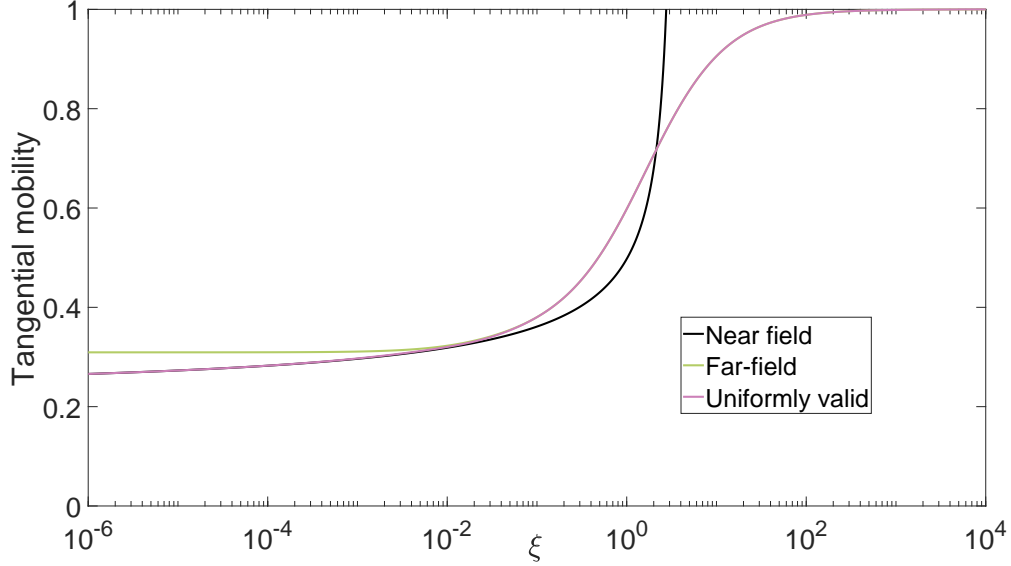


Figure 2.7: Tangential mobility for sedimentation from twin multipole (M_f), lubrication (M_n) and the uniformly valid expressions (M) at $\kappa = 0.9$. Here $e_1 = 2 \times 10^{-2}$ is used in equation (2.19) to obtain the uniformly valid M .

For the compound tangential mobility B in straining flow we first evaluate the far and near field tangential resistance components in linear flow. This analysis was performed by Jeffrey[58]. Using this result as well as the results for the components of the tangential mobilities in sedimentation it is possible to obtain the components of tangential mobility in straining flow without any matrix inversion (see Kim & Karrila[62]). Like the sedimentation problem the lubrication tangential mobility components in straining flow has the form $(f_0 \ln(\xi^{-1})^2 + f_1 \ln(\xi^{-1}) + f_2)/(\ln(\xi^{-1})^2 + f_3 \ln(\xi^{-1}) + f_4)$ where f_0, f_1, f_2, f_3, f_4 are constants depending only on κ . The twin-multipole tangential mobility components in straining flow is also a power series in $1/r$, albeit the first non-zero term is at a higher power than in the series for sedimentation. These individual components are combined to obtain the compound lubrication mobility B_n and compound twin-multipole mobility B_f see Kim & Karrila[62]). To obtain uniformly valid result,

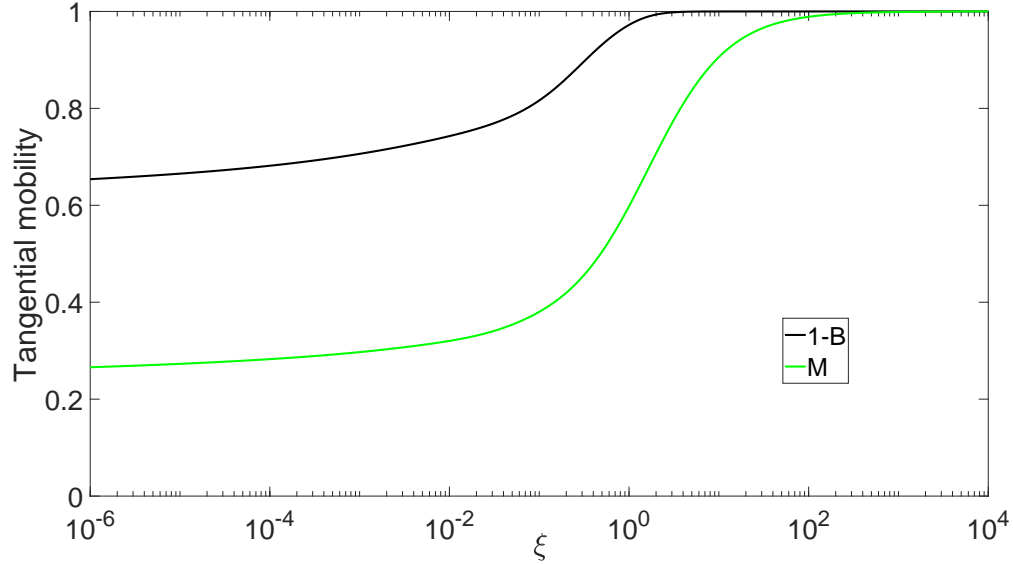


Figure 2.8: B and M as functions of ξ for $\kappa = 0.9$

just like M , we use exponential smoothing. This is given as,

$$B = B_n \exp\left(-\frac{\xi}{g_1}\right) + B_f [1 - \exp\left(-\frac{\xi}{g_1}\right)] \quad (2.20)$$

Here g_1 is set by the value of ξ at which B_f and B_n have the closest value.

Figure 2.8 shows B and M as a function of ξ at $\kappa = 0.9$. It can be seen that they tend to 1 at large separations and reach a non-zero value as $\xi \rightarrow 0$, with a smooth transition between these two regimes.

2.6 Collision rate with hydrodynamic interactions

The introduction of interparticle interactions means equation (2.10) is no longer valid as $P \neq 1$ at $r = 2$. However as $r \rightarrow \infty$ interparticle interactions decay and $P \rightarrow 1$. For the purposes of the calculation we take this large separation to be a large, but finite, value

$r = r_\infty$. Thus, we can calculate the collision rate K_{ij}^{HI} as,

$$\frac{K_{12}^{HI}}{n_1 n_2 \dot{\gamma} (a_1 + a_2)^3} = - \int_{r_\infty} (\mathbf{v} \cdot \mathbf{n}'')|_{\mathbb{S}} dA \quad (2.21)$$

\mathbb{S} denotes the collection of satellite spheres, in the large separation limit, that collide with the test sphere at $r = 2$, i.e., have $\mathbf{v} \cdot \mathbf{n}' < 0$ at the collision sphere. At r_∞ we have \mathbf{n}'' correspond to the outward normal of the area element of \mathbb{S} . \mathbf{v} is obtained from equations (2.6), (2.7) and (2.8) along with the mobilities obtained in §2.5 that capture the interparticle interactions. The integral in equation (2.21) is independent of r_∞ for $r_\infty \gg 1$ as the relative velocity is solenoidal for $r \gg 1$.

Equation (2.21) bypasses evaluation of the pair probability P . To apply this simpler formulation we use trajectory analysis. In this method a test sphere is placed at the origin and satellite spheres are evolved to determine those that collide, thus setting \mathbb{S} . The computational cost of trajectory evolution can be substantial if the initialization is over the spherical shell at r_∞ , because most of the satellite spheres starting on this surface do not come close to the test sphere. Instead we exploit the quasi-steady nature of the particle relative velocity and consider time-reversed trajectories that are initialized on the collision sphere. Seeding on the collision sphere greatly reduces the number of trajectories that must be computed.

To further reduce the number of initial seeding points for the satellite sphere we select only those positions where a collision can occur. This is achieved by considering the sign of the relative velocity at the collision sphere. However, $v_r = 0$ at exactly $r = 2$, since the radial mobilities decay even in the presence of non-continuum hydrodynamic interactions. Thus, we consider small separations $\xi \ll 1$. In this region, we can re-write the radial mobilities as,

$$1 - A = \frac{1}{2} \frac{1}{\Lambda_{11}} \frac{D_1 \Lambda_{22} + D_2 \Lambda_{12}}{\Lambda_{22} + \Lambda_{12}/\kappa} \quad (2.22)$$

$$L = \frac{1}{1 - \kappa^2} \frac{1}{\Lambda_{11}} \frac{\Lambda_{22} - \kappa^2 \Lambda_{12}}{\Lambda_{22} + \Lambda_{12}/\kappa} \quad (2.23)$$

Λ_{11} diverges as $\xi \rightarrow 0$. This causes $1 - A$, L and by extension the relative velocity, to decay to 0. However, the $1/\Lambda_{11}$ term does not change the sign of the relative velocity in equation (2.22) and (2.23) for $\xi \ll 1$. Thus, dividing equations (2.22) and (2.23) by $1/\Lambda_{11}$ removes the divergent quantities and we obtain a reduced radial mobility that is given as,

$$A_{red} = (A - 1)\Lambda_{11} = -0.5 \frac{D_1 \Lambda_{22} + D_2 \Lambda_{12}}{\Lambda_{22} + \Lambda_{12}/\kappa} \quad (2.24)$$

$$L_{red} = L\Lambda_{11} = \frac{\Lambda_{22} - \kappa^2 \Lambda_{12}}{\Lambda_{22} + \Lambda_{12}/\kappa} \frac{1}{1 - \kappa^2} \quad (2.25)$$

These reduced radial mobilities can be used to evaluate $v_{r,red}$ from equation (2.6) and will correctly indicate the sign of the relative velocity close to contact. This can be used to determine regions of influx, that contribute to the collision rate, and efflux, where collision does not occur, on the collision sphere.

For many cases satellite spheres which are in the same influx patch on the collision sphere will be 'close' to each other in the $r \rightarrow \infty$ limit. Hence, to determine \mathbb{S} only satellite sphere evolution starting at $v_{r,red} = 0$, the influx-efflux boundary, in the time-reversed problem is needed. This further reduces the number of computationally intensive trajectory calculations that need to be performed. Figure 2.9 shows this influx-efflux boundary for a few typical values of Q and α . For small Q , it can be seen that two distinct influx regions exist on the collision sphere, corresponding to the two axes of the compressional flow. Increasing Q focuses the trajectories leading to collision towards the direction of gravity and this results in the influx regions approaching each other. Eventually, at high enough Q , they merge but still show lobes corresponding to the lingering influence of the compression axes of the linear flow. Further increases in Q wash away the traces of

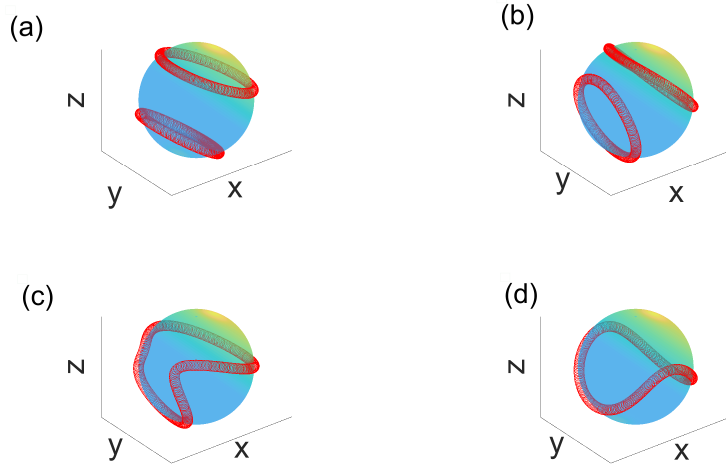


Figure 2.9: The influx-efflux boundary on the collision sphere is shown for various configurations. In (a) $Q = 10$ and $\alpha = 30^\circ$ and two distinct influx regions exist on the collision sphere. In (b), with $Q = 20$ and $\alpha = 60^\circ$, the two influx regions are close to each other. In (c), with $Q = 40$ and $\alpha = 45^\circ$, there is only one influx region, but the influx-efflux boundary is has two lobes reflecting the lingering effects of the uniaxial compressional flow. In (d), with $Q = 60$ and $\alpha = 89^\circ$, there is a single influx region and the two lobes are less prominent.

uniaxial compressional flow. These results for the influx-efflux boundary are independent of Kn since $1/\Lambda_{11}$, which incorporates non-continuum lubrication effects, is absent in $v_{r,red}$.

Due to the coupling of gravity, linear flow, and hydrodynamic interactions complex trajectory evolutions are possible under certain circumstances. They can, in the time-reversed flow, form closed trajectories that start and end on the collision sphere and so do not contribute to the collision rate. Under certain conditions these can open by satellite spheres taking circuitous paths leading to new routes to collision. Consequently these satellite spheres reach $r \rightarrow \infty$ with others from a different influx patch on the collision sphere. In other cases satellite spheres share the influx patch on the collision sphere and move together or $r \approx 1$ but get widely separated as $r \rightarrow \infty$ due to fixed points

encountered along their paths. Thus satellite spheres on the boundaries of \mathbb{S} no longer directly correspond to those from $v_{r,red} = 0$. To obtain new boundaries on the collision sphere we search on the influx region and test the behaviour of the trajectories. Instead of exhaustively spanning we perform a binary search, with the two extremes being a point on the influx-efflux boundary and the point with maximum $|v_{r,red}|$ in the influx patch enclosed by it. We span the great circle joining these two points to determine accurately the location of transition of trajectory behaviour by setting a high threshold for terminating the binary search, of 0.01° . Repeating this exercise allows determining accurately the boundary on the collision sphere that will translate to distinct boundaries for \mathbb{S} in the limit $r \rightarrow \infty$. These boundaries are shown in figure 2.10 for a few select cases and show the distortion induced by the complex trajectory evolution. We will discuss these results in more depth later in the section.

Once the angular positions of the seeding points are determined their radial position is slightly offset from the collision sphere. This is necessary because the very low values of v_r near $\xi = 0$ making trajectory computation very expensive. Converged results, without too much computational load, were obtained at an offset of $\xi = 10^{-9}$.

The trajectory evolution is performed using the relative velocity to obtain a set of differential equations in time for the coordinates of the centre of the satellite particle with the centre of the test sphere placed at origin. These can be obtained from the results given in equations (2.6), (2.7) and (2.8) along with the appropriate mobilities, calculated in §2.5. We use an in-built MATLAB solver, known as 'Ode45', to step in time and track the trajectory in the time reversed flow.

Important parameters governing the collision rate are Kn capturing non-continuum effects, κ describing the geometry of the interacting spheres, Q and α setting the strength and orientation of gravity relative to the uniaxial compressional flow respectively. We

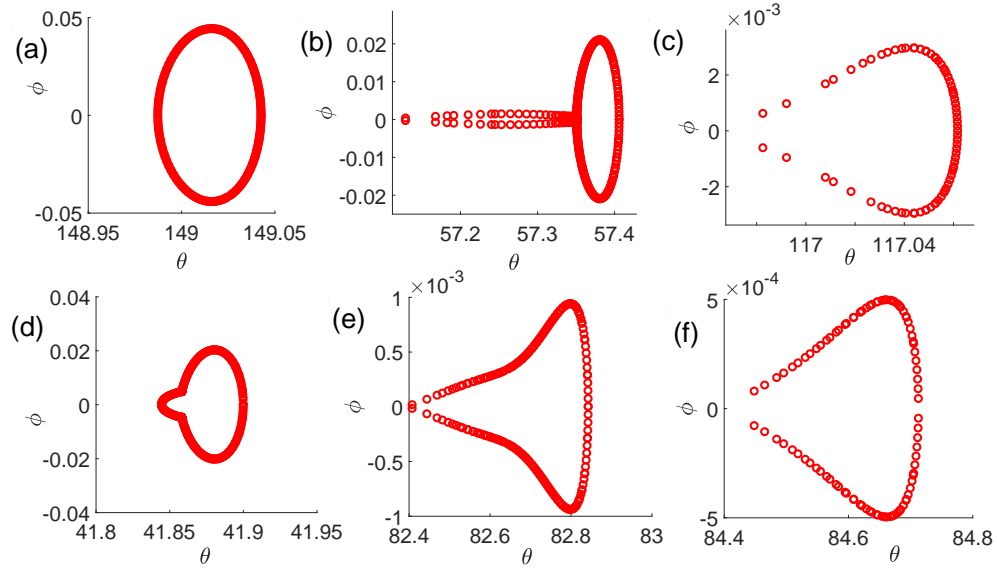


Figure 2.10: The boundaries of the collection of trajectories constituting \mathbb{S} (at r_∞) is shown for $\text{Kn} = 10^{-3}$. The angles are in degrees. In (a) $Q = 10$ and $\alpha = 30^\circ$. This configuration has two nearly identical patches at r_∞ and only one of them has been shown here. For $Q = 20$ and $\alpha = 60^\circ$ (b) and (c) shows two distinct envelopes of colliding trajectories at r_∞ . In (b) the trajectories through the traversal mechanism close to the collision sphere form the bump on the left end. For $Q = 40$ and $\alpha = 45^\circ$ there is only one envelope of colliding trajectories at r_∞ which is shown in (d). Only one envelope of colliding trajectories is expected at higher Q , except for $\alpha \approx \pi/2$. Two envelopes exist for $Q = 60$ and $\alpha = 89^\circ$, which are shown in (e) and (f) respectively.

will span them to obtain the important features of the collision dynamics. We consider size ratios κ of 0.9 and 0.5, which represent the spheres being nearly the same size and substantially different. The Knudsen number is varied from 10^{-1} to 10^{-2} and 10^{-3} , ranging from a case where non-continuum effects occur at the onset of lubrication to one with two decades of near-continuum lubrication. For any chosen size ratio and Kn , we will span Q from 0 to 100. This will capture uniaxial compressional flow dominated as well as differential sedimentation dominated regimes. The final parameter under consideration is α . We will first analyse $\alpha = 0$, the special case with the compressional axis aligned with the direction of gravity and then consider a few other orientations:

$\alpha = 30^\circ, 45^\circ, 60^\circ$ and 89° .

When $\alpha = 0$, i.e., the compressional axis is aligned with the direction of gravity, the analysis can be restricted to the $\phi = 0$ (X-Z) plane and only dr/dt and $d\theta/dt$ are needed to describe the trajectory of satellite spheres. The influx-efflux boundary is a circle on the collision sphere that can be reduced to a point (a single value of θ) on the intersection of the sphere with the X-Z plane. The boundary of colliding satellite spheres at large separations also is circular and again corresponds to a particular value of θ .

For $\kappa = 0.9$, figure 2.11 shows the collision rate as a function of Q for $\text{Kn} = 10^{-1}, 10^{-2}$, and 10^{-3} at $\alpha = 0$. The companion figure 2.12 shows the evolution of the trajectory of the satellite sphere at a few typical values of Q . For small Q there are two regions of influx on the collision sphere. One lies in the "northern hemisphere", where gravity aids the compressional flow and the other in the southern hemisphere where gravity and compressional flow oppose each other. In the northern hemisphere, as Q increases the flux increases steadily and smoothly. However, the behaviour of the trajectories lying in the southern hemisphere at $\xi \ll 1$ is non-trivial, so we examine the behaviour in the southern hemisphere in more detail. In figure 2.12 for $Q = 10$ there is nothing qualitatively different between the northern and southern hemisphere trajectories. However, at $Q = 26$, some of the time-reversed trajectories are closed, i.e., they start and end on the collision sphere. As a result, a larger than expected region of the southern hemisphere is not populated, in forward-time evolution, by satellite spheres which come from infinity and this region does not contribute to the net collision rate. The resulting decrease in collision rate persists as Q increases at large Kn . However, for $Q > 27$ and small Kn there is an uptick in the collision rate. This enhancement occurs as, in the time-reversed flow, the southern hemisphere satellite spheres that would have formed closed trajectories at smaller Q become open by going around the efflux re-

gion of the collision sphere. In the time-forward trajectories this corresponds to satellite spheres coming from positive infinity of the Z coordinate having a new region available for collision on the southern hemisphere. This additional avenue for collision is possible only under very specific circumstance and was not observed at $\text{Kn} = 10^{-1}$ and 10^{-2} or at $Q < 27$. Only when gravity and lubrication resistance are strong enough can the satellite spheres traverse around the collision sphere. This traversal mechanism causes southern hemisphere satellite spheres to reach, in the time-reversed problem, r_∞ with positive Z . For Q greater than about 31 this traversal mechanism is the only way satellite spheres from the southern hemisphere can contribute to the collision rate. In figure 2.13 the collision rate due to the two mechanisms operating on southern hemisphere satellite spheres is shown for $26 < Q < 33$ at $\text{Kn} = 10^{-3}$. It can be seen that the traversal mechanism is possible only over a short range of Q . The upper end of this range might be extended by decreasing Kn . Unfortunately, we have not tested this hypothesis for arbitrarily small Kn as the numerical calculation of the trajectory calculation becomes unstable. However, beyond $Q \approx 44$ there is no valid influx region in the southern hemisphere. Thus, the northern hemisphere is the only contributor to collision rate in this differential sedimentation dominated regime.

Figure 2.14 shows the variation of the collision rate for $\kappa = 0.5$ as a function of Q for $\text{Kn} = 10^{-1}, 10^{-2}, 10^{-3}$. Qualitatively the behaviour is similar to $\kappa = 0.9$. All the important characteristics including closed and traversal trajectories appear at roughly the same values of Q and Kn . The magnitude of the collision rate is, however, lower for the dissimilar spheres.

The collision rate for the inclined problem, of $\alpha = 30^\circ, 45^\circ, 60^\circ$, and 89° , is shown as a function of Q in figure 2.9 at $\kappa = 0.9$ and $\text{Kn} = 10^{-3}$ along with the $\alpha = 0$ result for comparison. Angular dependence vanishes in the $Q \rightarrow 0$ and $Q \rightarrow \infty$ limits but shows

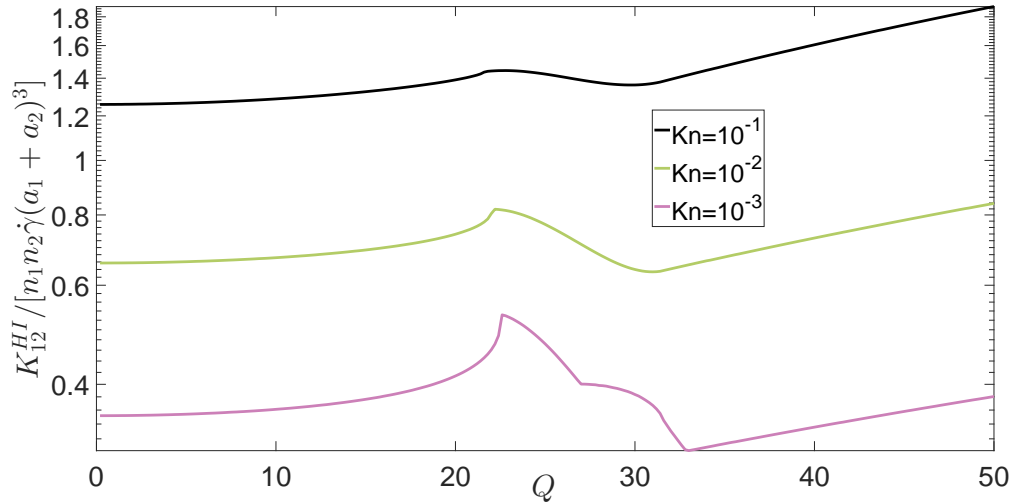


Figure 2.11: The collision rate is plotted as a function of Q , the relative strength of gravity to uniaxial compressional flow, for $\kappa = 0.9$, $\alpha = 0$, and $\text{Kn}=10^{-1}, 10^{-2}$, and 10^{-3} . The collision rate is higher for larger values of Kn

large variation at moderate values, much higher than the ideal rate result. The non-trivial behaviour discussed in §2.4 is further exacerbated by hydrodynamic interactions and primarily manifested through the complex trajectory evolution.

All the trajectory behaviour described for $\alpha = 0$ are relevant for $\alpha > 0$ and can be observed in the distortion of the boundaries of \mathbb{S} at r_∞ , shown in figure 2.10. Comparing against figure 2.9, showing the influx-efflux boundary on the collision sphere, it is evident that there is heavy warping along with some parts 'missing' or 'added' onto. Hydrodynamic interactions can significantly distort and this is evident in 2.10(d) compared against figure 2.9(c). The protrusion in (b) of figure 2.10 can be attributed to trajectories, time-reversed flow, originating in one of the influx regions and then turning around and ending up with trajectories originating from the other influx region at r_∞ . This has, along with the closed trajectories, depleted the boundary in 2.10(c). For these $\alpha > 0$ cases, though, the impact on the collision rate is not as dramatic.

Complex trajectories are possible even without hydrodynamic interactions leading to

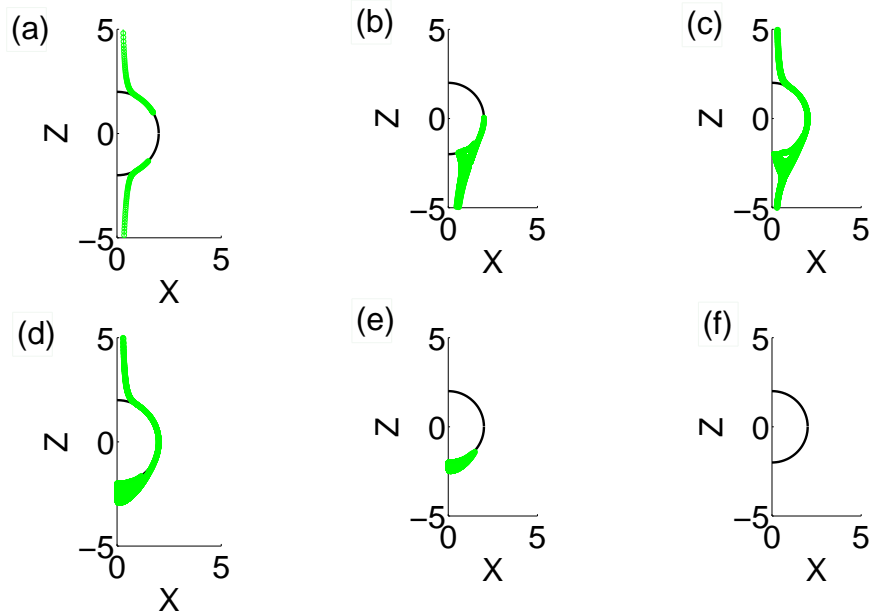


Figure 2.12: The time-reversed trajectories in the X-Z plane are shown for $\kappa = 0.9$, $\alpha = 0$ and $\text{Kn}=10^{-3}$. Symmetry is exploited to analyse only half of the collision sphere. In (a) $Q = 10$ and both the northern and southern trajectories are plotted. The subsequent plots only show trajectories which are in the southern hemisphere for $\xi \ll 1$. In (b) for $Q = 26$ closed trajectories start to appear. In (c) $Q = 30$ and a few southern hemisphere trajectories traverse over the efflux region of the collision sphere and pass around the northern hemisphere with increasing ξ . In (d) $Q = 32$ and it is only by passing around the northern hemisphere that southern hemisphere trajectories can contribute towards collision rate. In (e) $Q = 34$ and there is no route remaining for southern hemisphere trajectories to contribute towards collision. At $Q = 50$, as seen in (f) there are no trajectories arising in the southern hemisphere of the collision sphere.

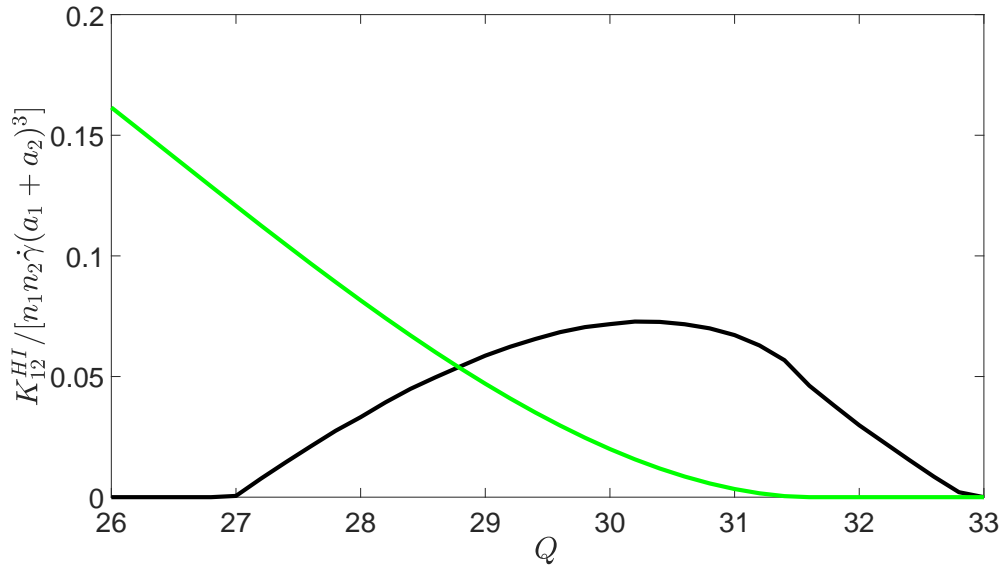


Figure 2.13: The collision rate is plotted for Q , the relative strength of gravity to uniaxial compressional flow, spanning 26 to 33 for $\kappa = 0.9$, $\alpha = 0$ and $\text{Kn}=10^{-3}$. The monotonically decreasing curve corresponds to the collision rate due to trajectories that stay in the negative Z half space at all separations. The curve with a maximum corresponds to the collision rate of traversal particles that collide in the southern hemisphere but have positive Z coordinates at large separations.

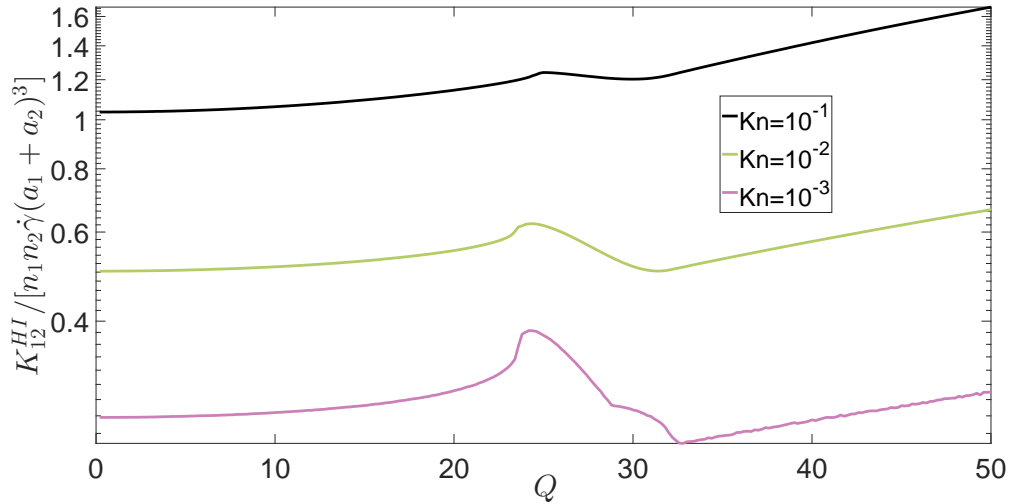


Figure 2.14: The collision rate is plotted as a function of Q , the relative strength of gravity to uniaxial compressional flow, for $\kappa = 0.5$, $\alpha = 0$, and $\text{Kn}=10^{-1}$, 10^{-2} , and 10^{-3} . The collision rate is higher for larger values of Kn

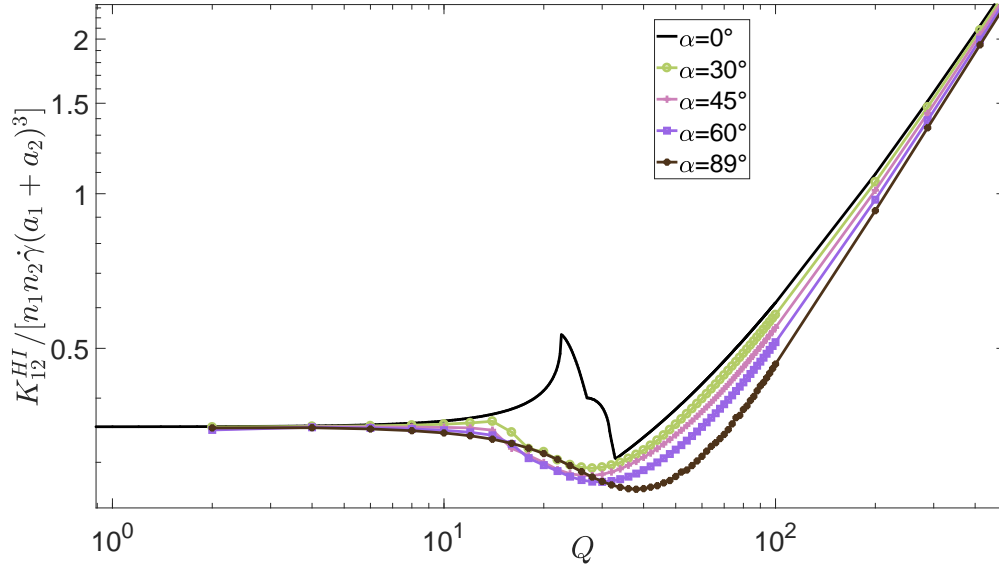


Figure 2.15: The collision rate is plotted as a function of Q , the relative strength of gravity to uniaxial compressional flow, for $\kappa = 0.9$, $\text{Kn}=10^{-3}$ and $\alpha = 30^\circ, 45^\circ, 60^\circ$ and 89° along with $\alpha = 0$ for comparison. They start off together at $Q = 0$ and converge in the $Q \rightarrow \infty$ limit. At intermediate Q the spread across α is large.

two widely separated regions for \mathbb{S} at r_∞ , seen in (e) and (f) of figure 2.10, even though there there is only one influx region, shown in figure 2.9(d). For $\alpha \approx 90^\circ$ and large Q trajectories that are close at $r \approx 1$ become separated as $r \rightarrow \infty$ due to the coupling of the uniaxial compressional flow and gravity. Gravity is strong at large Q and it sets the trajectory evolution around $r \approx 1$. However, as the separation increases the linear flow induced velocity increases and, for finite Q , always results in a fixed point in the velocity field. At radial separations greater than this satellite spheres follow, instead of the direction of gravity, the compressional axis with each direction of the compressional axis, nearly orthogonal to the direction of gravity, gets nearly equal number of satellite spheres. This fixed point occurs at $r = O(Q)$ and only observed for large Q , thus this diverging trajectory evolution is not driven by hydrodynamic interactions.

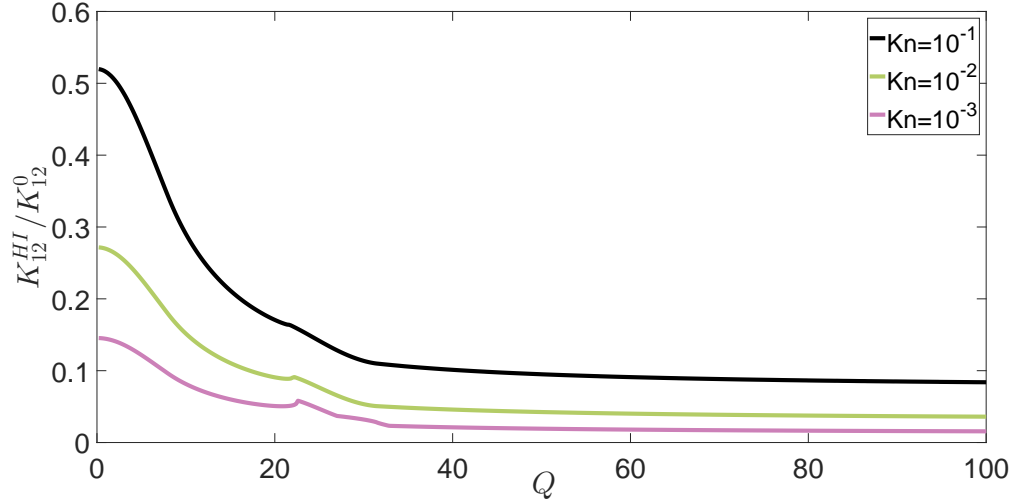


Figure 2.16: The collision efficiency is plotted as a function of Q , the relative strength of gravity and uniaxial compressional flow at $\alpha = 0$ for $\kappa = 0.9$ and $\text{Kn}=10^{-1}$, 10^{-2} , and 10^{-3} . The collision efficiency decreases with decreasing Kn .

2.7 Collision efficiency

The collision rate evaluated in §2.6 is reduced compared to the ideal rate computed in §2.4 as a result of non-continuum hydrodynamic interactions. To show the extent of this retardation and obtain insight into the hydrodynamics interactions, the collision efficiency is calculated. For $\kappa = 0.9$, the collision efficiency as a function of Q obtained by dividing the rate with interactions (from figure 2.11) by the ideal collision rate is shown in figure 2.16. Similarly, figure 2.17 shows the collision efficiency for $\kappa = 0.5$. These two figures span a larger range of Q than the figures for the collisions to better illustrate the large Q asymptotic behaviour. The collision efficiency asymptotes at large Q indicating that the sedimentation dominated regime has been reached. This asymptotic value is significantly lower than the $Q = 0$ result for both size ratios under consideration. Comparing the results at the two size ratio indicates that collision is more efficient for nearly similar spheres across all values of Q .

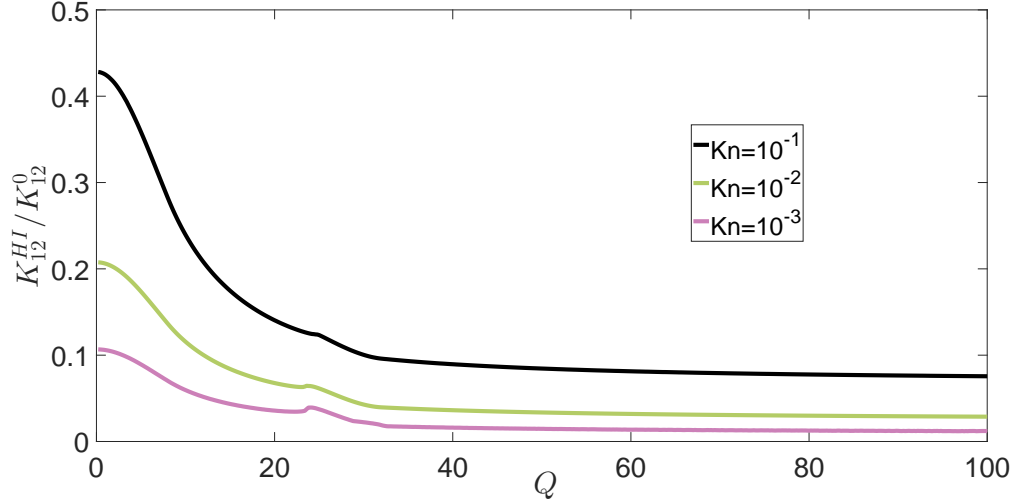


Figure 2.17: The collision rate is plotted as a function of Q , the relative strength of gravity and uniaxial compressional flow at $\alpha = 0$ for $\kappa = 0.5$ and $\text{Kn}=10^{-1}, 10^{-2}$, and 10^{-3} . For all Q and Kn the collision efficiency is lower than that for $\kappa = 0.9$.

In the asymptotic limits of $Q = 0$ and $Q \rightarrow \infty$, it is possible to obtain the collision efficiency without explicitly evaluating the collision rate through trajectory analysis. This analytical result was first derived by Batchelor & Green[10] for particles in linear flow and Batchelor[9] performed it for sedimenting particles. We extend it to the case of hydrodynamic interactions with breakdown of continuum in the lubrication regime. The procedure involves computing the pair probability evolution and is shown for the differential sedimentation dominated case, $Q \rightarrow \infty$. A similar derivation is possible for the pure uniaxial compressional flow, $Q = 0$.

The pair probability density satisfies,

$$v_r \frac{\partial P}{\partial r} + v_\theta \frac{1}{r} \frac{\partial P}{\partial \theta} = -P \nabla \cdot \mathbf{v} \quad (2.26)$$

Using the method of characteristic we obtain,

$$\ln \left[\frac{P|_{r=2}}{n_1 n_2} \right] = \int_2^\infty \frac{\nabla \cdot \mathbf{v}}{v_r} dr \quad (2.27)$$

along trajectories where

$$\frac{d\theta}{dr} = \frac{v_\theta}{rv_r} \quad (2.28)$$

Expanding $\nabla \cdot \mathbf{v}$ and simplifying we get,

$$\int_2^\infty \frac{\nabla \cdot \mathbf{v}}{v_r} dr = \int_2^\infty d(\ln v_r) + \int_2^\infty \left(\frac{2}{r} + \frac{1}{v_r} \frac{1}{r \sin \theta} \frac{\partial(v_\theta \sin \theta)}{\partial \theta} \right) dr \quad (2.29)$$

The relative velocity for the pair is

$$\begin{aligned} v_r &= -LQ \cos \theta \\ v_\theta &= MQ \sin \theta \end{aligned} \quad (2.30)$$

Using (3.12), it can be shown that $\nabla \cdot \mathbf{v}/v_r$ and thereby $P|_{r=2}$ are independent of θ . Hence the integral in equation (3.3) can be evaluated exactly and the resulting collision rate, with input from equations (3.12) and (3.11), is given as,

$$\frac{K_{12}}{n_1 n_2 \dot{\gamma} (a_1 + a_2)^3} = v_{r,\infty} \exp \left[\int_2^\infty dr \left[\frac{2}{r} + \frac{2MQ \cos \theta}{-rLQ \cos \theta} \right] \right] \quad (2.31)$$

Here, $v_{r,\infty}$ is the radial velocity at large separations. Using the ideal rate result from equation (2.31), the collision efficiency is,

$$\frac{K_{12}^{HI}}{K_{12}^0} = \exp \left[2 \int_0^\infty d\xi \frac{L - M}{(2 + \xi)L} \right] \quad (Q \rightarrow \infty) \quad (2.32)$$

Carrying out a similar analysis, the collision efficiency for pure uniaxial compressional flow is,

$$\frac{K_{12}^{HI}}{K_{12}^0} = \exp \left[3 \int_0^\infty d\xi \frac{B - A}{(2 + \xi)(1 - A)} \right] \quad (Q = 0) \quad (2.33)$$

The integrals over the radial coordinate in Equations (2.32) and (2.33) can be evaluated numerically to obtain the collision efficiency of the pure differential sedimentation and pure uniaxial compressional flow, respectively. For $\kappa = 0.9$ and $\kappa = 0.5$ these are shown in figure 2.18. The collision efficiency monotonically decreases with Kn at both

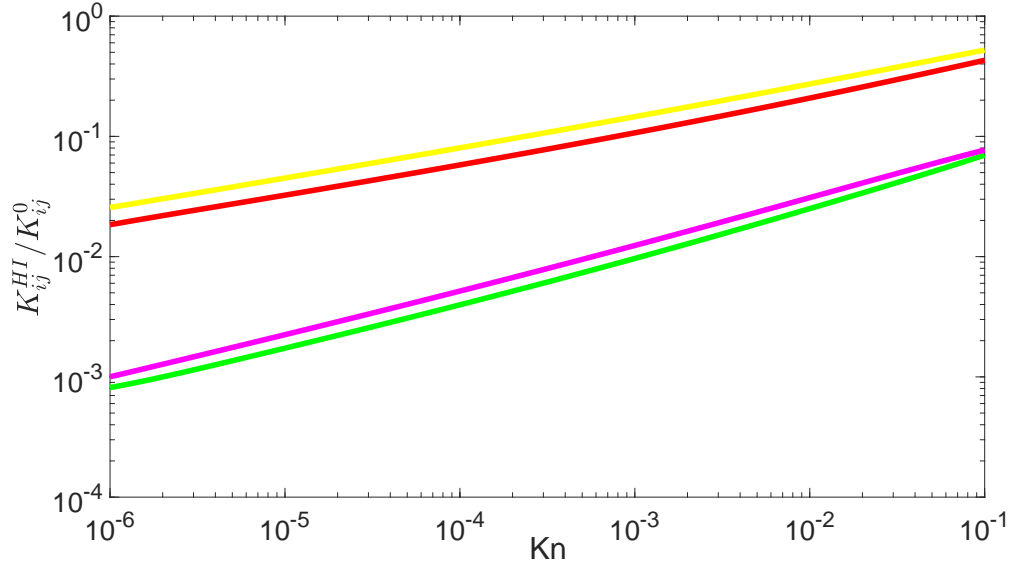


Figure 2.18: The collision efficiency is plotted as a function of Kn for the pure differential sedimentation and pure uniaxial compressional flow cases at $\kappa = 0.9$ and $\kappa = 0.5$. The two curves with the highest collision efficiency correspond to the pure uniaxial compressional flow while the two lowest are for pure differential sedimentation. In each case $\kappa = 0.9$ is more efficient than $\kappa = 0.5$ at all values of Kn .

the asymptotes in Q and at both size ratios. Consistent with figures 2.16 and 2.17 we observe that $\kappa = 0.9$ shows a higher collision efficiency at both the high and low Q asymptotes compared to $\kappa = 0.5$. However, the effects of Q and Kn on the collision efficiency is more pronounced than that of the size ratio.

Figure 2.18 shows a larger slope for collision efficiency variation of settling spheres driven when compared to those present in the uniaxial compressional flow. This linear flow has fixed points at θ of 0 and 90 degrees while differential sedimentation has it at 0 and 180 degrees. Thus, in collision through differential sedimentation the rate of change of tangential fluid velocity is lower relative to uniaxial compressional flow field. By mass conservation the radial component magnitude for the settling problem is lower, thus the integrand in equation (2.32) is higher when compared to the exponent in equation (2.33). Hence, differential sedimentation collision efficiency is more sensitive

to Kn and so results in a larger relative change for a given change in mean sphere size when compared to the uniaxial compression calculation.

2.8 Discussion

Our study is the first to evaluate the collision rate of a dilute suspension of spheres when frozen uniaxial compressional flow and gravity are coupled. Our analysis includes non-continuum hydrodynamics. This interparticle interaction is important for collision in gaseous media and has been rarely considered in the previous literature. The present study is the first to determine the collision rate using the correct form of non-continuum interactions based on the lubrication results of Sundararajakumar & Koch[113] for unequal spheres for coupled linear flow and differential sedimentation and for sedimentation dominated collisions.

The problem is set up in §2.3. We present the rate equation for the collision rate of two species of spheres. The suspension consists of inertia-less fluid and particles. The Stokes flow naturally leads to a characteristic velocity based on the compression rate and the characteristic length, which is the mean radius of the two spheres. Non-dimensional equations based on these scales contain a characteristic differential sedimentation velocity Q which becomes a parameter. The non-dimensionalised collision rate equation is in the form of a surface integral and needs input of the non-dimensional relative velocity as well as the pair probability at contact, representing the local species concentration relative to the bulk. We also demonstrated that the breakdown of continuum is important in the lubrication regime when collision occurs in a gaseous media. This demonstrated the applicability of our model to a wide range of systems such as 5-60 μm radius droplets in clouds and particles in industrial aggregators and aerosol analysis instruments.

§2.4 deals with the ideal collision rate, evaluated numerically based solely on relative velocity on the collision sphere. This relative velocity only depends on the background flow driving it as there are no interparticle interactions. The lack of interparticle interactions leads the local species concentration to remain equal to the bulk concentration at all locations and so the collision rate integral is significantly simplified. The calculated ideal collision rate was presented as a function of Q and the angle α that the compressional axis makes with gravity. The results differ significantly from a linear combination of the ideal uniaxial compressional flow and differential sedimentation collision rates and the ideal rate exhibits a weak α dependence.

The radial and tangential mobilities are computed in §2.5. While the non-continuum, radial mobilities decayed as $\xi \rightarrow 0$ the rate at which they decayed was weak, $O(1/\ln[\ln(\text{Kn}/\xi)])$, compared to the continuum mobility, $O(\xi)$, and this allows contact between the two spheres to occur in finite time. The continuum tangential mobilities take finite values as $\xi \rightarrow 0$, so corrections due to non-continuum gas flow were not considered. When $\xi \geq O(1)$ both the radial and tangential mobilities are governed by continuum hydrodynamics interactions. Uniformly valid approximations to the mobilities were developed that yield smooth variation between these lubrication and far-field regimes.

In §2.6 the mobilities from §2.5 are used to evaluate the collision rate when spheres interact with each other through hydrodynamic forces. This interparticle interaction affects the pair probability close to the collision sphere. To bypass calculating the pair probability, a trajectory analysis was used. The trajectory of the satellite sphere was tracked from large separations to the point of collision. At large separation the local species concentration approaches the bulk concentration and hydrodynamic interactions are negligible, so the flux can be readily calculated. To minimise the expensive trajectory

calculation time reversed motion is considered and only trajectories at the influx-efflux boundary on the collision sphere and boundaries between different types of trajectories are evaluated.

We have presented results for the ideal and actual collision rate due to the coupled effects of sedimentation and uniaxial compressional flow. For most circumstances, these results when scaled with the ideal collision rate due to compressional flow show an increased collision rate with increasing gravity Q as is evident from figure 2.3, 2.11, 2.14 and 2.15. However, the collision efficiency, presented in §2.7 and, plotted in figures 2.16 and 2.17 is considerably smaller at large Q . This can be attributed to the long-range hydrodynamic interactions due to the net force exerted by the particles on the fluid as they sediment. This weakening of the sedimentation driven collisions causes the transition from the relatively low collision rate seen in the uniaxial compression dominated regime to the gravity dominated regime, where it is linearly increasing with Q , to shift. For the ideal collision rate in figure 2.3, the shift occurs at $Q \approx 10$ while the transition occurs around 30 when hydrodynamic interactions are included (figure 2.11).

From the plots of collision efficiency, especially figure 2.18, we can observe that smaller values of Kn retard the collision process more. This can be understood by noting that a decrease in the relative thickness of the non-continuum layer leads the satellite spheres to experience stronger continuum lubrication forces.

The influence of hydrodynamic interactions on the collision rate is significantly more complex than a simple shift in the relative strength of gravity and linear flow or a reduction in collision rate. Hydrodynamic interactions play a crucial role in the appearance of complex trajectories. Surprisingly these trajectories lead to a non-monotonic dependence of the collision rate on Q in the range $10 < Q < 40$ for small enough Kn . These complex trajectories have been shown in figure 2.12 and the impact they have on

boundaries of \mathbb{S} at large separations given in figure 2.10. Their influence on the collision rate is highlighted in figure 2.13 which shows the collision rate caused by different types of trajectories in the intermediate Q range where the collision rate variation is non-monotonic.

Even without interactions complex trajectory behaviour is observed for large Q and α nearly 90° . In this limit there is a fixed point at large separations beyond which satellite spheres follow the compressional axis instead of gravity and trajectories have very sharp turns. The boundaries of all of these classes of trajectories have been resolved to accurately determine their impact on the collision rate.

While we have focused on only two size ratios, $\kappa = 0.5$ and 0.9 , the influence of the size ratio seems to be restricted to a moderate decrease of the collision efficiency with decreasing κ at all Q and Kn . This can be seen from the qualitative similarity between figure 2.16 showing the collision efficiency at $\kappa = 0.9$, and figure 2.17 for $\kappa = 0.5$. This is further evidenced in figure 2.18, where the collision efficiency for both size ratios are plotted together in the two limits of Q .

The collision rate variation across the α parameter space shows rich behaviour. In §2.4 the ideal rate deviation from the $\alpha = 0$ to the isotropic result as a function of Q exhibits a complex behaviour that appears to be a sum of two Gaussians. With hydrodynamic interactions the magnitude of this difference rises dramatically, with $\alpha = 0^\circ$ and 60° differing by little more than a factor of 2 at $Q \approx 10$ and $\text{Kn} = 10^{-3}$. There is not a monotonic behaviour with increasing α . Neither are all the curves in 2.15, showing different α , similar.

CHAPTER 3

COLLISION RATE OF BIDISPERSE SPHERES SETTLING IN A NON-CONTINUUM TURBULENT GAS FLOW

3.1 Abstract

Collision of a dilute poly-disperse suspension of sub-Kolmogorov spheres of negligible inertia settling in turbulent flow and interacting through hydrodynamics shaped by breakdown of continuum has been studied for the first time. The role of non-Gaussian turbulent statistics on collision rate is resolved by accessing Reynolds number based on the Taylor micro-scale much higher than current direct numerical simulation capabilities using a Lagrangian stochastic velocity gradient model. Without gravity we find a decrease in collision rate with increasing Taylor's Reynolds number and tails of the probability distribution. This variation is diminished and leads to a non-linear dependence with increasing gravity as it attenuates the fluctuations. This has been resolved by spanning in strength of differential sedimentation to turbulence velocity on the scale of the particles, which can take order one values while the ratio with the Kolmogorov velocity is very small thus retaining the accuracy of the Lagrangian result. The collision rates are diminished by interactions between the colliding spheres through uniformly valid hydrodynamic interaction. This comprise of non-continuum lubrication as well as full continuum hydrodynamic interactions at larger separations and govern collision dynamics of 3 to 100 μm radii droplets at standard temperature and pressure. Collision efficiency is used to report the reduced collision rates and it additionally depends on size ratio of the interacting spheres and Knudsen number, the ratio of the mean free path of the gas to the mean radius of the interacting spheres. To concisely report the large amount of data computed across the parameter space we develop an analytical approxi-

mation to the collision efficiency by solving, in a model system, for the pair probability evolution in the lubrication regime. To accurately reflect the original problem free parameters are allowed and determined by fitting against the computed data. This will provide an accurate closed form expression that can be used in evolution studies, such as water droplets in clouds or commercially valuable products in industrial aggregators.

3.2 Introduction

Collisional growth sets the particle size evolution in a wide range of systems. In clouds, collisions are the dominant growth mechanism when droplets are moderately large, about $15\ \mu\text{m}$ or larger radii, with differential sedimentation controlling sizes greater than $40\ \mu\text{m}$ and condensation below $15\ \mu\text{m}$ [48]. This leaves the $15\text{-}40\ \mu\text{m}$ size range, referred to as the 'size-gap', where it is not fully understood how droplets grow. The current understanding is that turbulence driven collision is important in this regime. Dynamics in the 'size-gap' will significantly shape the drop size distribution. This evolution informs rain formation as well as the cloud's thermal budget[105, 87, 41]. Thus, the study of the macro climate change to our atmosphere is critically dependent on collision rate of water droplets acting under the coupled action of gravity and turbulence. Studying the collision dynamics under this coupled configuration will be the focus of this study.

The turbulence driving collision in the 'size-gap' is experienced as a temporally varying linear flow by the droplets in clouds that lie within the Kolmogorov scale eddies of size $1\ \text{mm}$ in clouds. The water droplets of interest typically have radii less than $100\ \mu\text{m}$. Due to the high viscosity ratio of water and air, these can be modelled as hard spheres. Additionally these droplets interact with each other by disturbing the media. In gaseous media hydrodynamic interaction characterised by a breakdown of continuum in

the lubrication regime is expected to be dominant over other effects[113]. Thus, the collision rate analysis carried out in our study, that couples the differential sedimentation with the fluctuating linear flow field and includes interparticle hydrodynamic interactions shaped by breakdown of continuum, will lead to better predictions of dynamics in the 'size-gap'.

On a smaller environmental scale Niu et al[84] demonstrated that pollutants near an industrial furnace experience significant aggregation. Thus, understanding the coagulation process can aid in combating microclimate pollution. Analysis of coagulation also finds application in industrial settings, such as carbon black aggregation in aerosol reactors[21]. In all these cases the flow is turbulent and the collision dynamics is significantly influenced by gravitational effects or body forces that mimic the effect of gravity. The particles in these examples interact in gaseous media. Thus, their collision dynamics will be shaped by non-continuum hydrodynamics. The results of our study will be applicable to these and other situations beyond cloud physics.

The first treatment of collision in turbulent conditions was carried out by Saffman & Turner[97]. They modelled turbulence experienced by the sub-Kolmogorov particles as a quasisteady uniaxial compressional flow with a Gaussian distribution of strain rates and found the collision rate to be $(8\pi/15)^{1/2}(a_1+a_2)^3 n_1 n_2 (\epsilon/\nu)^{1/2}$, where a_1 and a_2 are the radii of the two spheres each with number density n_1, n_2 respectively, ϵ is the dissipation rate of the turbulent flow field, ν is the kinematic viscosity. Even when the background flow is allowed to fluctuate sub-Kolmogorov particles are expected to experience a local linear flow at any instant. A stochastic linear velocity field with Gaussian statistics was used in the study by Brunk et al[20] and Chun & Koch[27] but the role of non-Gaussian turbulent velocity statistics on collision of sub-Kolmogorov particles has not been explored in literature. At the other end of the spectrum Smoluchowski[106] calculated the

collision rate of settling spheres to be $2n_1n_2\rho g(a_2^2 - a_1^2)(a_1 + a_2)^2/(9\mu)$. Here g is the acceleration due to gravity, ρ the density of the particles and μ the dynamic viscosity of the media. Coupling differential sedimentation turbulence Li et al[73] performed direct numerical simulation (DNS) to study evolution of particle size distribution. However, they did not calculate collision rates beyond the case of no gravity. This result did not exhaustively span in Reynolds number based on Taylor microscale (Re_λ), only considering upto 158, whereas $O(10^4)$ is typical in clouds. We will explore this parameter along with the coupling of turbulence and differential sedimentation to determine the collision rate.

Collision dynamics in many systems is predominantly governed by two-body interactions. This is due to low particle volume fraction, about $O(10^{-6})$ ([for carbon black reactor see Balthasar et al [7] and droplets in clouds and Grabowski & Wang[48] for clouds). Hence, three and higher body interactions are neglected in this study.

Interparticle interactions, especially hydrodynamic interactions, play a dominant role in the motion of particles in a medium when particle separation is comparable to their sizes. However continuum lubrication forces do not allow collision to occur in finite time. One strategy is to underpredict this divergent force to allow collision in finite time[5]. However, this does not give collision rates representative of real particles because they collide through a combination of lubrication forces and various physical mechanisms that modifies its strength. In liquid media Van Der Waals forces allows collision in finite time and has been extensively studied in literature [10, 9, 32, 117]. In gaseous media the breakdown of continuum dominates over deformation, inter-facial mobility, or colloidal force over a large particle size range[113]. Collision studies with non-continuum hydrodynamics finds limited treatment in literature. Davis[32] uses the Maxwell slip approximation which is only valid when surface to surface particle sep-

aration is much greater than the mean free path. Chun & Koch[27] use the uniformly valid non-continuum resistance force calculated by Sundararajakumar & Koch[113] but only consider equal sized particles in turbulence. To obtain collision rate pertinent to a dilute polydisperse suspension, which is encountered with droplets in clouds and other practical applications, we study unequal particles colliding under the coupling of turbulence with differential sedimentation and influenced by hydrodynamic interaction that includes the breakdown on continuum.

We neglect the effects of inertia on collision dynamics. Fluid inertia is weak on sub-Kolmogorov scales. In clouds the Kolmogorov length scale is about 1 mm [48] and the droplets of interest are $O(10\mu\text{m})$. Similarly, in industrial reactors the particles are at most micron sized and the Kolmogorov scale is typically about $300\mu\text{m}$. Particle inertia can alter relative velocity as well as cluster them in certain regions of the flow. While the former can affect the collision dynamics only the latter makes any significant impact on the collision rate, through enhanced probability of particle encounter, when St is small, about 0.3 or less. Here the Stokes number St is the ratio of particle response time to characteristic fluid time. Small St is typical for most of the droplets smaller than drizzle size but $O(1)$ is also possible (figure 1 of Ayala et al[4]). Hence while the effects of inertia on collision dynamics might affect a few of the larger drops the results of our study will be accurate over a large range. Inertial clustering finds extensive treatment in literature [112, 95, 53, 34] and is beyond the scope of this study. In industrial reactors the particles sizes are smaller, reducing particle response time, but turbulent dissipation rate is also higher, reducing characteristic fluid time, and so similar estimates of St is expected. Due to the lack of inertia tracking of the evolution of the sphere pairs is accomplished by the mobility formulation. These mobilities take trivial values in the ideal flow and capture the inter-particle interactions when present, thus setting the relative velocity contribution of gravity and turbulence. The overall relative velocity,

that determines the motion of the sphere pairs, is given by the vector sum of these individual components.

The choice of the background homogeneous isotropic turbulent flow field is important for the fidelity of the collision rate calculation. It is numerically too expensive to carry out DNS of turbulence. With present capabilities it is not possible to access high enough Taylor's Reynolds number typically encountered in clouds and other systems. Hence we will use a velocity gradient model to resolve the flow experienced by the sub-Kolmogorov particles. Saffman & Turner[97] assumed a frozen uniaxial compressional flow with Gaussian distribution for the strain rate. Stochastic velocity gradient models were used by Brunk et al[20] and Chun & Koch[27]. However, these do not capture the non-Gaussian nature of the turbulent velocity gradient observed in DNS. The non-Gaussian behaviour has been incorporated into the Lagrangian velocity gradient model developed by Girimaji & Pope[44] through a log-normal behaviour of the pseudo-dissipation rate (the sum of squares of the velocity gradient components). Important features of the stochastic linear flow are captured, namely the correlation time of the straining flow and the orientation of the vorticity relative to the strain axes. We extend it to incorporate dependence on Re_λ of the pseudodissipation rate standard deviation as well as separation of time scales of dissipation to integral processes and use it in our study. Taylor's Reynolds number parameter space is spanned to examine the role of non-Gaussian nature of the velocity gradient statistics on the collision rate and we report, for the first time, a statistically significant variation.

The Lagrangian reference frame velocity gradient model will be used for the coupled configuration of turbulence with differential sedimentation. This is valid in the $\Delta S_{v,12} \ll 1$ limit, where $\Delta S_{v,12} = |\tau_{p,1} - \tau_{p,2}|g/u_\eta$, where u_η is the Kolmogorov velocity and $\tau_{p,i} = 2a_i^2/9\nu$. For collision dynamics, though, the relevant velocity is the one on the scale

of the spheres, $a^* = (a_1 + a_2)/2$, which is much smaller than η the Kolmogorov length scale. Hence, for the purposes of calculating the collision rate, the relative strength of differential sedimentation to turbulence scales as $\Delta S_{v,12}\eta/a^*$. It can take order one values and still be described by the Lagrangian reference frame result.

The collision rate of a sphere pair is given by the integral of the product of the pair probability and inward flux at contact. The pair probability, a measure of the local particle concentration relative to the bulk, is altered by hydrodynamic interactions along with the relative velocity. The relative velocity sets the trajectory of spheres pairs that must approach from initially large separations and is given by the coupling of turbulence with differential sedimentation. Even without hydrodynamic interactions Brunk et al[20] found re-collision events that should be excluded, as collision is for pairs approaching from large separation, and so impacts the observed collision rate. Hence, we will perform trajectory analysis, for all cases, to determine the sphere pairs that collide. For numerical efficiency a time reversed flow is considered and sphere pairs start together and move apart, with the trajectory analysis detecting and rejecting those that come back together. We perform a Monte Carlo integration over all possible starting positions in the time reversed flow and ensemble average over the various realisation of turbulence to obtain the collision rate.

The collision rate calculated spans a large parameter space. Hence we only report the ideal collision rate and collision efficiency, to capture retardation due to hydrodynamic interactions. The former depends on relative strength of differential-sedimentation to turbulent flow and Re_λ . The latter additionally varies over ratio of mean free path to mean sphere size and relative size of the interacting spheres. We present results at certain cases to provide qualitative insight. However, to report the large amount of data we use a fit for the ideal collision rate and make an analytical approximation for the colli-

sion efficiency. This analytical result will be constructed based on the analysis involving pair probability evolution of a special configuration of the sphere pair in the lubrication regime, which in turn will involve integrals of the mobilities in radial space. By cutting off this integral close to the breakdown of continuum we will obtain a function that captures important features of the collision efficiency as a function of the various parameters. By adapting this result and fitting the free parameters with the generated collision efficiency data we will obtain a concise expression for collision efficiency.

We will obtain the collision rate for spheres settling in turbulent flow. In §3.3 we will present the pertinent formulations and outline the procedure we will use to calculate the collision rate. We will present the results for the ideal case, i.e., no interparticle interaction, in §3.4. We will carry out the calculations with uniformly valid hydrodynamics, that includes non-continuum lubrication and far-field continuum interactions, in §3.5 and present the collision efficiency. The collision efficiency data spanning a large parameter space will be reported with an analytical approximation that we will derived in §3.6. Then in §3.7 we will discuss important results from our study and how it can be applied to cloud physics.

3.3 Formulation

In a dilute system the collision of two spheres sets the collision rate K_{ij} , given as,

$$K_{ij} = \frac{dn_i}{dt} = -C_{ij}n_in_j \quad (3.1)$$

n_i is the number density of species i in the bulk. The two species rate constant C_{ij} can be expressed by an area integral as,

$$C_{ij} = - \int_{(r'=a_1+a_2) \& (\mathbf{v}' \cdot \mathbf{n} < 0)} (\mathbf{v}' \cdot \mathbf{n}) P dA' \quad (3.2)$$

Here species i has radius a_i moving with relative velocity of \mathbf{v}' when separated by centre to centre distance of r' . In this study as a notational convention we will denote dimensional quantities with prime and their non-dimensional equivalents without it. At radial separation r' the pair probability, P , captures the local species concentration relative to the bulk and it takes non-trivial values due to inter-particle interaction. Contribution to collision rate comes only from the radially inward motion when spheres come into contact with each other. This is captured through $\mathbf{v}' \cdot \mathbf{n} < 0$, with \mathbf{n} being the outward normal at the surface on contact.

The equations in our study are scaled with a characteristic length $a^* = (a_1 + a_2)/2$ and a characteristic velocity $\Gamma_\eta a^*$, where the $\Gamma_\eta = (\epsilon/\nu)^{1/2}$ is the Kolmogorov shear rate, ϵ is the turbulent dissipation rate and ν the kinematic viscosity. Thus, the non-dimensional centre to centre distance r ranges from 2 (referred to as collision sphere) to ∞ (where one sphere does not influence the other). The strength of gravity is parametrized through Q the ratio of characteristic differential-sedimentation to turbulent velocity. This is given as $Q = (2\rho g(a_2^2 - a_1^2)/[9\mu])/(\Gamma_\eta a^*)$, where g is the acceleration due to gravity, ρ is density of the spheres, μ is the dynamic viscosity experienced by the spheres in the medium. The geometrical parameter, the size ratio given as $\kappa = a_2/a_1$, captures the poly-dispersity of the system and has a range of $\kappa \in (0, 1]$. Thus the collision rate can be scaled with $n_1 n_2 \Gamma_\eta (2a^*)^3$ and expressed through an integral over the collision sphere as,

$$\frac{K_{ij}}{n_1 n_2 \Gamma_\eta (2a^*)^3} = - \int_{(r=2) \& (\mathbf{v} \cdot \mathbf{n} < 0)} (\mathbf{v} \cdot \mathbf{n}) P dA \quad (3.3)$$

It should be noted that this formulation and scaling is valid in the absence of any inertia, both the particle and fluid. This is valid for sub-Kolmogorov particles with low particle response time relative to the fluid. In this inertia-less system we use mobility

formulation and the non-dimensional relative velocity \mathbf{v} is given as,

$$v_i = \Gamma_{ij}r_j - [A(r)\frac{r_i r_j}{r^2} + B(r)(\delta_{ij} - \frac{r_i r_j}{r^2})]\Gamma_{jk}r_k - [L(r)\frac{r_i r_j}{r^2} + M(r)(\delta_{ij} - \frac{r_i r_j}{r^2})]Q\delta_{j3} \quad (3.4)$$

$A(r), L(r)$ are radial mobilities and $B(r), M(r)$ are tangential mobilities for a linear flow and differential sedimentation, respectively. These mobilities capture hydrodynamic interactions and take trivial values in the ideal flow, i.e., in the absence of particles interacting with each other. Gravity is directed along the negative 3-direction and the other two directions in the Cartesian coordinate are degenerate. $\mathbf{\Gamma}$ is the velocity gradient of the local and instantaneous linear flow experienced by the sub-Kolmogorov spheres in homogeneous isotropic turbulence. $\mathbf{\Gamma}$ has been scaled with the Kolmogorov shear rate and is obtained from the model developed by Girimaji & Pope[44]. It captures the non-Gaussian probability distribution of the velocity gradient, through the log-normal behaviour of the pseudo-dissipation rate(sum of velocity gradient square) as well as its correlation over the integral time scale, and important features of the linear flow, such as correlation time of the straining flow as well as the relative orientation of vorticity, observed in DNS of homogeneous isotropic turbulence. We extended the validity of their velocity gradient model to arbitrary Taylor's Reynolds number (Re_λ) by incorporating results on the variance of the pseudo-dissipation rate and ratio of integral time scale to Kolmogorov time scale. Their dependence Re_λ have been studied in DNS[125] as well as experiments[107]. These have been compiled and a concise expression given in the appendix of Koch & Pope[63] and will be used in our study.

To evaluate the collision rate from equation (3.3) we also need information on P . This can be obtained from the governing equation that can be given as,

$$\frac{\partial P}{\partial t} + \nabla \cdot (\mathbf{v}P) = 0 \quad (3.5)$$

With the boundary condition $P \rightarrow 1$ as $r \rightarrow \infty$ which corresponds to the particles being

too far away to influence each other. Trajectories that do not start at $r \rightarrow \infty$ are set to $P = 0$ and this excludes re-collisions. A non-trivial evolution of the pair-probability is possible only for a non-solenoidal relative velocity. The solenoidal nature of the evolution is broken by hydrodynamic interactions.

The initial state of the sphere pairs constituting equation (3.3) is at a large separation from each other. It is numerically very expensive to evaluate for the case of satellite spheres evolving from r of ∞ to 2 since most of them will miss the test sphere placed at the origin. Hence, exploiting the Stokes flow reversibility a time-reversed calculation is performed. In this time-reversed flow the satellite spheres begin at $r = 2$ and those that reach the outer boundary, set as r_∞ , without returning to $r = 2$ will have non-zero contributions towards the integral in equation (3.3).

In the time-reversed flow the calculations begin by first seeding satellite spheres on the collision sphere. To span the initial angular positions we use a Monte-Carlo integration scheme. From the initial point on the collision sphere the satellite spheres start with a time offset of $1/\Gamma_\eta$ and are evolved using 'ODE45', an in-built adaptive time-stepping routine available in MATLAB, which takes as input the relative velocity given in equation (3.4). This stochastic flow field is updated every $0.1/\Gamma_\eta$ using the velocity gradient model. The satellite spheres only interact with the test sphere and are allowed to evolve for a long time, up to $150/\Gamma_\eta$. By this time more than 99% of the satellite spheres have either reached $r = 2$ or $r = r_\infty$, with r_∞ representing the separation at which sphere pairs no longer influence each other. We find convergent result for pair probability at contact when $r_\infty = 7$ and so the collision rate can be accurately calculated. The result depends on the specific realisation of turbulence in which the satellite sphere evolved. To ensemble average we obtain a different realisation of the turbulent flow by offsetting by $400/\Gamma_\eta$. This is multiple integral time scales apart, with even Re_λ as

high as 2500 corresponding to $200/\Gamma_\eta$ and much larger than the correlation time for both straining and rotational component of the linear flow, which are $2.3/\Gamma_\eta$, $7.2/\Gamma_\eta$ respectively. In addition to the ensemble averaged collision rate we also estimate the error, through standard deviation over the various realisations, and report one standard error.

3.4 Ideal collision rate

In the absence of hydrodynamic interactions $A(r) = 1$, $L(r) = 0$, $B(r) = 1$, $M(r) = 0$ and $P = 1$ or 0. Using this information as input into equation (3.4) we follow the procedure outlined in §3.3 to calculate the collision rate. To obtain this we ensemble average over the 200 realisations of the turbulent flow. For each realisation we perform Monte Carlo integration using 150 trajectory evolution. These satellite spheres, in the time-reversed flow, are assigned $P = 1$ if they reach r_∞ within the allotted simulation without going to $r = 2$ or 0 otherwise.

The ideal collision rate K_{ij}^0 is presented in figure 3.1 for the case of $Q = 0$, i.e. no effects of gravity included, as a function of the Taylor's Reynolds number. It is immediately evident that a non-trivial behaviour is observed, in contrast to the constant result predicted by Saffman & Turner[97]. In their analysis a pseudo-steady extensional flow with Gaussian statistics for the strain rate was used. Our result is expected to be more accurate as we use a stochastic flow with statistics of the velocity more closely aligned with the non-Gaussian nature predicted from DNS.

Re_λ influences the non-Gaussian statistics of the turbulent velocity. This is evident from the DNS and experimental studies on the pseudo-dissipation rate $\Phi = \Gamma_{ij}\Gamma_{ij}$ [125, 107]. The collision rate is proportional to $\mathcal{H}(-n_i\Gamma_{ij}n_j)$ evaluated on the col-

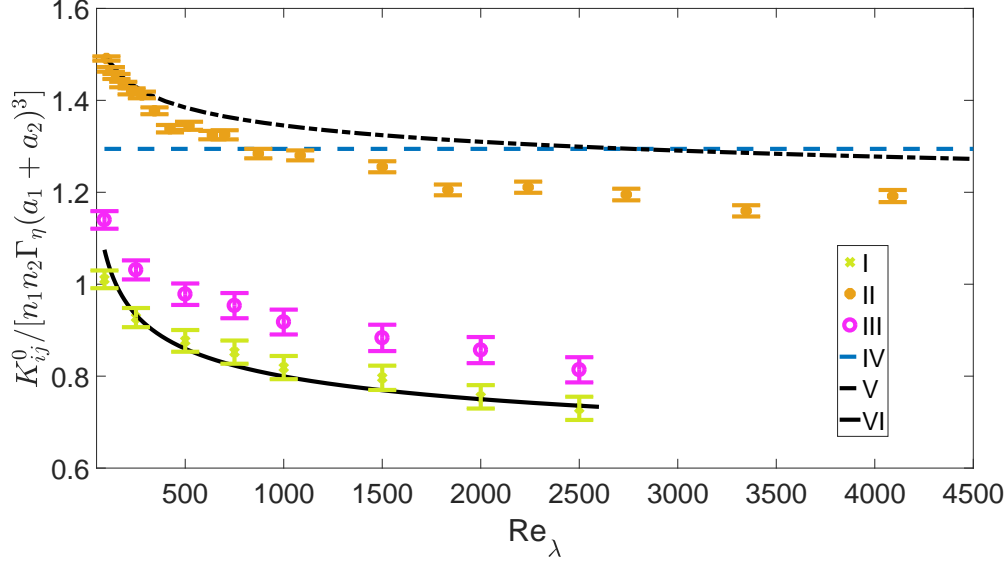


Figure 3.1: 'I' is ideal collision rate K_{ij}^0 given as a function of the Re_λ for $Q = 0$, i.e. no gravitational effects. Variation of the inward flux with Taylor's Reynolds number is given by 'II'. Calculations performed with frozen velocity gradient during any given satellite sphere evolution is denoted by 'III'. All the error bars shown correspond to one standard error. 'IV' is the reference calculation of Saffman & Turner[97] and is insensitive to Re_λ . $\int P_\Phi \Phi^{1/2} d\Phi$ decreases with increasing Taylor's Reynolds number and has been multiplied by $\int_{(r=2) \& (n_i \Gamma_{ij} n_j < 0)} dA n_i \Gamma_{ij} n_j / \Phi^{1/2} \approx 1.7$ and given in 'V'. The predictions of the ideal collision rate fit, given in equation (3.7), has been shown with 'VI'.

lision sphere, where \mathcal{H} is the Heaviside function. To test its dependence on Re_λ we calculate $\int P_\Phi \Phi^{1/2} d\Phi$, here P_Φ is the probability density function for Φ . This integral can be written as,

$$\int P_\Phi \Phi^{1/2} d\Phi = \frac{\int \epsilon^{1/2} P_\epsilon d\epsilon}{(\int \epsilon P_\epsilon d\epsilon)^{1/2}} \quad (3.6)$$

P_ϵ is the probability density function for ϵ , which is available in literature (See Koch & Pope[63]). To make it consistent with a collision rate result we multiply it with $\int_{(r=2) \& (n_i \Gamma_{ij} n_j < 0)} dA n_i \Gamma_{ij} n_j / \Phi^{1/2}$ which is approximately 1.7. This result is shown in figure 3.1 and decreases with Re_λ . Increasing Re_λ leads to fatter tails of the turbulent velocity probability distribution function and so the expected value for a low order moment

decreases. Since $\mathcal{H}(-n_i\Gamma_{ij}n_j)$ is at a lower order than Φ the observed decrease of the collision rate with Re_λ in figure 3.1 is expected.

Next we explicitly calculate collision rate obtained from $\mathcal{H}(-n_i\Gamma_{ij}n_j)$ by substituting $\mathbf{v}' \cdot \mathbf{n} = n_i\Gamma_{ij}n_j$ in equation (3.3). This result is shown in figure 3.1 and is the closest analogue to the analysis by Saffman & Turner[97] who determined the collision rate to be the inward radial velocity on the collision sphere. Our inward flux result, though, varies with Re_λ . At low Re_λ it is higher than the 1.29 prediction of Saffman & Turner[97]. At low Re_λ the DNS study by Chen et al[24] finds a slightly higher value for the collision rate than the Saffman & Turner[97] prediction, but the difference lies within the margin of error. Ireland et al[53] performed DNS over a larger range of Re_λ , from 88 to 597, and found inward flux dip by 10% but errors were about 10% as well. Hence while it is not conclusive there is strong reason to expect that the results of our study are supported by previous DNS studies. At higher Re_λ the inward flux result and the estimate based on $\Phi^{1/2}$ do not overlap due to the correlation between pseudodissipation and the velocity gradient. This, in turn, is expected from the coupled evolution equation for the velocity gradient[44].

In a stochastic flow Brunk et al[20] found a 20% reduction in collision rate due to satellite spheres, in the time-reversed configuration, starting and ending on the collision sphere. These re-circulating trajectories were attributed to the rotational component of the flow and stochasticity. However, their analysis assumed Gaussian distribution for velocity and so in the non-Gaussian calculation it is of interest to determine the impact of each component in generating re-circulating trajectories. For this purpose we perform an equivalent collision rate calculation that is identical to our original calculation except a frozen velocity gradient for any satellite sphere evolution. This result is given in figure 3.1 and is much closer to the original calculation than the inward flux. This indicates that

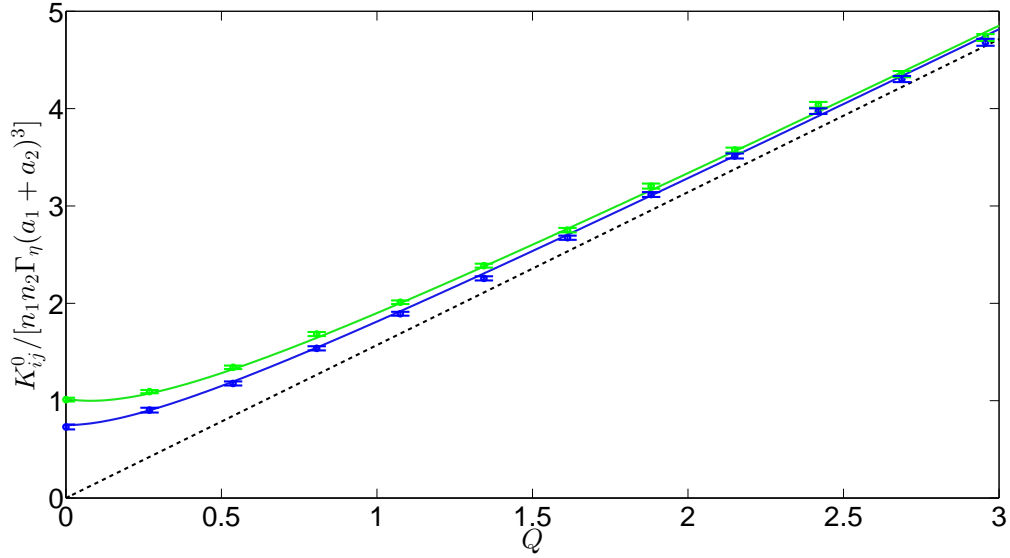


Figure 3.2: The ideal collision rate K_{ij}^0 is given as a function of Q at only $\text{Re}_\lambda = 90$ and 2500 for sake of conciseness. The symbols correspond to the numerically calculated collision rate and the solid lines to the fit. The higher Re_λ corresponds to lower collision rate. The error bars correspond to one standard error. For reference the ideal collision rate predicted by Smoluchowski[106] for spheres settling in quiescent flow is given by the dashed line.

the rotational component of the turbulent flow is responsible for a significant fraction of the re-circulating trajectories.

Figure 3.2 shows the ideal collision rate K_{ij}^0 as a function of Q . With increasing Q the ideal collision rate increases and converges to a line of slope $(\pi/2)$ and no intercept for all Re_λ . This asymptote corresponds to the ideal pure differential-sedimentation collision rate of $2n_1 n_2 \rho g (a_2^2 - a_1^2) (a_1 + a_2)^2 / (9\mu)$ calculated by Smoluchowski[106]. The convergence to this result with increasing Q , and the collapse of dependence of the ideal collision rate with Re_λ , is expected as gravity is not a stochastic process and it washes away all the intricacies, like re-circulating trajectories, arising from turbulence. Only $\text{Re}_\lambda = 90$ and 2500 are shown to avoid crowding in the plots. However, the behaviour described here is valid for a large range of Re_λ . To concisely capture the large amount

of data we have calculated across the parameter space in Q and Re_λ we use a fitting function. This is given as,

$$\frac{K_{ij}^0}{n_1 n_2 \Gamma_\eta (2a^*)^3} = \frac{f_1 \text{Re}_\lambda^{f_2}}{1 + f_Q Q} + \frac{\pi}{2} Q$$

Here, f_1 , f_2 and f_Q are fitting parameters. This form captures captures asymptotic behaviour in the large Q limit shown in figure 3.2 as well as the expected power law form for dependence on Re_λ shown in figure 3.1. We found that $f_1 = 1.55$, $f_2 = -0.09$ and $f_Q = 2.1$ gives best agreement with data. From this expression it is evident the coupling of gravity with turbulence leads to a non-trivial result that cannot be captured through a linear combination of the collision rate of gravity and turbulence.

3.5 Collision rate with hydrodynamic interactions

Hydrodynamic interactions alter the relative velocity and pair-probability and retard the collision rate (K_{ij}^{HI}) relative to the ideal flow result. The collision efficiency ($\beta = K_{ij}^{HI}/K_{ij}^0$) will be used to characterise this retardation due to non-continuum hydrodynamics with the breakdown of continuum parametrised through the Knudsen number, $\text{Kn} = \lambda_g/a^*$, where λ_g is the mean free path of the gas. The mobilities capturing this interaction depend only on the centre to centre distance and, more significantly, the important features are sensitive to the surface to surface distance. For this purpose a new radial coordinate $\xi = r - 2$ is used. This coordinate will also be useful to characterise the pair-probability evolution since it is intricately coupled with the mobilities.

Continuum hydrodynamic interaction mobilities have been calculated for the normal direction by Wang et al[117] by solving for the velocities in a bispherical coordinate. In the tangential direction Jeffrey&Onishi[59] and Jeffrey[58] have presented the twin multipole solution to determine the mobility. Both these series solution become less accurate

as ξ decreases and so require more terms to compensate. This becomes infeasible in the $\xi \ll 1$ limit and, instead, we use the lubrication results available in literature[10, 59, 58]. A smooth transition between the two regimes is made.

As the spheres approach each other the continuum lubrication force diverges at a rate that does not allow collision to occur in finite time[10]. The non-continuum lubrication force diverges at a weaker rate and allows for finite time collisions. These become important at $\xi = O(\text{Kn})$ and the normal force has been calculated for all separation by Sundararajakumar & Koch[113]. We incorporate this into the normal mobilities and obtain a uniformly valid result that captures breakdown of continuum at $\xi \leq O(\text{Kn})$, far-field continuum behaviour when $\xi \geq 1O(1)$, and smoothly transitions through continuum lubrication in $\text{Kn} \ll \xi \ll 1$.

In the limit of $\xi \rightarrow 0$ continuum tangential mobilities approach a finite value. Hence, in this direction, motion is not stalled and $O(\text{Kn})$ correction to the mobility is expected to be minimal. Thus, in our calculation, tangential mobilities are informed by continuum hydrodynamics at all ξ .

The hydrodynamic interactions, both continuum and non-continuum, have an impact on the pair probability. Its evolution along a trajectory can be obtained from equation (3.5) rewritten as,

$$P = \exp\left(- \int \nabla \cdot \mathbf{v} dt\right) \quad (3.7)$$

Here the integrand has the divergence of the relative velocity that is given as,

$$\begin{aligned} \frac{\partial v_i}{\partial r_i} = & -\frac{r_i \Gamma_{ij} r_j}{r} \left[3 \frac{A(r) - B(r)}{r} + \frac{dA(r)}{dr} \right] - \\ & Q s_j \delta_{j3} \left[2 \frac{L(r) - M(r)}{r} + \frac{dL(r)}{dr} \right] \end{aligned} \quad (3.8)$$

Non-zero contribution to the integral in equation (3.7) occurs for non-solenoidal

relative velocity. $\nabla \cdot \mathbf{v} \rightarrow 0$ as $r \rightarrow \infty$, due to decay in interactions between particles. Hence for numerical purposes we stop tracking evolution of P beyond a certain radial separation, which we have noted to be r_∞ in the end of §3.3. There we also discussed the necessity of a Monte Carlo integration and ensemble averaging. For the case with hydrodynamic interactions we integrate over 50 trajectory evolutions and average over 100 realisation of the turbulent flow to obtain the collision rate.

As the spheres approach each other the relative velocity decays to zero, albeit at the very slow rate of $O(1/\ln[\ln(\text{Kn}/\xi)])$ which allows for collision in finite time. Due to this decay, in the time-reversed flow, numerical issues arise if the satellite spheres begin very close to the test sphere. Instead we create an offset collision sphere of $r = 2 + \xi_0$ and seed satellite spheres on it. A small offset ξ_0 is required for accurate collision rate but a large value for finite \mathbf{v} . We find that $\xi_0 = 10^{-7}$ satisfies both these constraints.

Figure 3.3 shows a monotonic decrease in β with Kn at $\kappa = 0.7$ and $\text{Re}_\lambda = 2500$. We have shown it here for the $Q = 0$ case (figure 3.3 (a)) and the $Q \rightarrow \infty$ limit (figure 3.3 (b)). For intermediate values of Q it can be deduced from subsequent figures and not shown here for sake of brevity. This behaviour can be ascribed to the increased continuum lubrication resistance faced by spheres due to the decrease in the mean free path relative to their own size. Comparing the two figures it is also evident that the hydrodynamic interaction retards the differential sedimentation process more as well as leads to a higher relative change with Kn than pure turbulence. These qualitative behaviours have been observed at all values of κ .

Figure 3.4 shows collision efficiency as a function of κ at $\text{Kn} = 10^{-3}$ and $\text{Re}_\lambda = 2500$. As mentioned previously, the result for turbulent dominated flow ($Q = 0$, figure 3.4 (a)) has higher efficiency than the gravity dominated regime ($Q \rightarrow \infty$, figure 3.4 (b)). In both cases β decreases with κ and this behaviour is observed across the parameter space

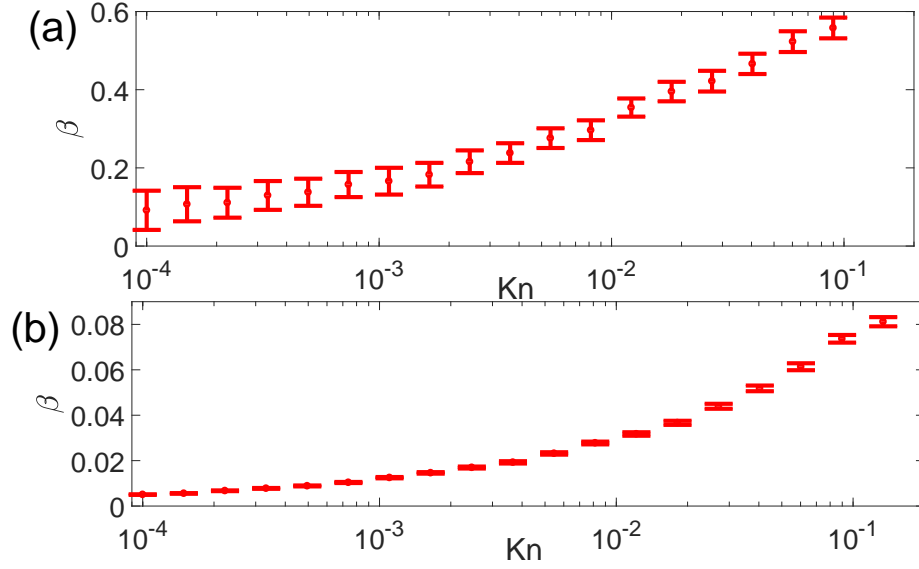


Figure 3.3: β decreasing with Kn is shown for $\kappa = 0.7$ and $Re_\lambda = 2500$. Figure (a) is in the pure turbulence limit ($Q = 0$) and figure (b) is for differential sedimentation limit ($Q \rightarrow \infty$).

in Kn and Q .

The probability distribution of strain rate magnitudes varies with Re_λ and it impacts the collision rate as noted in the discussion in §3.4 on the ideal collision rates. We show its role on the collision efficiency in figure 3.5, calculated at $Kn = 10^{-2}$ and $\kappa = 0.9$. We plot results in the turbulence dominated, turbulence competing with gravity, and gravity dominated regimes. Only the second one shows any statistically significant behaviour. When gravity is strong as the stochastic effects of turbulence are washed away. In the turbulence dominated regime, as a consequence of the linearity of the Stokes flow particle interactions, the collision efficiency depends only on the mobility functions. At intermediate Q there is a competition of turbulence with gravity which includes the differing extent by which hydrodynamic interactions retard the collision rate. The distribution of turbulent strain rates now leads to variations in the sensitivity of the particle motion to the linear-flow and sedimentation mobilities. At higher Re_λ , the mean inward velocity is smaller for a given value of $\langle \epsilon \rangle^{1/2}$. This makes the collision

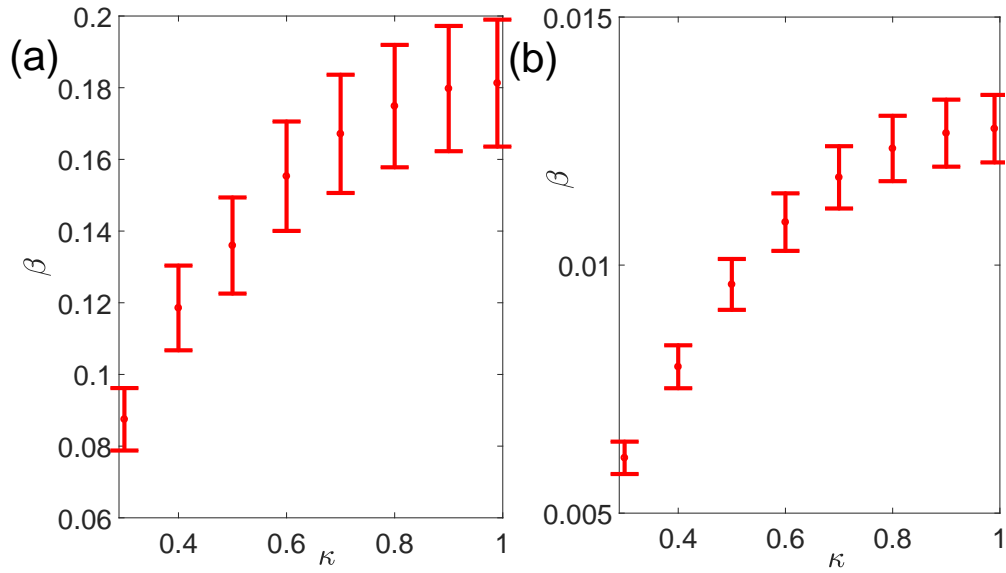


Figure 3.4: The collision efficiency is shown as a decreasing function of κ for $\text{Kn} = 10^{-3}$ and $\text{Re}_\lambda = 2500$. Figure (a) is in the absence of gravitational effects ($Q = 0$) and figure (b) is in a purely gravity driven flow ($Q \rightarrow \infty$). The error bars correspond to one standard error.

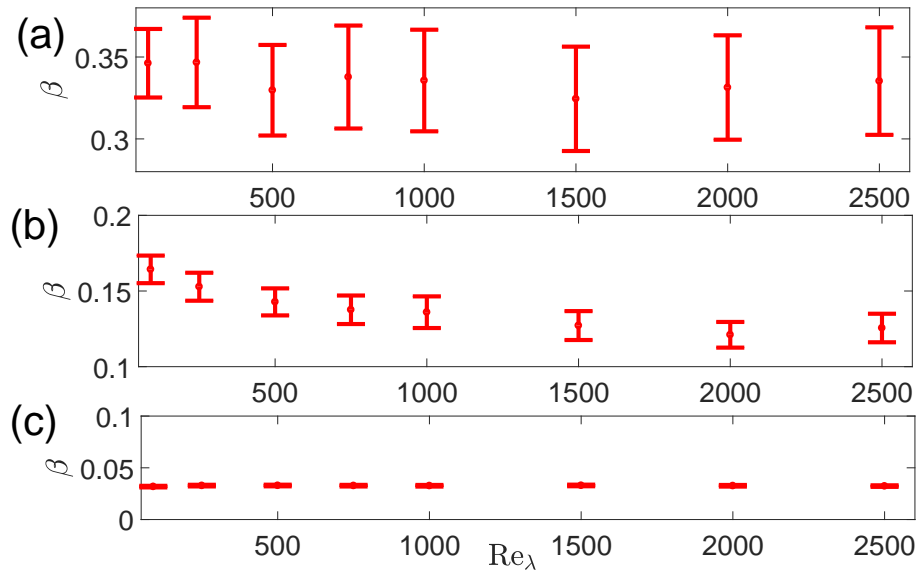


Figure 3.5: The dependence on Re_λ of the collision efficiency is shown here for $\text{Kn} = 10^{-2}$, $\kappa = 0.9$ at (a) $Q = 0$, (b) $Q \approx 1$ and (c) $Q \approx 10$. The error bars correspond to one standard error. β varies with Re_λ for moderate Q

efficiency more sensitive to sedimentation mobilities, so that β decreases with increasing Re_λ .

Figure 3.6 shows the variation of β at $Kn = 10^{-3}$, $\kappa = 0.5$ and $Re_\lambda = 2500$ as a function of Q . The decrease in collision efficiency with Q is observed at all values of Kn , κ and Re_λ we have considered. At high Q , i.e., gravity dominated collisions, the far-field hydrodynamic interaction persist for large separations, larger than in the turbulent dominated regime, of $Q \approx 0$. Hence, in turbulence, motion of interacting spheres is retarded to a lesser extent and reflected in the higher values of β .

The far-field hydrodynamic interaction argument is valid for any linear flow and not just the stochastic linear flow observed by sub-Kolmogorov spheres in turbulence. To demonstrate this β is calculated for a "persistent" background turbulence. For this frozen turbulence analysis we use an uniaxial compressional flow, the most likely realisation in turbulent flow[2], whose axis of compression is aligned with the direction gravity. To determine the extension rate ($\dot{\gamma}$) in terms of Kolmogorov quantities we equate the ideal collision rate in static uniaxial compressional flow, calculated by Zeichner & Schowalter[130] and given as $[4\pi/(3\sqrt{3})]n_1n_2\dot{\gamma}[2a^*]^3$, with the equivalent turbulent result, evaluated by Saffman & Turner[97] and given as $(8\pi/15)^{\frac{1}{2}}(2a^*)^3n_1n_2(\epsilon/\nu)^{\frac{1}{2}}$. Thus, we get $\dot{\gamma} = (18/[5\pi])^{1/2}(\epsilon/\nu)^{1/2}$. By following a non-dimensionalisation consistent with that outlined in §3.3 we evaluate β and Q for "persistent" turbulence and plot it along with the stochastic result in figure 3.6. Both show similar values of the collision efficiency across the parameter space in Q . Around $Q \approx 5$, though, the "persistent" turbulence result shows non-monotonic behaviour with Q . These intricate features in the collision efficiency arise due to satellite spheres moving in circuitous trajectories. They are washed away by the angular variation and time dependence of the strain fields in turbulence. A statistically significant difference in β between the stochastic and "persis-

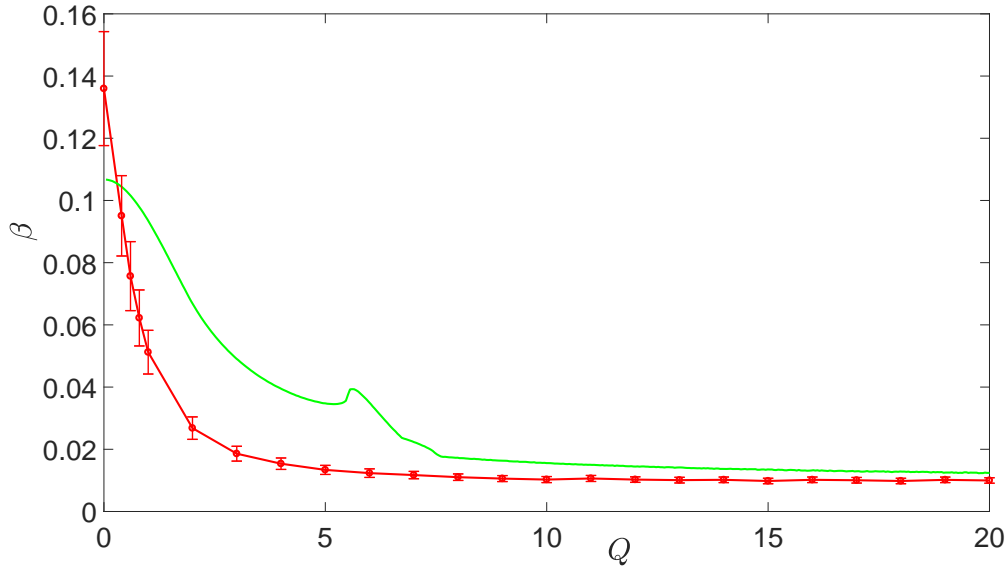


Figure 3.6: The variation of collision efficiency with Q is shown for $\text{Kn} = 10^{-3}$ and $\kappa = 0.5$. The curve with symbols corresponds to the stochastic linear flow field with $\text{Re}_\lambda = 2500$. The error bars show one standard error. The solid line is the for frozen uni-axial compressional flow calculation, with compression axis aligned with gravity.

tent” results is observed for small Q . This can be attributed to the difference in collision efficiency of the realisations of the linear flow that are not uniaxial compression, such as the planar extensional flow. The difference, even at $Q = 0$, is minimal indicating uniaxial compressional flow does make the dominant contribution.

3.6 Analytical approximation for the collision efficiency

In §3.5 we have presented β at some typical values of Taylor’s Reynolds number, size ratio of the spheres, relative strength of gravity to the turbulent flow and strength of non-continuum hydrodynamic interactions. We showed some of the important qualitative features but it is not feasible to present data on β that exhaustively spans the parameter space. Hence, in this section, we obtain an analytical approximation to the

collision efficiency. The analytically derived expression is based on the important physical characteristics of the pertinent parameters of the collision dynamics: Kn , Q , κ . Undetermined constants will be obtained by fitting with the available data on β . We have not included Re_λ as there is no fully theoretical understanding of the velocity gradient statistics. Instead we will carry out the analysis at $\text{Re}_\lambda = 2500$, as this is typical in clouds [48]. It is to be noted that the variation with Re_λ of β , while statistically significant, occurs over a narrow range and does not have as much as influence as other parameters. Hence, important aspects of turbulent fluctuations are captured by the ideal collision rate presented in §3.4. Including to this the closed form result for the collision efficiency, shown in this section, will give the overall collision rate with high fidelity.

Batchelor & Green[11] obtained an expression for the evolution of the pair probability in a linear flow, with an equivalent analysis in sedimenting flow by Batchelor[9]. It involved evaluating an integral, that combined the radial and tangential mobilities, over the radial separation. These were estimated for the very small and very large separation limits using appropriate approximations to the continuum mobilities. Chun & Koch[27] used this idea to obtain a closed form expression for collision efficiency in linear flow with interactions governed by non-continuum hydrodynamic lubrication. Non-continuum interactions are much weaker than the continuum forces and so it is possible to cut off the collision efficiency integral at $\xi = O(\text{Kn})$. By retaining only the leading order term they obtained a power law in Kn and fitted with collision efficiency data, computed for a monodisperse suspension in turbulent flow, to determine the pre-factor of the power law. This result does not account for difference in size of the interacting pair or the coupling of turbulence with differential sedimentation. Hence we derive a more general expression and retain an additional term in the mobility approximation to increase accuracy.

The critical component in computing the collision efficiency are the relative velocity and pair probability, its evolution given by equation (3.5) where it is coupled with the former. To evaluate these and obtain a closed form expression for β we consider a coupled system with frozen uniaxial compressional flow, the most likely linear flow in a turbulent velocity field [2], whose compressional axis is aligned with gravity. For sake of convenience, in this frozen flow calculation, we will use spherical coordinates (r, θ, ϕ) , where θ is the polar angle measured from the direction of gravity and ϕ is the azimuthal angle measured in the plane normal to gravity. This plane contains both the extensional axis of the uniaxial compressional flow. Without loss of generality we consider motion only in the $\phi = 0$ plane and, thus, equation (3.5) can be written as,

$$v_r \frac{\partial P}{\partial r} + v_\theta \frac{\partial P}{r \partial \theta} = -P \nabla \cdot \mathbf{v} \quad (3.9)$$

Here v_r and v_θ represent velocity in the r and θ direction respectively. Using the method of characteristics on the r derivative and simplifying we get,

$$\int_{r^*}^{\infty} d(\ln P) = \int_{r^*}^{\infty} -\frac{\nabla \cdot \mathbf{v}}{v_r} dr \quad (3.10)$$

Here, r^* denotes the lower bound of the integral. This integral is to be computed along the trajectory with velocities constrained as $(r \sin \theta) d\theta/dr = v_\theta/v_r$. Expanding $\nabla \cdot \mathbf{v}$ and simplifying we get,

$$\int_{r^*}^{\infty} \frac{\nabla \cdot \mathbf{v}}{v_r} dr = \int_{r^*}^{\infty} d(\ln v_r) + \int_{r^*}^{\infty} \left(\frac{2}{r} + \frac{1}{v_r} \frac{1}{r \sin \theta} \frac{\partial(v_\theta \sin \theta)}{\partial \theta} \right) dr \quad (3.11)$$

The relative velocity in spherical coordinates can be given as,

$$\begin{aligned} v_r &= r[1 - A(r)](1 - 3 \cos^2 \theta) - L(r)Q \cos \theta \\ v_\theta &= 3r[1 - B(r)] \cos \theta \sin \theta + M(r)Q \sin \theta \end{aligned} \quad (3.12)$$

Incorporating into equation (3.11) and subsequently into equation (3.3) the collision rate is determined to be,

$$\frac{K_{ij}}{n_1 n_2 \Gamma_\eta (2a^*)^3} = v_{r,\infty} \exp\left(\int_{r^*}^{\infty} dr \left[\frac{2}{r} + \frac{3[1 - B(r)](3 \cos^2 \theta - 1) + 2M(r)Q \cos \theta/r}{r[1 - A(r)](1 - 3 \cos^2 \theta) - L(r)Q \cos \theta} \right] \right)$$

Here, $v_{r,\infty}$ is the radial velocity at large separations. From this an expression for the ideal collision rate can be obtained and used to determine β . It is given, in the $\xi^* \ll 1$ limit, as

$$\beta = \exp\left(\int_{\xi^*}^{\infty} d\xi \left[\frac{3[1 - B(\xi)](3 \cos^2 \theta - 1) + M(\xi)Q \cos \theta}{2[1 - A(\xi)](1 - 3 \cos^2 \theta) - L(\xi)Q \cos \theta} - \frac{3(3 \cos^2 \theta - 1) + Q \cos \theta}{2(1 - 3 \cos^2 \theta) - Q \cos \theta} \right]\right) \quad (3.13)$$

This integral will give $\beta = 0$ when evaluated till $\xi^* = 0$ using continuum mobilities. Instead we use the asymptotic continuum lubrication mobilities in equation (3.13) and cut the integral off at separations comparable to the mean free path. From the work by Batchelor & Green[10] and Batchelor[9] it is known that $1 - A(\xi) \approx A_1\xi$, $L(\xi) \approx L_1\xi$. For tangential mobilities Jeffrey & Onishi[59] and Jeffrey[58] showed that $1 - B(\xi) \approx B_0 + B_1/\ln(\xi^{-1})$, $M(\xi) \approx M_0 + M_1/\ln(\xi^{-1})$. While $B_0, B_1, M_0, M_1, A_1, L_1$ only depend on κ we have $(r \sin \theta)d\theta/dr = v_\theta/v_r$ and so only numerical solutions are possible for equation (3.13). Thus, to obtain a closed form expression without introducing significant errors we assume θ is not a function of r , which is exact at $\theta = 0$ or π . Using this and the result of the continuum lubrication mobilities we evaluate equation (3.13). For the lower limit we set $\xi^* = \text{Kn}$. For the upper limit instead of evaluating till ∞ we leave it as a free parameter. This will allow us to fit with the extensive amount of data available on β and capture behaviour not accounted for in the analytical approximation. Thus we get,

$$\beta = p_1 \frac{\text{Kn}^{q_1}}{(p_2 + \ln \frac{1}{\text{Kn}})^{q_2}} \quad (3.14)$$

The exponents are given as,

$$\begin{aligned} q_1 &= \frac{3B_0(3 \cos^2 \theta' - 1) + M_0Q \cos \theta'}{2A_1(3 \cos^2 \theta' - 1) + L_1Q \cos \theta'} \\ q_2 &= \frac{3B_1(3 \cos^2 \theta' - 1) + M_1Q \cos \theta'}{2A_1(3 \cos^2 \theta' - 1) + L_1Q \cos \theta'} \end{aligned} \quad (3.15)$$

q_1 is associated with the leading order of the tangential lubrication to radial lubrication, while q_2 represents the next term of the tangential lubrication. These depend on the

κ	A_1	B_0	B_1	L_1	M_0	M_1
0.3	2.53	0.20	3.77	0.45	0.07	1.16
0.4	3.03	0.32	3.46	0.56	0.11	1.16
0.5	3.41	0.42	3.00	0.64	0.15	1.08
0.6	3.69	0.49	2.59	0.70	0.18	0.98
0.7	3.88	0.54	2.28	0.74	0.20	0.89
0.8	4.00	0.57	2.09	0.76	0.21	0.84
0.9	4.06	0.59	1.98	0.78	0.22	0.81
0.99	4.06	0.59	1.95	0.78	0.22	0.80

Table 3.1: Values of the coefficients of asymptotic forms of the continuum mobilities: $B_0, B_1, M_0, M_1, A, L_1$ at various values of κ . These have been obtained from the work by Jeffrey & Onishi[59] and Jeffrey[58]

coefficients of the asymptotic forms of the continuum mobilities, which have been given in table 3.1. p_1 is the upper limit of the integral in equation (3.13), while p_2 represents the fact that the cut-off of the integral at the lower limit need not happen exactly at $\xi^* = \text{Kn}$. p_1 and p_2 along with θ' will act as the free parameters.

Figure 3.7 shows β as a function of Kn for $\kappa = 0.4$, along with the output from equation (3.14). Figure 3.7 (a) shows it at $Q = 0$ and figure 3.7 (b) in the $Q \rightarrow \infty$ regime. The computed data agrees well with the analytical approximation, including reproducing the larger relative change in β for differential sedimentation over a given range of Kn when compared with the turbulence result. To account for this considerable difference between the two extremes we take p_1, p_2 to be $p_{1,\epsilon}, p_{2,\epsilon}$ and $p_{1,g}, p_{2,g}$ for the pure turbulent flow and pure differential-sedimentation case respectively. These have been determined by fitting with the computed collision efficiency in the $Q = 0$ and $Q \rightarrow \infty$ asymptotes respectively and presented in table 3.2 for κ from 0.3 to 0.99. It should be noted that in these limits the analytical approximation is independent of θ' and will come into play only at non-zero finite Q .

The dependence of β on κ is shown in figure 3.8 for $\text{Kn} = 10^{-2}$, along with the

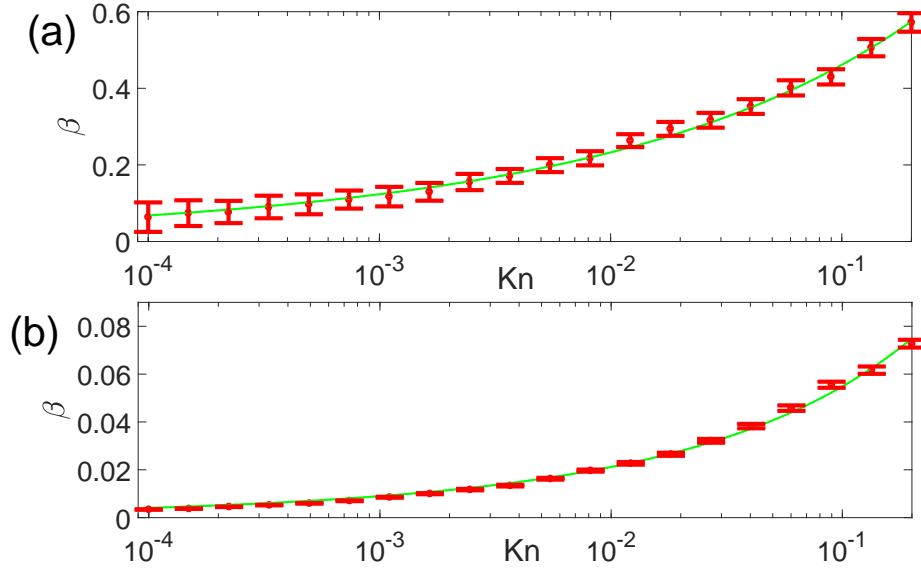


Figure 3.7: The collision efficiency is plotted as a function of Kn for $\kappa = 0.4$. Figure (a) is in the pure turbulence limit ($Q = 0$) and figure (b) is for pure-differential sedimentation ($Q \rightarrow \infty$). The symbols represent the results of the numerical calculation. The error bars correspond to one standard error. The solid lines are the analytical approximation, given in equation (3.14). The errors, when compared against the results of the numerical calculation, is minimal.

κ	$p_{1,\epsilon}$	$p_{2,\epsilon}$	$p_{1,g}$	$p_{2,g}$
0.3	89.83	8.11	13.68	5.95
0.4	40.49	8.776	7.99	6.40
0.5	19.27	8.99	4.40	6.71
0.6	12.08	9.54	2.74	6.73
0.7	8.83	9.90	1.97	6.73
0.8	7.39	10.29	1.62	6.73
0.9	6.801	10.64	1.46	6.73
0.99	6.64	10.75	1.42	6.72

Table 3.2: Values of the fit parameters $p_{1,\epsilon}$, $p_{2,\epsilon}$, p_{1g} and $p_{2,g}$ at various values of κ

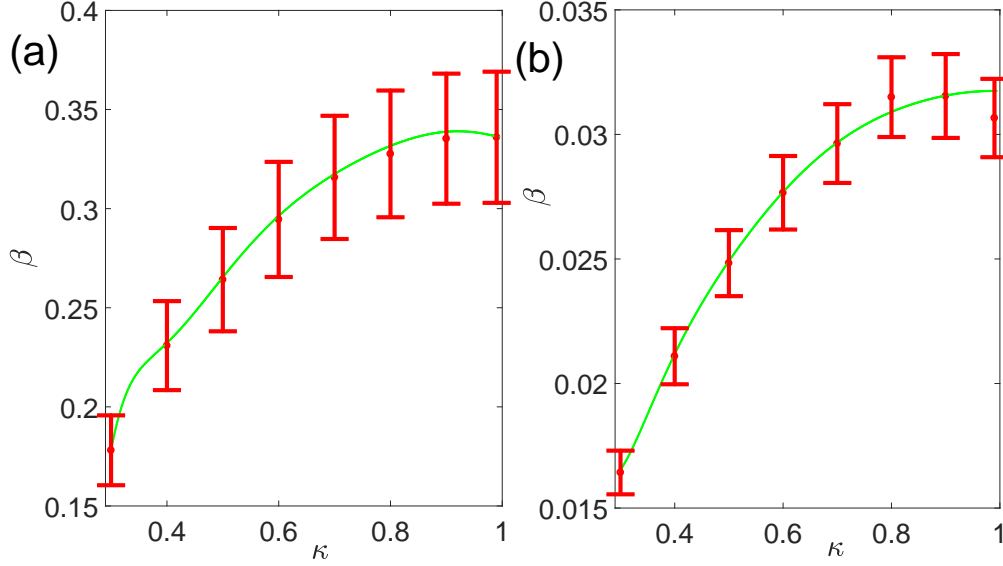


Figure 3.8: β is shown as function of κ at $\text{Kn} = 10^{-2}$. Figure (a) is in the absence of gravitational effects ($Q = 0$) and figure (b) is in a purely gravity driven flow ($Q \rightarrow \infty$). The symbols represent the results of the numerical calculation with errors bars of one standard error. The solid line is from equation (3.14) and agrees well with the data.

predictions of equation (3.14). Figure 3.8 (a) shows it at $Q = 0$ and figure 3.8 (b) in the $Q \rightarrow \infty$ regime. To smoothly span in size ratio the parameters $p_{1,\epsilon}$, $p_{2,\epsilon}$, p_{1g} and $p_{2,g}$ are fitted with a polynomial in κ . The resulting output of equation (3.14) lies well within the error bounds of the computed numerical data.

For any arbitrary Q the fitting parameters p_1 and p_2 in equation (3.14) are expected to take a value somewhere in-between those in the pure turbulent and pure differential sedimentation regime. Hence we take $p_1 = p_1(Q)$ and $p_2 = p_2(Q)$, with their functional form chosen to be,

$$\begin{aligned}
 p_1(Q) &= \exp(-l_1 Q) p_{1,\epsilon} + [1 - \exp(-l_1 Q)] p_{1,g} \\
 p_2(Q) &= \exp(-l_2 Q) p_{1,\epsilon} + [1 - \exp(-l_2 Q)] p_{2,g}
 \end{aligned}
 \tag{3.16}$$

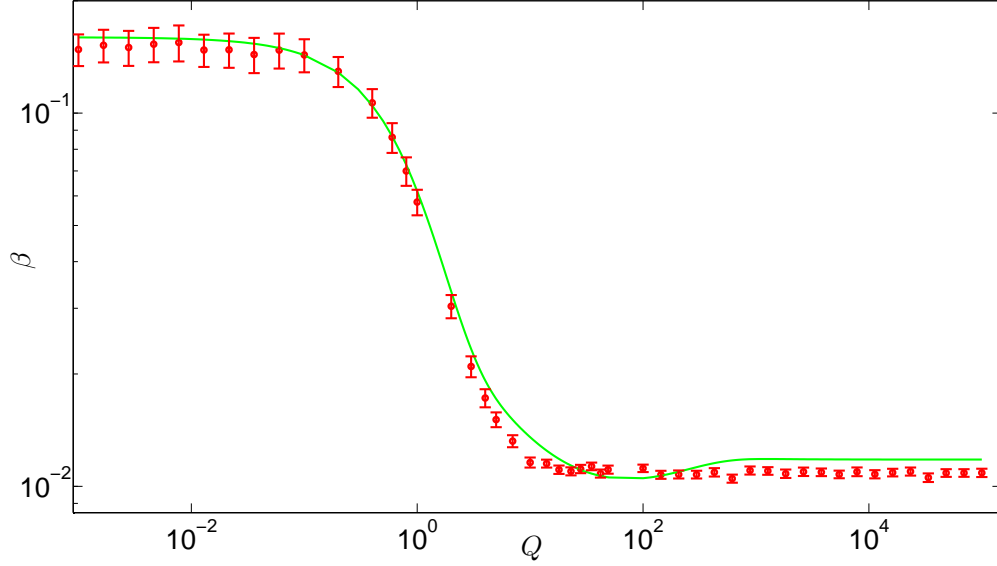


Figure 3.9: β versus Q is plotted for $\text{Kn} = 10^{-3}$ for $\kappa = 0.6$. The symbols represent the results of the numerical calculation and the error bars are at one standard error. The solid line is from the modified version of equation (3.14), with fitting parameters given in (3.16). The agreement is good across the parameter space.

The best agreement with computed data is found for,

$$\begin{aligned}
 \theta' &= 50^\circ \\
 l_1 &= 1 \\
 l_2 &= \frac{\text{Kn} \log_{10}\left(\frac{1}{\text{Kn}}\right)}{\kappa}
 \end{aligned} \tag{3.17}$$

β versus Q , both the computed data and the analytical approximation, is given in figure 3.9 for $\kappa = 0.6$ at $\text{Kn} = 10^{-3}$. We still use equation (3.14) but with the modified version of the fitting parameters, as given in equation (3.16). The complexity of the fitting function used reflects the underlying complexity of the coupling of the turbulence, gravity and non-continuum driven hydrodynamics.

3.7 Discussion

We study the, previously unexplored, coupling of gravity, turbulence and non-continuum hydrodynamics to evaluate the collision rate of a dilute suspension of spheres in an inertia-less system. We are the first to analyse the role of non-Gaussian turbulence statistics on collision rate and report a statistically significant dependence with Re_λ , which impacts the probability distribution function of turbulent quantities. This has been calculated in detail in §3.4 for pure turbulent flow and extended to all strengths of differential sedimentation to turbulence, with impact of non-continuum hydrodynamic interactions discussed in §3.5. These interactions retard the collision rate and strongly dependent on Kn , Q , and κ . To concisely report data across the large parameter space we develop, in §3.6, an analytical approximation for the collision efficiency. The set-up of the problem, including governing equations and scaling, has been presented in §3.3.

The non-dimensional collision rate at $Q = 0$ and no hydrodynamic interaction is not single-valued, decreasing with Re_λ . Increasing Taylor's Reynolds number leads to increase in the value of tails of the probability distribution of turbulent properties, including velocity gradients. To conserve total probability there is a slight decrease in the mean value. Non-extreme values determine collision rate as it is a lower order moment of the velocity gradient. Hence the observed negative slope in figure 3.1. Since a lower order is important the velocity gradient developed by Girimaji & Pope[44], and corrected for pseudodissipation rate dependence on Re_λ , will give accurate result and models that account for higher order correction, such as those developed by Pereira et al[88], are not expected to significantly improve accuracy.

The inclusion of gravity increases the non-dimensional collision rate. With increasing Q the stochastic fluctuations of the turbulent velocity field become less important

and the collision rate dependence on Re_λ vanishes in the differential-sedimentation dominated regime.

Hydrodynamic interactions create a much more complex picture. Dependence on Kn and κ is introduced and the collision rate is retarded, with collision efficiency used to quantify it. Increasing a^* and relative size leads to more efficient collisions. β , in contrast to the collision rate, decreases with increasing Q . At moderate Q the complex coupling between these two driving mechanisms and hydrodynamic interactions leads to a statistically significant dependence of β on Re_λ . This demonstrates the non-linear change of collision rate with Q and the non-trivial interplay between the various components we have considered in our study.

Since the collision efficiency depends on multiple parameters, each of which are extensively spanned, it is not possible to report all of them concisely. Instead we use an analytical approximation to β . This has been derived based on evolution of pair-probabilities along trajectories in a model system. We allow some free parameters to fit the extensive data generated. The fitting parameter provides useful insight into the underlying physics. p_1 estimates the far-field interactions. The value of p_2 indicates the separation at which the hydrodynamic interactions become weak. These have been shown, in the asymptotic limits, in table 3.2. θ' , l_1 , and l_2 measure the complex coupling of turbulence to differential sedimentation and their values have been given in equation (3.17).

The analytical result of the collision efficiency allows for a more intuitive way to understand the trends with various parameters. From the positive exponent to the power law in Kn , in equation (3.14), the decrease in β with increasing sphere size relative to the mean free path, corresponding to stronger continuum lubrication forces, is expected and seen in figures 3.3 and 3.7. With decreasing κ we find, from table 3.1, that M_0/L_1

(differential sedimentation driven collisions) and B_0/A_1 (turbulent collisions) decreases. Thus weaker exponents in equation (3.14) lead to lower collision efficiency. Similarly the comparison of the values of the continuum mobility asymptotes indicates a more rapid change in β with Kn in the differential sedimentation limit compared to the pure turbulent flow regime.

When one particle is smaller than the other, the resistance to the centre of mass motion of the pair is dominated by the resistance of the large particle and the centre of mass of the pair becomes close to the terminal velocity of the large particle. The small particle's motion relative to the larger particle is then driven by the fluid flow around the large particle. The tangential fluid velocity around the large sphere is a simple shear flow at small separations. Thus, the fluid velocity that drives the tangent motion of a small sphere is proportional to κ , the distance of the centre of mass of the small particle from the large particle surface. The tangent mobility is finite as $\xi \rightarrow 0$ and the sphere rolls at a speed κ . The normal fluid velocity pushing the small sphere toward the surface is a quadratic function of separation from the large particle surface so the small particle experiences a normal force $F' = O(\kappa^2)$. The normal velocity of the lubricating particle due to this force is $F'\xi/\kappa^2$ (with dimensional quantities: $F'h'/(\mu a_2^2)$, where h' is the dimensional surface to surface radial separation and $a_2 < a_1$). Thus the normal velocity is ξ , independent of κ for small κ and A_1 or L_1 is $O(1)$. We see then that a small particle rolls around the large particle at a slower $O(\kappa)$ speed but retains an $O(\xi)$ normal velocity. Hence, the exponent in equation (3.14) and so the collision efficiency become smaller at smaller κ .

If the size ratio becomes small enough, there is a range of separations where $h' \ll a_1$, for $a_2 < a_1$, so that the hydrodynamic interactions are strong and alter the pair distribution function significantly but $h' \leq O(a_2)$ so that the particles are not yet in

lubrication interaction. As a result there would be a significant change of P that is not captured by applying equation (3.14) which is based on lubrication scalings. This would explain the rapid change in p_1 shown in table 3.2. Thus, the discussion in the previous paragraph should be taken as a physical interpretation for moderately small κ rather than a guide to β for $\kappa \ll 1$.

To understand why differential sedimentation has a stronger dependence on Kn and a smaller β than turbulent flow we consider its most likely realisation, the uniaxial compressional flow[2], and analyse the fluid flow around a large particle. It has stagnation points at 0 and 90 degrees while sedimentation leads to zero velocity at 0 and 180 degrees. Considering the mass conservation equation for the velocity field \mathbf{u} ,

$$\nabla \cdot \mathbf{u} = \frac{\partial}{r^2 \partial r}(r^2 u_r) + \frac{\partial}{r \sin \theta \partial \theta}(u_\theta \sin \theta) = 0 \quad (3.18)$$

We can expect the particle radial velocity near the surface to be larger when the angular velocity changes more rapidly with angular position. Thus, particles in compressional flow, by extension the turbulent flow, should have a larger radial velocity and smaller exponent in the β versus Kn relationship than sedimentation. Thus, in compressional flow the larger radial velocity tends to push particles together efficiently and β is larger and more weakly dependent on Kn than in sedimentation.

The fit has been carried out using data on β extensively spanning the relevant parameter space. However, it is not feasible to span all possible values. The natural question that arises is whether it is possible to interpolate the data and achieve good fidelity. To answer this we observe β across κ , Q , and Kn find it to be smooth. This is true of the β data not shown here and so the analytical approximation is expected to perform well when spanning the parameter space. Additionally the smooth behaviour of continuum near field mobility coefficients and the fitting parameters, with respect to κ , gives further credence to the idea that the same qualitative behaviour will be observed across the

parameter space and an interpolation of the fitting function will be able to capture β accurately.

The results of our study can be used to accurately model the collision-coalescence growth of droplets in clouds. Of particular interest is the 'size-gap', from 15 to 40 μm radius where droplets are too large to grow by condensation but too small to experience significant gravitational collisional motion. One of the unanswered questions about the 'size-gap' relates to the time taken for rain formation in warm clouds. Experimental studies suggest that drops grow fast, faster than expected from purely gravity driven collision [15, 64, 103, 12]. To understand the 'size-gap' problem we first consider evolution from cloud condensation nuclei through condensation. It dominates growth of droplets below 15 μm radius and, through favouring smaller droplets over large ones, leads to a nearly mono-disperse distribution at the beginning of the 'size-gap'. Thus models that rely on differential sedimentation driven collision and do not properly account for coupling with turbulence will predict unrealistically large characteristic times for collision events and crossing the 'size-gap'. The rate of droplet growth in this coupled problem is strongly influenced by hydrodynamic interactions and for the droplets of interest in clouds the breakdown of continuum upon close approach plays a critical role[113] and does not have extensive treatment in literature. These issues can be resolved through the use of the physically accurate collision rate presented in this study that properly accounts for the non-continuum lubrication as well as the far-field hydrodynamics along with coupling of gravity to turbulent flow. Since our study spans a large parameter space in Q , Kn , and κ it will be adept at resolving the important features of the evolution of the droplet spectra in the 'size-gap' regime where both the gravity and turbulence are expected to be important and many sizes and relative sizes come into play.

Our collision rate results indicate a significant growth rate of droplets through the

'size-gap'. This is expected because of the high collision efficiency of small droplets of similar size. It will favour collisional growth of the nearly monodisperse droplet distribution at the beginning of the 'size-gap' through it.

CHAPTER 4

A MODEL FOR THE RADIAL DISTRIBUTION FUNCTION OF POLYDISPERSE INERTIAL SPHERES SETTLING IN HOMOGENEOUS, ISOTROPIC TURBULENCE

4.1 Abstract

Differential sedimentation will have a major impact on the frequency of collision observed between particles through rapid decorrelation of particle clusters formed due to inertial lag. To accurately capture this inertia driven concentration enhancement under the coupling of turbulence and differential sedimentation we have developed a model that draws on previous theories, direct numerical simulation (DNS) results and add the effect of differential sedimentation. To obtain this we first develop a closed form expression for the radial distribution function, used to characterise clustering, without gravity for equal sized particles that incorporates asymptotic results at different scales of turbulence and fit it with DNS data to make it valid at all particle separations and Stokes number. This clustering, for unequal particle sizes, will be limited by the difference in acceleration and so we estimate, in the small Stokes number limit, an effective diffusion due to differential sedimentation for a bidisperse pair. This, along with the inward drift from an equivalent monodisperse calculation, is used to solve a drift-diffusion governing inertial clustering and the order one constant associated with the differential sedimentation diffusion estimate is obtained by fitting with available DNS data. The model is validated against DNS results available for inertial clustering in the limit of particles contacting each other. Comparison is made against multiple experimental results and the predictions of our model, evaluated over the reported polydisperse particle size distribution, show good agreement. The results of this study is used to calculate the

enhancement in collision rate of droplets in clouds. For typical conditions we show the extent of enhancement and its rapid decay due to the spread in distribution, thus giving insight into the role inertial clustering will have on droplet size evolution.

4.2 Introduction

Particle inertia causes a delay in the particle's response to the background fluid field. This leads to accumulation in certain regions of the flow causing a local enhancement in particle concentration relative to a randomly distributed bulk. Due to the increased probability of particles encountering each other collision events are more likely. Thus, particle inertia, through concentration enhancement, can significantly influence evolution of the size distribution of coalescing drops or coagulating particles even when its direct effect on collision dynamics is negligible. Particle inertia is expected to cluster droplets in clouds[4] and so cloud models will require input of the concentration enhancement. These enhancements rapidly decay due to differential sedimentation acting through the spread in sizes[4]. Current analytical results are inadequate in resolving across this parameter space and very limited direct numerical simulation (DNS) results are available. Our model resolves the differential sedimentation decorrelation and thus allowing for a way to continuously span in the relative strength of gravity to turbulence. This coupled configuration result will directly inform evolution of $O(10\mu m)$ droplets in clouds, where both differential sedimentation and turbulence are expected to be important. Inertial clustering is also expected to play a role in protoplanetary disks leading to a boost in probability of planetesimal formation[85]. The accuracy of these astrophysical models will be improved by the outcome of our study. Other potential applications include aggregation driven growth of commercially valuable products in industrial reactors and agglomeration of pollutants in air. In these cases particle inertia is expected

to play a role and our study will inform the increase in observed collision rate due to clustering.

For a monodisperse suspension the Stokes number is the most important predictor of inertial clustering. For species i it is $St_i = \tau_{p,i}/\tau_\eta$, the ratio of the particle to fluid response time. Here the particle response time is $\tau_{p,i} = 2a_i^2/9\nu$ for radii a_i , with g the acceleration due to gravity, and ν the kinematic viscosity. We consider clustering of sub-Kolmogorov particles in turbulent flow which gives the fluid response time to be the Kolmogorov time scale τ_η . This can be expressed as $\tau_\eta = (\nu/\epsilon)^{1/2}$, where ϵ is the dissipation rate of the turbulent process. In the low St limit particles nearly follow the fluid and increases in St leads to enhanced local particle concentration. At the large St limit particles do not respond to the fluid and this leads to a random distribution of particles which does not correspond to a significant enhancement in local concentration. Thus $O(1)St$ is expected to lead to maximum local concentration enhancement for a monodisperse system. In spanning the St parameter space DNS studies are only possible at certain values in the large possible range. Asymptotic results are available at certain length scales of turbulence[26, 17]. In the small St limit Chun et al and Zaichik & Alipchenkov[126, 26] derived an analytical expression for inertial clustering in the dissipative range. In the inertial sub-range Bragg et al[17] obtained a result for small scale dependent Stokes number, the ratio of the particle response time to the turnover time of an eddy of size r , the separation between the particles. It is given as $St_r = St(\eta/r)^{-2/3}$, where η is the Kolmogorov length scale the size of the smallest eddies in turbulence. A universally valid inertial clustering result was obtained through a model for the probability distribution of pair relative velocity by Zaichik & Alipchenkov[126, 127, 129]. However, Ireland et al[53, 54] showed that to accurately predict inertial clustering some of the inputs need to be obtained from DNS. Additionally closed form solutions are available only in certain cases. Solutions for St greater than 0.3 are also shown to be inaccurate due to non-local

effects[16], where particles are sling-shot from one eddy to another. To resolve all of these issues we develop a closed form expression for inertial clustering, when all the spheres are of equal size, that incorporates many of the important asymptotic results and fitted with DNS data. We choose DNS clustering results reported at Re_λ , the Reynolds number based on the Taylor microscale, of 597 by Ireland et al[53]. This is closest to Re_λ of $O(10^4)$ typical in clouds and other real-world turbulent flows. The errors introduced, relative to the large Re_λ limit, by fitting with DNS data at $Re_\lambda = 597$ is expected to be minimal as Ireland et al showed that clustering is not sensitive to this parameter in the limit of large Re_λ [53]. Thus our monodisperse inertial clustering result is expected to be accurate over a large range of Re_λ , St , and particle-particle separation.

The inclusion of gravity changes how particles sample the flow field. DNS studies on this configuration was carried out for monodisperse distribution by Ireland et al[54]. A theoretical treatment of equal sized spheres in the low St and rapid settling limit was performed by Rani et al[94]. However, this effect does not alter inertial clustering nearly as much as differential sedimentation decorrelation of different sized particles. To understand this we consider the non-dimensional difference in settling velocity that is given as, $\Delta S_{v,ij} = |\tau_{p,i} - \tau_{p,j}|g/u_\eta$, where u_η is the Kolmogorov velocity. The effect of differential sedimentation on inertial clustering becomes important when $\Delta S_{v,ij}\eta/r$ is order one, whereas the effect of gravity in altering the sampling of the flow field requires S_v to be order one. Thus, even a small $\Delta S_{v,ij}$ can impact inertial clustering and so we focus only on the differential sedimentation aspect of gravity on inertial clustering in our study.

Size difference in particle pairs induces acceleration that can decorrelate them. The effect of differential sedimentation driven acceleration is hard to resolve and the study by Ayala et al[3] performs a fit without any attempts towards incorporating the underlying

physics. Turbulent acceleration, without any gravity, was considered by Chun et al[26] in the low St limit. They found an exact analytical result by solving the drift-diffusion through treating decorrelation due to turbulent acceleration resulting as an effective diffusivity. This results in a cross-over separation for the particle pairs above which the inertial clustering behaviour mimics that of a monodisperse system and below which it enhancement is insensitive to separation. Lu et al[76] incorporate an estimate of differential sedimentation into the cross-over length to determine inertial clustering in the dissipative range. We improve upon this analysis, in addition to utilising clustering results valid over all scales of turbulence instead of just the dissipative range, by creating an estimate for diffusion due to differential sedimentation and use it to obtain a solution to the drift-diffusion equation governing inertial clustering. The order one constant for the estimate of diffusion due to differential sedimentation is obtained by comparing against DNS results by Dhariwal & Bragg[34]. To validate our model we compare against the DNS results of inertial clustering enhancement at particle contact that has been calculated by Ayala et al[4] and find good agreement.

Our inertial clustering model is compared against experimental data from studies by Salazar et al, Saw et al, and Petersen et al[99, 100, 90]. To account for polydispersity in experiments the inertial clustering enhancement is calculated for a large number of particle pairs chosen based on the reported information on distribution and averaged. This polydisperse inertial clustering predictions agree well with the published data from the above mentioned experiments. Our model is also compared against reported fits evaluated using experimental data. These fits show significant errors, especially when extrapolated to separations comparable to the particle size, and is attributed to experimental limitations. This will be used to demonstrate the necessity of a comprehensive model for inertial clustering, such as the one developed in this study. Comparisons have also been made against Yavuz et al[124]. However, our model does not agree with their

data. We discuss some of the problems with the observed trend of the reported experimental data and conclude that it is not reasonable to expect agreement with our model.

Having developed and validated the model for inertial clustering we will use it to predict the enhancement of collision rate in a practical application. We choose the collision rate experienced by water droplets in clouds. For this purpose we use the inertia-less collision rate result from §3 and modify it based on enhancement in local concentration due to droplet inertia. We evaluate this collision rate over a large span the parameter space in water droplet mean radius and standard deviation, at typical conditions in a cloud, and report the enhancement due to droplet inertia. We find a significant boost to the observed collision rate as well as a rapid decay as the distribution becomes wide and differential sedimentation becomes important. This reinforces the necessity for an accurate resolution of the differential sedimentation decorrelation, such as the one carried out in the present analysis, as a naive monodisperse result will severely over-predict collision rate.

The study is organised as follows. We first develop the model and validate it against DNS data in §4.3. Next we compare the predictions of our model with reported experimental data in §4.4. Then in §4.5 we use the inertial clustering results to determine the enhancement in collision rate of $O(10\mu\text{m})$ water droplets in clouds as a function of mean size and standard deviation of the distribution. Finally in §4.6 we summarise the important findings of our study.

4.3 Inertial clustering model

The radial distribution function $g_{ij}(r)$ measures the enhancement in the probability of finding species i and j separated by a distance r relative to a randomly distributed bulk.

For sake of convenience whenever particles are indistinguishable, i.e., $i = j$, we will denote it as $g(r)$.

We first derive an expression for $g(r)$ valid at all scales of turbulence for the monodisperse case without gravity. For this purpose we consider two important results. The first is in the dissipative range, corresponding to $r \ll \eta$. Here, Reade & Collins[95] found a power law for $g(r)$ which was later analytically derived for $St \ll 1$ [126, 26]. This is given as,

$$g(r) = c_0 \left(\frac{\eta}{r}\right)^{c_1} \quad (4.1)$$

Here c_0 and c_1 are constants depending only on St . In the $St \rightarrow 0$ limit it has been found that $c_1 = c_1^* St^2$ where c_1^* is independent of St . Spanning a larger range of St Ireland et al showed that c_0 and c_1 are independent of Re_λ [53]. Zaichik & Alipchenkov[127] showed that the power law for inertial clustering accurately describes $g(r)$ for $r \rightarrow 0$ when St is below a critical value. Above this value $g(r)$ flattens and it is possible to capture this with appropriate values of c_0 and c_1 . In fact Ireland et al[53] used this power law for all St under consideration in their DNS calculations. Hence it will be used in our model as well.

The next important result was derived by Bragg et al[17] in the inertial sub-range. This is given as,

$$g(r) = \exp[c_3 r^{-\frac{4}{3}}] \quad (4.2)$$

Here c_3 is a constant that depends on St and set by the difference between the average strain rate and rotation rate experienced by the particles. Since it is beyond the scope of this study to resolve this we treat c_3 as an undetermined constant. This result is valid for $Re_\lambda \rightarrow \infty$ and $St_r \ll 1$.

To smoothly transition from dissipative to inertial sub-range we combine equations

(4.1) and (4.2) with c_3 as the free parameter. The exact form is chosen to agree best with DNS data from Ireland et al[53]. This is given as,

$$g(r) = \exp\left(\frac{\log c_0}{\left(1 + \frac{r}{2\eta(1+St^{3/2})}\right)^{\frac{4}{3}}}\right)\left(1 + \frac{\eta}{r}\right)^{c_1} \quad (4.3)$$

This fit accounts for mechanisms not explicitly included, in particular the sling-shot effect of particles from one eddy ending up in another and leading to velocity not being single valued in space. These non-local effects depend on path history of particles and is expected to start at around St of 0.3, though any noticeable deviations from our model only show up at very high St . This can be seen in figure 4.1, where our model, shown in equation (4.3), is compared against DNS data generated by Ireland et al[53] at $Re_\lambda = 597$. The c_0 and c_1 , obtained from DNS, have been fitted with St . This fit is given as,

$$\begin{aligned} c_0 &= 1 + \exp[0.0005 St^7 - 0.0042 St^6 - 0.0060 St^5 \\ &\quad + 0.0803 St^4 + 0.0030 St^3 - 0.7018 St^2 + \\ &\quad 0.4144 St + 1.8686] \\ c_1 &= \exp[-0.0230 St^3 - 0.4411 St^2 - 0.2423 St \\ &\quad - 0.3750] \end{aligned} \quad (4.4)$$

Equation (4.3) contains asymptotes in the dissipative and inertial-subrange but not to the integral length scales. It is expected that $g(r)$ will decay to 1 at these large separations. The inertial sub-range result in equation (4.2) naturally transitions to 1 for $r \rightarrow \infty$, hence so does equation (4.3). This captures DNS data for Re_λ as low as 398, corresponding to large separation between the length scales of turbulence. Hence this result will be accurate for typical conditions in clouds, where Re_λ is $O(10^4)$, and many other real-world systems. However, when separation of scales is not large and inertial sub-range is non-existent, corresponding to low Re_λ , the transition of inertial clustering

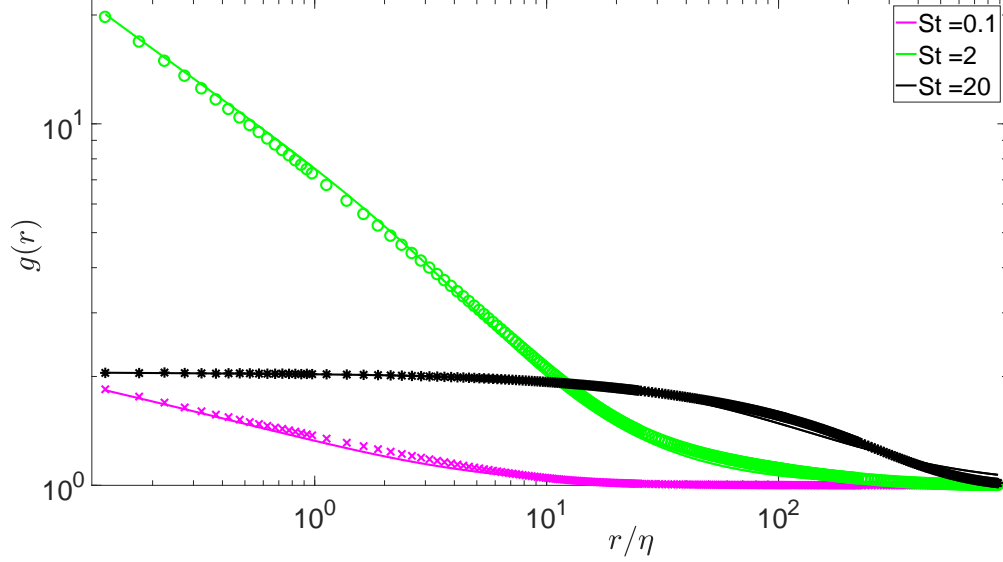


Figure 4.1: $g(r)$ is shown as a function of r/η for $Re_\lambda = 597$ at $St = 0.1, 2, 20$ with symbols denoting DNS data from Ireland et al [53] and solid lines our model shown in equation (4.3). There is good agreement between the model and DNS results across the parameter space. As $r \rightarrow 0$ the highest value of $g(r)$ is at the intermediate value of St , which is in line with expected behaviour.

from the dissipative range to integral scales is needed. The radial distribution function $g'(r)$ for the case of not very large L/η with L the Integral length scale is given as,

$$g'_{ij}(r) = 1 + (g_{ij}(r) - 1) \exp\left[-\left(\frac{r}{0.6L}\right)^2\right] \quad (4.5)$$

Here, 0.6 is the order one factor to fit the model with DNS data. This result is valid even when the particles are not of equal size and can be applied to the bidisperse results that we derive later in this section. It can be seen that equation (4.5) becomes the expression in (4.3) in the large Re_λ , corresponding to large L , limit. For some typical values of Re_λ the comparison of DNS data and our $g'(r)$ is shown in figure 4.2. For sake of convenience we will not be explicitly using primes and instead note whenever we use the expression given in equation (4.5).

When gravity is included into the calculation for monodisperse spheres extensive

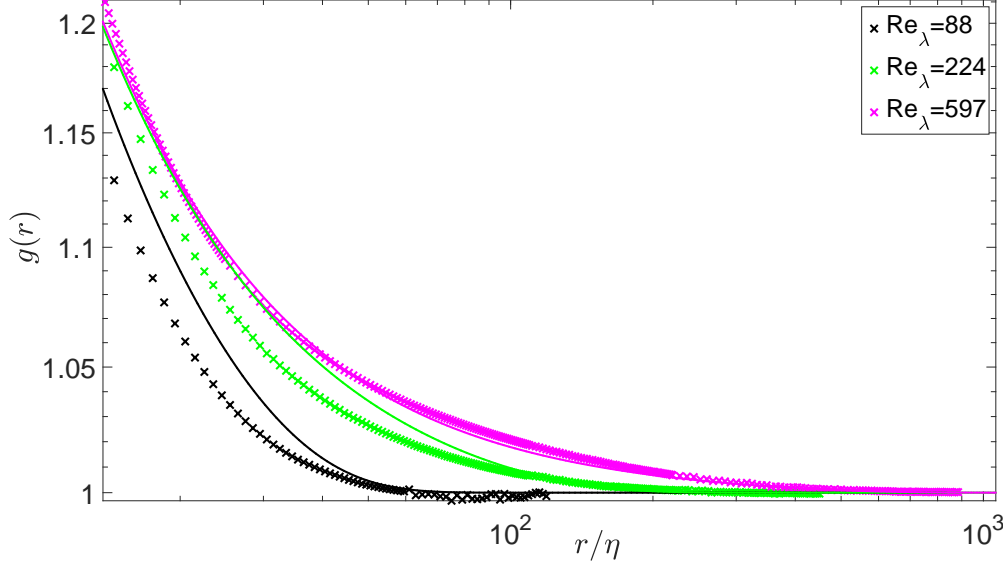


Figure 4.2: $g(r)$ is shown as a function of r for $St = 0.5$ and $Re_\lambda = 88, 224, 597$ with symbols denoting DNS data from Ireland et al[53] and solid lines are the radial distribution function obtained from equation (4.5). There is good agreement between the model and DNS results across the parameter space.

asymptotic analysis, such as those in the absence of gravity, are not available. DNS data, from Ireland et al[54], on this configuration is very limited. Hence this avenue is not explored further. However, some treatment of this case is still possible and is explored in the appendix chapter §A §A.1.

To introduce bidispersity and differential sedimentation we first consider the governing equation for monodisperse $g(r)$. This drift-diffusion equation for low St is given as[26],

$$B_{\parallel} \frac{dg(r)}{dr} + V_r g(r) = 0 \quad (4.6)$$

Here, \mathbf{B} diffusion of the pair of particles due to turbulent shear, with \parallel indicating it is the component parallel to the line of centres of the particle pair. $-V_r$ is the radial velocity and so $V_r > 0$ indicates a net inward drift velocity along the lines of centres. From the

analysis by Zaichik & Alipchenkov[126] B_{\parallel} can be expressed as,

$$B_{\parallel} = S_{\parallel}(r)T_{Lr}(r) \quad (4.7)$$

Here $\mathbf{S}(r)$ is the Eulerian structure function, defined as the second moment of the relative velocity of the fluid velocity at two points and one time. $T_{Lr}(r)$ is the Lagrangian time scale of an eddy of size r . For the different scales of turbulence it has been calculated by Zaichik & Alipchenkov[126, 127]. The uniformly valid result is given by Pan & Padoan[86] and Dhariwal et al[35]. The final component to evaluate $g(r)$ is V_r and has been calculated by Chun et al[26] for $St \ll 1$ in the dissipative range. For a larger range of St Zaichik & Alipchenkov[126] have an expression for the inward radial velocity driving clustering. When particle size is different an expression similar to equation (4.6) governs clustering and is given as,

$$(B_{\parallel,ij} + D_{ij})\frac{dg_{ij}(r)}{dr} + V_{r,ij}g_{ij}(r) = 0 \quad (4.8)$$

Here the subscripts i and j denote each of the two species constituting the bidisperse suspension. D_{ij} is the diffusion due to difference in acceleration experienced by the particle pairs. Only turbulent acceleration was considered by Chun et al[26] and Zaichik & Alipchenkov[128]. In our diffusion model of gravity we extend it to include the effects of differential sedimentation.

We first consider $V_{r,ij}$ and $B_{\parallel,ij}$ in equation (4.8). These have been calculated for unequal particles by Chun et al[26] and Zaichik & Alipchenkov[128]. The former is only valid under a narrow range of conditions while the latter is not expected to be accurate based on the analysis by Bragg & Collins[16] and Ireland et al[53] due to non-local effects. Instead we calculate $V_{r,ij}$ and $B_{\parallel,ij}$ from an equivalent monodisperse suspension, in line with the analysis of Chun et al[26]. The drift velocity and turbulent shear diffusion do not capture the bidispersity of the particle pair, with Stokes number St_1 and St_2 , and so a first order estimate of these components is obtained from an equivalent

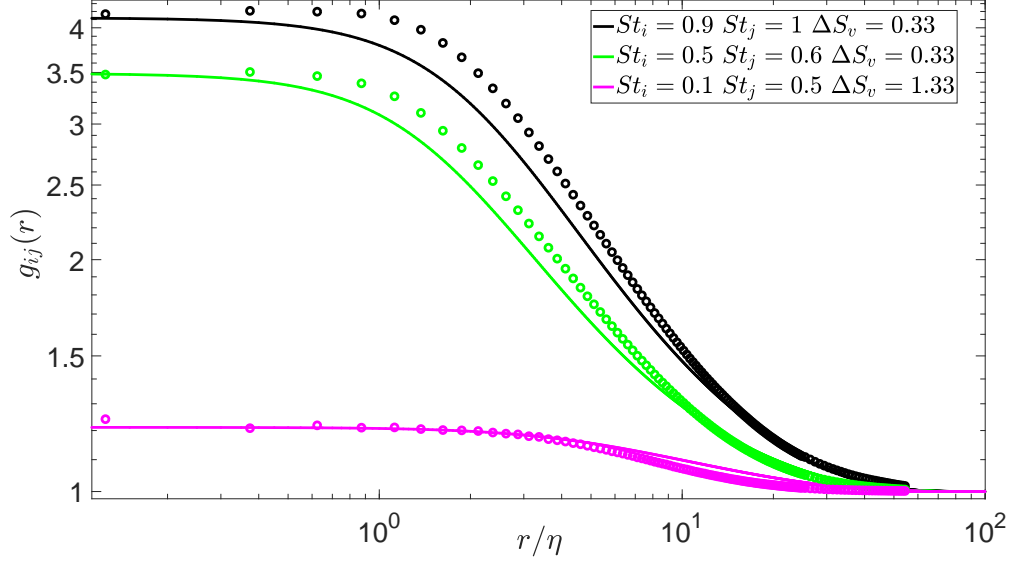


Figure 4.3: $g_{ij}(r)$ is shown as a function of r/η for three bidisperse calculations performed at $Re_\lambda = 90$ and $Fr = 0.3$. The symbols denote DNS data from Dhariwal & Bragg[34] and solid lines, representing our inertial clustering model, agree well with it.

monodisperse system with $St = (St_1 + St_2)/2$. At this St turbulent shear diffusion can be evaluated as it is known at all scales of turbulence[86, 35]. No such information is available on the drift velocity and so equation (4.6) is used to obtain it as $B_{||}$ and $g(r)$ are fully known.

For a bidisperse system with low St in the absence of gravity turbulent acceleration induces a relative velocity $|\tau_{p,i} - \tau_{p,j}|A$, here A is the turbulent acceleration. This diffuses the particles and the effective diffusion is given as,

$$D_{ij} = (\tau_{p,i} - \tau_{p,j})^2 \int_{-\infty}^t \langle A_r(t)A_r(t') \rangle dt \quad (4.9)$$

Here, D_{ij} is along the lines of centres of the particles and A_r is the turbulent acceleration along the line of centre. Differential sedimentation due to gravitational acceleration, like turbulent acceleration, acts to separate particle pairs with different response times and limit the degree of clustering for non-monodisperse cases. While gravitational acceleration is steady and acts in a single direction leading to an angular dependence of

the pair probability, a simple estimate of its effect can be obtained based on an isotropic approximation. When the turbulent shear acts on a particle pair it rotates the pair so that the gravitational acceleration along the lines of centers can fluctuate and change sign. In this sense gravity might be modelled in a qualitative way, as suggested by Lu et al[76] as giving rise to an isotropic relative diffusion, $D_{g,ij}$, that is given as,

$$D_{g,ij} = (\tau_{p,1} - \tau_{p,2})^2 \int_{-\infty}^t \langle g_r(t)g_r(t') \rangle dt \quad (4.10)$$

where, g_r is the component of gravity along the lines of centres of the particles. This leads to an estimate of the dispersion due to gravity of,

$$D_{g,ij} = U_{\text{sed}}^2 \tau_g \quad (4.11)$$

$U_{\text{sed}} = |\tau_{p,1} - \tau_{p,2}| \tau_g$ and τ_g is correlation time for the component of gravity along the line of centres. The decorrelation of g_r occurs as a result of the angular component of the relative shear diffusion tensor \mathbf{B} . Since this angular component is of the same order of magnitude as the radial component, we approximate the correlation time as,

$$\tau_g = k_g \frac{r^2}{B_{\parallel}} \quad (4.12)$$

k_g is an order one constant. Thus g_{ij} is given as,

$$g_{ij}(r) = \exp\left(\int_r^{\infty} \frac{-V_r(r')}{B_{\parallel}(r') + D_{ij} + D_{g,ij}} dr'\right) \quad (4.13)$$

To complete the description k_g needs to be determined. This is done by fitting with DNS data from Dhariwal & Bragg[34] and evaluated to be $0.02 + 7.6 \frac{St_1 + St_2}{2} |St_2 - St_1|$.

The inertial clustering model developed is compared against DNS calculations by Dhariwal & Bragg[34] performed at $Fr = 0.3$, where the Froude number $Fr \equiv \epsilon^{3/4}/(\nu^{1/4}g)$ sets the strength of gravity to turbulence, and $Re_{\lambda} = 90$. To accurately predict inertial clustering at large particle separations for such low Taylor Reynolds number we use the correction for small separation of length scale, given in equation (4.5) on the

$g_{ij}(r)$ calculated from equation (4.13). This is plotted as a function of the particle pair separation along with DNS data at three sets of Stokes number in figure 4.3. Our inertial clustering model reproduces DNS data with high fidelity, including the plateau in the dissipative range and the transition to it from the larger length scales.

The variation of the radial distribution function with St and $\Delta S_{v,ij}$ has been accurately resolved in our inertial clustering model. This will be crucial in predicting concentration enhancement during collision of two particles. To demonstrate the accuracy of the inertial clustering model predictions we consider water droplets in clouds. For these droplets Ayala et al[4] have performed DNS calculations to determine $g_{ij}(a_i + a_j)$ at $\epsilon = 0.04m^2/s^3$ and $Re_\lambda = 72.41$. We compare against this DNS data by fixing a_i at $40\mu m$ and a_j varying from 5 to $65\mu m$ in figure 4.4. Due to the low value of Re_λ we use the correction given in equation (4.5), though it will not alter results on such small particle separations. We find good agreement between our model results and DNS data on the decay of inertial clustering as the particle sizes becomes disparate and differential sedimentation decorrelates the clusters. The deviation for the monodisperse data point is also minimal. This highlights the weak effect gravity has on inertial clustering of equal sized particles and justifies our neglect of this mechanism.

The inertial clustering model presented here is valid over a large range of St and $\Delta S_{v,ij}$. To evaluate it the integral in equation (4.13) can be calculated orders of magnitude faster than DNS. However, it might still be slow for evolution studies. Hence, in appendix chapter §A §A.2 we develop a model for $g_{ij}(r)$ that is a closed form expression.

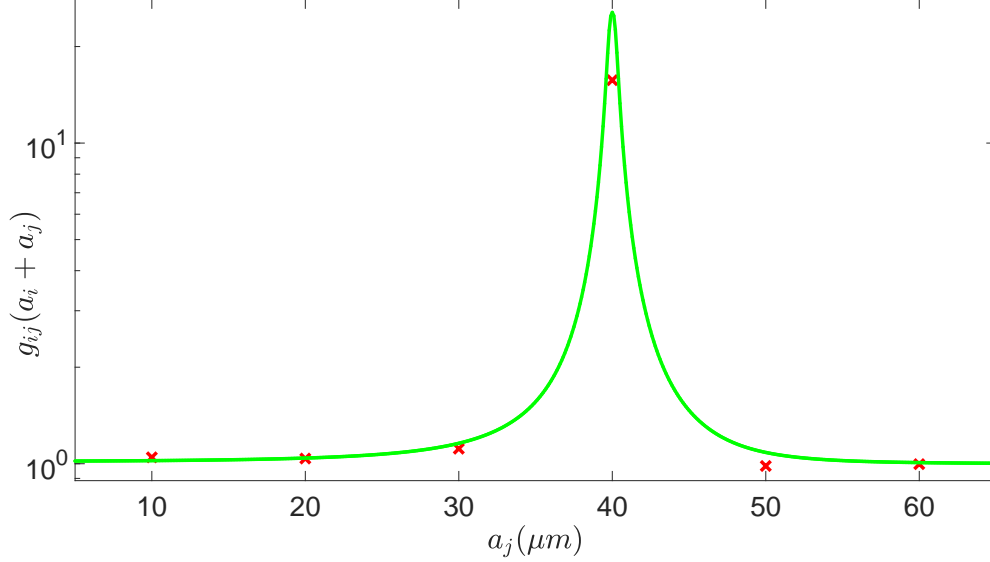


Figure 4.4: $g_{ij}(a_i + a_j)$ is plotted as a function of a_j , with $a_i = 40\mu m$. This corresponds to a variation of St from 0.06 to 2.23. The DNS data from Ayala et al[4], calculated at $\epsilon = 0.04m^2/s^3$ and $Re_\lambda = 72.41$, is shown with symbols, while the solid lines show the results of our model. The errors are minimal at all points of comparison.

4.4 Comparison against experiments

The model for radial distribution function developed in section 4.3 is valid across a large parameter space. In this section we will use it to predict Inertial clustering observed in experiments. Experimental studies evaluating the radial distribution only explore certain regions of the vast parameter space. Hence we will draw from multiple sources, namely Salazar et al, Saw et al, Yavuz et al, and Petersen et al[99, 100, 124, 90].

While our models have been developed assuming bidispersity even the most carefully designed experiments will possess some spread in the distribution of the particle sizes. To account for this we average the radial distribution function over the reported size distribution of the particles, which is given as $g(r) = \int g_{ij}^*(r)P^*(a_i)P^*(a_j)da_ida_j$. Here $P^*(a)$ is the probability of finding a particle of radius a . In this section we will use

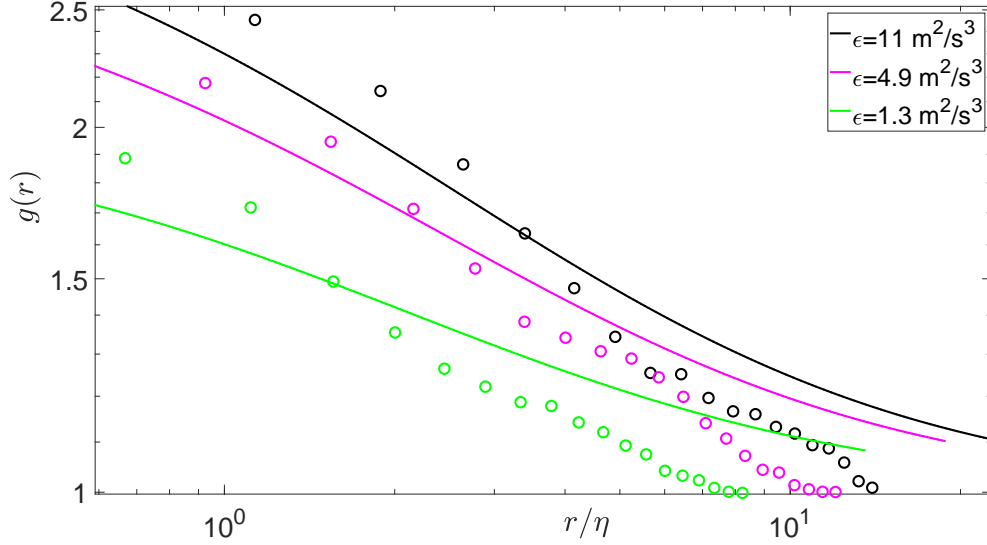


Figure 4.5: $g(r)$ is plotted as a function of r/η , with symbols corresponding to the experimental data from Salazar et al[99] and solid lines the predictions by our model. Here $\epsilon = 1.33, 4.9, 11 \text{ m}^2/\text{s}^3$ corresponds to Re_λ of 108, 134, 147 and a mean $St = 0.08, 0.13, 0.2$.

$g_{ij}^*(r)$ that includes the correction of small separations of turbulent length scales, given is equation (4.5), since most experiments are performed at low Re_λ .

The radial distribution function of silver-coated hollow-glass spheres in a turbulent air chamber has been experimentally measured by Salazar et al[99]. They performed calculations under three different flow conditions and we make comparisons against all of them in figure 4.5. In making this comparison we use their reported size distribution of particles, with mean and standard deviation of 3 and 2 μm respectively, that excludes particles below a radius of 2.5 μm . This high pass filter mimics the small particles missed by the camera used in the experiment. There is relatively good agreement between the output of our model and experimental data, with near overlap at small separation. At large separations though the experimentally measured $g(r)$ rapidly falls off and this is likely due to experimental errors introduced by the use of finite size box in which experiments are carried out.

Higher Re_λ than those considered by Salazar et al[99] are more typical in real world turbulent flows, such as atmospheric clouds[48]. A more realistic Re_λ , of 440, has been achieved in the experimental study by Saw et al[100]. They measured inertial clustering of water droplets in a wind tunnel. The Stokes number of these droplet were found to follow a log-normal distribution and the radial distribution function has been calculated by binning a certain range. This binning approach allows them to look at an effectively bidisperse suspension and so is relevant to both real world application and our inertial clustering model. In generating results from our model to compare against their experimental results we mimic the binning and calculate $g_{ij}(r) = \int g_{ij}^*(r)P_i^*(a_i)P_j^*(a_j)da_ida_j$. This comparison is shown in figure 4.6 for experimental condition corresponding to $\epsilon = 0.6m^2/s^3$ and $Re_\lambda = 440$. Very good agreement is found between the predictions of our model and experimental data even though our model has not been fitted for these conditions. The trends with St and r are reproduced. Significant deviations only show up at large r where the experimentally measured radial distribution function goes below 1 and can be attributed to experimental errors. At the smallest St under consideration there is some discrepancy between our model and experimental data. These correspond to very small droplets and we believe experimental uncertainty is resolving them leads to the observed error.

To compare against the effects of gravity in inertial clustering we consider the experiments by Petersen et al [90]. They study particles experiencing turbulence through an array of jets and reach $Fr \approx 1$. Unfortunately they only test nearly equal sized particles and so the plateauing due to differential sedimentation, that can be estimated to occur when $\Delta S_{v,ij}\eta/r$ is order one, lies well within the dissipative range and beyond the reach of the experiment. Still our model is expected to perform well in the reported separation range, as we have already argued that the role of gravity on the inertial clustering of a monodisperse distribution of particles is minimal. We compare against their ex-

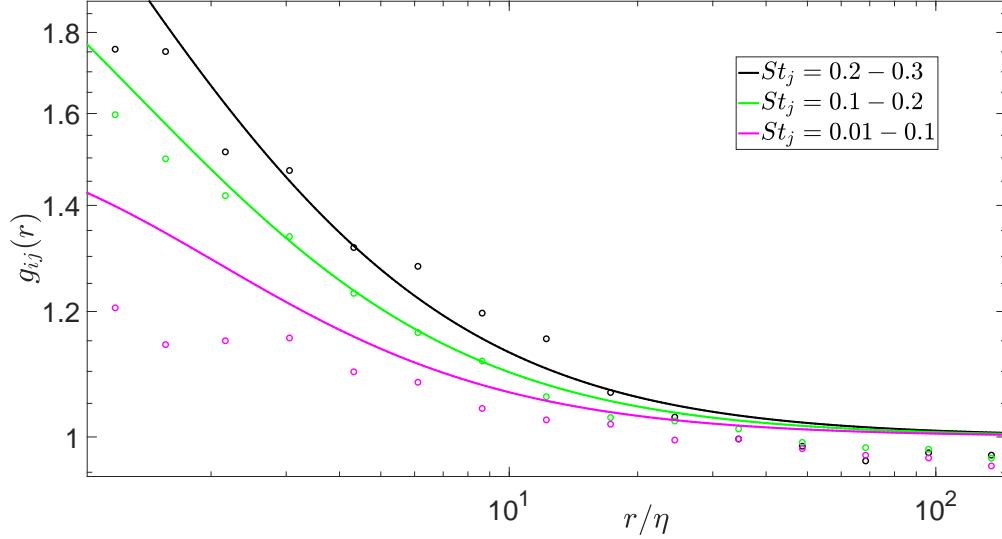


Figure 4.6: $g_{ij}(r)$ is shown as a function of r/η , with symbols denoting the experiment by Saw et al[100] performed at $\epsilon = 0.6m^2/s^3$ and $Re_\lambda = 440$ while the solid lines show the results of our model under these conditions. The binning of the reported size distribution is done with $St_i = 0.2 - 0.3$ and three different St_j , thus capturing both an effective monodispersity as well as bidispersity of droplets.

periments on Lycopodium particles with mean and standard deviation of the radius 15 and 1 μm respectively and assume a Gaussian distribution with these parameters for the particle radius probability. The flow conditions correspond to $Fr = 1.2$, $Re_\lambda = 300$, and Kolmogorov length scale of 0.27 mm, leading to a mean St of 0.63. For this case they fitted the experimental data, with the fitting function based on the power law behaviour expected in the dissipative range. We show this, along with the experimental data and the results of our model, in figure 4.7. Good agreement is observed between their experimental data and our model. To test their fit we plot $g(r)$ till separations comparable to the particle size and find significant under prediction of inertial clustering. This error in their fit can be attributed to not enough experimental data, especially in the dissipative range thus demonstrating the necessity of a comprehensive model for clustering.

The final inertial clustering experimental result we consider is the work by Yavuz

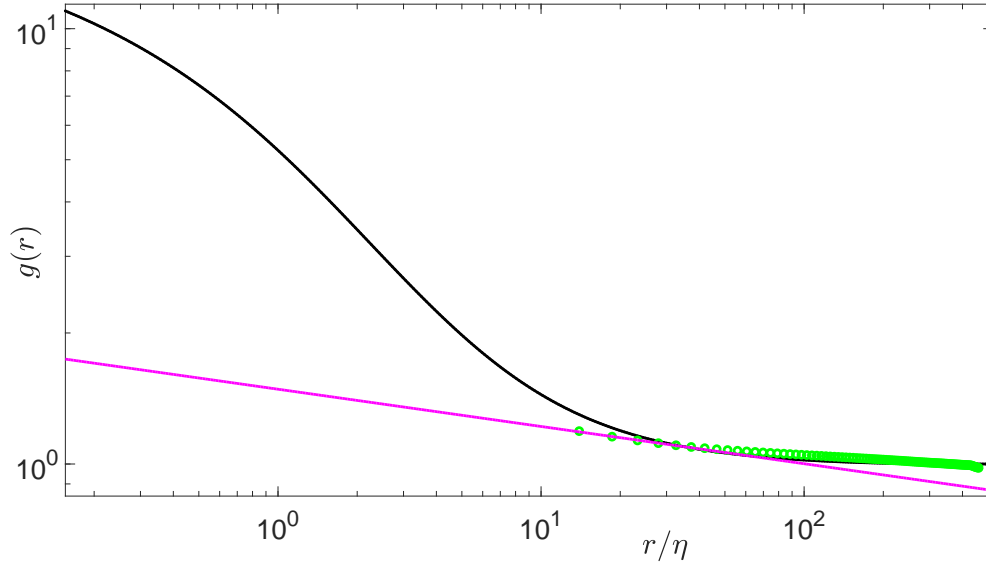


Figure 4.7: $g(r)$ is shown as a function of r/η for $\text{Re}_\lambda = 300$, $Fr = 1.2$, mean $St = 0.63$, and $\eta = 0.27\text{mm}$. The symbols and dashed line are the DNS data from the experiments and predictions of the fit by Petersen et al [90] respectively. The solid line shows our model which agrees with available experimental data and demonstrates the weakness of the reported experimental data based fit.

et al[124]. They study water droplets placed in a soccerball-shaped chamber, within which turbulence is driven through a collection of loudspeakers, and resolve down to sub-Kolmogorov particle separation. We compare against three of their reported experimental results of $g(r)$, by assuming a Gaussian distribution for the droplet radii defined by their reported mean and standard deviation, in figure 4.8. The agreement across the parameter space is poor. However, there are some issues immediately evident in the available experimental data. At all separations the reported radial distribution function is not increasing with St for $St < 1$. This goes against current understanding and experiments performed under similar values of St , such as those by Salazar et al[99] and Saw et al[100]. At small particle separations the experimental data is nearly collapsed for the three cases shown. This corresponds to a significantly higher than expected $g(r)$ when the lowest St experimental result is considered and, presently, there is no known physi-

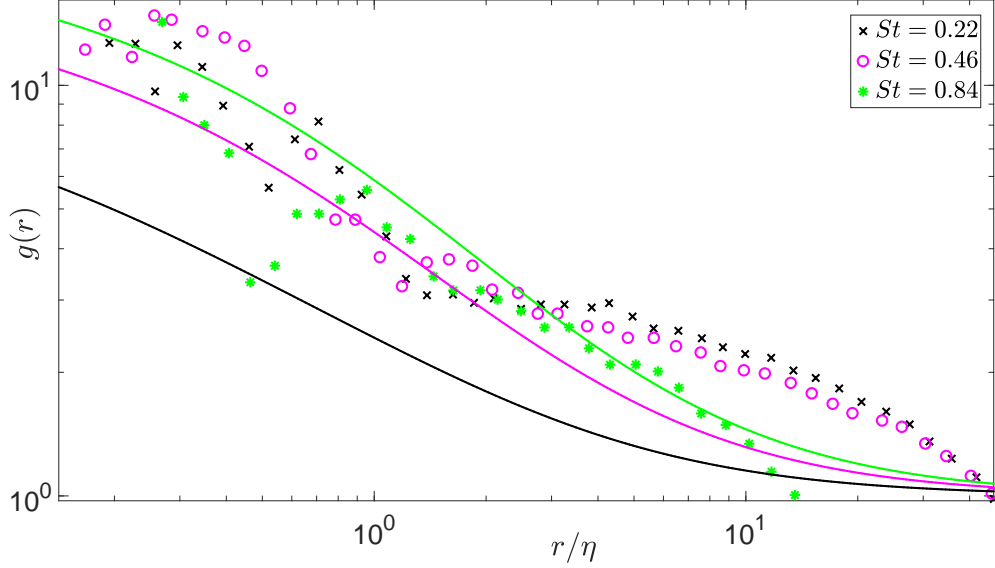


Figure 4.8: $g(r)$ is shown as a function of r/η . The symbols are the experimental data from Yavuz et al[124] while the solid lines are the predictions of our inertial clustering model. We compare against three experimental configurations corresponding to a mean $St = 0.22, 0.46, 0.84$, a mean radius of $7.1, 10, 20.7\mu\text{m}$ and standard deviation of $0.3, 0.6, 0.7\mu\text{m}$ respectively. The flow condition for the first two correspond to $\epsilon = 2.1\text{m}^2/\text{s}^3$, $\text{Re}_\lambda = 229$ while the last one is at $\epsilon = 0.3\text{m}^2/\text{s}^3$ and $\text{Re}_\lambda = 155$. Poor agreement is seen across the parameter space and is attributed to experimental errors.

cal mechanism to account for such a dramatic enhancement. Hydrodynamic interactions were shown by Brunk et al to enhance inertial clustering by $O(1)$ [19]. This would be insufficient to account for the order of magnitude increase of $g(r)$. Due to these serious issues with the experimental data we do not attempt to reconcile our inertial clustering model with it and any agreement is attributed to be a coincidence.

4.5 Application in cloud system

In §4.3 we have developed a model for $g(r)$ that couples differential sedimentation with turbulence which has been compared against multiple experimental results in §4.4. This

inertial clustering model will inform the effective collision rate experienced between particle pairs. To demonstrate this, in this section, we consider atmospheric clouds, where turbulence and gravity are both expected to be important for droplet growth.

Cloud droplet evolution for droplets of radii 15 to 40 μm is an active area of research in climate science. Referred to as the 'size-gap', here differential sedimentation and condensation growth are weak and it is not fully understood how droplets grow out of it[48]. Inaccurate models in this regime lead to cause significant errors between prediction and observation. In-situ measurements of drop size distribution in clouds does not match current models. Neither does the predictions of time to precipitation, which depends on how fast the distribution evolves, agree with field measurements. Multiple mechanisms have been proposed ranging from turbulent collisions[65] to polydispersity induced by mixing[68], and ultra-giant condensation nuclei[69] to name a few. Studies, such as those by Vaillancourt et al[115], have investigated the role of inertial clustering driven enhancement of the collision rate to cross the 'size-gap' and we will focus on this mechanism in this section. We will use our inertial clustering model that accurately resolves how particle inertia driven clustering occurs under the coupled action of turbulence and differential sedimentation.

The droplets in clouds have St typically less than 1 but not negligible and so inertial clustering will play an important role in shaping the observed collision rate[4]. Since it is beyond the scope of this study to do a full evolution simulation we will only calculate the effective collision rate experienced by a distribution of droplets. We will span the mean radius a_m from 10 to 100 μm , the size range of interest in cloud modelling efforts[48]. To capture polydispersity, and thus the influence of differential sedimentation, we assume a Gaussian distribution and vary the standard deviation σ_a from 0.1 to 5 μm .

While droplet inertia based on the mean size is not negligible in §2 it was show that

St based on the relative velocity of droplets is very weak. Hence inertia will not alter the collision dynamics and only enhance the collision rate through inertial clustering leading to droplets being more likely to see each other. This can be expressed as,

$$K_{ij} = g_{ij}(a_i + a_j)K_{ij}^0 \quad (4.14)$$

Here, K_{ij} is the actual collision rate between species i and j while K_{ij}^0 is the collision rate obtained from the work presented in §3 performed at $St = 0$. For the assumed Gaussian distribution we obtain the effective collision rates without (K^0) and with inertial clustering (K) as,

$$\begin{aligned} K^0 &= \int K_{ij}^0 P^*(a_i) P^*(a_j) da_i da_j \\ K &= \int g_{ij}(a_i + a_j) K_{ij}^0 P^*(a_i) P^*(a_j) da_i da_j \end{aligned} \quad (4.15)$$

To obtain the collision rates we assume conditions typical in clouds, of $\epsilon = 0.01 m^2/s^3$, mean free path of air of 70 nm , and $Re_\lambda = 2500$. We choose 100 particle pairs from the Gaussian distribution to evaluate equation (4.15). The enhancement in the effective collision rate is presented as a contour plot of $\log_{10}(K/K^0)$ over a_m and σ_a . $K/K^0 > 1$ always and so droplet inertia always favours growth. Significant enhancement of the collision rate is observed at monodispersity. This is in line with expectation that bidispersity, through differential sedimentation, decorrelates particle pairs and $g(a_1 + a_2)$ goes to 1. We also observe maximum enhancement near $50 \mu\text{m}$ mean size, which corresponds to $O(1)St$ and maximum clustering.

It is important to note that while the global maxima may not lie in the 'size-gap' significant enhancement of collision rate is seen within it. Equally critical, though, is the rapid decay in enhancement as the distribution becomes broad. To clearly illustrate this we plot K/K^0 as a function of σ_a at a few typical values of a_m in figure 4.10. Thus, while inertial clustering can lead to a big enhancement in collision rate, it acts in a very 'focused' manner. It is expected to preferentially collide nearly similar sized droplets

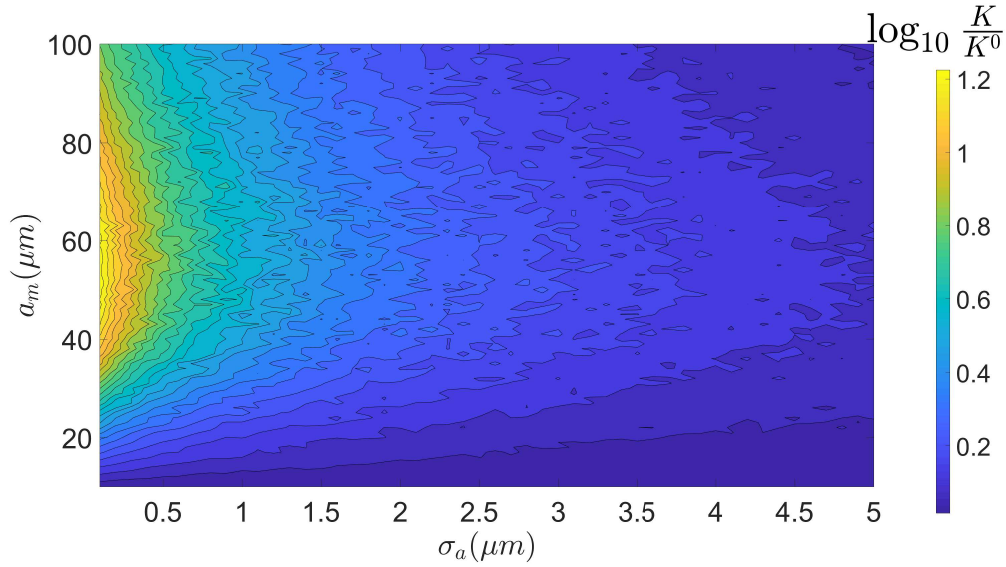


Figure 4.9: $\log_{10}(K/K^0)$ is shown using a contour plot spanning a_m and σ_a . Significant enhancement is observed across the parameter space. $g(r)$ plays the strongest role close to monodispersity and in size range of about 40 to 70 μm .

and so promote polydispersity. Unequal sizes dramatically enhances the differential sedimentation collision rate[106]. Also, since $St < 1$ throughout the 'size-gap' inertial clustering will favour growth of larger droplets. Both of these effects are expected to accelerate growth through and beyond the 'size-gap'. Hence, inertial clustering will be crucial in shaping the evolution of the drop size distribution. Consequently, the results of our study is expected to be integral for a detailed drop evolution simulation.

4.6 Summary

We have developed models for inertial clustering of particles settling in turbulent flow. The models incorporate known asymptotic results, such as the power law behaviour of the radial distribution function in the dissipative range, as well as develop new insights, especially a model for diffusion due to differential sedimentation. However, there are

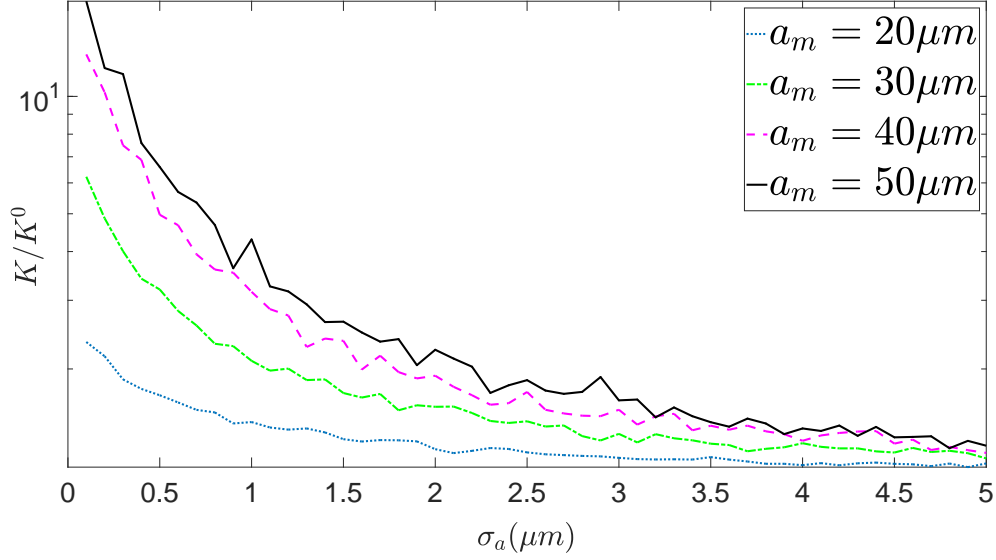


Figure 4.10: K/K^0 is shown as a function of σ_a at $a_m = 20, 30, 40, 50 \mu m$, representing typical sizes in and around the 'size-gap'. For the sizes shown here larger sizes leads to more enhancement. Rapid decay is observed with σ_a at all values of a_m .

still too many unknown components and developing a theory for them is beyond the scope of this study. Instead we obtain corrections from DNS results. The resulting model, for monodisperse and bidisperse case, agrees well with DNS and experimental data. Finally we apply it to a sample order one problem, of collision rate pertinent to droplets in clouds.

For a monodisperse suspension we have developed a closed form expression for the radial distribution, in §4.3, that is valid at all length scales of turbulence and St . Known results in the dissipative range as well as inertial sub-range have been incorporated and it is fitted with DNS results[53] to account for behaviour for which there is not a simple theoretical result, such as the non-local movement of particles between eddies. This result is complete and does not require additional inputs from turbulence.

For a bidisperse distribution of particles the differential sedimentation decorrelation of clusters is modelled through an estimate of diffusion it generates. This is used, along

with estimates for inward flux of particles and diffusion due to turbulent shear and acceleration, to solve a drift-diffusion equation and obtain $g(r)$. The order one constant in the correlation time for diffusion due to gravity is calculated by comparing against available DNS data from Dhariwal & Bragg[34]. The accuracy of the model is demonstrated by comparing $g(a_1 + a_2)$ with DNS data from Ayala et al[4] over a range of sizes.

Having developed a comprehensive model for clustering we use it to make comparisons against available experimental results in §4.4. Comparisons are made by accounting for the reported polydispersity in the experiments. Good agreement is found against the low Re_λ experiments by Salazar et al[99] who report $g(r)$ and $g_{ij}(r)$ calculated in the experiments by Saw et al[100] performed at higher Re_λ of 440. The effects of gravity on inertial clustering has been experimentally measured by Petersen et al[90] for a moderately high Re_λ of 300 and we find our model predicts the reported values of $g(r)$ accurately. Petersen et al[90] also report a fit based on the asymptotic result of power law in the dissipative range. We show how this is inadequate when extrapolated to separations comparable to the size of the particles. We argue that this error is due to insufficient experimental data, especially in the dissipative range. Finally we consider $g(r)$ reported by Yavuz et al[124] performed at low Re_λ . We find that their reported radial distribution function does not follow expected trends with St and r . There is no known physical mechanism to account that can potentially account for these experimental results, especially the dramatic enhancement of clustering in the dissipative range. Hence we do not attempt to reconcile our model with their experimental results.

Having developed and tested our model we apply it to of droplets in clouds in §4.5. Since it is beyond the scope of this study to do a full evolution simulation we only calculate the enhancement in collision rate over a large range of size distribution of droplets. We find significant, even if not the global maximum, enhancement of collision

rate within the 'size-gap'. This enhancement rapidly decays away as the distribution becomes broad. We use these insights to argue how inertial clustering will play an important role in the size distribution evolution and the critical role an inertial clustering result that smoothly spans a wide range of differential sedimentation strength, such as the one we have developed, will play in accurately modelling the drop evolution.

CHAPTER 5

THE EFFECT OF TURBULENCE, GRAVITY AND MICROPHYSICS ON DROP SIZE DISTRIBUTION IN CLOUDS

5.1 Abstract

The evolution of $O(10\mu m)$ droplets in clouds is studied with focus on the 'size-gap' regime of 15-40 μm radius, where condensation and differential sedimentation are least effective in promoting growth. This bottleneck leads to inaccurate growth models and turbulence can potentially rectify disagreement with in-situ cloud measurements. The role of turbulent collisions, mixing of droplets, and water vapour fluctuations in crossing the 'size-gap' has been analysed in detail. Collisions driven by the coupled effects of turbulent shear and differential sedimentation are shown to grow drizzle sized droplets. Growth is also promoted by turbulence-induced water vapour fluctuations, which maintain polydispersity during the initial condensation driven growth and facilitate subsequent growth by differential sedimentation driven coalescence. The collision rate of droplets is strongly influenced by non-continuum hydrodynamics and so the size evolution beyond the condensation regime is found to be very sensitive to the mean free path of air. Turbulence-induced inertial clustering leads to a moderate enhancement in the growth rate but intermittent turbulent collisions are not very effective. The coupled influence of all these phenomena are evaluated by evolving a large number of droplets within an adiabatically rising parcel of air using a Monte Carlo scheme that captures turbulent intermittency and mixing.

5.2 Introduction

The distribution of water droplets in clouds sets the thermal budget while its evolution controls precipitation and so is an important component in the study of our atmosphere [87, 48]. In clouds small droplets, typically of radii smaller than $15 \mu\text{m}$ radius, grow by condensation while large ones, typically of radius greater than $40 \mu\text{m}$ radius, collide through differential sedimentation to coalesce. However, the growth rate in the 'size-gap', of $15\text{-}40 \mu\text{m}$ radii, is not fully understood and it leads to significant errors in predictions of time to growth of drizzle-sized droplets and width of the size-distribution [23, 48]. To reconcile models to in-situ cloud measurements various mechanisms have been proposed and we will study in detail the role of turbulence in inducing polydispersity and collisions, collision rate set by non-continuum hydrodynamic interactions, and collision frequency enhancement due to inertial clustering. To obtain qualitative and quantitative estimates of their importance we perform a droplet distribution evolution.

The growth of small droplets is controlled by condensation. We simulate it with an adiabatic air parcel rising which changes the thermodynamic quantities, such as temperature and water vapour pressure, leading to diffusion of water vapour onto the droplets. It creates a monodisperse distribution and makes relative velocity due to gravity vanish. Additionally, condensation cannot grow very large droplets and so droplets cannot generate enough relative velocity by their own weight to drive collision. This represents the 'size-gap' and we test the role of the aforementioned mechanisms in breaking through it.

For growth of droplets through the 'size-gap' intermittent turbulent collisions are expected to play a role [65] along with its coupling with differential sedimentation, as

both are expected to be important in the 'size-gap'. Thus we use the collision rates calculated in §3 that properly couples these mechanisms. This coupling is not properly carried out in previous evolution studies, such as those by Xue et al[121] and Grabowski & Wang[47]. Li et al[73] perform direct numerical simulations (DNS) with particles settling in turbulence but do not incorporate hydrodynamic interactions which are a very important component in the droplet motion as they approach each other. Studies by Xue et al[121] and Grabowski & Wang[47], inspite of not properly coupling turbulence with gravity, include hydrodynamic interactions. But these are not accurate as they do not include the breakdown of continuum as the droplets approach each other which is expected to be important for a large size range in air over Van Der Waals forces and surface deformation[113](See §2). Finally high Reynolds number based on Taylor microscale (Re_λ), of $O(10^4)$ typical in clouds, have not been reached in the DNS studies by Li et al[73] and can lead to errors upto 20% in the observed collision rate. All of these issues have been properly resolved in the collision rate calculated in §3 and will be used in this evolution study.

Droplets possess inertia causing it to lag the background flow. For conditions typical in clouds droplet response time is significantly less than the characteristic fluid time, corresponding to the Kolmogorov time scale for the sub-Kolmogorov droplets[4]. In these conditions the leading order effect of droplet inertia is the enhancement of local concentration[26]. This inertial clustering depends on the bidispersity of the pairwise interaction and coupling of gravity with turbulence. We use the analytical expression from §4 that spans a large parameter space, pertinent to the droplets of interest, and reproduces reported DNS results as well as important physics. The enhanced local concentration increases the likelihood of collision events and will be incorporated into our droplet evolution model.

The turbulent mixing of water vapour leads to its fluctuations on the scale of the droplets without violating the overall adiabatic condition. These fluctuations have Gaussian statistics and can play an important role in droplet evolution by generating polydispersity[67, 22, 74]. Broadening of the drop size distribution is also expected via mixing of droplets[68, 104]. We model both of these mechanisms using packets, with any given packet representing a collection of droplets with an unique history of turbulent velocities and water vapour fluctuations. The water vapour fluctuations, on any particular packet, is approximated with a Stochastic mean-reverting process, with standard deviation typically about 1% of the mean content[67, 22], and attenuated by condensation. Mixing of droplets is modelled by moving it between packets. Since mixing is governed by motion of the large scale eddies both the rate of reversion of the turbulent water vapour fluctuations and rate of droplet mixing is chosen to be the inverse of the integral time scale of turbulence.

There are a large number of droplets, about 10^8 per m^3 , in a typical cloud[72]. It is numerically not feasible to track all of them while still accounting for all the mechanisms in play. Thus, we use a Monte Carlo scheme with one Monte Carlo droplet representing many real droplets to retain the discrete nature of the drop size distribution. This discrete distribution, relative to a continuous one, better captures the stochastic growth driven by the various modes of turbulence and is complemented by the use of packets to capture different realisation of turbulence. The collection of all the packets represents the adiabatic air parcel rising from the ground.

The model developed here focuses on growth of water droplets in turbulent clouds. However, it can be easily extended to other cases such as industrial aggregators. For industrial aggregators Buesser & Pratsinis[21] discuss the critical role of particle collision in growing carbon black, pigments, and other commercially valuable products when

starting from an initial phase controlled by diffusional growth. This mimics the droplets in clouds with the body force on the particles taking on the role of gravity. The high temperatures of the operation will potentially lead to large enough mean free path for the turbulent gas that collisions of the sub-micron particles are governed by non-continuum effects.

In this study we first develop the Monte Carlo method and all pertinent formulation for the cloud packet model in §5.3. We utilise it to obtain evolution of the drop size distribution. Important results and insights obtained from this calculation is presented in §5.4. Finally in §5.5 we summarise and give highlights of some of the important insights our study.

5.3 Formulation

Water droplets in clouds typically start out through condensation onto sub-micron dust or aerosol particles. It is possible that a few very large, about tens of micron radii, nucleation sites could impact the evolution in the 'size-gap' and this has been studied by Feingold et al and Lasher-Trapp et al[41, 69]. However, for the vast majority of nucleation sites condensation along with the turbulent water vapour fluctuations will control growth rate and shape of the distribution to sizes in the lower end of the 'size-gap'[67, 22, 74]. Hence we include condensation in our model to obtain an accurate description of the drop size evolution and not focus on the initial cloud condensation nuclei.

To model condensation we simulate an adiabatic parcel of air rising from the ground starting with initial 100% relative humidity at a typical updraft velocity of 1 m/s [118]. As it rises the water vapour carrying capacity decreases and it diffuses onto the droplets.

For a droplet of species k with radius a_k the growth rate is given as,

$$\frac{da_k}{dt} = \frac{D}{\rho a_k}(\rho_\infty - \rho_a) \quad (5.1)$$

Here, D is the diffusivity of water vapour, ρ is the density of water, ρ_a is the water vapour density on the surface of the droplet, and ρ_∞ is water vapour density of air in the vicinity of the droplet. Different regions of the air parcel can have differing amounts of ρ_∞ due to large scale turbulent eddies acting on the mean water vapour gradient and generating fluctuations with Gaussian statistics[67, 22]. To model this we discretise the air parcel into N_p packets of equal volume V , each with its own collection of droplets. The water vapour content of each packet m is given as, $w_m = \rho_{\infty,m}V$ and $w_m - \langle w \rangle$, in the absence of condensation, is simulated with an Ornstein–Uhlenbeck process with a characteristic time for reversion of T_E , the Eulerian integral time scale, corresponding the largest turbulent eddies. The standard deviation of the process is a fixed fraction the mean water vapour content $\langle w \rangle$, which we shall denote as f . Typically, f is 1%, but we will explore this parameter space. Condensation acts as a sink for w_m through droplets draining water vapour from its vicinity. We resolve this continuous evolution along with the stochastic behaviour, due to turbulent water vapour fluctuations, to accurately simulate the condensation growth of water droplets in turbulent clouds.

Similar to water vapour turbulence will also mix droplets. To model this we move droplets from one packet to another to mimic movement from one history of water vapour fluctuation and local conditions to another. The rate at which this occurs set to be $1/T_E$.

In contrast to continuous condensation driven droplet growth the collisions are discrete. Hence in our evolution study we track the discrete drop size distribution. However, there are a large number of droplets and we take the typical value of 10^8 per m^3 [72]. It is beyond the scope of our study to track the trajectory of these droplets within the

large volumes swept out by the air parcel as it rises from the ground. Instead we track collisional growth through Monte Carlo simulation of the rate law. Binning multiple real droplets into a Monte Carlo droplet allows for increased computational efficiency while still retaining accuracy and the discrete nature of the distribution.

This two-species rate law for collisional growth is given as,

$$\frac{dn_i}{dt} = -C_{ij}n_in_j \quad (5.2)$$

where n_i corresponds to the number density of species i in the bulk. Only two species interaction is considered due to the dilute nature of the cloud system (Grabowski & Wang[48] suggest volume fraction to be $O(10^{-6})$). C_{ij} is the rate constant set by the turbulent flow, gravity, non-continuum hydrodynamic interactions and inertial clustering. However, within a packet multiple pairs can potentially collide and coalesce. In fact, in a given packet, for N Monte Carlo droplets, each of which represents N_d real droplets, $N(N - 1)/2$ Monte Carlo droplet collisions are possible. For any given Monte Carlo droplet pair with $N_{d,i} \leq N_{d,j}$ real droplets in a given time step dt the probability of collision P^* is,

$$P^* = \frac{C_{ij}N_{d,j}dt}{V} \quad (5.3)$$

Due to computational constraints we will test, at any given time step, $\mathcal{G}(N/2)$ randomly chosen pairs within a packet for collisions, where \mathcal{G} is the greatest integer function. Thus, the new probability of collision P of any chosen Monte Carlo droplet pair is given as,

$$P = \frac{1}{\mathcal{G}(N/2)} \frac{N(N - 1)}{2} \frac{C_{ij}N_{d,j}dt}{V} \quad (5.4)$$

If this P is greater than a random number collision and subsequent coalescence is allowed. In this case the radii of the Monte Carlo droplet i and N_d of Monte Carlo droplet

j is updated. If $N_{d,i} = N_{d,j}$ they are assigned $\mathcal{G}(N_{d,i}/2)$ and $\mathcal{G}(N_{d,i}/2) + 1$ droplets respectively, along with the updated radii on both of them. By allowing N_d to vary this scheme allows resolving appearance of a few large droplets without additional computational resources.

To calculate P in equation (5.4) information on C_{ij} is needed. To evaluate this we consider the nature of the collisions, specifically the role droplet inertia plays. An estimate of droplet inertia is the non-dimensional Stokes number, given as $St = \tau_p/\tau_f$. Here, the particle response time is $\tau_p = 2a^2g/9\nu$, with g the acceleration due to gravity, and τ_f the characteristic fluid time. Two definitions of τ_f , and thus Stokes number, are pertinent to the collision dynamics. The first is based on the relative velocity V_{rel} given as a/V_{rel} . This St_{rel} was shown in §2 to be very small for conditions typical in clouds and so droplet inertia will not influence the collision dynamics. However, St based on Kolmogorov time scale τ_η is found to be significant, even reaching $O(1)$ under some conditions in clouds[4]. This will significantly enhance the local concentration and so increasing the frequency of collisions. Thus, it is possible to describe the rate constant as,

$$C_{ij} = g(r)|_{r=a_i+a_j} K_{ij} \quad (5.5)$$

Here K_{ij} is evaluated at zero droplet inertia and $g(r)$ is the radial distribution function, capturing local concentration enhancement due to droplet inertia at a separation r from a test droplet.

In the absence of droplet inertia the ideal collision rate for pure differential sedimentation was calculated by Smoluchowski[106] and shown to be sensitive to difference in size. An equivalent calculation in turbulent flow was carried out by Saffman & Turner[97] but it did not include dependence on Reynolds number based on the Taylor microscale of turbulence Re_λ . Variation with this parameter has been studied in §3

where a 20% change in collision rate is found between $Re_\lambda = 90$, typical in DNS studies, and the more realistic value of 2500 encountered in turbulent clouds. Both turbulence and differential sedimentation are expected to be important for collisions in the 'size-gap' and this coupling has been resolved in their collision rate study. Since the droplets are present in air hydrodynamic interactions, shaped by the breakdown of continuum upon close approach of the droplets, are expected to strongly influence collision events while Van Der Waals effects and droplet deformation are not expected to play an important role[113]. While a few studies have calculated collision rate with non-continuum effects[32, 27] the most comprehensive analysis is in §2. They calculate the retardation due to hydrodynamic interactions and report the collision efficiency (β) as a function of relative size of the interacting droplets, Knudsen number $Kn=2\lambda_g/(a_1 + a_2)$ where λ_g is the mean free path of air and relative strength of characteristic settling velocity of differential sedimentation to turbulence. The sedimentation velocity includes non-linear Stokes drag calculated from the expression given in table 5.2 of Clift et al[28]. The turbulent velocity depends on the local shear rate Γ_0 . The probability distribution function of local Kolmogorov properties exhibits large tails, indicating increased likelihood of intermittent shear rates relative to a normal distribution. Γ_0 was modelled by Koch & Pope[63] as a log-normal distribution, with the constitutive Gaussian statistics obtained from an Ornstein–Uhlenbeck process dependent on both the Kolmogorov and integral scales of turbulence. We take this result and create a unique realisation of the turbulent shear rate on each packet. Thus, in addition to resolving intermittent collisions, we also capture multiple realisations of turbulence.

Droplet inertia creates a delay in response to the background turbulence leading to clustering in certain regions of the flow. In addition to St based on individual droplet motion, it depends on the strength of differential sedimentation, captured through the difference in the settling parameter $\Delta S_{v,ij} = |\tau_{p,i} - \tau_{p,j}|g/u_\eta$. Here u_η the Kolmogorov

velocity given as $(\nu\epsilon)^{1/4}$. $St = O(1)$ leads to maximum inertial clustering. However DNS studies by Ayala et al[4] and Dhariwal & Bragg[34] showed that decorrelation through differential sedimentation occurs rapidly as the particle pair sizes become different, indicating $g(r)$ is large for $\Delta S_{v,ij} \ll 1$. All of these effects have been captured and $g(r)$ validated against DNS results in the inertial clustering model developed in §4. This will be used in our evolution study.

λ_0 and ν are sensitive to temperature and pressure. These thermodynamic quantities change due to condensation and the cloud packets rising. To determine the corresponding instantaneous viscosity we use the Sutherland viscosity law that is a function of temperature[114]. To obtain the instantaneous mean free path we use the expression given by Jennings[60] that is a function of ν , temperature, and pressure. We evolve λ_0 and ν accordingly unless explicitly stated.

5.4 Results and discussion

Due to the wide range of parameters under consideration we will use typical values for the turbulent and microphysical parameters unless otherwise stated. Their default values are $\epsilon = 0.01m^2/s^3$, $Re_\lambda = 2500$, $f = 1\%$, ground temperature T_0 is 293 K, ground pressure P_0 is 1 bar and up-draft velocity of 1 m/s. λ_0 and μ evolve accordingly unless otherwise explicitly stated. The default simulation parameters are: $V = 1m^3$, initial Monte Carlo droplet per packet of 100, $N_p = 100$, initial droplet radius is a uniform random distribution between 0.1 to 1 μm . For this default case the drop size distribution is shown in figure 5.1 at 600, 4800 and 7200 seconds using the number density per unit radius (n_a) vs radius. In the early evolution the drop size distribution is nearly Gaussian due to water vapour fluctuations statistics following a Normal spread. As the air parcel

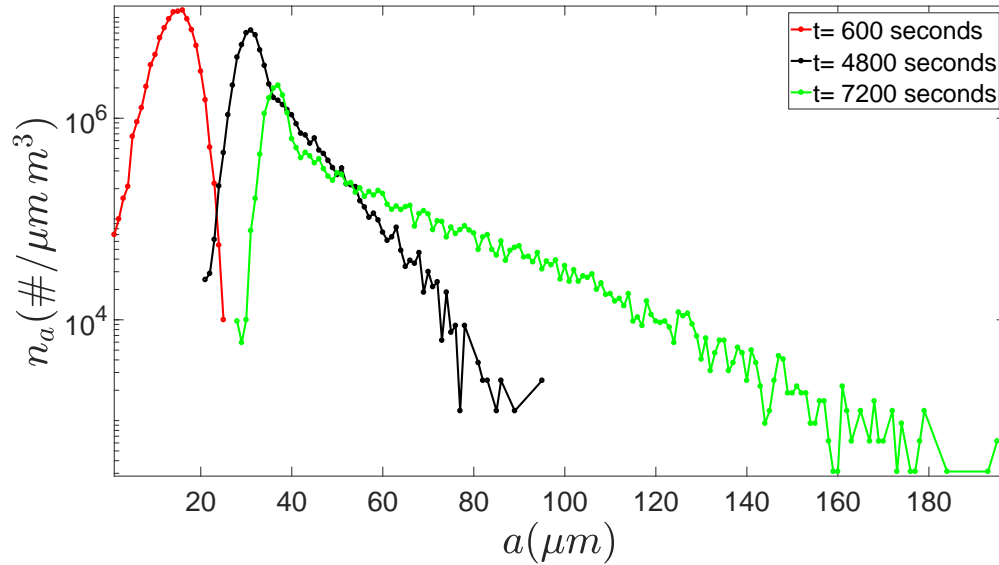


Figure 5.1: The number density of droplets per given radius n_a is plotted against radius at early (600 seconds), intermediate (4800 seconds) and long (7200 seconds) time evolution of our model. The drop size distribution does not conform to any specific form at all times. Starting off Gaussian it transitions to a skewed distribution as the system evolve.

evolves collisions take over growing of large droplets. The process is not Gaussian and is reflected of formation of a long tail. This tail on the right side, corresponding to large droplets, becomes prominent at long times. In this skewed distribution large droplets promote further collisions, thus draining the Gaussian bulk to lengthen the tail of the distribution. These long tails indicate a power law for the differential sedimentation collision controlled regime. A power law behaviour was observed by Westbrook et al[119] for particles settling slower than than velocities induced by differential sedimentation. However, there is not a theoretical result in the limit considered in our evolution study and so we do not explore characterising the tails through a power law in this study.

While the full drop size distribution can provide useful insight it is not feasible to report it at every instant for all the simulations performed. Instead we will report two metrics of the distribution, namely the volume averaged mean radius a_v and dispersion

\mathcal{D} . a_v is a measure of the size of drops as seen by the liquid water content and is given as,

$$a_v = \frac{\sum a_i^4}{\sum a_i^3} \quad (5.6)$$

\mathcal{D} is a non-dimensional estimate of the spread of the distribution and is given as,

$$\mathcal{D} = \frac{\sigma_a}{\langle a_i \rangle} \quad (5.7)$$

where, σ_a is the standard deviation and $\langle a_i \rangle$ is the number averaged radius of the distribution.

In the early evolution condensation dominates and the growth it generates is not sensitive to the initial micron-sized distribution. This is due to condensation favouring growth of smaller droplets to larger ones. To demonstrate this we consider evolution due to only condensation driven by the cloud packet rising, with $f = 1\%$. We start off with a few different mean and width of a Gaussian distribution as initial condition. For this evolution a_v and \mathcal{D} are shown in figure 5.2. All the cases collapse in a matter of minutes and at sizes at which growth is expected to be condensation dominated. Thus, in our study, we consider sub-micron sized cloud condensation nuclei and not explore the parameter space of the initial distribution further.

The condensation controlled growth shown figure 5.2 has a rate that is inversely proportional to the radius. Hence the radius goes as $t^{1/2}$ and will reach a maximum value that lies within the 'size-gap'. If collisions driven purely by differential sedimentation are allowed it is still not enough to grow droplets beyond what is possible through pure condensation. This ineffectiveness of differential-sedimentation is because it requires difference in droplet size to drive collisions. Despite water vapour fluctuations, all the droplets in the packet experience the same history and evolve to the same size. At very small sizes, when polydispersity is still present within the packet, the relative velocities

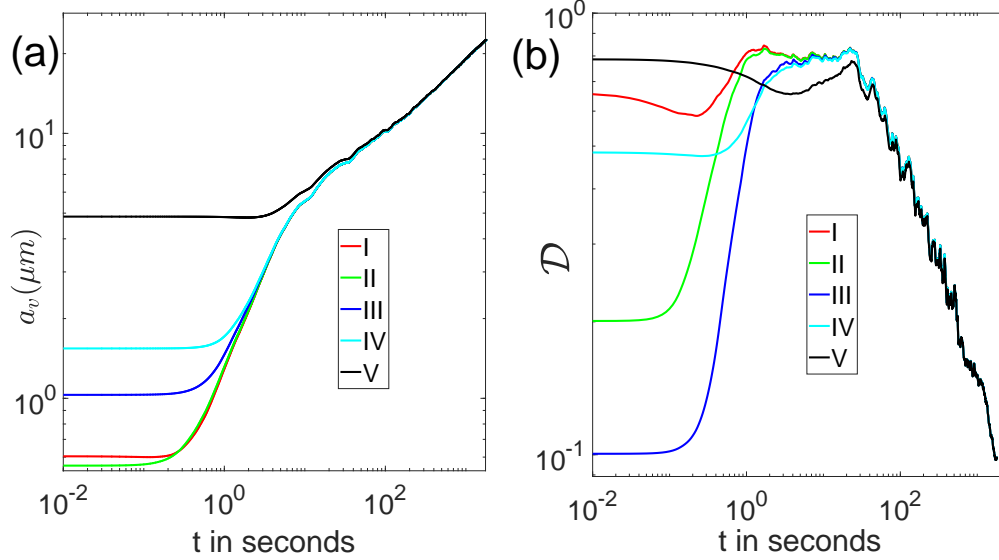


Figure 5.2: Shown is the evolution under the influence of condensation and water vapour fluctuations and it leads to a nearly monodisperse drop size distribution insensitive to initial conditions. Figure (a) shows evolution of a_v while figure (b) shows \mathcal{D} . In the Legend 'I', 'II', 'III', 'IV', and 'V' correspond initial Gaussian drop size distributions with means of 0.25, 0.5, 1, 1, 2 μm and standard deviations of 0.25, 0.1, 0.1, 0.5, 2 μm , respectively.

generated by gravity is ineffective towards driving collisional growth. This leads to droplets being unable to grow beyond 40 μm radius. This represents the 'size-gap' problem and turbulence, beyond its direct role on condensation, is needed to resolve this.

When condensation and collisions driven purely by differential sedimentation are considered then growth beyond 'size-gap' is possible through the coupled action of turbulent mixing of droplets and water vapour fluctuations. For this configuration the evolution of a_v and \mathcal{D} is shown in figure 5.3 for $f = 0.1\%$ to 1% . Initially \mathcal{D} decreases due to attenuation by condensation. However, enough polydispersity persists when the droplets are moderately large to initiate collisional growth. Consequently larger values of f correspond to faster growth rate of a_v .

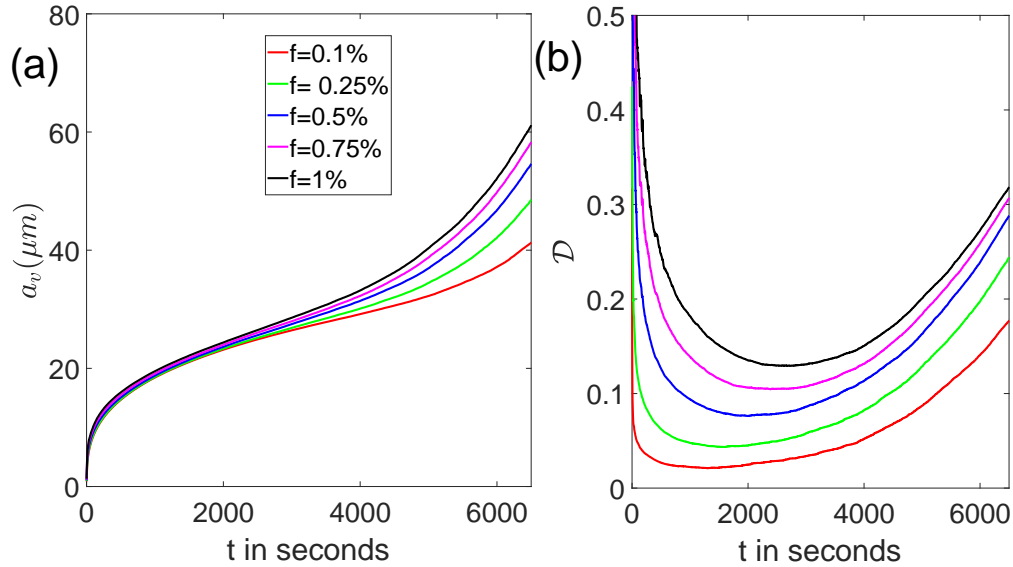


Figure 5.3: a_v (a) and \mathcal{D} (b) are shown as a function of time for droplets evolving by condensation, gravitational collisions, turbulent mixing of droplets, and water vapour fluctuations. Increasing f from %0.1 to %1 enhances the growth rate.

To demonstrate the role of turbulent collisions we use collision rates that couple it with differential sedimentation and exclude water vapour fluctuations as well as turbulent mixing of droplets. We include inertial clustering as it impacts the observed collision frequency. These results are shown in figure 5.4 for multiple dissipation rates. In the early evolution \mathcal{D} is small for all ϵ as there is no polydispersity generating mechanism and condensation drives to a nearly monodisperse distribution. When the drops are about $20\mu\text{m}$ turbulent collisions start to takeover. The rate at which the 'size-gap' is crossed increases with higher dissipation rates, corresponding to higher average Γ_0 .

Having explored how droplets can grow to differential-sedimentation dominated sizes, we show the evolution of droplet size including all features of the model as solid lines in figure 5.5 for several turbulent dissipation rates. The dashed lines show the calculation without mixing of droplets and water vapour fluctuations for the lowest and highest dissipation rates. As expected lower dissipation rate leads to slower growth.

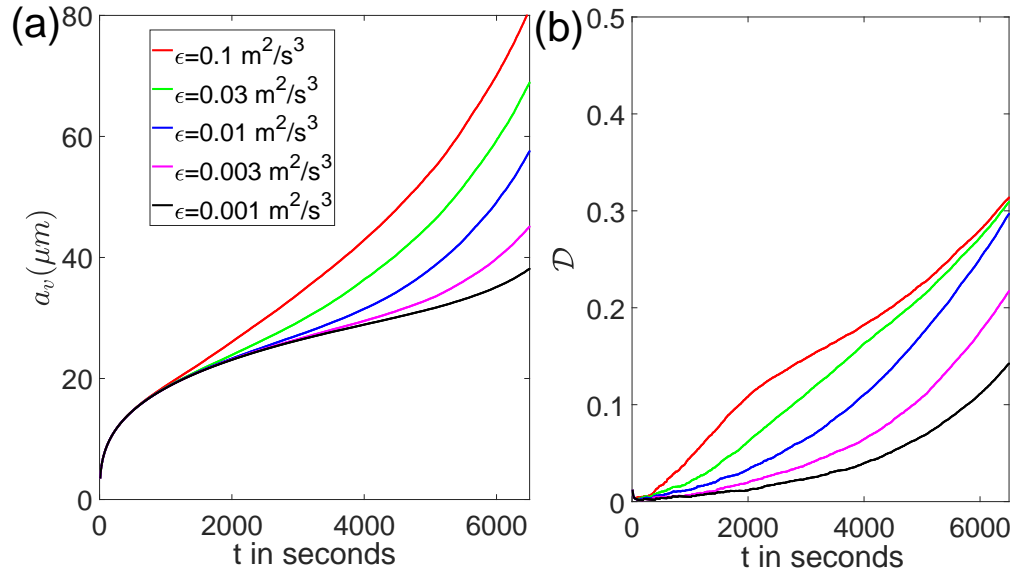


Figure 5.4: The growth across the 'size-gap' due to turbulent collisions is shown by varying ϵ from 0.001 to $0.1 \text{ m}^2/\text{s}^3$. The collision rate used couples turbulence with differential sedimentation and the evolution dynamics include condensation but exclude turbulent mixing of droplets and water vapour fluctuations. Figure (a) shows evolution of a_v , while figure (b) shows \mathcal{D} .

Surprisingly, though, the variation of droplet radius with dissipation rate in the collision controlled sizes is reduced for the full calculation. In the early, condensation controlled, evolution the drop size distribution growth is higher in the full calculation due to water vapour fluctuations and turbulent droplet mixing induced polydispersity. Later on this polydispersity enhances the collisional growth at low dissipation rates where differential sedimentation is the predominant collision mechanism by increasing the difference in settling velocities. In contrast, at high dissipation rates, polydispersity hinders growth which implies that a significant fraction of the collisions are caused by turbulence driven collisions. The ideal turbulent collision rate $n_1 n_2 \Gamma_0 (a_1 + a_2)^3$ is insensitive to difference in size of colliding droplet pairs. Instead the dependence on a_2/a_1 arises from the non-continuum hydrodynamic interactions, which result in a collision efficiency that is 30% smaller at $a_2/a_1 = 0.4$ than at $a_2/a_1 = 0.9$ (see §3), and inertial clustering, which is

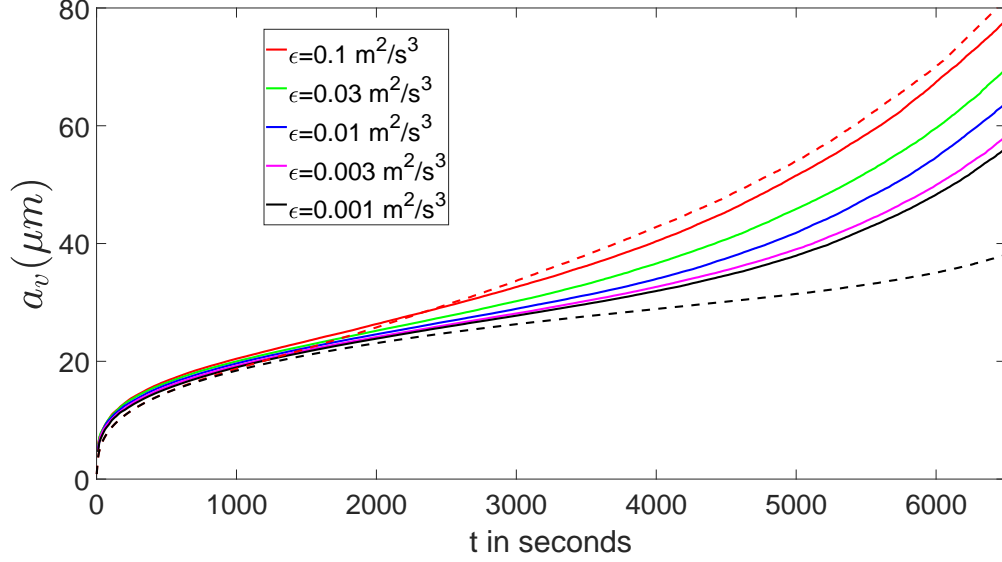


Figure 5.5: The complex role turbulence plays in crossing the 'size-gap' is shown by plotting a_v against time for the full calculation (solid lines) and the result from figure 5.4 with only condensation, and coupled turbulent-gravitational collisions (dashed lines). The dashed curve with larger radius growth corresponds to $\epsilon = 0.1 m^2/s^3$ while the other is for $\epsilon = 0.001 m^2/s^3$.

less effective in enhancing collision frequency as polydispersity increases. Thus, coalescence dominated by turbulent shear is hindered by polydispersity. It should be noted that collision efficiency for differential sedimentation also decreases (by 50%) when a_2/a_1 is decreased from 0.9 to 0.4 (see §3). However, the dependence of the ideal rate, $n_1 n_2 \frac{2}{9} \rho g (a_2^2 - a_1^2) (a_1 + a_2)^2 / \mu$, on the size ratio more than makes up for the deficit.

Figure 5.6 highlights the effects of the collision efficiency due to non-continuum hydrodynamics β , large intermittent turbulent shear rates driving collision of a few lucky drops, and the clustering of drops (measured by $g(r)$) due to inertial dynamics in the turbulent flow on the growth of drop radius. The figure compares the full calculation with a calculation that neglects hydrodynamic interactions $\beta = 1$, a simulation with no fluctuations in the local Kolmogorov shear rate ($\Gamma_0 = 1/\tau_\eta$), and one that neglects inertial clustering $g(r) = 1$. Clearly the common practice of neglecting droplet interactions

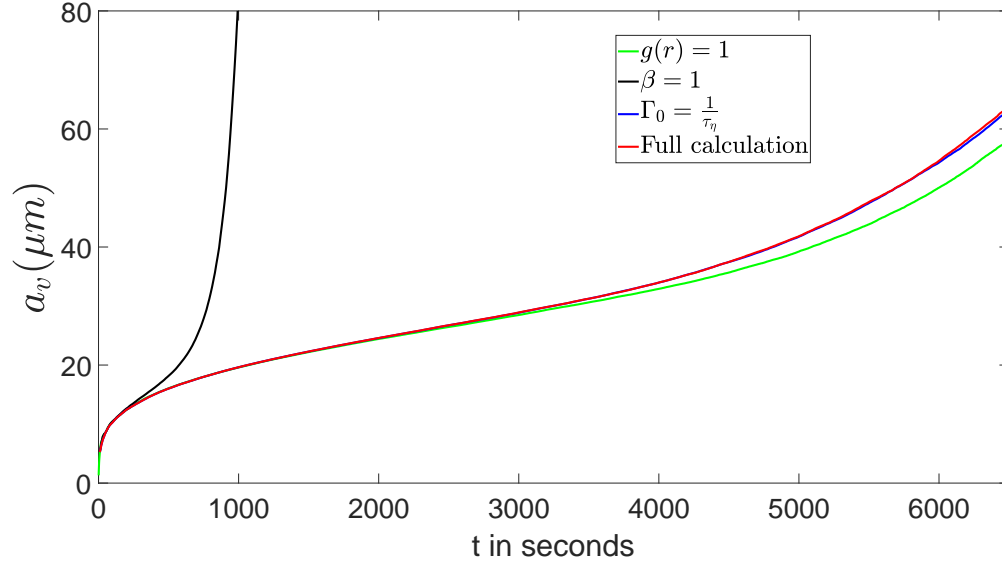


Figure 5.6: a_v evolution for $\beta = 1$, $g(r) = 1$, and $\Gamma_0 = \frac{1}{\tau_\eta}$ along with the full calculation for reference is shown.

setting the collision efficiency equal to one greatly over estimates the drop growth. In contrast, inertial clustering causes a modest enhancement of the growth rate and intermittent turbulent collision a much weaker impact.

Turbulent statistics are typically characterised by fat tails in the probability distribution function. Using this idea Kostinski & Shaw[65] proposed that a few 'lucky' droplets can collide due to abnormally large local turbulent shear rates and thus cross the 'size-gap'. However, our calculations in figure 5.6 show that these 'lucky' droplets do not grow large enough to significantly influence the evolution of the whole distribution. In fact the formation of not too large 'lucky' drops leads to polydispersity driven retardation in growth at the higher dissipation rate that we discussed previously (not shown for sake of brevity).

Inertial clustering has a more pronounced role in the drop size evolution. Yet it does not lead to an order of magnitude enhancement of growth rate (see figure 5.6). To understand this we plot the cumulative average of $g(a_1 + a_2)$ of all the successful collision

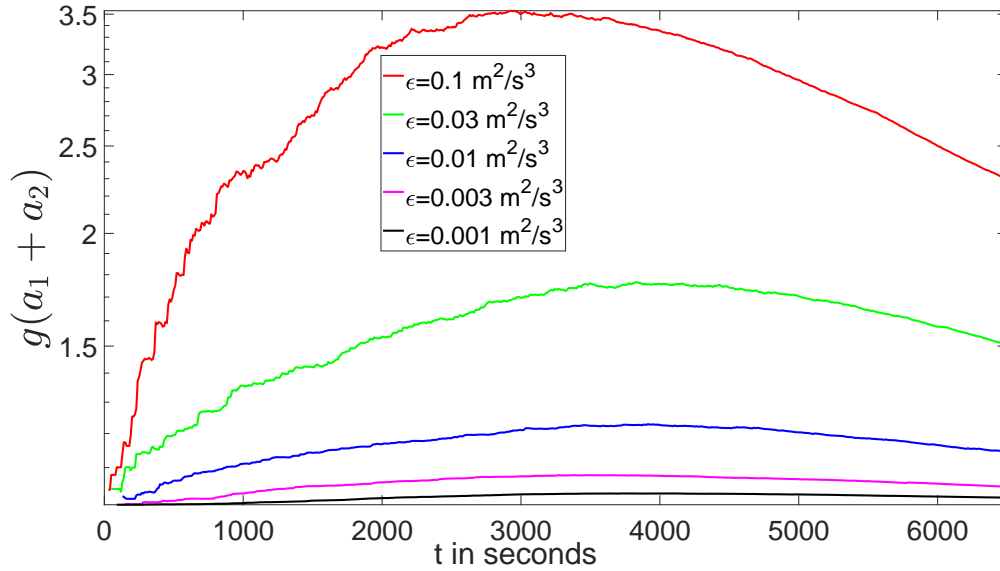


Figure 5.7: Cumulative average of $g(a_1 + a_2)$ for the full calculation is shown for $\epsilon = 0.001, 0.003, 0.01, 0.03, 0.1 \text{ m}^2/\text{s}^3$. A non-monotonic behaviour with time is observed for the enhancement of collision rate due to inertial clustering.

events. This is shown in figure 5.7 for the full calculation evolution at all the values of the dissipation rate chosen in figure 5.5. A monotonic behaviour is not observed, instead a peak appears in the inertial clustering enhancement at about 1 hour of simulated rise of the cloud packet. To obtain insight into the peak and its modest value we consider the mean St and difference in S_v . These have to be $O(1)$ and negligible respectively to have maximum enhancement of collision frequency via inertial clustering. The cumulative average of these two parameters is shown in figure 5.8. Evolution of St is shown in figure 5.8 (a) which does monotonically increase with time across the parameter space. However, it does not reach $O(1)$ for the lower dissipation rates before ΔS_v does (figure 5.8 (b)). When turbulent collisions are dominant, as we have seen for $\epsilon = 0.1 \text{ m}^2/\text{s}^3$, inertial clustering can reduce time to reach $40 \mu\text{m}$ radius by about 15%. This is line with the significantly large peak of $g(a_1 + a_2)$ for $\epsilon = 0.1 \text{ m}^2/\text{s}^3$ observed from figure 5.8 (a).

Hydrodynamic interactions, that includes breakdown of continuum of the gaseous

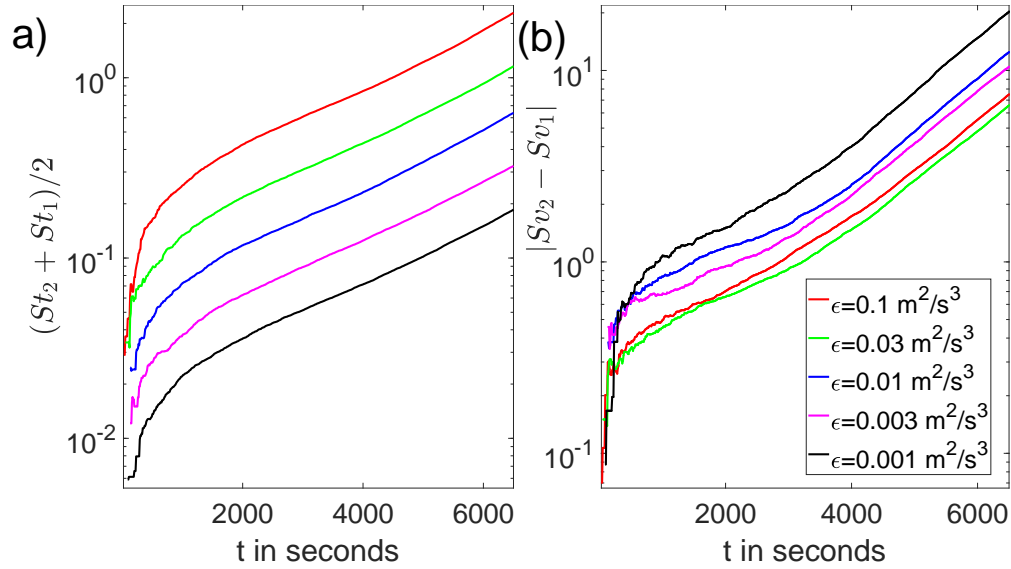


Figure 5.8: Evolution of the two important parameters of inertial clustering as a function of time shown for $\epsilon = 0.001, 0.003, 0.01, 0.03, 0.1 \text{ m}^2/\text{s}^3$. Figure (a) shows the mean Stokes number and figure (b) the magnitude of the difference in non-dimensional settling velocity.

media upon close approach, are very important for collision dynamics of water droplets in clouds [113] and we have shown, in figure 5.6, its significant impact on the evolution. The lubrication force of this hydrodynamic interaction is set by the mean free path, which at standard temperature and pressure is 70nm and can vary with these parameters. Thus, to obtain better insight into the role of λ_g on evolution of the droplet distribution we fix it (and by extension ν) during the rise of the air parcel and carry out multiple simulations to span this parameter. This is shown in figure 5.9 along with the reference case of $\beta = 1$. It is evident that $\beta = 1$ result is approached as λ_g and the resistance to collision decreases. Under typical conditions though, of λ_g of about $70\text{-}100 \text{ nm}$, β is small. It can range from 10% to 30% for turbulent collisions and fall below 1% for differential sedimentation dominated collisions (see §3). This is the reason for the large spread in λ_g parameter space in figure 5.9.

In addition to informing terrestrial clouds, the variation over λ_g can provide insight

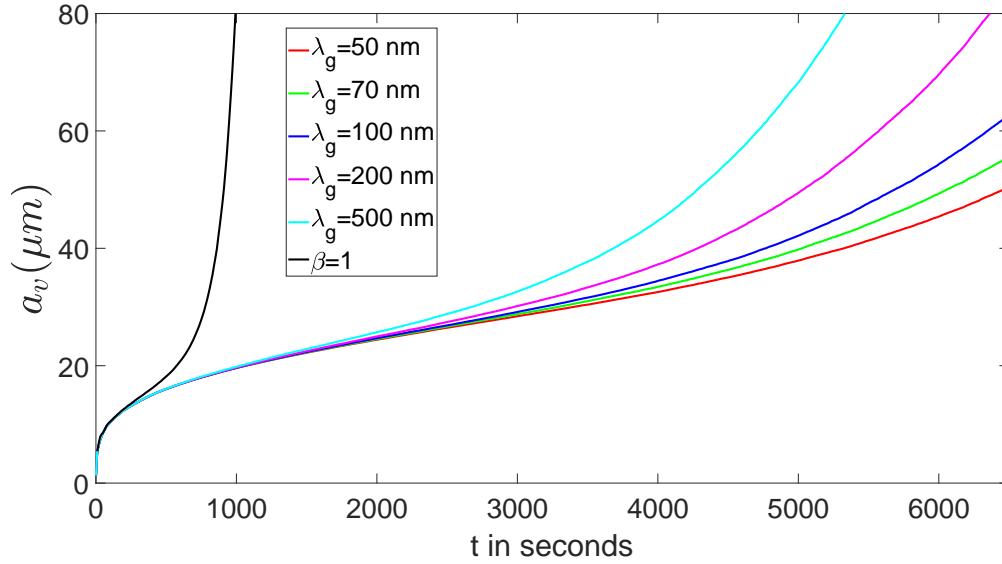


Figure 5.9: Evolution of the drop size distribution is shown the full calculation performed at fixed mean free path. Figure (a) shows evolution of a_v while figure (b) shows \mathcal{D} . $\lambda_g = 50, 70, 100, 200, 500$ nm are chosen along with $\beta = 1$ calculation for reference.

into droplet size evolution in extra-terrestrial atmosphere. For sulphuric acid precipitation on Venus and hydrocarbon rain on Titan the Van Der Waals strengths are about the same as water droplets on Earth. The surface conditions indicate that mean free path will be much smaller[120]. However significant precipitation activity can occur in Venus at altitudes of a few tens of kilometres[43]. Perron et al[89] discuss the possibility of precipitation on Titan through the convective rise of air parcel upto heights of 40 kilometres. At these high altitudes the mean free path can become large enough for non-continuum hydrodynamics to be significant. Hence, in figure 5.9 we have performed calculations with λ_g over a large range, including significantly larger values than those encountered in terrestrial clouds.

An alternate route to study the role of λ_g on size evolution is to vary the ground pressure and temperature in the full calculation. We consider some typical values of T_0 and P_0 and show the resulting evolution of a_v in figure 5.10. Lower P_0 (figure 5.10 (a))

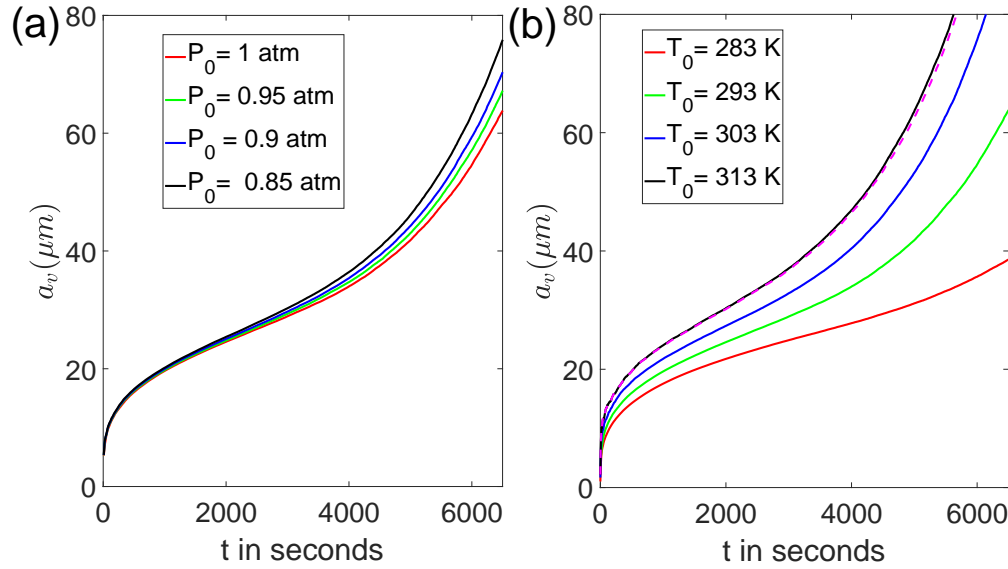


Figure 5.10: Impact of varying initial ground conditions is shown by tracking a_v . Figure (a) considers different initial pressures, from $P_0 = 1$ to 0.85 atmospheres. In figure (b) we vary the initial temperature from $T_0 = 283$ to 313 K. The dashed line corresponds to evolution with $T_0 = 313K$ but λ_g given a history of evolution corresponding to $T_0 = 293K$

and higher T_0 (figure 5.10 (b)) lead to lower λ_g which, in turn, cause accelerated growth rate due decrease in lubrication resistance to collision.

While changing P_0 predominantly alters λ_g increases in T_0 significantly enhances the water vapour carrying capacity. Starting off with 100% relative humidity the droplets from hotter ground can grow to larger sizes through condensation alone. Even if condensation can grow the droplets by an extra 10% the turbulent collision rate, which depends on size as $(a_1 + a_2)^3$, increases by 30% with a similar enhancement for differential sedimentation collision rate. To demonstrate this we perform a calculation with $T_0 = 313K$ but λ_g alone is given a history of evolution corresponding to $T_0 = 293K$. The resulting evolution of a_v is shown in figure 5.10 (b). This result nearly tracks the simulation performed at $T_0 = 313K$. The difference is similar to the variation observed while changing P_0 , which is directly attributable to changes in λ_g .

5.5 Conclusion

Previously unexplored important physics in cloud droplet dynamics have been analysed in our study. We have considered a collision rate that properly couples turbulence with differential sedimentation and includes non-continuum hydrodynamics to analyse growth through the 'size-gap', where it is not fully understood how droplet growth occurs [48]. We also considered the role of polydispersity through turbulence induced mixing of droplets and water vapour fluctuations. The importance of all of these has been analysed in detail.

Condensation was shown to have an important role in the early evolution washing away any memory of the initial micron sized distribution. The polydispersity induced by different histories of condensation, arising due to turbulent fluctuation of local water vapour content, was shown to enable crossing of the 'size-gap' in figure 5.3. Large amount of condensation, due to enhanced water vapour content in the air parcel, was shown in figure 5.10 (b) to increase collisions through creating bigger drops in the 'size-gap'.

Turbulent collisions were shown in figure 5.4 to be sufficient in crossing the 'size-gap' without necessity for any polydispersity inducing mechanisms. The inclusion of polydispersity did not result in additive growth. Instead a small retardation was observed in the turbulent dominated cases due to the nature of the hydrodynamic interactions and weakening of inertial clustering.

The critical role of hydrodynamic interactions, that includes the breakdown of continuum on close approach of droplets, has been demonstrated in figures 5.6 and 5.9. We explored the more moderate impact of inertial clustering through evolution of some important parameters in figures 5.7 and 5.8. Crossing the 'size-gap' through intermit-

tent turbulent collisions was shown to not be an effective route. Very few droplets grow to large sizes due to intermittency. For those that do the differential sedimentation velocity induced is not large enough to make a significant impact on the evolution. This weaker than expected gravity induced velocity is due to non-linear stokes drag and the significant retardation in relative motion due to non-continuum hydrodynamics.

The results of this study can be extended to model industrial reactors and extra-terrestrial weather. For this purpose we have extensively spanned in the λ_g parameter space in figure 5.9. We have varied initial temperature and pressure in figure 5.10 to both capture different ground conditions on Earth and as well give insight into the interplay of the various mechanisms in shaping the size evolution.

CHAPTER 6

THE HYDRODYNAMIC LIFT OF A SLENDER, NEUTRALLY BUOYANT FIBRE IN A WALL BOUNDED SHEAR FLOW AT SMALL REYNOLDS NUMBER

6.1 Abstract

The hydrodynamic lift velocity of a neutrally buoyant fibre in a simple shear flow near a wall is determined for small, but non-zero, fibre Reynolds number, illustrating the role of non-sphericity in lift. The rotational motion and effects of fibre orientation on lift are treated for fibre positions that induce and do not induce solid-body wall contacts. When the fibre does not contact with the wall its lift velocity can be obtained in terms of the Stokes flow field by using a generalized reciprocal theorem. The Stokes velocity field is determined using slender-body theory with the no-slip velocity at the wall enforced using the method of images. To leading order the lift velocity at distances large compared with the fibre length and small compared with the Oseen length is found to be $0.0303\rho\dot{\gamma}^2 l^2 a / (\mu \ln[2l/a])$, where l and a are the fibre half-length and radius, ρ is the density, $\dot{\gamma}$ is the shear rate and μ is the viscosity of the fluid. When the fibre is close enough to the wall to make solid-body contact during its rotational motion, a process known as pole vaulting coupled with inertially induced changes of fibre orientation determines the lift velocity. The order of magnitude of the lift in this case is larger by a factor of l/a than when the fibre does not contact the wall and it reaches a maximum of $0.013\rho\dot{\gamma}^2 l^3 / (\mu \ln[l/a])$ for the case of a highly frictional contact and about half that value for a frictionless contact. These results are used to illustrate how particle shape can contribute to separation methods such as those in microfluidic channels or cross-flow filtration processes.

6.2 Introduction

Hydrodynamic lift is the motion of a particle transverse to the streamlines of the imposed flow and the direction of any body force on the particle. It results from the stresses on the particle caused by fluid inertia when the particle Reynolds number is finite. Hydrodynamic lift plays an important role in separation processes such as microfluidic focusing [79] and cross-flow filtration[38]. While there is extensive literature analysing the lift on a spherical particle[98, 80, 81, 25, 37], relatively little is known about the lift on non-spherical particles. To gain insight into the role of non-sphericity we derive the lift velocity of a neutrally buoyant high aspect ratio cylindrical fibre in a wall-bounded simple shear flow at small, but finite, particle Reynolds number $Re = \rho\dot{\gamma}l^2/\mu$. Here, l is the fibre half-length, ρ is the fluid density, $\dot{\gamma}$ is the shear rate and μ is the viscosity of the fluid. In addition to providing a large contrast to the commonly studied spherical shape, the choice of fibres allows the use of slender-body theory to describe the flow induced by the fibre, facilitating a quasi-analytical treatment.

Much is known about the hydrodynamic lift on a spherical particle in simple shear flow at small, but non-zero, particle Reynolds number. This lift requires breaking the symmetry of the flow to allow cross-streamline motion. This is achieved by either a body force acting on the particle parallel to the flow direction or a nearby wall. Saffman[98] calculated the lift on a sphere in an unbounded shear flow induced by a body force parallel to the streamlines for the case in which the relative velocity due to the body force is much smaller than the imposed shear velocity, $\dot{\gamma}a$, where a is the sphere radius. McLaughlin[80] generalized this investigation to cover all ratios of the relative velocity and shear velocity. The nature of the analysis for the lift on a particle in the presence of a wall depends on the relative magnitude of the separation from the wall h^* and the Oseen length $L_0 = [\mu/(\rho\dot{\gamma})]^{1/2}$. McLaughlin[81] studied hydrodynamic lift on spheres

at separations comparable to or larger than the Oseen length. This outer analysis involves a singular perturbation analysis that includes a viscous dominated inner region spanning distances of $O(a)$ from the particle and an outer region at separations of $O(L_0)$ where inertial and viscous effects are comparable. However, when the particle is closer to the wall than the Oseen length, the inertial effects can be treated as a regular perturbation from the Stokes flow solution. This inner analysis was carried out by Cherukat & McLaughlin[25] to evaluate the lift force on spheres. The special case of this result, corresponding to no force along the streamlines, can be used in conjunction with appropriate Stokes flow resistance functions to evaluate the lift velocity of a neutrally buoyant particle. The lift velocity is expected to exhibit very different qualitative and quantitative behaviour due to non-sphericity. This will be especially pronounced in the inner analysis where the fibre geometry has close interaction with the wall. Thus, the focus of this study will be on fibres in the inner region, $h^* \ll L_0$, where a regular perturbation analysis in terms of Re is applicable.

The study of the lift on non-spherical particles is very limited compared to the literature available on the lift on spheres. One of the earliest treatments on non-spherical shapes was carried out by Harper & Chang[50] who calculated the lift force on three dimensional bodies in unbounded shear flow in the strong shear limit of Saffman[98]. Shin et al[102] studied the lift on a fibre due to a body-force induced relative velocity and a weak, unbounded shear flow. Numerical studies of the lift-induced trajectories of an elliptical particle have been carried out by Feng et al[42] in Couette and Poiseuille flows, considering both neutrally buoyant and sedimenting particles. Qi[92] has numerically studied the lift of rectangular particles. However, there is no analytical treatment of the lift on a force-free fibre. Neither is there any literature available for the hydrodynamic lift of a particle with high aspect ratio (fibre) as a function of the distance from the wall in the presence of a shear flow.

Hydrodynamic lift can play an important role in separating particles of different types and separating particles from fluid. A common method of separating particles in microchannels is to allow hydrodynamic lift to cause different types of particles to migrate to different positions in the channel. A bifurcation in the channel can then be used to harvest the desired particle type. While such separations have conventionally been based on particle size, Masaeli et al[79] have demonstrated experimentally that particle shape plays an important role. In cross-flow filtration, a suspension of particles flows through a channel with porous walls, while fluid filtrate is drawn out through the walls. A major advantage of cross-flow filtration is that the shearing motion helps to limit the formation of a filter cake of particles at the porous membrane surface. Belfort and Drew and co-investigators[37, 38, 13] have argued that hydrodynamic lift, in addition to hydrodynamic diffusion and Brownian diffusion, helps to limit the particle concentration at the membrane surface. Many targets for such separation processes have non-spherical prolate shapes, including biological particles such as bacteria and viruses as well as cellulose fibres of current interest in the production of biofuels. Thus understanding non-spherical particles' hydrodynamic behaviour will go a long way in improving their filtration in industrial and laboratory settings.

The order of magnitude of the lift velocity of a neutrally buoyant sphere in a shear flow near a wall at small Reynolds number can be understood in a simple way. The characteristic Stokes fluid velocity disturbance in the vicinity of a sphere is $\dot{\gamma}a$. However, any cross-stream motion of a particle in Stokes flow would violate Stokes flow reversibility. Thus, the lift velocity is the result of fluid inertia, which is quantified by the particle Reynolds number $Re_a = \rho\dot{\gamma}a^2/\mu$. The lift velocity of a sphere is thus proportional to $\dot{\gamma}aRe_a = \rho\dot{\gamma}^2a^3/\mu$.

One can estimate some properties of nonspherical particles in low Reynolds number

flows as those associated with an equivalent sphere. For example, a common means of estimating the drag on an object in Stokes flow is as the drag on a circumscribing sphere. However, we will see that the lift on a slender fibre at small but finite Reynolds number differs in order of magnitude from that of a circumscribing sphere and furthermore the dependence of lift on separation from the wall is qualitatively different for fibres and spheres. One important reason for this difference is the role that fibre rotation plays in the lift. A fibre rotates in a periodic motion through a Jeffery orbit[57] spending most of its time near the flow direction and a shorter time flipping through other orientations. Since the fluid velocity disturbance made when the fibre is nearly aligned with the flow direction is much smaller than while it is flipping, its lift behaviour does not resemble that of any equivalent sphere.

Since the lift velocity of a fibre depends on its orientation, a specification of the time dependent orientation of the fibre is required to predict its spatial migration. In Stokes flow, a fibre rotates periodically in time in one of a set of Jeffery orbits parameterized by the orbit constant C . At small but finite Reynolds numbers, Subramanian & Koch[110] showed that the fibre spirals gradually through orbits and eventually rotates in the $C = \infty$ orbit corresponding to orientations within the flow-gradient plane. This has been verified by lattice Boltzmann simulations carried out by Rosén et al[96]. A linear stability analysis of particle motion in the $C = \infty$ orbit for arbitrary aspect ratio at small Re by Einarsson et al[39, 40] confirms the predicted slender fibre dynamics. The prediction by Subramanian & Koch[110] of migration across orbits has been extended to finite aspect ratio spheroids by Einarsson et al[40] and Dabade et al[31], thereby validating the original result. Thus, we will consider the time-averaged lift that occurs when the fibre has been in the shear flow long enough to reach the $C = \infty$ orbit.

The lift velocity of a fibre that does not make contact with the wall but is within

the viscous dominated region, i.e., $l < h^* \ll L_0$, can be determined using a regular perturbation analysis for $\text{Re} \ll 1$. In carrying out this analysis we will use the generalised reciprocal theorem to avoid the expensive evaluation of the order Reynolds flow field. This enables the $O(\text{Re})$ fibre velocity to be related to a volume integral involving the Stokes fluid velocity field and a comparison field driven by a fibre with a unit force acting perpendicular to the wall. The Stokes flow field consists of the imposed shear flow and a disturbance flow created by the fibre and its hydrodynamic interaction with the wall. The disturbance velocity field due to the particle is represented by a line of Stokeslets distributed along the particle axis. The force distribution on the particle is evaluated by solving the integral equations of the slender-body theory, developed by Batchelor[8], under the simplifying assumption of high aspect ratio. The hydrodynamic interaction of the fibre with the wall is included by using, for each Stokeslet distributed along the fibre, a set of image singularities which Blake & Chwang[14] demonstrated will satisfy the no-slip boundary condition. The high aspect ratio allows expansion in terms of $\epsilon = \frac{1}{\ln 2\kappa}$, which is the small parameter, with $\kappa = l/a$ being the aspect ratio. We retain terms of $O(\epsilon)$ and $O(\epsilon^2)$ in this study.

While a sphere makes contact with a wall at only one separation $h^* = a$ and has zero lift velocity owing to lubrication forces at this separation, a fibre can contact the wall for $a < h^* < l$ and we will see that its lift velocity is non-zero in this range. As first observed experimentally by Stover & Cohen[108], the edge of a fibre in Stokes flow with $a < h^* < l$ makes a solid-body contact with the wall. To span the range of behaviors that can arise due to fibre-wall friction, we will consider the two extreme cases of a frictionless contact and a no-slip sticking contact. In both cases, the resulting contact force pushes the fibre away from the wall and shifts its orientation toward smaller C , corresponding to migration away from the flow-gradient plane, in a dynamic motion the authors referred to as pole vaulting. We will show that the coupling of pole vaulting with

the fluid-inertia-induced orientational changes predicted by Subramanian & Koch[110] drives an evolution of the fibre trajectory that tends to move it away from the wall. This drift away from the wall is analytically evaluated and represents the lift velocity experienced by the fibre in this case.

Fibre-fibre interactions can lead to cross-channel migration of fibres in non-dilute suspensions[109]. However, for dilute suspensions this effect is expected to be weak and it is not considered in our study.

In the following sections we derive the lift velocity for a slender, neutrally buoyant, cylindrical fibre to $O(\text{Re})$. In §6.3, we use the generalized reciprocal theorem, slender-body theory and hydrodynamic wall images to determine the lift for a fibre not touching the wall, i.e $l < h^* \ll L_0$. In §6.4, the case of a fibre colliding with the wall is considered. Finally, in §6.5, we will summarise our findings, discuss the variation of the hydrodynamic lift velocity over all distances from the wall, and consider the way this result affects the sample application of cross-flow filtration.

6.3 Lift velocity of a fibre in the absence of wall contact

When a fibre in wall-bounded shear flow does not make contact with the wall, the asymmetric fluid stress distribution on it accounts for the hydrodynamic drift. This stress distribution can be obtained by solving the Navier-Stokes equation:

$$\nabla \cdot \boldsymbol{\sigma} = \text{Re} \left[\frac{\partial \mathbf{u}}{\partial t} + \mathbf{u} \cdot \nabla \mathbf{u} \right] \quad \nabla \cdot \mathbf{u} = 0 \quad (6.1)$$

where \mathbf{u} is the fluid velocity $\boldsymbol{\sigma} = -p\mathbf{I} + 2\mathbf{e}$ is the stress, p is the pressure, and $\mathbf{e} = \frac{1}{2} [\nabla \mathbf{u} + \nabla \mathbf{u}^\top]$ is the strain rate. Here, lengths, velocities and stresses are non-dimensionalized by $l, \dot{\gamma}l$, and $\mu\dot{\gamma}$ respectively. The dimensional variables will be ex-

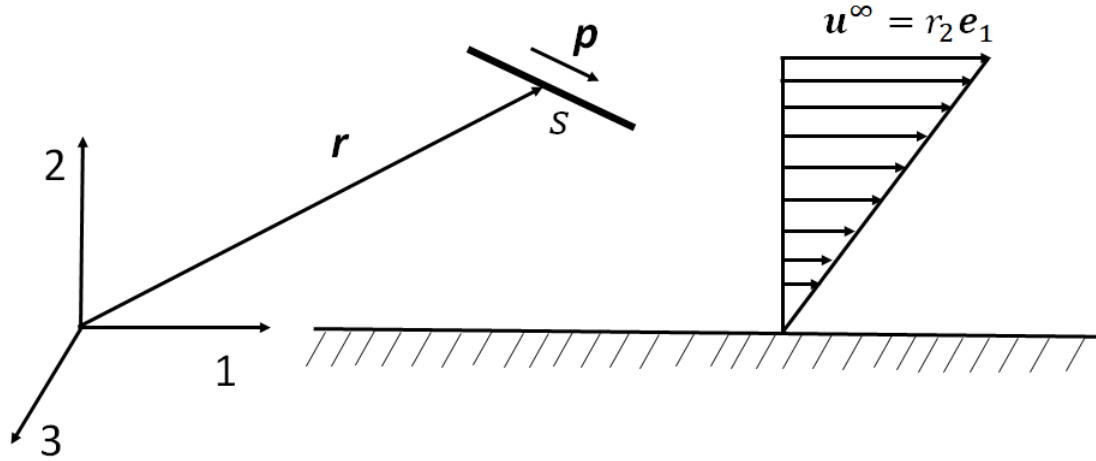


Figure 6.1: Sketch of fibre motion in the flow gradient plane of the imposed shear flow inner region close to a wall. '1' is along the direction of the flow, '2' is the velocity gradient direction which is normal to the wall and '3' is along the vorticity of the imposed flow. The fibre is oriented along the unit vector \mathbf{p} , with s being the coordinate along the fibre.

pressed with * and their non-dimensionalised counterparts without. With reference to our chosen Cartesian coordinate system, with position vector \mathbf{r} describing any point in the domain, the imposed shear flow is $\mathbf{u}^\infty = r_2 \mathbf{e}_1$. Here r_2 is the distance from the wall, r_1 a coordinate in the flow direction, \mathbf{e}_1 is a unit vector in the 1-direction, and r_3 the coordinate in the vorticity direction of the imposed flow. This coordinate system is illustrated in figure 6.1. As illustrated s is the coordinate along the axis of the fibre. If \mathbf{p} is the unit vector along the axis of the fibre with centre at \mathbf{r}^c then any point on the fibre, \mathbf{r}^f , is given as $\mathbf{r}^f = \mathbf{r}^c + \mathbf{p} s$.

The fibre experiences no net force $\mathbf{F} = \int dA \mathbf{n} \cdot \boldsymbol{\sigma} = 0$ and no net torque $\mathbf{L} = \int dA \mathbf{r} \times (\mathbf{n} \cdot \boldsymbol{\sigma}) = 0$, with \mathbf{n} being the outward normal from the area A into the fluid volume V , and the fluid velocity is zero on the wall. Stokes flow reversibility implies that a fibre should not experience any net drift perpendicular to the wall at zero Reynolds number. Consistent with this expectation Yang & Lean[123] computed a time oscillatory fibre translation in the 2-direction with no net drift as the fibres rotated in a periodic

motion that approximated Jeffery orbits[57]. A net drift away from the wall is expected at finite Re along with the persistence of this oscillatory behaviour.

To obtain the lift velocity of the fibre at small Reynolds number in the case where the fibre lies within the viscous dominated inner region near the wall, $h^* \ll L_0$, we can expand the fluid velocity, pressure and fibre velocity in regular perturbation expansions in the small parameter Re of the form $\mathbf{u} = \mathbf{u}^0 + Re \mathbf{u}^1$, $p = p^0 + Re p^1$, and $\mathbf{v} = \mathbf{v}^0 + Re \mathbf{v}^1$, respectively. The lift velocity can then be obtained by averaging $Re \mathbf{v}^1$ over the Jeffery period of rotation of the fibre. The derivation of the perturbed fluid velocity \mathbf{u}^1 would be difficult. However, we can use a generalized reciprocal theorem to express the fibre velocity \mathbf{v}^1 in terms of a volume integral involving the Stokes flow field \mathbf{u}^0 for the shear flow problem and a comparison flow field \mathbf{u}' driven by a fibre translating in the 2-direction. In the following discussion, we first present the generalized reciprocal theorem. Next the Stokes flow field and comparison field is expressed using slender-body theory and hydrodynamic images with the wall. After that we discuss the averaging of the lift velocity over the Jeffery period of rotation to obtain a time-averaged result. To complete the analysis we will evaluate the finite Re perturbations to the Jeffery orbit. This and other details of the time-averaged lift velocity calculation will be discussed in depth.

The generalized reciprocal theorem for a problem with weak fluid inertia[75] can be obtained by considering the volume integral

$$\int \nabla \cdot [\boldsymbol{\sigma}^1 \cdot \mathbf{u}' - \boldsymbol{\sigma}' \cdot \mathbf{u}^1] dV \quad (6.2)$$

where \mathbf{u}' and $\boldsymbol{\sigma}'$ are the fluid velocity and stress field for a Stokes flow comparison problem that satisfies

$$\nabla \cdot \boldsymbol{\sigma}' = 0$$

and

$$\nabla \cdot \mathbf{u}' = 0$$

along with boundary conditions $\mathbf{n} \cdot \boldsymbol{\sigma}' = \frac{1}{A_f} \mathbf{e}_2$ on the fibre and $\mathbf{u}' = \mathbf{0}$ on the walls and at large distances from the fibre. Here A_f is the surface area of the fibre.

Using the divergence theorem, one can obtain

$$\begin{aligned} \int \nabla \cdot [\boldsymbol{\sigma}^1 \cdot \mathbf{u}' - \boldsymbol{\sigma}' \cdot \mathbf{u}^1] dV &= \int_{\text{fibre}} dA \mathbf{n} \cdot [\boldsymbol{\sigma}' \cdot \mathbf{u}^1 - \boldsymbol{\sigma}^1 \cdot \mathbf{u}'] + \int_{\text{wall}} dA \mathbf{n} \cdot [\boldsymbol{\sigma}' \cdot \mathbf{u}^1 - \boldsymbol{\sigma}^1 \cdot \mathbf{u}'] \\ &+ \int_{\infty} dA \mathbf{n} \cdot [\boldsymbol{\sigma}' \cdot \mathbf{u}^1 - \boldsymbol{\sigma}^1 \cdot \mathbf{u}'] \end{aligned} \quad (6.3)$$

The no-slip boundary condition implies that the integral on the wall vanishes. The fluid velocity disturbance due to the fibre decays as $\frac{1}{r^2}$ in both the shear and comparison problem so the integral on the bounding surface vanishes as its distance goes to infinity. Finally, the rigid-body motion, no-force and no-torque conditions on the fibre in shear flow along with the specified force density on the fibre ($\int dA \mathbf{n} \cdot \boldsymbol{\sigma}' = \mathbf{e}_2$) in the comparison problem simplify the surface integral on the fibre to yield

$$\int \nabla \cdot [\boldsymbol{\sigma}^1 \cdot \mathbf{u}' - \boldsymbol{\sigma}' \cdot \mathbf{u}^1] dV = \mathbf{v}^1 \cdot \mathbf{e}_2 \quad (6.4)$$

The equations of motion for the shear flow and comparison problem yield

$$\int \nabla \cdot [\boldsymbol{\sigma}^1 \cdot \mathbf{u}' - \boldsymbol{\sigma}' \cdot \mathbf{u}^1] dV = \text{Re} \int \left[\frac{\partial \mathbf{u}^0}{\partial t} + \mathbf{u}^0 \cdot \nabla \mathbf{u}^0 \right] \cdot \mathbf{u}' dV \quad (6.5)$$

Combining (6.4) and (6.5), we obtain an expression for the inertia-induced translational velocity of the fibre perpendicular to the wall in terms of the Stokes flow shear and comparison fluid velocity fields

$$\mathbf{v}^1 \cdot \mathbf{e}_2 = \text{Re} \int \left[\frac{\partial \mathbf{u}^0}{\partial t} + \mathbf{u}^0 \cdot \nabla \mathbf{u}^0 \right] \cdot \mathbf{u}' dV \quad (6.6)$$

The Stokes flow field \mathbf{u}^0 consists of the imposed flow (\mathbf{u}^∞) and the disturbance field (\mathbf{u}^D), created by the presence of the fibre and the no-slip wall. This disturbance velocity

field can be captured by a collection of singularities along with the driving force behind it. The driving force experienced by the fibre in quiescent flow is qualitatively and quantitatively different from when it is placed in a shear flow. However, the system of singularities remains the same in both cases.

A thin fibre in low Re flow can effectively be replaced by a collection of Stokeslets, the fundamental singularities in a Stokes flow. A Stokeslet near a no-slip wall was studied by Blake & Chwang[14]. They found that a no-slip wall at $(r_1, r_2 = 0, r_3)$, in the presence of a Stokeslet placed at \mathbf{r}^f , can be replaced by another Stokeslet as well as a force dipole and a potential dipole placed at $\mathbf{r}^{im} = (r_1^f, -r_2^f, r_3^f)$. These singularities are mathematically represented by a Green's function. The overall non-dimensional Green's function of the fibre and no-slip wall system causing disturbance to the fluid velocity at \mathbf{r} is given by,

$$\mathbf{G}(\mathbf{r}, s) = \mathbf{G}^S(\bar{\mathbf{r}}) - \mathbf{G}^S(\bar{\mathbf{r}}^{im}) - 2(r_2^f)\mathbf{G}^{FD}(\bar{\mathbf{r}}^{im}) + 2(r_2^f)^2\mathbf{G}^{PD}(\bar{\mathbf{r}}^{im}) \quad (6.7)$$

Here, $\bar{\mathbf{r}} = \mathbf{r} - \mathbf{r}^f$ and $\bar{\mathbf{r}}^{im} = \mathbf{r}^{im} - \mathbf{r}^f$. \mathbf{G}^S is the Stokeslet, \mathbf{G}^{FD} is the force dipole. and \mathbf{G}^{PD} is the potential dipole. The individual functions, non-dimensionalised by μ , are given as,

$$G_{ij}^S(\mathbf{r}) = \frac{1}{8\pi r} \left[\delta_{ij} + \frac{r_i r_j}{r^2} \right] \quad (6.8)$$

$$G_{ij}^{FD}(\mathbf{r}) = \frac{1}{8\pi} \left[r_2 G_{ij}^{PD}(\mathbf{r}) \pm \frac{\delta_{j2} r_i - \delta_{i2} r_j}{r^3} \right] \quad (6.9)$$

$$G_{ij}^{PD}(\mathbf{r}) = \pm \frac{1}{8\pi r^3} \left[\delta_{ij} - 3 \frac{r_i r_j}{r^2} \right] \quad (6.10)$$

In equations (6.9) and (6.10) there is a plus sign for $j = 1$ and 3 and a minus sign for $j = 2$. Thus it is possible to obtain \mathbf{u}^D at any fluid location \mathbf{r} through an integral in s , spanning the whole length of the fibre as,

$$u_i^D(\mathbf{r}) = \int_{-1}^1 ds f_j(s) G_{ji}(\mathbf{r}, s) \quad (6.11)$$

where $\mathbf{f}(s)$ is the force distribution on the fibre.

To evaluate \mathbf{u}^D the force per unit length $\mathbf{f}(s)$ needs to be determined. From slender-body theory[8] the governing equation for $\mathbf{f}(s)$ is given as,

$$\begin{aligned} v_i^0 + \epsilon_{ijk} \Omega_j p_k s &= w_i(\mathbf{r}^c + \mathbf{p} s) + \frac{f_j}{4\pi} [\delta_{ij} + p_i p_j] [\ln 2\kappa + \ln \left[\frac{[1 - s^2]^{\frac{1}{2}}}{a(s)} \right]] \\ &+ \frac{f_j}{8\pi} [\delta_{ij} - 3p_i p_j] + \frac{f_j}{8\pi} [\delta_{ij} + p_i p_j] \int_{-1}^1 \frac{f_j(s') - f_j(s)}{|s - s'|} ds' \end{aligned} \quad (6.12)$$

where \mathbf{v}^0 and $\mathbf{\Omega}$ are the fibre centre of mass translational and rotational velocities at zero Re , $a(s)$ is the radius of the fibre at any given location on the fibre normalized with the characteristic radius. $a(s) = 1$ for a cylindrical fibre. $\kappa = \frac{l}{a}$ is the aspect ratio. \mathbf{w} is the far field velocity consisting of the imposed shear flow and image velocity. In solving equation (6.12) we assume the fibre has a large aspect ratio and expand in terms of the small parameter $\epsilon = \frac{1}{\ln 2\kappa}$. This leads to a perturbation in ϵ for \mathbf{f} as well as \mathbf{v}^0 , \mathbf{w} , \mathbf{u}^D and $\dot{\mathbf{p}}$. These can be expressed as,

$$\begin{aligned} \mathbf{f} &= \epsilon \mathbf{f}_1 + \epsilon^2 \mathbf{f}_2 + \dots \\ \dot{\mathbf{p}} &= \dot{\mathbf{p}}_0 + \epsilon \dot{\mathbf{p}}_1 + \dots \\ \mathbf{v}^0 &= \mathbf{v}_0^0 + \epsilon \mathbf{v}_1^0 + \dots \\ \mathbf{w} &= \mathbf{w}_0 + \epsilon \mathbf{w}_1 + \dots \\ \mathbf{u}^D &= \epsilon \mathbf{u}_1^D + \epsilon^2 \mathbf{u}_2^D + \dots \end{aligned} \quad (6.13)$$

The subscripts here denote the order of the term with respect to the expansion in ϵ . In this study we compute the lift velocity to $O(\epsilon^2)$ by retaining the terms indicated in equation (6.13) for the force per unit length, fibre rotation and translation rate, far field velocity and fluid velocity disturbance.

To obtain \mathbf{u}_1^D , the leading order disturbance velocity field in the ϵ expansion, we

evaluate \mathbf{f}_1 . The force distribution on the fibre at $O(\epsilon)$ is given as,

$$\frac{1}{4\pi} f_{1,i} [\delta_{ij} + p_i p_j] = v_i^0 + \epsilon_{ijk} \Omega_j p_k s - w_{0,i}(\mathbf{r}^c + \mathbf{p} s) \quad (6.14)$$

At leading order in ϵ , the far field velocity \mathbf{w}_0 is the imposed shear flow \mathbf{u}^∞ . In a simple shear flow the dynamics of the fibre motion at finite Re was studied by Subramanian & Koch[110]. They showed that inertia forces the fibre towards motion in the flow-gradient plane. This constraint simplifies equation (6.14) to,

$$\mathbf{f}_1 = 4\pi \mathbf{p} s \cos \phi \sin \phi \quad (6.15)$$

Here ϕ is the dihedral angle between the flow-vorticity and the fibre-vorticity planes.

To obtain \mathbf{u}_2^D we require the force distribution at $O(\epsilon^2)$ which is,

$$f_{2,j} = \pi p_i \sin 2\phi [2s \ln[1 - s^2] - 3s] - 4\pi [\delta_{ij} - \frac{p_i p_j}{2}] w_{1,i}(\mathbf{r}^c + \mathbf{p} s) \quad (6.16)$$

To evaluate \mathbf{w}_1 we use the disturbance velocity result from equation (6.11) and evaluate only the image component. This is given as,

$$\mathbf{w}_1(\mathbf{r}) = \int_{-1}^1 ds f_{1,j}(s) G_{ji}^I(\mathbf{r}, s) \quad (6.17)$$

Here $G_{ji}^I(\mathbf{r}, s)$ is due to the image system that captures wall reflection. This is given as,

$$\mathbf{G}^I(\mathbf{r}, s) = -\mathbf{G}^S(\bar{\mathbf{r}}^{im}) - 2(r_2^f) \mathbf{G}^{FD}(\bar{\mathbf{r}}^{im}) + 2(r_2^f)^2 \mathbf{G}^{PD}(\bar{\mathbf{r}}^{im}) \quad (6.18)$$

With a complete description of $\mathbf{G}(\mathbf{r}, s)$ and $\mathbf{f}(s)$ known at the first two orders in ϵ , equation (6.11) can be evaluated to find \mathbf{u}^D and by extension \mathbf{u}^0 . To evaluate equation (6.6) and obtain lift velocity information on \mathbf{u}' is also needed. In the quiescent comparison flow the disturbance velocity field is calculated using equation (6.11) with a specified force distribution $\int \mathbf{f}'(s) ds = \int d\mathbf{A} \mathbf{n} \cdot \boldsymbol{\sigma}' = \mathbf{e}_2$.

The fibre rotates in a shear flow and samples all possible orientations in the flow-gradient plane. Orientation plays an important role in determining $\mathbf{f}(s)$, as evident by

the strong dependence on ϕ in equation (6.15) and (6.16). The temporal evolution of fibres in Stokes was studied by Yang & Leal[123] who found that, at zero Re, they undergo periodic flipping motion. This periodic motion is expected to persist at small, but finite, Re. At zero Re Jeffery[57] studied the periodic orbits of ellipsoidal particles in an unbounded simple shear flow. Jeffery's calculation properly captures the flipping motion of fibres near a wall, as shown in experimental studies carried out by Stover & Cohen[108] and Moses et al[82]. In this study we will assume that these periodic orbits (commonly referred to as Jeffery Orbits) describe the temporal dynamics of the fibre at finite Re near a wall.

During the flipping motion of the fibre near a wall its centre of mass executes oscillatory motion in the 2-direction in Stokes flow. The fibre translates away from and towards the wall in the compressional and extensional quadrants respectively Yang & Leal[123] The symmetry of this oscillatory motion is broken by fluid inertia leading to a net drift away from the wall. The symmetry breaking occurs in two ways. First, the inertial correction to the fluid velocity induces a net positive velocity in the 2-direction. Second, inertial effects change the rotation rate of the fibre causing it to spend more time in the compressional quadrant than the extensional quadrant, so that the viscous forces lead to a net drift away from the wall.

The finite inertia correction to the evolution of the orientation dynamics of a fibre was studied by Subramanian & Koch[110]. For dynamics in the flow-gradient plane this is given as,

$$\dot{\phi} = \frac{-1}{\kappa^2 + 1} [\kappa^2 \sin^2 \phi + \cos^2 \phi] - \frac{\text{Re}}{\ln \kappa} \sin \phi \cos \phi \left[\frac{1}{6} \sin^2 \phi - \frac{1}{15} \cos^2 \phi \right] \quad (6.19)$$

Equation (6.19) includes a correction of a typographical error in the original paper that was first noted in Shin et al[102].

The time period T for one revolution in a Jeffery orbit is given as,

$$T = 2\pi \left[\kappa + \frac{1}{\kappa} \right] \quad (6.20)$$

The finite inertia correction to the time period is $O(\text{Re}^{3/2})$ for fibres much smaller than the Oseen length[78]. Thus, it does not influence the lift velocity at leading order in Re .

Due to the rapid variation of drift over a Jeffery orbit it is of interest to obtain a time-averaged result $\int dt \mathbf{v} \cdot \mathbf{e}_2 / T$. For ease of analysis it can be transformed into ϕ coordinates using equation (6.19). This is given as,

$$v_l = \frac{\text{Re}}{T} \int_0^{2\pi} \pi d\phi \int dV \left[\frac{\partial \mathbf{u}^0}{\partial t} + \mathbf{u}^0 \cdot \nabla \mathbf{u}^0 \right] \cdot \mathbf{u}' \frac{1}{\dot{\phi}^0} + \frac{\text{Re}}{T} \int_0^{2\pi} d\phi \mathbf{v}^0 \cdot \mathbf{e}_2 \left(\frac{-\dot{\phi}^1}{(\dot{\phi}^0)^2} \right) \quad (6.21)$$

The orientation evolution has been expanded based on a regular perturbation in Re that is given as, $\dot{\phi} = \dot{\phi}^0 + \text{Re} \dot{\phi}^1 + \dots$ and the second term in equation (6.21) was obtained through a binomial expansion. The first term on the RHS was obtained using equation (6.6). A regular perturbation in ϵ similar to those expressed in equation (6.13) can be extended to this time-averaged lift velocity and is given as,

$$v_l = \epsilon v_{l1} + \epsilon^2 v_{l2} + \dots \quad (6.22)$$

It is evident that $v_{l0} = 0$ due to the nature of the force distribution. We will evaluate the first two non-zero terms v_{l1} and v_{l2} in this study.

Owing to the quasi-steady nature of Stokes flow the partial time derivative of the fluid velocity appearing in (6.21) can be related to the time variation of the fibre orientation and centre of mass position,

$$\frac{\partial \mathbf{u}^0}{\partial t} = \frac{\partial \mathbf{u}^0}{\partial \phi} \dot{\phi}^0 + \frac{\partial \mathbf{r}^c}{\partial t} \cdot \nabla \mathbf{u}^0 \quad (6.23)$$

While computing the $O(\epsilon)$ lift velocity, the time dependence of \mathbf{r}^c can be removed by adopting a reference frame translating with the $O(1)$ particle translational velocity and

$\partial\phi/\partial t$ can be evaluated using the Jeffery orientation evolution in equation (6.19). At $O(\epsilon^2)$ there are additional contributions to the time derivatives of the fibre orientation and position caused by the $O(\epsilon)$ wall reflection fluid velocity disturbance. These are given as,

$$\begin{aligned}\dot{p}_{1,i} &= \frac{3}{2} \int_{-1}^1 ds [\delta_{ij} - p_{0,i}p_{0,j}]w_{1,j}(\mathbf{r}^c + \mathbf{p} s)s \\ \mathbf{v}_1^0 &= \frac{1}{2} \int_{-1}^1 ds \mathbf{w}_1(\mathbf{r}^c + \mathbf{p} s)\end{aligned}\quad (6.24)$$

\mathbf{w}_1 is given in equation (6.17).

$\mathbf{v}_0^0 \cdot \mathbf{e}_2 = 0$ so the non-zero contribution to the second term on the RHS of equation (6.21) involves \mathbf{v}_1^0 , which is $O(\epsilon)$. The finite Re correction to the orientation dynamics is also $O(\epsilon)$. Thus, the leading contribution to lift velocity due to finite Re perturbations of the rotational dynamics appears in v_{l2} .

The lift velocity calculation involves nested integrals spanning a large domain. The spatial co-ordinate r_i spans $-\infty$ to ∞ when $i = 1, 3$ and 0 to ∞ for $i = 2$, thus capturing all of the fluid volume. Based on symmetry, the angular integration in ϕ from 0 to 2π can be related to 4 times the integral from 0 to $\pi/2$. The disturbance velocity field driving the lift velocity involves an integral over s , thus capturing the net effect of the singularities of the fibre and its images. The higher order (in ϵ) force distribution as well as unsteadiness (see equation (6.24)) depends on the image velocity, which in turn requires integration over s for the image singularities. All of these nested integrals are numerically evaluated using an adaptive quadrature scheme. For this purpose a combination of the 'integral' and 'integral2' routines available in MATLAB is used.

The dimensional lift velocity (v_l^*) of a fibre will be proportional to the characteristic shear velocity $\dot{\gamma}l$ based on the chosen non-dimensionalization. However it is modified by three factors: fluid inertia, flipping motion in a Jeffery orbit and the thinness of the

fibre. In the absence of fluid inertia, i.e Stokes flow, there is no net migration. At small but finite Reynolds number, the lift velocity is proportional to Re . In a Jeffery orbit the time period is $O(\kappa)$ whereas the flipping motion, during which significant migration away from the wall occurs, takes place over $O(1)$ time. Thus a factor of κ^{-1} appears in the time-averaged lift velocity. Finally, the disturbance velocity field, that drives the migration away from the wall, is shaped by the geometry of the fibre. For a high aspect ratio fibre this is characterised by ϵ . Thus, the scaling of the lift velocity can be given as $\rho\dot{\gamma}^2 l^2 a / (\mu \ln \left[\frac{2l}{a} \right])$ when not making contact with the wall.

In contrast to a fibre, the hydrodynamic lift on a sphere, while also being a finite Re effect, has none of the complexities associated with orientation and aspect ratio. Thus, the dimensional lift velocity of a sphere scales as, $\rho\dot{\gamma}^2 a^3 / \mu$, where a is the characteristic length of the sphere which is its radius. Figure 6.2 gives the variation of the lift velocity of a sphere with distance from the wall in the inner region. The lift velocity is scaled as $\rho\dot{\gamma}^2 a^3 / \mu$ in this plot. This result is obtained using the lift force derived by Cherukat & McLaughlin[25] for the special case of no force along the streamline, along with the appropriate Stokes resistance function[18, 29]. The lift force does not go to zero as the sphere approaches the wall but the Stokes resistance function, due to lubrication effects, diverges leading to a decay of the lift velocity of a sphere to zero. Conversely the resistance decays away from the wall and so the lift velocity approaches a constant at separations that are large but still lie within the inner region.

Figure 6.3 presents the computed lift velocity for the fibre at $O(\epsilon Re)$. The lift velocity presented is scaled as $\rho\dot{\gamma}^2 l^2 a / (\mu \ln \left[\frac{2l}{a} \right])$ and given as a function of the non-dimensional distance of the centre of the fibre from the wall. When the fibre approaches the wall its lift velocity, unlike a sphere, does not tend to zero. This can be attributed to the finite Stokes resistance for the sharp edges of the fibre as pointed out by Harlen et

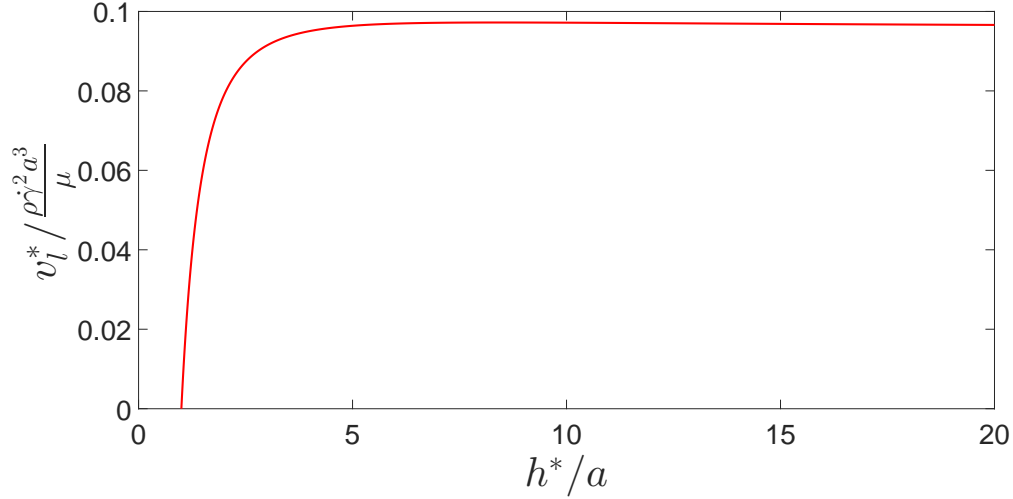


Figure 6.2: Lift velocity for a sphere as a function of distance from the wall in the inner region. h^* represents the dimensional distance of the sphere of radius a from the wall. The lift velocity is obtained using the lift force calculation of Cherukat & McLaughlin[25] in conjunction with Stokes resistance functions [18, 29]

al[49]. These sharp ends can make contact with the wall in finite time. Additionally, the fibre end only contacts the wall at one instant in time during the fibre's periodic motion when $h^* = l$. As the distance from the wall increases the Stokes resistance experienced decreases and the lift velocity increases monotonically. At large distances from the wall, but still in the inner region, the lift velocity asymptotes at leading order to a value of $0.0303\rho\dot{\gamma}^2 l^2 a / (\mu \ln \left[\frac{2l}{a} \right])$. Qualitatively, at $O(\epsilon)$, the lift velocity captures the breaking of the stress symmetry that leads to a net migration due to a simple interaction of the imposed shear flow with a thin geometry.

Figure 6.4 shows the $O(\text{Re})$ fibre lift velocity based on the first two terms of the slender body theory expansion at various κ plotted as a function of the non-dimensional distance from the wall. Despite scaling the lift velocity with the leading order scaling of $\rho\dot{\gamma}^2 l^2 a / (\mu \ln \left[\frac{2l}{a} \right])$, there remains a significant dependence on the aspect ratio with the lift velocity reaching significantly higher values at smaller aspect ratio. Even at an

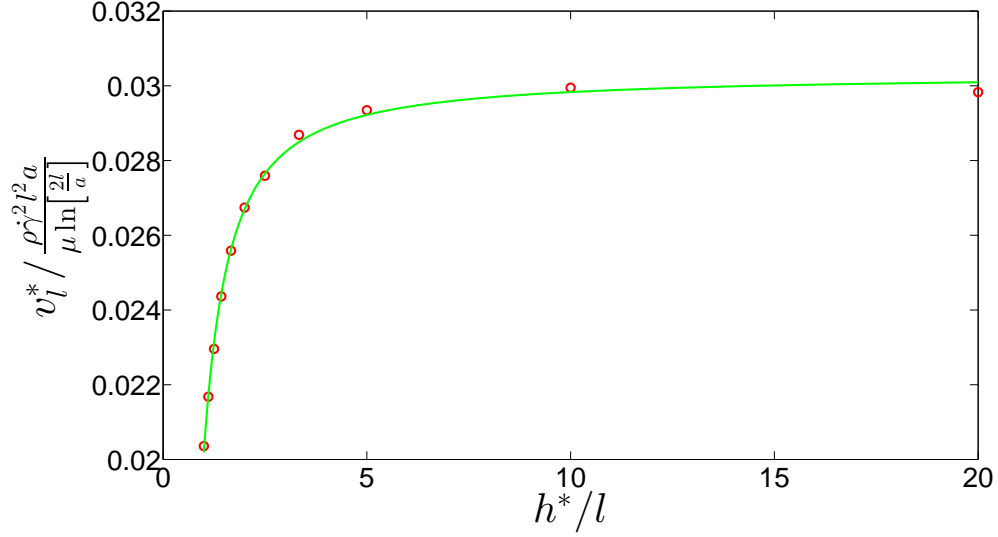


Figure 6.3: Variation of the $O(\epsilon\text{Re})$ fibre lift velocity as a function of distance from the wall. Circles show the evaluated data and the line shows the fit given by $v_{l1} = -0.0057/h^2 - 0.0044/h + 0.0303$.

aspect ratio as high as 10^4 , the asymptotic value of the total lift velocity is about 50% larger than the $O(\epsilon)$ lift velocity. This indicates that a significant contribution to the lift velocity comes from the $O(\epsilon^2)$ term. This higher order term includes a number of qualitative features not present at $O(\epsilon)$ including the influence of the wall reflection, the oscillatory translation of the fibre perpendicular to the wall, finite Re perturbations of the periodic motion of the fibre, and the effects of the precise variation of the fibre thickness as captured by the $\ln[(1 - s^2)^{1/2}/a(s)]$ term in equation (6.12). At $O(\epsilon^3)$ and higher orders no qualitatively new mechanisms come into play. Quantitatively the first two terms in slender body theory are expected to dominate the lift velocity calculation. To test this we calculate, using the analysis of Batchelor[8], the stresslet of a slender body and find that even for the lowest chosen κ , of 25, the $O(\epsilon^3)$ term only changes the result by 6%. We expect similar errors for the lift velocity when two terms of the slender body theory are retained and κ of 25 is considered.

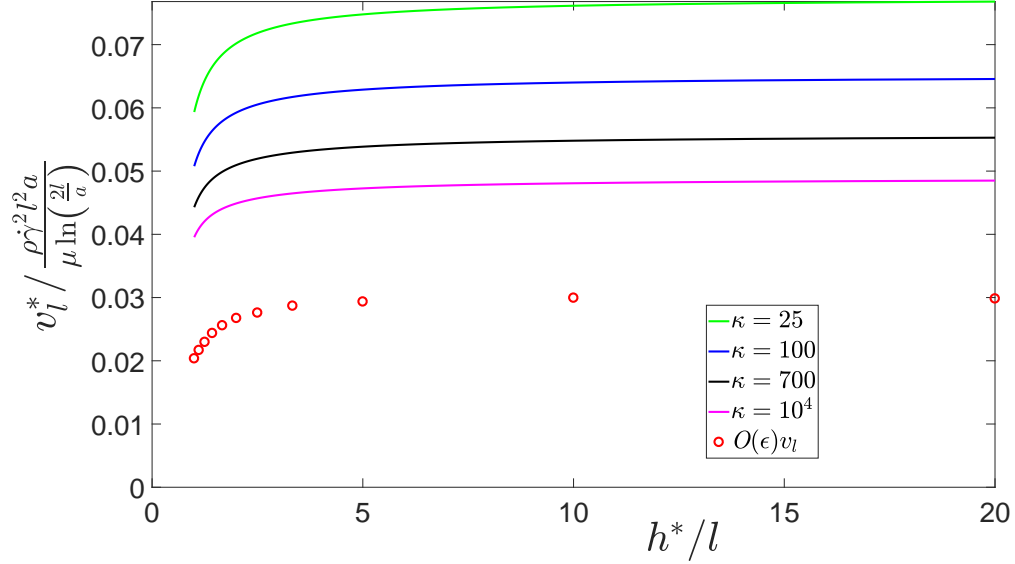


Figure 6.4: Variation of the $O(\text{Re})$ lift velocity calculated based on the first two terms of the slender body theory expansion for a fibre and expressed as a function of distance from the wall at various aspect ratios. The aspect ratio of the curves going from highest to lowest asymptote values are 25, 100, 700, and 10^4 . Circles represent the lift velocity at $O(\epsilon)$.

6.4 Lift velocity of a fibre experiencing wall contacts

When $h < 1$ the dominant contribution to the lift velocity of a fibre in wall-bounded shear flow of small but finite inertia comes from the contact force due to solid-body interactions coupled with inertial rotation. For $h < 1$ the orbit in the flow-gradient plane preferred based on inertial rotation is no longer accessible. Thus, the inertial torque driving the fibre toward the flow-gradient plane and the wall contact force compete to influence the fibre orientation. In this section, we will analyse the coupled action of these two mechanism. First we will track the trajectory of the fibre for $h < 1$. Then we will develop an analytical model for the lift velocity in the $h < 1$ regime by assuming the fibre follows a quasi-steady Jeffery orbit that just grazes the wall. Wall interactions are shaped by friction as well as normal forces. Thus, we consider the two limiting case of a frictionless contact and a no-slip sticking solid-body contact. Our model for both

these cases are validated against numerically computed trajectories.

A fibre in a simple shear flow adjacent to a wall is pushed away from it by the wall contact force. In addition, any fibre with an orientation out of the flow-gradient plane is pushed further out of the plane. This effect was experimentally observed by Stover & Cohen[108] and they referred to it as pole vaulting. A number of studies [66, 56, 101, 83] have built on Stover and Cohen's work and analysed the trajectory of wall-bounded fibres in Stokes flow. At finite Re many studies have looked at dynamics of spheroids in an unbounded flow [61, 110, 39, 40, 31, 78], but none have considered the effects of wall contact. Hence, in this study, we will couple the displacement and orientation perturbation due to pole vaulting with the inertial orientation drift predicted by [110] to numerically compute the fibre trajectory. This fibre trajectory calculation does not include the direct effects of inertial translation discussed in §6.3. It will be shown a posteriori, through the analytical model of the wall contact lift velocity and its scaling, that inertial translation is weaker by a factor of the aspect ratio compared to motion driven by inertial rotation coupled with wall contact.

[110] showed that a fibre orientation at finite Re tends to move towards the flow-gradient plane. They showed this by first computing the finite Re correction to the equations governing the orientation of the fibre. \mathbf{p} can be fully described through θ , the polar angle between the fibre axis and the vorticity direction, and ϕ . These evolve in time as,

$$\dot{\theta}_I = \frac{\kappa^2 - 1}{\kappa^2 + 1} \sin \theta \cos \theta \sin \phi \cos \phi \left[1 + \frac{7\epsilon' \text{Re}}{30} \sin^2 \theta \sin \phi \cos \phi \right] \quad (6.25)$$

$$\dot{\phi}_I = \frac{-1}{\kappa^2 + 1} [\kappa^2 \sin^2 \phi + \cos^2 \phi] - \epsilon' \text{Re} \sin \theta \sin \phi \cos \phi \left[\frac{1}{6} \sin \theta \sin^2 \phi - \frac{1}{15} \sin \theta \cos^2 \phi \right] \quad (6.26)$$

The subscript I indicates that this rotation includes effects of fluid inertia and excludes

the influence of the wall. In contrast to equation (6.19), this result involves θ in addition to ϕ and is valid for all orientations. It should be noted that a slightly different definition of the small parameter was used in their study. It is given as $\epsilon' = \frac{1}{\ln \kappa}$. In these equations the $\sin \theta \cos \theta \sin \phi \cos \phi$ term is the original Jeffery result for θ evolution without inertia. The equivalent inertia-less component for ϕ is $-(\kappa^2 \sin^2 \phi + \cos^2 \phi)/(\kappa^2 + 1)$. The inclusion of the inertial correction to these Jeffery equations leads to $\theta \rightarrow \pi/2$. This corresponds to drift of the fibre motion towards the flow-gradient plane.

At zero Re each of the unique Jeffery orbits is associated with an orbit constant given as,

$$C = \frac{\tan \theta \left[\kappa^2 \sin^2 \phi + \cos^2 \phi \right]^{\frac{1}{2}}}{\kappa} \quad (6.27)$$

that is invariant during its evolution and ranges from 0 (vorticity axis) to ∞ (flow-gradient plane). Small, but finite, inertia acts to shift the fibre from a lower orbit constant to a higher one, eventually spiralling to $C = \infty$. On the other hand, pole vaulting shifts the fibre to a lower orbit constant [108]. Thus C acts as a useful metric to study the evolution of the fibre when $h < 1$.

The finite inertia correction to the Jeffery orbit was computed in an unbounded shear flow, but it can be used to describe the leading order rotation in the $0 < h < 1$ regime. The effects of the hydrodynamic wall reflections on the orientational drift are $O(\epsilon')$ smaller than the leading order result captured by (6.25) and (6.26). In addition, the fibre spends most of the time without direct contact with the wall so that the effects of wall contact and fluid inertia on orientational drift can be superimposed.

When $0 < h < 1$, the fibre can make solid-body contact with the wall during its flipping motion. A numerical study by Harlen et al[49] illustrates the idea of using a solid-body wall-fibre contact when the sharp edges of a high aspect ratio fibre contact

a surface (that of a falling ball in their study). Harlen et al[49] argued that wall contact can occur due to the sharp edge of a fibre reducing the lubrication resistance. Even for smooth edged fibres, it was argued that the driving force pushing the fibre toward the wall scales with the fibre length while the lubrication force scales with the much smaller radius, so that lubrication breaks down and wall contact is achieved.

During the short period when the fibre makes solid-body contact with the wall a constraint that the fibre end touches the wall is applicable, i.e., $r_2^{\text{end}} = 0$ with the position of the end of the fibre given as $\mathbf{r}^{\text{end}} = \mathbf{r}^c + \mathbf{p}$. During contact, equations (6.25) and (6.26) are no longer applicable and instead we derive expressions for the contact-influenced translation and rotation of the fibre in Stokes flow. The contact-induced translational \mathbf{v}_N^0 and rotational $\boldsymbol{\Omega}_N$ velocities of the fibre to leading order in ϵ' are given by,

$$\frac{1}{4\pi\epsilon'} f_{N,j} [\delta_{ij} + p_i p_j] = v_{N,i}^0 + \epsilon_{ijk} \Omega_{N,j} p_k s - w_i(s) \quad (6.28)$$

Here, \mathbf{w} , the far-field velocity, corresponds to only the imposed shear flow since the image disturbance velocity is higher order in ϵ' . The subscript N, in this section, denotes that the effect arises due to wall contact. The net hydrodynamic force of the fibre on the fluid due to the contact balances the contact force \mathbf{F}_N , so that

$$\int_{-1}^1 \mathbf{f}_N ds = \mathbf{F}_N \quad (6.29)$$

The torque balance is given as,

$$\int_{-1}^1 s \mathbf{p} \times \mathbf{f}_N ds = \mathbf{p} \times \mathbf{F}_N \quad (6.30)$$

Solving equation (6.28) in conjunction with equations (6.29) and (6.30) gives the contact-induced motion of the centre of the fibre as,

$$v_{N,i}^0 = \frac{F_{N,j}}{8\pi\epsilon'} [\delta_{ij} + p_i p_j] \quad (6.31)$$

The contact-induced change of the fibre's orientation vector is given as,

$$\dot{p}_{N,i} = \frac{3F_{N,j}}{8\pi\epsilon'} [\delta_{ij} - p_i p_j] \quad (6.32)$$

To calculate \mathbf{F}_N we use kinematic constraints on the end of the fibre making contact with the wall. To obtain this the full dynamics of the fibre is required. This is given as,

$$\begin{aligned}\mathbf{v}^0 &= \mathbf{v}_N^0 + h \mathbf{e}_1 \\ \dot{\theta} &= \dot{\theta}_N + \dot{\theta}_I \\ \dot{\phi} &= \dot{\phi}_N + \dot{\phi}_I\end{aligned}\tag{6.33}$$

The exact form of the kinematic constraints, and the contact forces, depend on the nature of the solid-body wall contact. In the absence of frictional forces $\dot{r}_2^{\text{end}} = 0$ and the contact force is given as $\mathbf{F}_N = F_N \mathbf{e}_2$. This is evaluated to be,

$$F_N = \frac{8\pi\epsilon' [-\dot{p}_{I,2}]}{[4 - 2p_2^2]}\tag{6.34}$$

The resulting evolution of fibre evolution during contact is given as,

$$\begin{aligned}v_2^0 &= \frac{F_N}{8\pi\epsilon'} [1 + p_2^2] \\ \dot{p}_2 &= \dot{p}_{I,2} + \frac{3F_N}{8\pi\epsilon'} [1 - p_2^2]\end{aligned}\tag{6.35}$$

In the case of a sticking contact $\dot{\mathbf{r}}^{\text{end}} = 0$ and all three components of \mathbf{F}_N are non-zero. This force is given as,

$$F_{N,i} = -8\pi\epsilon' \left[\frac{\dot{p}_{I,j}}{4} + \frac{h\delta_{j1}}{4} \right] (\delta_{ij} + p_i p_j)\tag{6.36}$$

The evolution of the fibre during contact is given as,

$$\begin{aligned}v_i^0 &= \frac{F_{N,j}}{8\pi\epsilon'} [\delta_{ij} + p_i p_j] + h\delta_{i1} \\ \dot{p}_i &= \dot{p}_{I,i} + 3 \frac{F_{N,j}}{8\pi\epsilon'} [\delta_{ij} - p_i p_j]\end{aligned}\tag{6.37}$$

The contact forces act only during a short interval of the Jeffery orbit but are responsible for the evolution of h and significantly influence the fibre angles. To track the trajectory of the fibre due to all of these effects we integrate equations (6.33) with results

supplied from equations (6.25), (6.26), (6.32), and the contact force. The choice of time steps is important in the trajectory evolution as both flipping and wall contact are very short lived phenomena. The short lived flipping can be expected from the Jeffery orbit component of equation (6.26) and evident from figure 6.5 showing evolution of h . Based on the zero inertia component of equation (6.26) flipping can be properly captured by choosing a time step of about $T/2\pi\kappa$. The wall contact is even shorter as it results from the small inertial perturbation of the fibre orbit between two successive wall contacts. An adaptive time stepping is used to capture the wall contact.

Wall contact occurs during a very small fraction of the orbital motion of the fibre, close to $\phi = -\pi/2$ and θ near its extrema of θ_m , but it is the sole pathway to increasing the height of the fibre. This is evident in figure 6.5 where h behaves like a step function with the transitions corresponding to solid-body contact with the wall. These jumps at wall contact are additive. Eventually a fibre starting at any $0 < h < 1$ ends up at $h = 1$. This can be observed in figure 6.6 which shows the evolution of h observed over a longer duration. The upward drift of the centre of mass of the fibre can be considered its lift velocity ($v_{l,N}$). To obtain this lift velocity we consider a quasi-steady orbit that, for the given value of h , just makes contact with the wall. In this configuration we will find the shift in the height of the centre of mass of a fibre and average it over the time period of the orbit to obtain the lift velocity. A model evolution based on this lift velocity $dh^{\text{model}}/dt = v_{l,N}(h^{\text{model}})$ agrees well with the full trajectory calculation, as evident from figure 6.6.

In the quasi-steady orbit model, we assume that the fibre makes contact with the wall at exactly $\phi = -\pi/2$ and $\theta = \theta_m$. We evaluate the shift in height of the fibre using the kinematic constraint. This will capture the total drift of the fibre from the wall as it evolves in a sequence of quasi-steady orbits while the fibre end continues to brush the

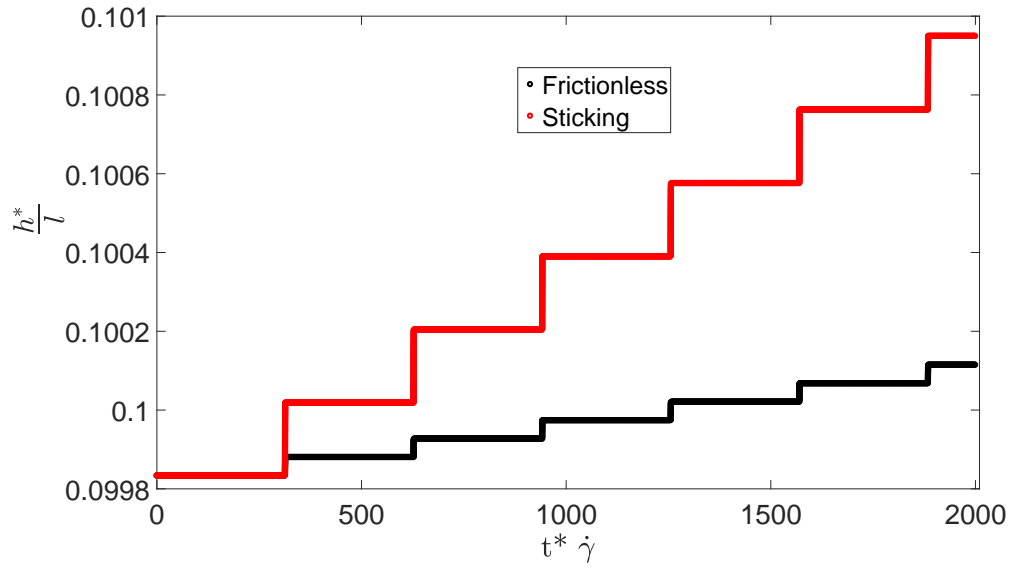


Figure 6.5: Trajectory of the fibre centre-of-mass for $\kappa = 100$ in a flow with $\text{Re}=10^{-3}$.

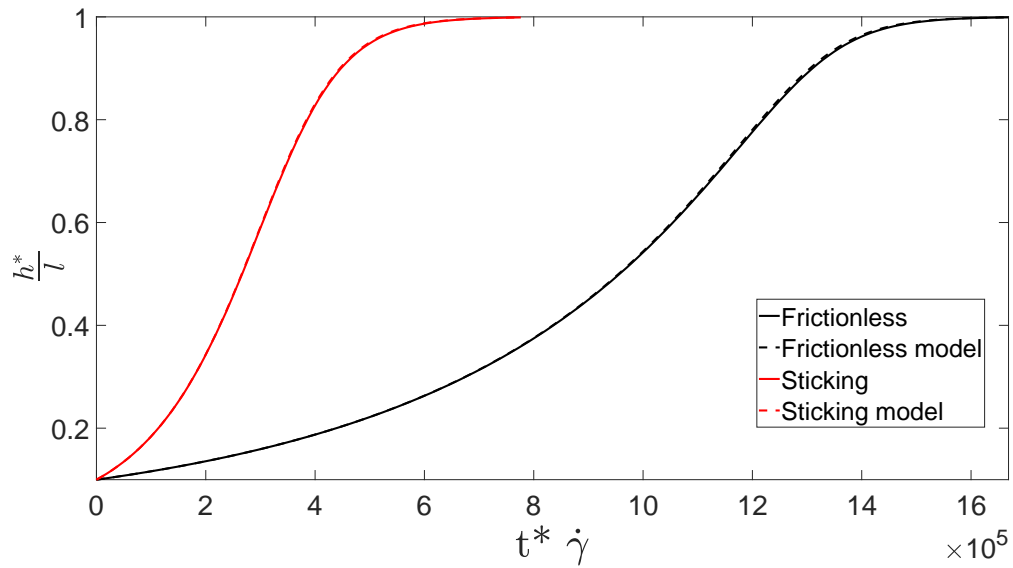


Figure 6.6: Trajectory of the fibre centre-of-mass for $\kappa = 100$ in a flow with $\text{Re}=10^{-3}$ shown over a long period of time. The rate at which the fibre moves away from the wall is faster for a sticking contact. The model evolution from equations (6.48) and (6.49) agrees well with the full simulation.

wall. The resulting evolution of the fibre centre of mass is,

$$\Delta h = -\cos \theta_m \Delta \theta \quad (6.38)$$

Here $\Delta \theta$ is the net change of θ during a Jeffery orbit. This includes effects of both the inertial drift $\Delta \theta_I$ and the wall contact $\Delta \theta_N$. The perturbation to the fibre motion due to wall contact is captured through $\Delta \theta_N$ evaluated at $\phi = -\pi/2$. For the case of frictionless contact this can be obtained from equation (6.35) as,

$$\frac{\Delta \theta_N}{\Delta h} = -\frac{3 \cos \theta_m}{1 + \sin^2 \theta_m} \quad (6.39)$$

For sticking contact, from equation (6.37), at $\phi = -\pi/2$ it can be shown that,

$$\Delta \theta_N = 0 \quad (6.40)$$

The inertial perturbation to the quasi-steady Jeffery orbit between two consecutive wall contacts is found based on the change in C between $\phi = -\pi/2$ and $\pi/2$. To obtain this, first we consider the temporal evolution of C that accounts for the effects of finite inertia. This is given as,

$$\dot{C}_I = \frac{\text{Re } C \epsilon'}{2} 2 \sin^2 \theta \sin^2 \phi \cos^2 \phi \left[\frac{1}{30} + \frac{\kappa^2}{\kappa^2 \sin^2 \phi + \cos^2 \phi} \left[\frac{\cos^2 \phi}{15} - \frac{\sin^2 \phi}{6} \right] \right] \quad (6.41)$$

Integrating over $\phi = -\pi/2$ to $\pi/2$, which corresponds to motion over half of a Jeffery period gives the change in orbit constant, due to inertial effects, to be,

$$\Delta C_I = \frac{\pi \text{Re } \kappa \epsilon' C}{30} \left[1 + \frac{2}{\kappa^2 C^2} - 2 \sqrt{\frac{1}{\kappa^2 C^2} + \frac{1}{\kappa^4 C^4}} \right] \quad (6.42)$$

For slender fibres, the term, κC term is large except in a very small portion of orientation space that corresponds to orbits close to the flow-vorticity plane. These orientations only predominate when h is close to zero. Thus, we assume $\kappa C \gg 1$ so that equation (6.42) reduces to,

$$\Delta C_I = \frac{\pi \text{Re } \kappa \epsilon' C}{30} \quad (6.43)$$

To relate this to a perturbation in θ we take the derivative of equation (6.27) at $\phi = -\pi/2$.

This gives,

$$\Delta\theta_I = \cos^2 \theta_m \Delta C_I \quad (6.44)$$

so that

$$\Delta\theta_I = \frac{\pi \text{Re } \kappa \epsilon' \sin \theta_m \cos \theta_m}{30} \quad (6.45)$$

We can now obtain the drift of the fibre by considering motion through a half Jeffrey orbit. For frictionless contact equation (6.38) along with inputs from equation (6.39) and (6.45) give:

$$\Delta h = -\cos \theta_m \left[\frac{\pi \text{Re } \kappa \epsilon' \sin \theta_m \cos \theta_m}{30} - \Delta h \frac{3 \cos \theta_m}{1 + \sin^2 \theta_m} \right] \quad (6.46)$$

Solving for Δh and dividing by the Jeffrey half period ($\pi\kappa$, see equation (6.20) for the time period) gives the lift

$$v_{l,N}(h) = \frac{\text{Re } \epsilon'}{30} \left[\frac{\sin \theta_m \cos^2 \theta_m [1 + \sin^2 \theta_m]}{4 - 2 \sin^2 \theta_m} \right] \quad (6.47)$$

At wall contact and by extension throughout the Jeffrey orbit, the height of the fibre is given as $\sin \theta_m = h$. Thus,

$$v_{l,N}(h) = \frac{\text{Re } \epsilon'}{30} \left[\frac{h - h^5}{4 - 2h^2} \right] \quad (6.48)$$

For a sticking contact we can perform a similar analysis using equation (6.40) instead of (3.15). This gives,

$$v_{l,N}(h) = \frac{\text{Re } \epsilon'}{30} [h - h^3] \quad (6.49)$$

Next, we rationalize the scaling of the lift velocity with wall contacts. All velocities are driven by the shear velocity $\dot{\gamma}l$. However, the orientational drift that drives wall

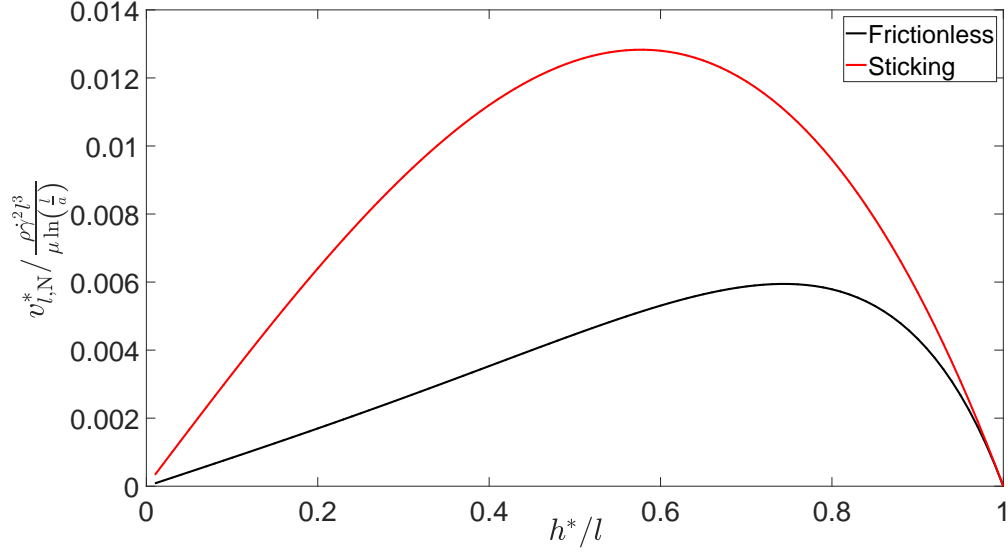


Figure 6.7: Lift velocity experienced by the fibre for $h < 1$

collisions is a finite Re effect caused by an $O(\epsilon')$ disturbance velocity field that is important only during the $O(\kappa^{-1})$ fraction of the time when the fibre is flipping, leading to an $O(\epsilon' \kappa^{-1} \text{Re})$ factor. Thus, the scaling of the dimensional lift velocity $v_{l,N}^*$ due to contact and inertial orientation drift averaged over the Jeffery orbit is $\rho \dot{\gamma}^2 l^3 / (\mu \ln [\frac{l}{a}])$.

Figure 6.7 shows the variation of wall contact lift velocity as a function of the height of the centre of the fibre for both the sticking case and the frictionless contact. The lift velocity is small near $h = 0$, because the fibre is confined to orbits close to the flow-vorticity plane where its fluid velocity disturbance and inertial rotation are small. The lift velocity for a frictionless solid-body contact grows approximately linearly with h until $h \approx 0.7$. Beyond this height, the change of orientation and lift velocity diminish as the fibre approaches the flow-gradient plane. All the important features are observed for the sticking case as well but with a higher magnitude of lift velocity at all h and shifted peak location.

In figure 6.6 we compare the evolution of the centre of mass of the fibre obtained

by tracking the trajectory with $dh^{\text{model}}/dt = v_{I,N}(h^{\text{model}})$. It can be seen that the model captures the change in position accurately for both the frictionless and sticking contacts. This confirms that at small Reynolds number, the constraint set by the accessible orbits that do not penetrate the wall captures the change of position obtained using a full description of the contact event.

There is a significant difference in fibre evolution between sticking and frictionless contact. To understand this we consider how the fibre orientation drift due to inertia, over the whole Jeffery orbit, is converted to positional displacement during the short-lived solid body contact. A sticking contact allows the pole vaulting fibre to push its center of mass a way from the wall efficiently using the large normal contact force needed to prevent the rotational motion from pushing the fibre end into the wall. A fibre with a frictionless contact has an additional tangent translational motion associated with the sliding of the contact which accommodates part of the fibre rotation with a smaller normal contact force and normal displacement. Thus we expect reduced net displacement from the wall for frictionless contact relative to the sticking case. This is reflected in the fibre evolution profiles and the analytically derived lift velocities.

The lift velocity presented in this section is driven by inertial drift of orientation and wall contact driven pole vaulting that breaks Stokes flow reversibility. This lift velocity is stronger by a factor of κ when compared to translation induced by inertia that was discussed in §6.3. Thus, to leading order, the direct effect of inertial drift of the centre of mass of the fibre does not contribute to wall contact lift velocity or the fibre dynamics in the $h < 1$ regime.

6.5 Discussion

In the previous sections we have discussed the behaviour of a fibre migrating away from a wall in shear flow in two regions: one where the fibre makes contact with the wall and one where it rotates freely in the shear flow. We now combine the results of the two previous sections and present the variation of lift velocity over the whole inner region $h^* \ll L_0$ as a function of the non-dimensionalised distance of the centre of the fibre from the wall in figure 6.8. In this plot the lift velocity is scaled as $\rho\dot{\gamma}^2 l^3 / (\mu \ln \left[\frac{l}{a} \right])$ and is shown at two values of κ . The global peak of the scaled lift velocity occurs at $h < 1$ even at a moderate aspect ratio of 25 and the frictionless case. This is expected as the inertial lift force on a freely suspended fibre is weaker than the contact force driven by the inertial drift of orientation. This contact driven motion diminishes to zero due to the driving force becoming less and less effective as $h \rightarrow 1^-$. Thus, there is a thin $O(1/\kappa)$ region around $h \rightarrow 1^-$ where the fibre makes contact with the wall but the inertially induced translational velocity is the dominant contributor to the lift velocity. In figure 6.8, the lift velocity in this very small region is approximated by the value computed for $h \rightarrow 1^+$.

To complete the description of the manner in which the lift velocity varies with h , we briefly consider the lift velocity in the outer region $h^* \geq O(L_0)$. Although a detailed analysis of lift on a fibre has not been performed in this region, it can be noted that the qualitative dependence of the lift velocity on h is likely to be similar to that for spheres, because both can be viewed as point-force-dipoles on the length scale L_0 , although the force dipole of a fibre varies periodically with time. Mclaughlin[81] showed that the lift force on a sphere has a maximum nearly equal to the large separation asymptote of the inner region, when $l \ll h^* \ll L_0$, and decays with wall separation in the outer region. It is reasonable to expect that the lift velocity of fibres exhibits a similar behaviour. Since

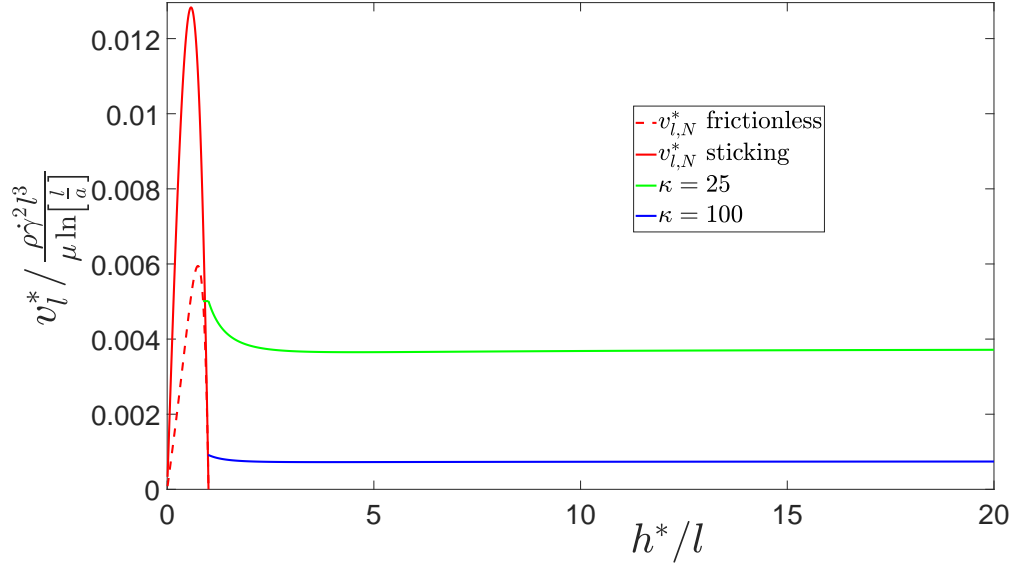


Figure 6.8: Variation of lift velocity v_l over the inner region, at aspect ratios of 25 and 100. For $h > 1$ the curves are in ascending order of aspect ratio going from top to bottom. For $h < 1$ the scaled velocity is independent of aspect ratio and both the sticking and frictionless contact cases are shown.

the lift velocity maximum of the outer region corresponds to the inner region asymptote, it can be inferred that the maximum at $h \approx 0.7$ is likely to be the global maximum for high aspect ratio fibres for all forms of contact while the value $0.03\rho\dot{\gamma}^2l^2a/(\mu \ln \left[\frac{2l}{a} \right])$ will be the global maximum lift velocity without wall contact.

Hydrodynamic lift on a fibre in wall-bounded shear flow is applicable to the design of cross-flow filtration. Cross-flow filtration is performed by flowing a suspension of particles through a channel or tube with a fluid filtrate drawn out through the porous walls. In conventional operation, the pores of the membrane block the passage of the particles, while transport processes in the channel including hydrodynamic lift, shear-induced hydrodynamic diffusion and molecular diffusion limit the accumulation of particles at the membrane surface [1]. Transport is the dominant filtration mechanism in sieve-free operation of cross-flow filtration where pores are large enough to pass the particles and only transport mechanisms, such as inertial lift, prevent particles from flowing through

the membrane with the filtrate [13, 52]. This mode of operation has the advantage of reducing fouling and being less sensitive to colloidal interactions between the particles and the wall. In microfluidic separation the transport mechanism is exploited to focus the particles in certain regions of the channel, with bifurcation of the channel achieving the desired separation. This focusing can be achieved by inertial lift [36, 79]. Thus, our analysis on hydrodynamic inertial lift will inform microfluidic separators.

In experiments on microfluidic separation by Masaeli et al[79] particles with small Reynolds number, from 0.3 to 0.75, have been shown to inertially focus in certain regions of the channel. The asymptotic Re results of our study will inform particle transport in these conditions. This is expected as an equivalent calculation on spheres by Hood et al[51] showed that inertial lift force is governed by the asymptotic Re result for particle Reynolds number as high as 10. At higher Re fibre motion can potentially halt due to competition between Jeffery orbit rotation and inertia. Subramanian & Koch[110] showed that this will happen above a critical Reynolds number $Re_m = 30 \ln(\kappa)/\kappa$ Masaeli et al[79]. The moderate aspect ratio particles studied by Masaeli et al[79] fall outside the range for which slender-body theory is quantitatively accurate. However, by keeping terms of $O(1/(\ln \kappa)^2)$, the present study provides qualitative insight into phenomena that become more important at moderate aspect ratio including wall reflections, oscillatory translation of the non-spherical particle perpendicular to the wall, inertially induced breaking of the symmetry of finite aspect ratio particle rotation, and the effects of the precise variation of particle thickness as captured by the $\ln[(1 - s^2)^{\frac{1}{2}}/a(s)]$ term in equation (6.12).

For sieve-free operation of cross-flow filtration Levesley & Bellhouse[71] performed experiments on sub-millimetre diameter particles and demonstrated inertial lift driven separation. Common targets for filtration, however, are micron sized and experiments

by Subramony[111] demonstrated the importance of inertial lift for these particles sizes. While these studies focus on separation by size the extent of non-sphericity can act also as a distinguishing feature in filtration. Our study provides the analytical framework for such an approach. This approach will be of particular interest to micron sized biological and industrial particles with non-spherical shapes[79].

To understand how design of cross-flow filtration is informed by the results of our study we consider the profile of the lift velocity as a function of h as described in figure 6.8. This can determine the position at which particles would concentrate as a result of the balance of lift and permeate velocities. If the permeate velocity is sufficiently small, the particles will remain in the outer region $h^* > L_0$ far from the membrane. As the permeate velocity is increased, the wall separation of the fibres will decrease gradually until the permeate velocity reaches the value $0.0303\rho\dot{\gamma}^2l^2a/(\mu \ln\left[\frac{2l}{a}\right])$ corresponding to the maximum lift velocity occurring in the matching region $l \ll h^* \ll L_0$. When the permeate velocity exceeds this value, the concentrated band will jump to a position near $h = 1$ in which the fibres make contact with the wall. If we take an example of a filtration system where the permeate velocity is $20\mu\text{m}/\text{s}$ and the shear rate is $\dot{\gamma} = 6 \times 10^4 \text{s}^{-1}$ with filtrate and particles characteristics $\rho = 10^3 \text{kg}/\text{m}^3$, $\mu = 10^{-3} \text{Pa s}$, $l = 2\mu\text{m}$ and $\kappa = 10$, the resultant maximum lift velocity without contact is about $29\mu\text{m}/\text{s}$ and the particle is retained in the channel. If the permeate velocity is increased, say to $50\mu\text{m}/\text{s}$, the non-spherical particle is pushed towards the membrane that acts as the wall. At this boundary, however, the lift velocity is $75\mu\text{m}/\text{s}$ for frictionless contacts and $163\mu\text{m}/\text{s}$ for sticking contacts. The permeate velocity could be increased to substantially higher values but the retention of the fibres in the channel would depend on the details of the collisions of fibres with a porous boundary. The degree to which spherical particles can be retained in a porous channel due to their excluded volume interactions with the wall has been studied theoretically by Yan et al[122] and experimentally by Van et al[116].

No comparable analysis has yet been performed for non-spherical particles whose interactions with the pores can play an important role, especially if they are of comparable size, as is typical in sieve-free operation.

Our study has provided insight into the role of non-sphericity in inertial drift. Many real world targets of sieve-free cross flow filtration, microfluidic separators, and other systems that rely on inertia-induced transport possess some degree of deviation from ideal spheres. Instead of treating non-sphericity as a hindrance our study paves the way to exploit it to achieve better outcomes. Our study also combines the non-hydrodynamic wall contact forces with inertial effects. This will provide a framework for future studies that look at particle geometry with wall effects.

6.6 Conclusions

We have studied the hydrodynamic lift velocity of a neutrally buoyant fibre in the presence of a wall at small, but finite, Reynolds number. While the lift of spheres has been studied extensively, this is the first analytical study of the lift on non-spherical, neutrally buoyant particles in wall-bounded shear flow. The disturbance fluid velocity is dominated by viscous effects provided that $h^* < L_0$. Thus the lift due to inertial effects can be obtained as a regular perturbation of the Navier-Stokes equation in terms of Reynolds number. The lift velocity has a strong dependence on geometry. The non-sphericity allows for wall contact and the fibre's lift velocity, when $a < h^* < l$, is dominated by its interactions with the wall. An equivalent case does not exist for a sphere.

For the freely rotating fibre with $h^* > l$, the lift velocity arises from the asymmetry of the flow around the fibre induced by inertial effects. In §6.3, we used a generalized reciprocal theorem to capture the first effects of inertia on the fibre velocity in terms of

integrals involving the Stokes velocity field of a fibre in wall-bounded shear flow and a Stokes comparison problem with a fibre experiencing a force normal to the wall. The force distribution on the fibre was evaluated using slender-body theory and retaining non-dimensional forces per unit length of the fibre of $O(\frac{1}{\ln 2\kappa})$ and $O(\frac{1}{[\ln 2\kappa]^2})$. The boundary conditions on the wall were satisfied using the wall reflection image singularities associated with a Stokeslet as determined by Blake & Chwang[14]. The retention of $O(\frac{1}{[\ln 2\kappa]^2})$ forces is required to obtain quantitatively accurate predictions even for aspect ratios as high as 10^4 . Terms of this order also capture a number of qualitative features that are not present at $O(\frac{1}{\ln 2\kappa})$ including a complex interaction of the fibre geometry with the imposed shear flow, the modification of the fibre force distribution due to wall interactions, the oscillatory motion of the fibre perpendicular to the wall, and the inertia-induced asymmetry of fibre rotation.

While the lift velocity of a sphere depends only on its distance from the wall, the lift velocity of a fibre depends on the wall separation as well as the fibre orientation. The force distribution on a fibre, driving the lift velocity, changes as it rotates in the shear flow. The temporal dynamics thus become important and are captured by Jeffery orbits. In particular, the Jeffery orbit $C = \infty$, corresponding to rotation in the flow-gradient plane, was shown by Subramanian & Koch[110] to be the preferred configuration when fluid inertia is present. A high aspect ratio fibre spends most of its time nearly aligned with the flow direction making a very small fluid velocity disturbance and an $O(\kappa^{-1})$ fraction of its orbit rotating through other orientations where it makes a larger disturbance. This behaviour causes the time averaged lift velocity to be a factor of κ^{-1} smaller than the value for a sphere with the same maximum dimension. The fibre lift velocity is reduced further by a factor of $\frac{1}{\ln 2\kappa}$ due to the small magnitude of the velocity disturbance of a slender body even when its axis has a substantial projection along the extensional axis of the imposed flow. These two factors cause the fibre lift velocity to have a non-

trivial scaling with its half-length l and radius a and to reach a maximum value, for $l \ll h^* \ll L_0$, of $0.0303\rho\dot{\gamma}^2 l^2 a / (\mu \ln \left[\frac{2l}{a} \right])$ in contrast to the simpler result of $0.1\rho\dot{\gamma}^2 a^3 / \mu$ for a sphere. A further qualitative difference between the lift velocity of a fibre and a sphere is that the lift velocity of a fibre changes by only a small amount as $h^* \rightarrow l$ while the lift velocity of a sphere vanishes as $h^* \rightarrow a$. This difference arises because the hydrodynamic resistance to translation of the fibre normal to the wall remains finite because of its thin cross-section and sharp edges while the lubrication resistance to normal motion of the sphere diverges.

Our study in §6.4 is the first to analyze the coupled effects of fluid-inertia induced orientational changes and pole vaulting of fibres due to wall contact. To account for the various types of solid-body interactions with the wall we consider frictionless and sticking contacts. All solid-body contacts between the fibre and wall push the fibre away from the wall and, if it is out of the flow-gradient plane, to an orbit further out of the plane. Inertial drift tends to bring the fibre to an orbit closer to the flow-gradient plane. The interplay of these two effects can be modelled as causing the fibre to drift across a sequence of quasi-steady orbits producing a net lift velocity. A detailed simulation of the orientational and translational trajectory of a fibre during wall contact was shown to be in good agreement with a model trajectory based on the quasi-steady orbit approximation. The scaling of the lift velocity due to wall contacts for $a < h^* < l$ was found to be $\rho\dot{\gamma}^2 l^3 / (\mu \ln \left[\frac{l}{a} \right])$ which is larger than the case for no wall contact by a factor of the aspect ratio. This analytically derived lift velocity showed an initial increase which is almost linear with distance from the wall, then reached a maximum of about $0.013\rho\dot{\gamma}^2 l^3 / (\mu \ln \left[\frac{l}{a} \right])$ for the sticking contact and $0.006\rho\dot{\gamma}^2 l^3 / (\mu \ln \left[\frac{l}{a} \right])$ for the frictionless contact, and decreased to zero as $h \rightarrow 1$. This maximum was shown to be the global maximum even for fibres of moderate κ in §6.5.

The lift velocity finds application in industrial processes such as cross-flow filtration and laboratory processes including microfluidic separation. In §6.5 we have briefly described how knowledge of the lift velocity can be used to better control particle separations in the flow channels. In cross-flow filtration the results can be used to design a separation based on shape as well as size and one that does not rely upon the detailed interaction of the particles with the porous membrane. Criteria were derived for the shear rate and permeate velocity range which retains particles within the bulk of the channel as well as a range that leads to pole vaulting on the membrane surface. These criteria make a distinction based on geometry and will be useful in many industrial and laboratories systems where the target particles are not spherical.

APPENDIX A
INERTIAL CLUSTERING MODEL

A.1 Inertial clustering of monodisperse spheres with gravity

The inertial clustering of equal sized particles settling has not been extensively studied in literature. A treatment of low St particles rapidly settling was performed by Rani et al[94] but there is not a simple closed form result to generate an expression similar to equation (4.3). Even DNS data is very limited, with Ireland et al [54] performing calculations only at $Fr = 0.052$. However, their DNS results show only a small shift in $g(r)$ in this gravity dominated case and so we fit this with the expression in equation (4.3) unchanged and updated c_0 and c_1 . These constants are given as,

$$\begin{aligned}
 c_0 &= 1 + \exp[-0.0282 St^3 - 0.2118 St^2 \\
 &\quad + 0.7936 St + 1.3664] \\
 c_1 &= \exp[0.0121 St^3 - 0.1729 St^2 + 0.1915 St \\
 &\quad - 0.5860]
 \end{aligned} \tag{A.1}$$

Figure A.1 makes the comparison between the prediction and DNS. A good agreement is seen but we are unable to further explore in Fr parameter space, due to the above stated limitations. Hence it is not further explored in this study.

A.2 Algebraic model for inertial clustering

The inertial clustering result presented in equation (4.13) requires integrating over the drift and diffusion results over separations spanning the many scales of turbulence.

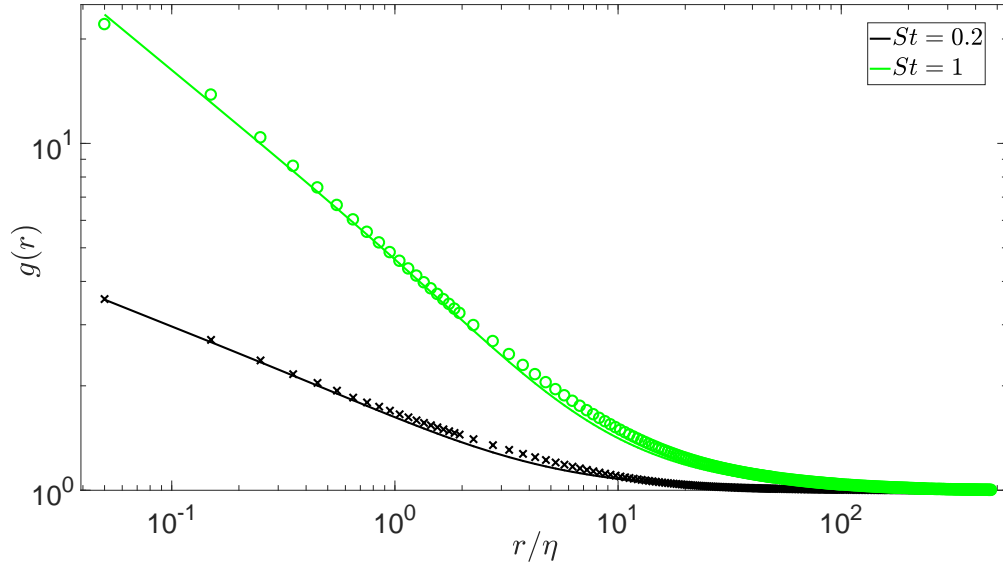


Figure A.1: $g(r)$ is shown as a function of r/η for $Re_\lambda = 398$ at $Fr = 0.052$ and $St = 0.2, 1$ with symbols denoting DNS data from Ireland et al[54] and solid lines our model shown in equation (4.3). There is good agreement between the model and DNS results across the parameter space.

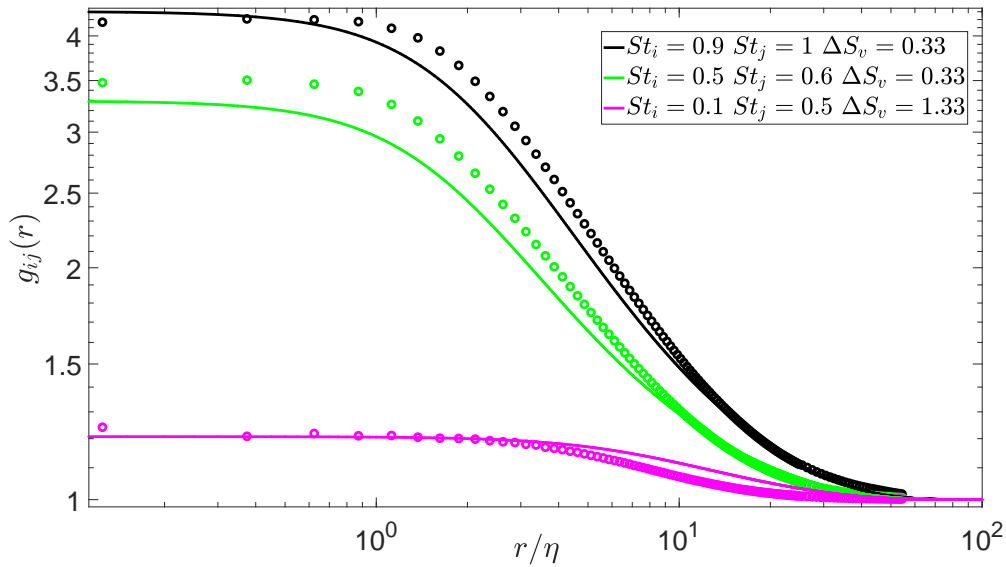


Figure A.2: $g_{ij}(r)$ is shown as a function of r/η for three bidisperse calculations performed at $Re_\lambda = 90$ and $Fr = 0.3$. The symbols denote DNS data from Dhariwal & Bragg[34] and the solid lines are the predictions of the algebraic model of inertial clustering shown in equation (A.2). Good agreement is observed across the parameter space.

While this is dramatically faster than obtaining $g_{ij}(r)$ from a DNS calculation it might still prove to be a stumbling block for evolution models where calculations need to be performed over a large parameter space. Hence a closed form algebraic expression for $g_{ij}(r)$ is derived. It is motivated by the idea of a cut off to the power law, described in equation (4.1), representing the transition from monodisperse behaviour at large separations to bidispersity flattening out the radial distribution function when the particle pairs are close to each other. While this result is exact for small St and the absence of gravity a similar result was postulated for bidisperse spheres driven by turbulence in the discussion by Lu et al[76] who only considered the dissipative range. We extend their analysis to the uniformly valid monodisperse result of equation (4.3) and obtain,

$$g_{ij}(r) = \exp\left(\frac{\log c_0}{\left(1 + \frac{\sqrt{r^2 + r_c^2}}{2\eta(1 + (\frac{St_i + St_j}{2})^{3/2})}\right)^{\frac{4}{3}} \left(1 + \frac{\eta}{\sqrt{r^2 + r_c^2}}\right)^{c_1}}\right) \quad (\text{A.2})$$

Here, c_0 and c_1 are evaluated at $St = \frac{St_i + St_j}{2}$. We have characteristic separation r_c setting the crossover from monodisperse behaviour to bidisperse plateau of $g(r)$. This cross over length is set by the competition between the characteristic settling and turbulent velocities. It is given as,

$$r_c = k_c \frac{g|St_2 - St_1| \tau_\eta (15\nu)^{\frac{1}{2}}}{\epsilon^{\frac{1}{2}}} \quad (\text{A.3})$$

Here k_c is the order one constant and, similar to the integral model, is obtained by fitting with DNS results from Dhariwal & Bragg[34] and determined to be $1 + 5 \frac{St_i + St_j}{2} |St_2 - St_1|$.

The algebraic model for inertial clustering is compared against DNS calculations by Dhariwal & Bragg[34] in figure A.2. These were carried out at $Fr = 0.3$ and $Re_\lambda = 90$ and so the correction for small Re_λ given in equation (4.5) is needed for large particle separation. From the figure it is evident that all the important features of the radial

distribution function, including variation with r , St , and $\Delta S_{v,ij}$, have been captured with reasonable accuracy.

BIBLIOGRAPHY

- [1] FW Altena and G Belfort. Lateral migration of spherical particles in porous flow channels: application to membrane filtration. *Chemical Engineering Science*, 39(2):343–355, 1984.
- [2] Wm T Ashurst, AR Kerstein, RM Kerr, and CH Gibson. Alignment of vorticity and scalar gradient with strain rate in simulated navier–stokes turbulence. *The Physics of fluids*, 30(8):2343–2353, 1987.
- [3] O Ayala, B Rosa, and L-P Wang. Effects of turbulence on the geometric collision rate of sedimenting droplets. part 2. theory and parameterization. *New Journal of Physics*, 10(7):075016, 2008.
- [4] O Ayala, B Rosa, L-P Wang, and WW Grabowski. Effects of turbulence on the geometric collision rate of sedimenting droplets. part 1. results from direct numerical simulation. *New Journal of Physics*, 10(7):075015, 2008.
- [5] Q Ayala, WW Grabowski, and L-P Wang. A hybrid approach for simulating turbulent collisions of hydrodynamically-interacting particles. *Journal of Computational Physics*, 225(1):51–73, 2007.
- [6] G A Bach, DL Koch, and A Gopinath. Coalescence and bouncing of small aerosol droplets. *Journal of fluid mechanics*, 518:157–185, 2004.
- [7] M Balthasar, F Mauss, A Knobel, and M Kraft. Detailed modeling of soot formation in a partially stirred plug flow reactor. *Combustion and Flame*, 128(4):395–409, 2002.
- [8] GK Batchelor. Slender-body theory for particles of arbitrary cross-section in stokes flow. *Journal of Fluid Mechanics*, 44(3):419–440, 1970.
- [9] GK Batchelor. Sedimentation in a dilute polydisperse system of interacting spheres. part 1. general theory. *Journal of Fluid Mechanics*, 119:379–408, 1982.
- [10] GK Batchelor and J-T. Green. The hydrodynamic interaction of two small freely-moving spheres in a linear flow field. *Journal of Fluid Mechanics*, 56(2):375–400, 1972.
- [11] GK Batchelor and JT Green. The determination of the bulk stress in a suspension of spherical particles to order c^2 . *Journal of Fluid Mechanics*, 56(3):401–427, 1972.

- [12] K V Beard and H T Ochs III. Warm-rain initiation: An overview of microphysical mechanisms. *Journal of Applied Meteorology*, 32(4):608–625, 1993.
- [13] G Belfort, RH Davis, and AL Zydney. The behavior of suspensions and macromolecular solutions in crossflow microfiltration. *Journal of Membrane Science*, 96(1-2):1–58, 1994.
- [14] JR Blake and AT Chwang. Fundamental singularities of viscous flow. *Journal of Engineering Mathematics*, 8(1):23–29, 1974.
- [15] A M Blyth, S G Lasher-Trapp, W A Cooper, C A Knight, and J Latham. The role of giant and ultragiant nuclei in the formation of early radar echoes in warm cumulus clouds. *Journal of the atmospheric sciences*, 60(21):2557–2572, 2003.
- [16] A D Bragg and L R Collins. New insights from comparing statistical theories for inertial particles in turbulence: I. spatial distribution of particles. *New Journal of Physics*, 16(5):055013, 2014.
- [17] A D Bragg, P J Ireland, and L R Collins. Mechanisms for the clustering of inertial particles in the inertial range of isotropic turbulence. *Physical Review E*, 92(2):023029, 2015.
- [18] H Brenner. The slow motion of a sphere through a viscous fluid towards a plane surface. *Chemical engineering science*, 16(3):242–251, 1961.
- [19] BK Brunk, DL Koch, and LW Lion. Hydrodynamic pair diffusion in isotropic random velocity fields with application to turbulent coagulation. *Physics of Fluids*, 9(9):2670–2691, 1997.
- [20] BK Brunk, DL Koch, and LW Lion. Turbulent coagulation of colloidal particles. *Journal of Fluid Mechanics*, 364:81–113, 1998.
- [21] B Buesser and SE Pratsinis. Design of nanomaterial synthesis by aerosol processes. *Annual review of chemical and biomolecular engineering*, 3:103–127, 2012.
- [22] K K Chandrakar, W Cantrell, K Chang, D Ciochetto, D Niedermeier, M Ovchinnikov, R A Shaw, and F Yang. Aerosol indirect effect from turbulence-induced broadening of cloud-droplet size distributions. *Proceedings of the National Academy of Sciences*, 113(50):14243–14248, 2016.
- [23] L Chaumat and J-L Brenguier. Droplet spectra broadening in cumulus clouds.

- part ii: Microscale droplet concentration heterogeneities. *Journal of the atmospheric sciences*, 58(6):642–654, 2001.
- [24] M Chen, K Kontomaris, and JB McLaughlin. Direct numerical simulation of droplet collisions in a turbulent channel flow. part ii: collision rates. *International journal of multiphase flow*, 24(7):1105–1138, 1999.
- [25] P Cherukat and J B McLaughlin. The inertial lift on a rigid sphere in a linear shear flow field near a flat wall. *Journal of Fluid Mechanics*, 263:1–18, 1994.
- [26] J Chun, D L Koch, S L Rani, Aruj A, and L R Collins. Clustering of aerosol particles in isotropic turbulence. *Journal of Fluid Mechanics*, 536:219–251, 2005.
- [27] J Chun and DL Koch. Coagulation of monodisperse aerosol particles by isotropic turbulence. *Physics of Fluids*, 17(2):027102, 2005.
- [28] Roland Clift, John R Grace, and Martin E Weber. *Bubbles, drops, and particles*. Courier Corporation, 2005.
- [29] R G Cox and H Brenner. The slow motion of a sphere through a viscous fluid towards a plane surface—ii small gap widths, including inertial effects. *Chemical Engineering Science*, 22(12):1753–1777, 1967.
- [30] ASG Curtis and LM Hocking. Collision efficiency of equal spherical particles in a shear flow. the influence of london-van der waals forces. *Transactions of the Faraday Society*, 66:1381–1390, 1970.
- [31] V Dabade, N K Marath, and G Subramanian. The effect of inertia on the orientation dynamics of anisotropic particles in simple shear flow. *Journal of Fluid Mechanics*, 791:631–703, 2016.
- [32] RH Davis. The rate of coagulation of a dilute polydisperse system of sedimenting spheres. *Journal of Fluid Mechanics*, 145:179–199, 1984.
- [33] RH Davis, JA Schonberg, and JM Rallison. The lubrication force between two viscous drops. *Physics of Fluids A: Fluid Dynamics*, 1(1):77–81, 1989.
- [34] R Dhariwal and AD Bragg. Small-scale dynamics of settling, bidisperse particles in turbulence. *Journal of Fluid Mechanics*, 839:594–620, 2018.
- [35] R Dhariwal, S L Rani, and D L Koch. Stochastic theory and direct numerical

- simulations of the relative motion of high-inertia particle pairs in isotropic turbulence. *Journal of Fluid Mechanics*, 813:205–249, 2017.
- [36] Dino Di Carlo, Jon F Edd, Daniel Irimia, Ronald G Tompkins, and Mehmet Toner. Equilibrium separation and filtration of particles using differential inertial focusing. *Analytical chemistry*, 80(6):2204–2211, 2008.
- [37] D A Drew. The lift force on a small sphere in the presence of a wall. *Chemical engineering science*, 43(4):769–773, 1988.
- [38] D A Drew, J A Schonberg, and G Belfort. Lateral inertial migration of a small sphere in fast laminar flow through a membrane duct. *Chemical engineering science*, 46(12):3219–3224, 1991.
- [39] J Einarsson, F Candelier, F Lundell, JR Angilella, and B Mehlig. Effect of weak fluid inertia upon jeffery orbits. *Physical Review E*, 91(4):041002, 2015.
- [40] J Einarsson, F Candelier, Fredrik Lundell, JR Angilella, and B Mehlig. Rotation of a spheroid in a simple shear at small reynolds number. *Physics of Fluids*, 27(6):063301, 2015.
- [41] G Feingold, W R Cotton, S M Kreidenweis, and J T Davis. The impact of giant cloud condensation nuclei on drizzle formation in stratocumulus: Implications for cloud radiative properties. *Journal of the atmospheric sciences*, 56(24):4100–4117, 1999.
- [42] J Feng, HH Hu, and DD Joseph. Direct simulation of initial value problems for the motion of solid bodies in a newtonian fluid. part 2. couette and poiseuille flows. *Journal of fluid mechanics*, 277(271):271–301, 1994.
- [43] Peter Gao, Xi Zhang, David Crisp, Charles G Bardeen, and Yuk L Yung. Bimodal distribution of sulfuric acid aerosols in the upper haze of venus. *Icarus*, 231:83–98, 2014.
- [44] SS Girimaji and SB Pope. A diffusion model for velocity gradients in turbulence. *Physics of Fluids A: Fluid Dynamics*, 2(2):242–256, 1990.
- [45] A Gopinath, SB Chen, and DL Koch. Lubrication flows between spherical particles colliding in a compressible non-continuum gas. *Journal of Fluid Mechanics*, 344:245–269, 1997.

- [46] A Gopinath and DL Koch. Collision and rebound of small droplets in an incompressible continuum gas. *Journal of Fluid Mechanics*, 454:145–201, 2002.
- [47] W W Grabowski and L-P Wang. Diffusional and accretional growth of water drops in a rising adiabatic parcel: effects of the turbulent collision kernel. *Atmospheric Chemistry and Physics*, 9(7):2335–2353, 2009.
- [48] W W Grabowski and L-P Wang. Growth of cloud droplets in a turbulent environment. *Annual review of fluid mechanics*, 45:293–324, 2013.
- [49] O G Harlen, RR Sundararajakumar, and D L Koch. Numerical simulations of a sphere settling through a suspension of neutrally buoyant fibres. *Journal of Fluid Mechanics*, 388:355–388, 1999.
- [50] EY Harper and I-Dee Chang. Maximum dissipation resulting from lift in a slow viscous shear flow. *Journal of Fluid Mechanics*, 33(2):209–225, 1968.
- [51] Kaitlyn Hood, Sungyon Lee, and Marcus Roper. Inertial migration of a rigid sphere in three-dimensional poiseuille flow. *Journal of Fluid Mechanics*, 765:452–479, 2015.
- [52] M F Hurwitz and J D Brantley. Shear separation: a promising method for protein fractionation. *Le Lait*, 80(1):121–127, 2000.
- [53] PJ Ireland, AD Bragg, and LR Collins. The effect of reynolds number on inertial particle dynamics in isotropic turbulence. part 1. simulations without gravitational effects. *Journal of Fluid Mechanics*, 796:617–658, 2016a.
- [54] PJ Ireland, AD Bragg, and LR Collins. The effect of reynolds number on inertial particle dynamics in isotropic turbulence. part 2. simulations with gravitational effects. *Journal of Fluid Mechanics*, 796:659–711, 2016b.
- [55] A Jaworek, AT Sobczyk, A Krupa, A Marchewicz, T Czech, and L Śliwiński. Hybrid electrostatic filtration systems for fly ash particles emission control. a review. *Separation and Purification Technology*, 2018.
- [56] C Jayageeth, Vivek Inder Sharma, and Anugrah Singh. Dynamics of short fiber suspensions in bounded shear flow. *International Journal of Multiphase Flow*, 35(3):261–269, 2009.
- [57] G B Jeffery. The motion of ellipsoidal particles immersed in a viscous fluid.

In *Proceedings of the Royal Society of London A: Mathematical, Physical and Engineering Sciences*, volume 102, pages 161–179. The Royal Society, 1922.

- [58] DJ Jeffrey. The calculation of the low reynolds number resistance functions for two unequal spheres. *Physics of Fluids A: Fluid Dynamics*, 4(1):16–29, 1992.
- [59] DJ Jeffrey and Y Onishi. Calculation of the resistance and mobility functions for two unequal rigid spheres in low-reynolds-number flow. *Journal of Fluid Mechanics*, 139:261–290, 1984.
- [60] SG Jennings. The mean free path in air. *Journal of Aerosol Science*, 19(2):159–166, 1988.
- [61] RE Khayat and RG Cox. Inertia effects on the motion of long slender bodies. *Journal of Fluid Mechanics*, 209:435–462, 1989.
- [62] S Kim and SJ Karrila. *Microhydrodynamics: principles and selected applications*. Courier Corporation, 2013.
- [63] D L Koch and S B Pope. Coagulation-induced particle-concentration fluctuations in homogeneous, isotropic turbulence. *Physics of Fluids*, 14(7):2447–2455, 2002.
- [64] A N Kolmogorov. A refinement of previous hypotheses concerning the local structure of turbulence in a viscous incompressible fluid at high reynolds number. *Journal of Fluid Mechanics*, 13(1):82–85, 1962.
- [65] A B Kostinski and R A Shaw. Fluctuations and luck in droplet growth by coalescence. *Bulletin of the American Meteorological Society*, 86(2):235–244, 2005.
- [66] X Ku and J Lin. Effect of two bounding walls on the rotational motion of a fiber in the simple shear flow. *Fibers and Polymers*, 10(3):302–309, 2009.
- [67] Markku Kulmala, Üllar Rannik, Evgeni L Zapadinsky, and Charles F Clement. The effect of saturation fluctuations on droplet growth. *Journal of aerosol science*, 28(8):1395–1409, 1997.
- [68] S G Lasher-trapp, W A Cooper, and A M Blyth. Broadening of droplet size distributions from entrainment and mixing in a cumulus cloud. *Quarterly Journal of the Royal Meteorological Society: A journal of the atmospheric sciences, applied meteorology and physical oceanography*, 131(605):195–220, 2005.

- [69] S G Lasher-Trapp, C A Knight, and J M Straka. Early radar echoes from ultragiant aerosol in a cumulus congestus: Modeling and observations. *Journal of the atmospheric sciences*, 58(23):3545–3562, 2001.
- [70] F Laurent and M Massot. Multi-fluid modelling of laminar polydisperse spray flames: origin, assumptions and comparison of sectional and sampling methods. *Combustion theory and modelling*, 5(4):537–572, 2001.
- [71] JA Levesley and BJ Bellhouse. Particulate separation using inertial lift forces. *Chemical engineering science*, 48(21):3657–3669, 1993.
- [72] X-Y Li, A Brandenburg, N EL Haugen, and G Svensson. Eulerian and Lagrangian approaches to multidimensional condensation and collection. *Journal of Advances in Modeling Earth Systems*, 9(2):1116–1137, 2017.
- [73] X-Y Li, A Brandenburg, G Svensson, N EL Haugen, B Mehlig, and I Rogachevskii. Effect of turbulence on collisional growth of cloud droplets. *Journal of the Atmospheric Sciences*, 75(10):3469–3487, 2018.
- [74] X-Y Li, G Svensson, A Brandenburg, and N EL Haugen. Cloud-droplet growth due to supersaturation fluctuations in stratiform clouds. *Atmospheric Chemistry and Physics*, 19(1):639–648, 2019.
- [75] P M Lovalenti and J F Brady. The hydrodynamic force on a rigid particle undergoing arbitrary time-dependent motion at small reynolds number. *Journal of Fluid Mechanics*, 256:561–605, 1993.
- [76] J Lu, H Nordsiek, and R A Shaw. Clustering of settling charged particles in turbulence: theory and experiments. *New Journal of Physics*, 12(12):123030, 2010.
- [77] H Malá, P Rulík, V Bečková, J Mihalík, and M Slezáková. Particle size distribution of radioactive aerosols after the fukushima and the chernobyl accidents. *Journal of environmental radioactivity*, 126:92–98, 2013.
- [78] N K Marath and G Subramanian. The effect of inertia on the time period of rotation of an anisotropic particle in simple shear flow. *Journal of Fluid Mechanics*, 830:165–210, 2017.
- [79] M Masaeli, E Sollier, H Amini, W Mao, K Camacho, N Doshi, S Mitragotri, A Alexeev, and D Di Carlo. Continuous inertial focusing and separation of particles by shape. *Physical Review X*, 2(3):031017, 2012.

- [80] J B McLaughlin. Inertial migration of a small sphere in linear shear flows. *Journal of Fluid Mechanics*, 224:261–274, 1991.
- [81] J B McLaughlin. The lift on a small sphere in wall-bounded linear shear flows. *Journal of Fluid Mechanics*, 246:249–265, 1993.
- [82] K B Moses, S G Advani, and A Reinhardt. Investigation of fiber motion near solid boundaries in simple shear flow. *Rheologica acta*, 40(3):296–306, 2001.
- [83] M Nagel, P-T Brun, H Berthet, A Lindner, F Gallaire, and C Duprat. Oscillations of confined fibres transported in microchannels. *Journal of Fluid Mechanics*, 835:444–470, 2018.
- [84] H Niu, W Cheng, W Pian, and W Hu. The physiochemical properties of submicron particles from emissions of industrial furnace. *World Journal of Engineering*, 13(3):218–224, 2016.
- [85] L Pan, P Padoan, J Scalo, A G Kritsuk, and M L Norman. Turbulent clustering of protoplanetary dust and planetesimal formation. *The Astrophysical Journal*, 740(1):6, 2011.
- [86] Liubin Pan and Paolo Padoan. Turbulence-induced relative velocity of dust particles. i. identical particles. *The Astrophysical Journal*, 776(1):12, 2013.
- [87] Y Peng, U Lohmann, R Leitch, C Banic, and M Couture. The cloud albedo-cloud droplet effective radius relationship for clean and polluted clouds from race and fire. *Journal of Geophysical Research: Atmospheres*, 107(D11):AAC–1, 2002.
- [88] R M Pereira, L Moriconi, and L Chevillard. A multifractal model for the velocity gradient dynamics in turbulent flows. *Journal of Fluid Mechanics*, 839:430–467, 2018.
- [89] J Taylor Perron, Michael P Lamb, Charles D Koven, Inez Y Fung, Elowyn Yager, and Máté Ádámkovics. Valley formation and methane precipitation rates on titan. *Journal of Geophysical Research: Planets*, 111(E11), 2006.
- [90] A J Petersen, L Baker, and F Coletti. Experimental study of inertial particles clustering and settling in homogeneous turbulence. *Journal of Fluid Mechanics*, 864:925–970, 2019.

- [91] M Pinsky and A Khain. Formation of inhomogeneity in drop concentration induced by the inertia of drops falling in a turbulent flow, and the influence of the inhomogeneity on the drop-spectrum broadening. *Quarterly Journal of the Royal Meteorological Society*, 123(537):165–186, 1997.
- [92] D Qi. Lattice-boltzmann simulations of particles in non-zero-reynolds-number flows. *Journal of Fluid Mechanics*, 385:41–62, 1999.
- [93] J Qian and CK Law. Regimes of coalescence and separation in droplet collision. *Journal of Fluid Mechanics*, 331:59–80, 1997.
- [94] S L Rani, V K Gupta, and D L Koch. Clustering of rapidly settling, low-inertia particle pairs in isotropic turbulence. part 1. drift and diffusion flux closures. *Journal of Fluid Mechanics*, 871:450–476, 2019.
- [95] W C Reade and L R Collins. Effect of preferential concentration on turbulent collision rates. *Physics of Fluids*, 12(10):2530–2540, 2000.
- [96] T Rosén, F Lundell, and CK Aidun. Effect of fluid inertia on the dynamics and scaling of neutrally buoyant particles in shear flow. *Journal of Fluid Mechanics*, 738:563–590, 2014.
- [97] PGf Saffman and JS Turner. On the collision of drops in turbulent clouds. *Journal of Fluid Mechanics*, 1(1):16–30, 1956.
- [98] PGT Saffman. The lift on a small sphere in a slow shear flow. *Journal of fluid mechanics*, 22(02):385–400, 1965.
- [99] J PLC Salazar, J De Jong, L Cao, S H Woodward, H Meng, and L R Collins. Experimental and numerical investigation of inertial particle clustering in isotropic turbulence. *Journal of Fluid Mechanics*, 600:245–256, 2008.
- [100] E-W Saw, R A Shaw, J PLC Salazar, and L R Collins. Spatial clustering of polydisperse inertial particles in turbulence: Ii. comparing simulation with experiment. *New Journal of Physics*, 14(10):105031, 2012.
- [101] A Scheuer, E Abisset-Chavanne, F Chinesta, and R Keunings. Second-gradient modelling of orientation development and rheology of dilute confined suspensions. *Journal of Non-Newtonian Fluid Mechanics*, 237:54–64, 2016.
- [102] M Shin, D L Koch, and G Subramanian. Structure and dynamics of dilute suspen-

- sions of finite-reynolds-number settling fibers. *Physics of Fluids (1994-present)*, 21(12):123304, 2009.
- [103] H Siebert, M Wendisch, T Conrath, U Teichmann, and J Heintzenberg. A new tethered balloon-borne payload for fine-scale observations in the cloudy boundary layer. *Boundary-layer meteorology*, 106(3):461–482, 2003.
- [104] A P Siebesma, C S Bretherton, A Brown, A Chlond, J Cuxart, P G Duynkerke, H Jiang, M Khairoutdinov, D Lewellen, C-H Moeng, et al. A large eddy simulation intercomparison study of shallow cumulus convection. *Journal of the Atmospheric Sciences*, 60(10):1201–1219, 2003.
- [105] A Slingo. Sensitivity of the earth’s radiation budget to changes in low clouds. *Nature*, 343(6253):49, 1990.
- [106] M v Smoluchowski. Versuch einer mathematischen theorie der koagulationskinetik kolloider lösungen. *Zeitschrift für physikalische Chemie*, 92(1):129–168, 1918.
- [107] KR Sreenivasan and P Kailasnath. An update on the intermittency exponent in turbulence. *Physics of Fluids A: Fluid Dynamics*, 5(2):512–514, 1993.
- [108] C A Stover and C Cohen. The motion of rodlike particles in the pressure-driven flow between two flat plates. *Rheologica Acta*, 29(3):192–203, 1990.
- [109] S Strednak, S Shaikh, J E Butler, and É Guazzelli. Shear-induced migration and orientation of rigid fibers in an oscillatory pipe flow. *Physical Review Fluids*, 3(9):091301, 2018.
- [110] G Subramanian and D L Koch. Inertial effects on fibre motion in simple shear flow. *Journal of Fluid Mechanics*, 535:383–414, 2005.
- [111] Sharanya Subramony. Employing shear induced hydrodynamic lift to achieve sieve-free separation based on size in cross-flow filtration. 2017.
- [112] S Sundaram and LR Collins. Collision statistics in an isotropic particle-laden turbulent suspension. part 1. direct numerical simulations. *Journal of Fluid Mechanics*, 335:75–109, 1997.
- [113] RR Sundararakumar and D L Koch. Non-continuum lubrication flows between particles colliding in a gas. *Journal of Fluid Mechanics*, 313:283–308, 1996.

- [114] W Sutherland. Lii. the viscosity of gases and molecular force. *The London, Edinburgh, and Dublin Philosophical Magazine and Journal of Science*, 36(223):507–531, 1893.
- [115] PA Vaillancourt, MK Yau, P Bartello, and W W Grabowski. Microscopic approach to cloud droplet growth by condensation. part ii: Turbulence, clustering, and condensational growth. *Journal of the atmospheric sciences*, 59(24):3421–3435, 2002.
- [116] AMC Van Dinther, CGPH Schroën, A Imhof, HM Vollebregt, and RM Boom. Flow-induced particle migration in microchannels for improved microfiltration processes. *Microfluidics and nanofluidics*, 15(4):451–465, 2013.
- [117] H Wang, AZ Zinchenko, and RH Davis. The collision rate of small drops in linear flow fields. *Journal of fluid mechanics*, 265:161–188, 1994.
- [118] J Warner. The microstructure of cumulus cloud. part iii. the nature of the updraft. *Journal of the Atmospheric Sciences*, 27(4):682–688, 1970.
- [119] CD Westbrook, RC Ball, PR Field, and AJ Heymsfield. Theory of growth by differential sedimentation, with application to snowflake formation. *Physical Review E*, 70(2):021403, 2004.
- [120] J-P Williams, C H van der Bogert, A V Pathare, G G Michael, M R Kirchoff, and H Hiesinger. Dating very young planetary surfaces from crater statistics: A review of issues and challenges. *Meteoritics & Planetary Science*, 53(4):554–582, 2018.
- [121] Y Xue, L-P Wang, and W W Grabowski. Growth of cloud droplets by turbulent collision–coalescence. *Journal of the Atmospheric Sciences*, 65(2):331–356, 2008.
- [122] Zong-Yi Yan, Andreas Acrivos, and Sheldon Weinbaum. Fluid skimming and particle entrainment into a small circular side pore. *Journal of Fluid Mechanics*, 229:1–27, 1991.
- [123] S-M Yang and L G Leal. Particle motion in stokes flow near a plane fluid–fluid interface. part 2. linear shear and axisymmetric straining flows. *Journal of Fluid Mechanics*, 149:275–304, 1984.
- [124] MA Yavuz, RPJ Kunnen, GJF Van Heijst, and HJH Clercx. Extreme small-scale

- clustering of droplets in turbulence driven by hydrodynamic interactions. *Physical review letters*, 120(24):244504, 2018.
- [125] PK Yeung and SB Pope. Lagrangian statistics from direct numerical simulations of isotropic turbulence. *Journal of Fluid Mechanics*, 207:531–586, 1989.
- [126] L I Zaichik and V M Alipchenkov. Pair dispersion and preferential concentration of particles in isotropic turbulence. *Physics of Fluids*, 15(6):1776–1787, 2003.
- [127] L I Zaichik and V M Alipchenkov. Refinement of the probability density function model for preferential concentration of aerosol particles in isotropic turbulence. *Physics of Fluids*, 19(11):113308, 2007.
- [128] L I Zaichik, O Simonin, and V M Alipchenkov. Collision rates of bidisperse inertial particles in isotropic turbulence. *Physics of Fluids*, 18(3):035110, 2006.
- [129] Leonid I Zaichik and Vladimir M Alipchenkov. Statistical models for predicting pair dispersion and particle clustering in isotropic turbulence and their applications. *New Journal of Physics*, 11(10):103018, 2009.
- [130] GR Zeichner and WR Schowalter. Use of trajectory analysis to study stability of colloidal dispersions in flow fields. *AIChE Journal*, 23(3):243–254, 1977.